Department of Chemistry

University College London

Hydrogenation Reactions Catalysed by Organometallic Complexes

A thesis submitted for the degree of Doctor of Philosophy

by

Hsin-Yi Chen

January 2012

Declaration

I, Hsin-Yi Chen, confirm that the work presented in this PhD thesis is my own. Where information has been derived from other sources, I confirm that this has been indicated.

Hsin-Yi Chen

January 2012

Acknowledgements

Heartfelt appreciation goes to my supervisor Prof. Richard Catlow and Dr. Devis Di Tommaso. Without their generous support, guidance, advice, ideas and time during my entire PhD, I would not have been able to become an independent and confident scientist. I also thank them for their prompt and patient editing of my publication papers, proofreading of my thesis, and for many other useful discussions related to my PhD.

Many thanks to Dr. Graeme Hogarth for his helpful discussions, guidance and support on not only projects but also other perspectives that a PhD student should learn and know, i.e., presentation skills, writing a CV, interview tips and future planning.

Thanks are also due to our collaborators — Prof. Jianliang Xiao, Dr. Chao Wang and Dr. XiaoFeng Wu at the University of Liverpool — for inspiring me to enter the field of organometallic catalysis, and for their patience in answering my questions.

I am very grateful to the UCL, EPSRC, and the Ministry of Education in Taiwan, for having kindly provided full funding for my PhD studies. I also thank Director Lee, Miss Huei-Chun and Miss Eileen of the Cultural Division, Taipei Representative Office in the UK for their constant caring concern.

I would like to thank Dr. Jyh-Pin Chou, Dr. Xinzheng Li, Mr. Raimondas Galvelis and Dr. Florian Schiffmann for their helpful computational discussions. I thank Prof. Steven Bishop, Prof. Ching-Ming Wei, Prof. Fu-Su Yen, Prof. Jing-Jong Shyue, Prof. Ya-Ping Chiu, Prof. Hui-Yu Chen, Prof. Richard Oldman, Prof. Peijun Hu, Prof. Angelos Michaelides, Prof. Gopinathan Sankar, Dr. Antonio Torrisi, Dr. Luis Gómez-Hortigüela, Dr. Cheng-Rong Hsing, Dr. Aron Walsh, Dr. David Scanlon, Dr. Malek Deifallah, Dr. Miguel Mora Fonz and Dr. Boutheina Kerkeni for talking me through a great variety of topics, providing helpful guidance.

I would also like to thank Miss Lillian Chia and Mr. Zamaan Raza for their efforts in proofreading this thesis.

There are too many other people to whom I also owe a debt of gratitude, in particular my friends, whose company has provided much-needed laughter in my PhD life. Their companionship, help and support have helped ease my stress and frustration. Thank you, Aisha, Alastair, Alexey, Alice, Andrew, Andy, Ben, Christine, Claire, Crispin, Erlend, George, Hameedah, Husn Islam, Iman, Ivan, Isaac, Jeff, Jiri, Joh, Kamilah, Kerry, Kim, Mark, Martin, Martijn, Martina, Miller, Mohamed, Myung Hee, Nenna, Nazar, Ricardo, Richard, Rozie, Saima, Scott, Stephen, Sushan, Szymon, Vladimir, and members of the ZK Association in Taiwan. To anyone who might have been left out here: I am thankful all the same.

For administrative assistance, I would next like to thank Dr. Ian Watts, Kay Awan, Laura Mulcahy, Liz Read, Ninik Smith, Mary Lou and Shazia Riaz. For technical assitance, I am grateful to Charles Willoughby, David Ladd and Jörg Saßmannshausen and Tony Field of the Department of Chemistry.

Lastly, and most importantly, I am eternally grateful to my parents and my extended family for their unconditional love, concern, understanding, moral support and encouragement during all the stressful times over the last few years. Special thanks go to "Mother" for inspiring me with energy and clarity, and for wordless guidance and support in helping me overcome all the challenges and hardship.

Publications

- H. Y. T. Chen, D. Di Tommaso, G. Hogarth, and C. R. A. Catlow, "The effects of ligand variation on enantioselectivity hydrogenation catalysis by $Ru(H)_2$(diphosphine)(amine) complexes" *Dalton Transactions 40th Anniversary issue*, DOI:10.1039/C1DT11244A. (accepted)

- H. Y. T. Chen, D. Di Tommaso, G. Hogarth, and C. R. A. Catlow, "Correlating enantioselectivity with activation energies in the asymmetric hydrogenation of acetophenone catalysed by Noyori-type complexes" *Catalysis Letters* **141**, 1761 (2011)

- H. Y. T. Chen, D. Di Tommaso, G. Hogarth, and C. R. A. Catlow, "*trans*-$Fe^{II}(H)_2$(diphosphine)(diamine) complexes as alternative catalysts for the hydrogenation of ketones? A DFT study" *Dalton Transactions*, **40**, 402 (2011). (hot article)

Abstract

In this thesis we have computationally studied two types of reduction processes which can be classified as asymmetric hydrogenation of ketones and reduction of imines. Density functional theory has been applied throughout the thesis.

The reduction of acetophenone to phenylethanol catalysed by the *trans*-Ru(II)H_2(diphosphine)(diamine) has been studied with an emphasis on the effect of the structure of the diphosphine and diamine ligands. The computed reaction pathways of the Ru(II)H_2(diphosphine)[(*S*,*S*)-DPEN] catalysed reactions with different (*S*)-diphosphine ligands (XylBINAP, TolBINAP and BINAP) shows that the presence of two methyl groups in the *meta* position is critical to obtaining a high difference in activation energy for the reaction pathways associated with the (*R*)- and (*S*)-alcohols, and consequently high enantioselectivity. The effect of the diamine structure, while keeping the TolBINAP and XylBINAP fixed, has also been analysed. To enhance the enantioselectivity of the TolBINAP system, the addition of two methyl groups and the removal of a phenyl group on the diamine (DMAPEN) create the necessary steric interactions. We conclude this section by reporting a correlation between the enantiomeric excess and the difference in the computed activation energies along the two most favourable (*S*)- and (*R*)-reaction pathways, which shows that the computational procedure adopted could be used to predict the enantiomeric excess of ketone hydrogenation reactions catalysed by Noyori-type catalysts, and assist in the choice of ligands when optimising the enantiomeric excess.

Calculations yield new insights into the structural, electronic and catalytic properties of the hydrogenation of ketones catalysed by the simplified Fe(II)H_2(PH_3)$_2$(en) and real Fe(II)H_2(diphosphine)(diamine) complexes. Calculations conducted using several different functionals on the *trans*- and *cis*-isomers of Fe(II)H_2[(*S*)-XylBINAP][(*S*,*S*)-DPEN] complexes show that, as with the Ru(II)H_2(diphosphine)(diamine) complexes, the *trans*-[Fe(II)H_2(diphosphine)(diamine)] complex is the more stable isomer. Analysis of the spin states of the *trans*-[Fe(II)H_2(diphosphine)(diamine)] complexes also shows that the singlet state is significantly more stable than the triplet and quintet states, as with the Ru(II)H_2(diphosphine)(diamine) complexes. Calculations on the catalytic cycle for the hydrogenation of ketones using the two simplified *trans*-[M(II)H_2(PH_3)$_2$(en)] catalysts, where M is either Ru or Fe, show that the mechanism of reactions as well as the activation

energies are very similar, in particular: (a) the ketone/alcohol hydrogen transfer reaction occurs through the metal–ligand bifunctional mechanism, with energy barriers of 3.4 kcal/mol and 3.2 kcal/mol for the ruthenium- and iron-catalysed reactions respectively; (b) the heterolytic splitting reactions of H_2 across the M=N bond for the regeneration of the ruthenium and iron catalysts have activation barriers of 13.8 kcal/mol and 12.8 kcal/mol respectively, and the heterolytic splitting steps are expected to be the rate-determining steps for both catalytic systems. The reduction of acetophenone by the *trans*-[Fe(II)H_2\{(*S*)-XylBINAP\}\{(*S*,*S*)-DPEN\}] complexes along the two competitive reaction pathways shows that the intermediates for the iron catalytic system are similar to those responsible for a high enantioselectivity of (*R*)-alcohol in the *trans*-[Ru(II)H_2\{(*S*)-XylBINAP\}\{(*S*,*S*)-DPEN\}] catalysed acetophenone hydrogenation reaction. Thus, the high enantiomeric excess in the hydrogenation of acetophenone could, in principle, be achieved using iron catalysts.

In experimental work, Xiao and co-workers discovered cyclometalated iridium complexes in imine reduction with an unusually broad substrate scope, which shows that the more positive hydricity of iridium hydride affords a higher activity. To study these systems computationally, we initially tested parameters, including exchange-correlation functionals, basis sets and pseudopotentials, subsequently studying the charge and molecular orbital properties of isolated iridium(III) catalysts with different electron-donating and withdrawing functional groups, and investigating their mechanistic details. Three possible reaction pathways in the hydride formation step and six possible reaction pathways in the hydride transfer step have been suggested to locate transition states in both the gas phase and methanol solution. Our results show that hydride formation is the rate-determining step and with explicit methanol included in the reaction, the activation energies in the hydride formation and hydride transfer steps drop by *ca.* 10 and 4 kcal/mol respectively, compared with those computed in the gas phase.

Contents

List of Tables

List of Figures

List of Schemes

Abbreviations

Symbol	Definition
DFT	density functional theory
ee	enantiomeric excess
EX	exchange correlation functionals
$\mathbf{E_a}$	activation energy
$\mathbf{\Delta E_a}$	difference in activation energy
LUMO	lowest unoccupied molecular orbital
HOMO	highest occupied molecular orbital
$\boldsymbol{\tau}$	out-of-plane bending of the carbonyl carbon
$\boldsymbol{\gamma}$	torsional angle of the phenyl group along the C-C(=O)
RA	reductive amination
Ar	aryl group
Cp*	pentamethylcyclopentadiene
Me	methyl group
Ph	phenyl group
BINAP	2,2'-bis(diphenylphosphino)-1,1'-binaphthyl
TolBINAP	2,2'-bis(di-4-tolylphosphino)-1,1'-binaphthyl
XylBINAP	2,2'-bis(diphenylphosphino)-1,1'-binaphthyl
DPEN	1,2-diphenylethylenediamine
DMDPEN	*N*,*N*-dimethyl-1,2-diphenylethylenediamine
DMAPEN	2-dimethylamino-1-phenylethylamine
INT	intermediate
TS	transition state
PRO	product + intermediate species
HF	hydride formation
HT	hydride transfer

Chapter 1 **General Introduction**

1.1 Overview and Aims

The aim of chemical synthesis is the production of compounds in an economical, energy-efficient, environmentally-friendly and sustainable way. Moreover, health care requires the development of efficient and effective pharmaceuticals with minimal side effects. These concerns have increased the demand for chemical processes with a higher selectivity, a minimum amount of waste and high purity products.

H_2 is the simplest stable molecule; hydrogen gas is a clean and abundant resource, therefore hydrogenation is a core process in chemical synthesis[1]. In the pharmaceutical industry, one of the key steps in a reaction is the catalytic hydrogenation of polar bonds, such as C=O and C=N, and their asymmetric counterparts. Over the past 40 years, ruthenium complexes have been one of the successful catalysts applied in homogeneous hydrogenation[2] and have achieved a high reactivity and selectivity[1a,3]. It has been found that certain ruthenium complexes with amine ligands are much more active than other metal complexes for the H_2-hydrogenation of ketones[3]. A major breakthrough in chiral-catalysed hydrogenation was made by Noyori and co-workers who were awarded the Nobel Prize in 2001[3a]. However, developing new catalysts that can be applied to a wider range of substrates is still challenging; it is therefore important to develop a technique by which chemists can rapidly evaluate the selectivity of proposed new catalysts. The work in this thesis is based on Noyori's findings and uses computational techniques to firstly investigate the asymmetric hydrogenation of ketones catalysed by ruthenium(II) diphosphine diamine complexes to correlate the enantioselectivity and activation energy. Secondly, we examine the possibility of replacing ruthenium with iron in this type of catalytic process. Thirdly, we turn to the reduction of imino bonds, which is a practically useful reaction, but is still an under-developed process where there are challenges to be overcome. Here, in collaboration with Xiao, at the University of Liverpool, we have investigated imine reduction, an intermediate step in reductive amination by a cyclometalated iridium(III) complex, in order to develop an asymmetric transfer hydrogenation with a high activity and selectivity. In particular, we have studied the mechanistic details of imine reduction catalysed by achiral cyclometalated iridium(III) complexes.

1.2 Structure of the thesis

The results in this thesis are divided into two main parts. Part I (Chapters 4 and 5) concerns the asymmetric hydrogenation of ketones catalysed by the ruthenium(II)-based and iron(II)-based Noyori-type complexes. Part II (Chapter 6) concerns imine reduction catalysed by the cyclometalated iridium(III) complexes. The main objective of Part I is firstly to examine the correlation between the difference in activation energy and enantioselectivity and secondly to search for a sustainable catalyst. The goal of Part II is to understand the mechanism operative in the novel iridium-based catalysis.

The following two chapters provide the necessary background to the results reported later. Chapter 2 delineates the experimental and computational background relevant to the field. Chapter 3 is devoted to the computational theories and methodology; the subsequent three chapters focus on the three systems: the asymmetric hydrogenation of acetophenone catalysed by the *trans*-[RuH_2(diphosphine)(diamine)] complexes (Chapter 4); the exploration of acetophenone hydrogenation reactions using the proposed *trans*-[FeH_2(diphosphine)(diamine)] catalysts (Chapter 5); imine reduction catalysed by the cyclometalated iridium(III) complexes (Chapter 6). These are followed in Chapter 7 by conclusions and possible future work.

Chapter 2 **Asymmetric Synthesis and Imine Reduction: Background**

2.1 The importance of asymmetric synthesis

A molecule is "chiral" when it cannot be superimposed on its mirror image. The two molecules are enantiomers and are said to be enantiomeric with each other. Enantiomers have the same chemical and physical properties when they interact in a non-chiral environment. When they interact with another chiral object, differences are apparent.

Many macromolecules in living systems occur in only one enantiomeric form. Only biological compounds with the correct chirality can interact with its receptor site in a chiral manner, hence it can be deduced that enantiomers may interact differently with the receptor, accounting for different effects[4]. In practice, two-thirds of prescription drugs are chiral compounds, and often the interest is focused on one of the two enantiomers[5]. For example, in pharmaceuticals and pesticides, usually only one of the enantiomers has the desired biological activity, while the other can be inactive or can have damaging, fatal or undesired effects. The use of agrochemicals of the correct chirality may reduce the impact on the environment. Clearly, the optimal properties of chiral compounds can only be obtained when they are processed in a pure single enantiomeric form and indeed some enantiomers are harmful[6]. The rising public awareness of health requires the development of drugs with higher selectivity; legal and regulatory issues also require the pharmaceutical industry to prepare and commercialise their products as single enantiomers[7].

Optically-active compounds are prepared mainly by asymmetric synthesis. A search for the keywords "asymmetric synthesis" and "asymmetric and enantioselective" on the ISI Web of Knowledge (Figure 2.1) demonstrates the rapid growth of this field. Amongst all of the procedures for obtaining single-enantiomerical compounds, asymmetric catalysis is probably the most economical, efficient and environmentally-friendly method[8].

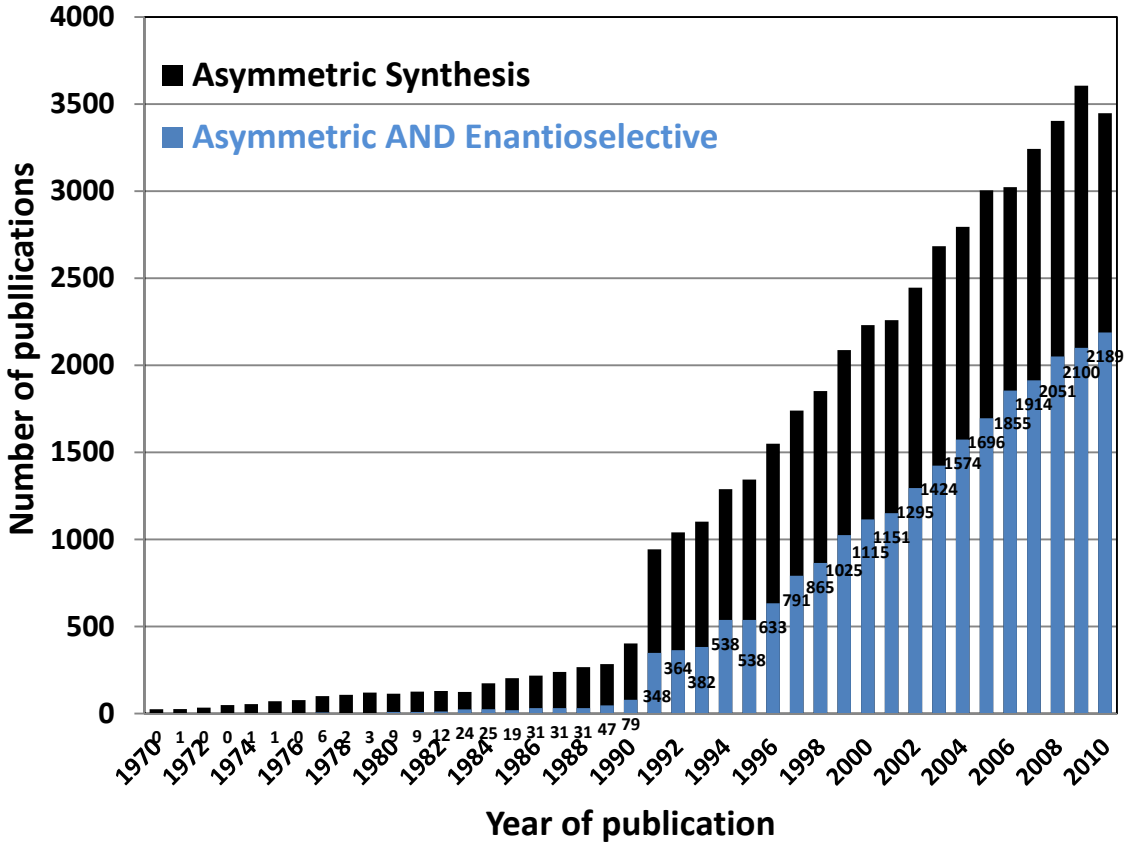

Figure 2.1: Number of publications containing the keywords "asymmetric synthesis" and "asymmetric AND enantioselective" in their title versus year of publication. Data are extracted from the ISI Web of Knowledge.

2.2 Asymmetric hydrogenation

Asymmetric hydrogenation is a reaction involving hydrogen transfer from a hydrogen donor to a hydrogen acceptor. It may be the most attractive approach in asymmetric catalysis in view of the economic advantage and environmentally-benign nature of the processes, yielding by-products without waste and free from hazard as well as being operationally simple. Therefore, asymmetric hydrogenation has been increasingly significant in practical organic synthesis. In particular, the hydrogenation of prochiral compounds to enantiomerically-pure alcohols is one of the most widely-applied processes

in organic chemistry due to the demand for optically-active secondary alcohols for both pharmaceuticals and advanced materials. Moreover, this type of asymmetric catalysis can benefit not only the development of pharmaceuticals, agrochemicals, and pesticides, but also flavours, fragrances, fungicides and pheromones[8a,8b]. In the late 1960s, the first asymmetric hydrogenation emerged with the rhodium-based catalysts developed by Knowles, which could convert a non-chiral substrate to a chiral product[9]. In 1971, Izumi revealed a reduction of methyl acetoacetate to methyl-hydroxybutyrate using Raney nickel modified with tartaric acid, which affords an enantiomeric excess (*ee*) of up to 80%[10]. The first industrial application of Knowles's method was in Monsanto's production of L-DOPA (a drug used in the treatment of Parkinson's Disease)[11].

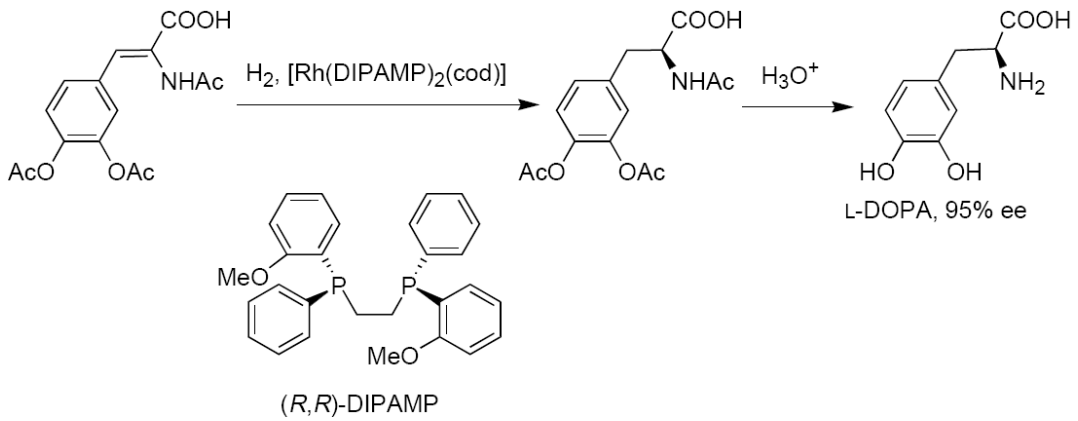

Scheme 2.1: Asymmetric hydrogenation of Monsanto's production of L-DOPA.

In 1981, it was shown by Bianchi *et al.* that ruthenium-based complexes could effect the asymmetric transfer reduction of a prochiral ketone using *i*-PrOH[12]. Further progress was made in 1996 when Noyori *et al.* reported a chiral ruthenium(II) complex system consisting of diphosphine and 1,2-diamine ligands, which when dissolved in the presence of a base and 2-propanol enabled the enantioselective reaction of aromatic ketones with high efficiency at room temperature[13].

Transition metals play a fundamental role in asymmetric hydrogenation catalysis. In particular, the later transition metals, such as ruthenium (Ru), rhodium (Rh), palladium (Pd),

iridium (Ir) and platinum (Pt) perform well in homogeneous catalysed reactions. In this thesis, the focus has been on ruthenium- and iridium-based catalysts, but with an exploration of the possibility of developing iron-based catalysts.

2.3 Prediction of enantiomeric excess (*ee*)

Figure 2.2 shows the reaction coordinate diagram of an asymmetric reaction generating equal amounts of (*R*)- and (*S*)- configurations in products that are racemate with an *ee* of 0%. Figure 2.3 shows the reaction coordinate diagram of an asymmetric reaction generating different amounts of (*R*)- and (*S*)-configurations of enantiomers, in which the activation energy favours the (*S*)-product.

Enantioselectivity is the preferential formation of molecules of one chirality (enantiomer) over the other and is usually measured as the enantiomeric excess (*ee*):

$$ee = \frac{R-S}{R+S}\%, \qquad 2.1$$

where *R* and *S* are stereochemical descriptors defined in the Cahn-Ingold-Prelog (CIP) system[14]; [*R*] denotes the number of moles of one enantiomer and [*S*] indicates that of the other enantiomer.

Enantioselective reactions are usually under kinetic control at a certain temperature and therefore the final [*S*]/[*R*] ratio is given as follows:

$$\frac{[S]}{[R]} = e^{-\Delta\Delta G_{S-R} / N_A k_B T} \quad , \qquad 2.2$$

where ΔΔG is the difference in free energies of activation for the (*S*)- and (*R*)-products respectively; N_A is the Avogadro constant; k_B is. the Boltzmann constant.

The Curtin-Hammett principle[15] postulates that in a reaction having a pair of reactive intermediates which interconvert rapidly, with each going irreversibly to a different

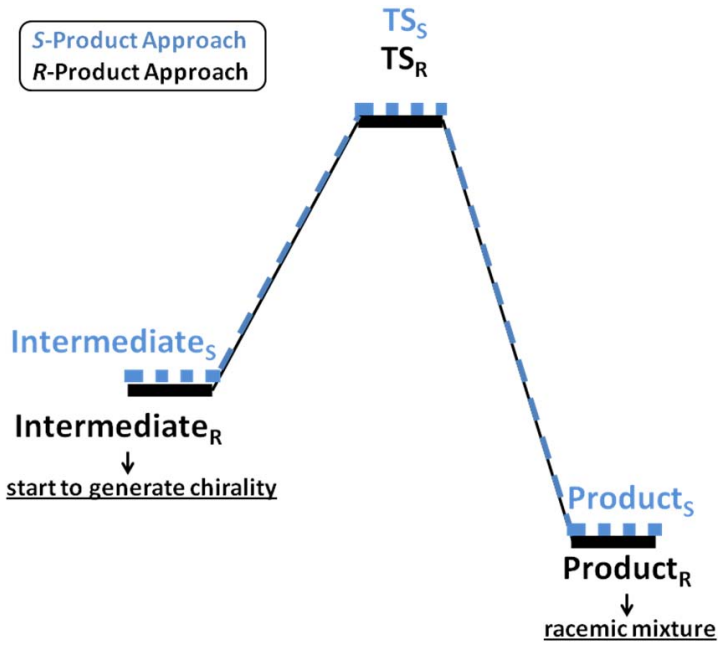

Figure 2.2: A typical asymmetric reaction generating (*R*)- and (*S*)- configuration of products — racemic mixture[16].

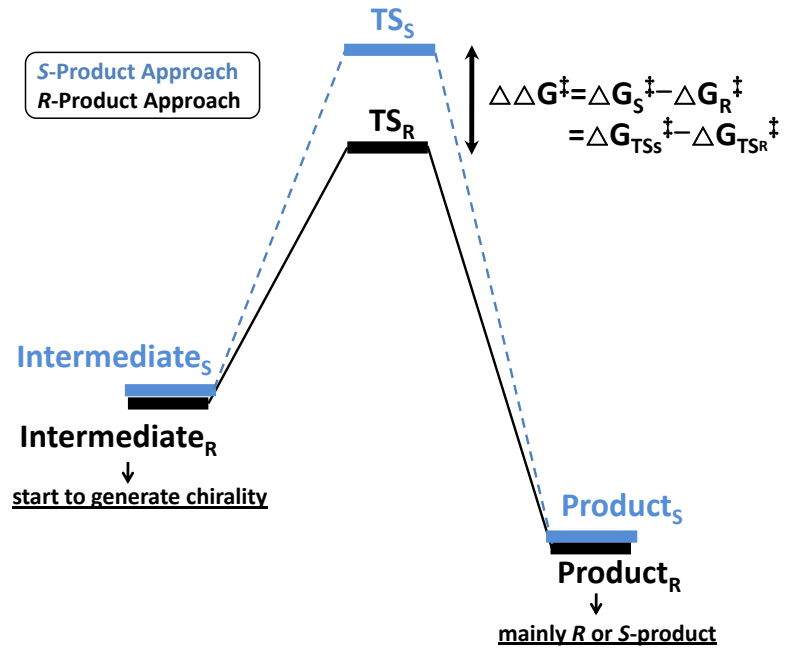

Figure 2.3: A typical asymmetric reaction generating (*R*)- and (*S*)- configuration of products — non-racemic mixture[16].

product, the product ratio will depend only on the difference in the free energy of the transition state associated with each product, and will be independent of the difference in the free energy of the intermediates. Thus, once we have obtained the free energy, we can predict the value of the *ee* based as follows:

$$\%ee_{theory}\left(\Delta\Delta G\right)=\frac{1-e^{-\Delta\Delta G_{S-R}/N_A k_B T}}{1+e^{-\Delta\Delta G_{S-R}/N_A k_B T}}\times 100\,. \qquad 2.3$$

However, in the large Noyori-type catalysts, it is very difficult to evaluate vibrational contributions to the entropies which are needed to obtain free energies at the DFT level of theory. The free energies can be expected to be dominated by the electronic energy, as shown in the recent work of Harvey *et al.*[17]; therefore the difference in free activation energies (ΔΔG) may be approximated by the difference in activation energies (ΔE_a).

2.4 Asymmetric reduction of C=O bonds using ruthenium complexes with BINAP

In organometallic asymmetric catalysis, an appropriate combination of a metal species and chiral ligands is crucial to synthesising high-performance catalysts for asymmetric hydrogenation. The electron-donating organic ligands enhance the hydride-donating ability of the catalyst. In addition, the stereochemical control of attractive or repulsive interactions has a crucial influence on attaining a high catalytic activity.

Noyori and co-workers pioneered the development of the ruthenium-based diphosphine-diamine complexes as effective and efficient catalysts for the selective hydrogenation of ketones[18]. The most commonly-used diphosphine and diamine ligands of the Noyori-type catalysts are BINAP [(*S* or *R*)-2,2'-bis(diphenylphosphino)-1,1'-binaphthyl][19], DPEN [(*S*,*S* or *R*,*R*)-1,2-diphenylethylenediamine] and their derivatives[18a,20]. BINAP is a fully aromatic, axially dissymmetric C_2-chiral diphosphane which has strong steric and electronic effects, resulting from well-designed phosphine ligands, on transition-metal complexes. The structures of (*S*)-BINAP and (*R*)-BINAP are displayed in Scheme 2.2.

The chiral diphosphine and diamine ligands act in a cooperative manner to improve activity and control enantioselectivity[21], and their modification allows the generation of efficient and tuneable hydrogenation catalysts[8a]. For example, in Scheme 2.3, when using identical (*S*,*S*)-DPEN diamine, [**1a/2a**] (*S*-XylBINAP/*S*,*S*-DPEN) is able to reduce acetophenone (ACP) to (*R*)-phenylethanol with an enantiomeric excess (*ee*) of 99%[22], whereas when the reaction is catalysed by either [**1b/2a**] (*S*-TolBINAP/*S*,*S*-DPEN) or [**1c/2a**] (*S*-BINAP/*S*,*S*-DPEN), the *ee* decreases to 82%[23] and 83%[24] respectively, the ligands differing only in the position of the methyl group on the aryl rings. However, upon alteration of the diamine by fixing (*S*)-TolBINAP, the reaction catalysed by [**1b/2b**] (*S*-TolBINAP/*S*,*S*-DMDPEN) affords the (*R*)-phenylethanol in only 22% *ee*[25], whilst the reactions catalysed by [**1b/2c**] (*S*-TolBINAP/*S*-DMAPEN) and [**1b/2d**] (*S*-TolBINAP/*R*-DMAPEN) generate (*S)*-phenylethanol in 43% and 91% *ee* respectively[25]. As with [**1b/2d**], but on extending alkyl groups on R^4, [**1b/2e**] and [**1b/2f**] generate (*R)*-phenylethanol in 31% and 26% *ee* respectively[25]. Replacing the hydrogen in the position X of RuH_2[(*R*)-BINAP][(*R*)-DPEN] (Scheme 2.3) in **1c** with Cl (**3b**), Me (**3c**), Br (**3d**) and $P(O)(OH)_2$ (**3e**), generates (*S)*-phenylethanol in 83%, 86%, 90%, 89% and 97% *ee* respectively.

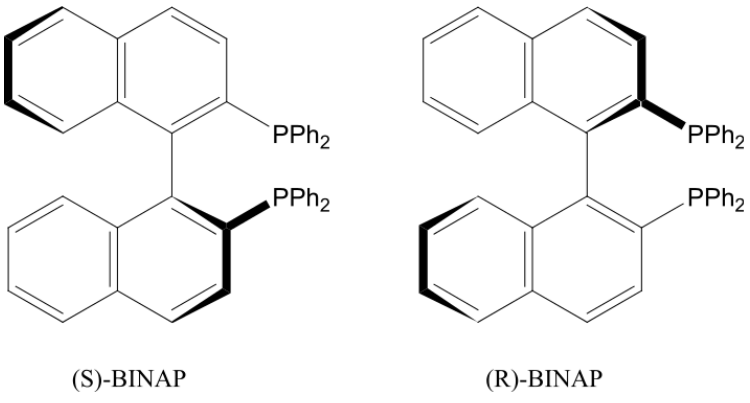

(S)-BINAP (R)-BINAP

Scheme 2.2: Illustration of (*S*)-BINAP and (*R*)-BINAP.

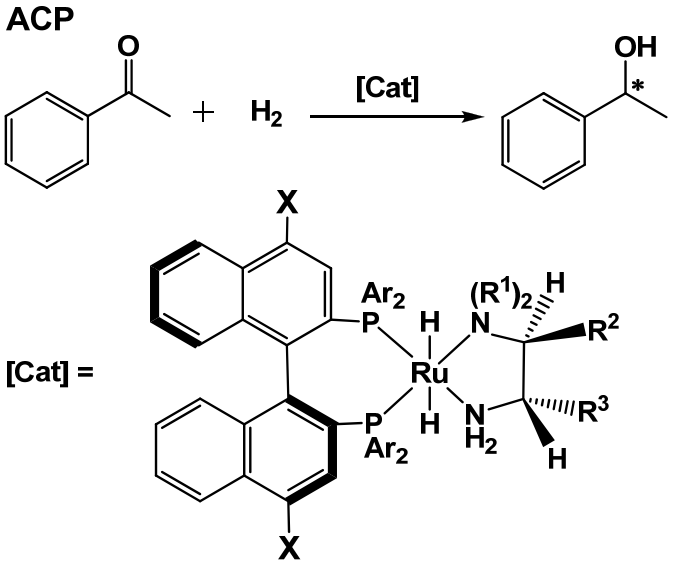

X = H

Ar = 3,5-$(CH_3)_2C_6H_3$; (*S*)-XylBINAP **1a**	R^1=H, R^2=R^3=Ph; (*S*,*S*)-DPEN **2a**	
Ar = 4-$(CH_3)C_6H_4$; (*S*)-TolBINAP **1b**	R^1=CH_3, R^2=R^3=Ph; (*S*,*S*)-DMDPEN **2b**	
Ar = C_6H_5; (*S*)-BINAP **1c**	R^1=CH_3, R^2=H, R^3=Ph; (*S*)-DMAPEN **2c**	
	R^4=CH_3, R^5=H, R^6=Ph; (*R*)-DMAPEN **2d**	
	R^4=C_2H_5, R^5=H, R^6=Ph; (*R*)- **2e**	
	R^4=n-C_4H_9, R^5=H, R^6=Ph; (*R*)- **2f**	

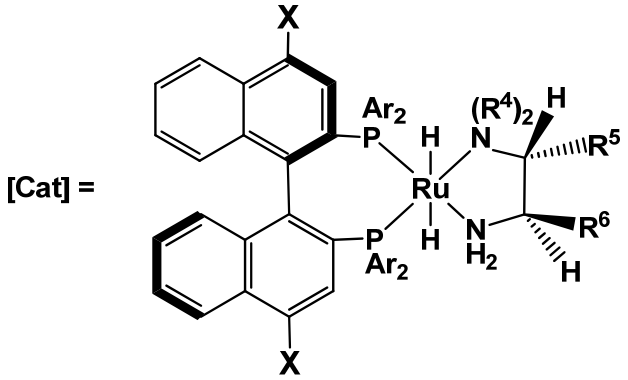

Ar = C_6H_5; (R)-BINAP, R^4=H, R^2=R^3=Ph;(R)-DPEN

X =H **1c**
X =Cl **3b**
X =Me **3c**
X =Br **3d**
X =P(O)$(OH)_2$ **3e**

Scheme 2.3: Asymmetric hydrogenation of acetophenone catalysed by *trans*-[RuH_2(diphosphine)(diamine)] complexes.

2.4.1 Mechanisms

The mechanism of this type of hydrogenation has been well characterised by several research groups using methods that include kinetics of product formation[26], deuterium exchange studies[27], computational studies[17,28] and stoichiometric reactions of intermediates and model compounds[29]. Among all of the possible mechanisms reported in the hydride transfer step, the metal-ligand bifunctional mechanism **I** in an outer-sphere fashion[35,37,44,51-53] — proposed by Noyori and co-workers — is widely accepted to be responsible for the high enantioselectivity in the hydrogenation of prochiral ketones catalysed by the RuH_2(diphosphine)(diamine) complexes[30]. Specifically, this mechanism (Scheme 2.4) shows that the ketone coordinates to the outer coordination sphere of the dihydride metal complex, and the nucleophilic metal-bound hydride and the protic hydrogen on the nitrogen are transferred simultaneously to the carbon and oxygen of the ketone respectively, *via* a six-membered pericyclic transition state (TS), although we note that some recent studies considered the possibility of forming a partial Ru-O bond in the hydride transfer for a transition state (Mechanism **II** in Scheme 2.4)[29a]. The 18-electron hydride-amino metal complex consequently becomes a 16-electron hydrido-amido metal species, which then undergoes a rate-determining heterolytic splitting of dihydrogen directly over the Ru-amido bond along three possible transition states: a four-membered pericyclic transition state (Mechanism **i** in Scheme 2.4)[26d,30d,31], a proton shuttle involving the alcohol solvent (Mechanism **ii** in Scheme 2.4)[26d], or deprotonation of a cationic dihydrogen complex by the alcohol solvent (Mechanism **iii** in Scheme 2.4). Regarding the effect of the solvent, it has been shown in previous computational studies[32] that solvent molecules could be involved in the proton transfer step between the N and O(=C) atoms, suggesting that the hydride and proton transfers in the metal-ligand bifunctional mechanism may not be entirely concerted. However, there is no evidence of the direct involvement of solvent molecules during the hydride transfer between Ru(-H) and C(=O) atoms. A previous study has shown that the hydride-transfer between Ru(-H) and C(=O) atoms occurs first; therefore it is the hydride-transfer step that controls the enantioselectivity in the ketone hydrogenation reactions[28a]. Following previous computational work[28a28c], in the present study we focus on Mechanisms **I** and **i**.

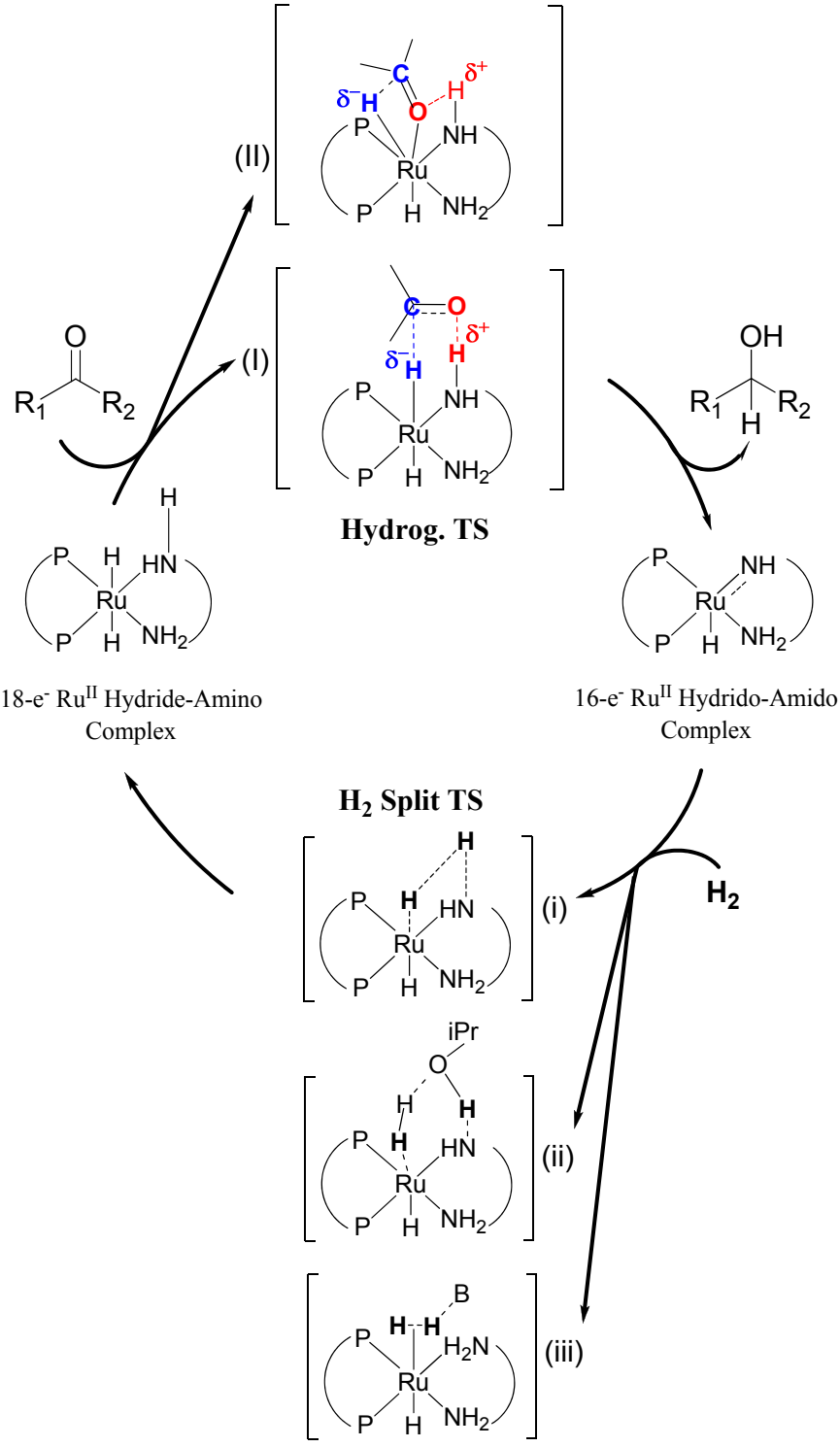

Scheme 2.4: Possible mechanisms for the hydrogenation of ketones using the *trans*-[Ru(II)H_2(diphosphine)(diamine)] complexes.

The aforementioned mechanisms occur in a neutral environment. Okuma proposed a catalytic cycle of hydrogenation of ketones using the Ru(II)H_2(TolBINAP)(1,2-diamine) complex[25], shown in Scheme 2.5. The catalyst precursor RuXY(TolBINAP)(DPEN) **A** (X, Y = Cl, Cl or η^1-BH_4, H) is converted to [RuH(TolBINAP)(DPEN)]$^+$ **B** in 2-propanol with or without alkaline base. **B** and H_2 reversibly form a cationic complex **C**, followed by deprotonation resulting in the active complex **D**. A ketone is rapidly reduced by **D** to generate the alcohol and a 16-electron amide species **E** in the presence of an alcoholic solvent and then regenerates species **B**, while **E** partially returns to **D** by the reaction with H_2. The reaction is expected to proceed through a transition state **F** from **D** to **E** using the same metal-ligand bifunctional mechanism with a six-membered pericyclic ring.

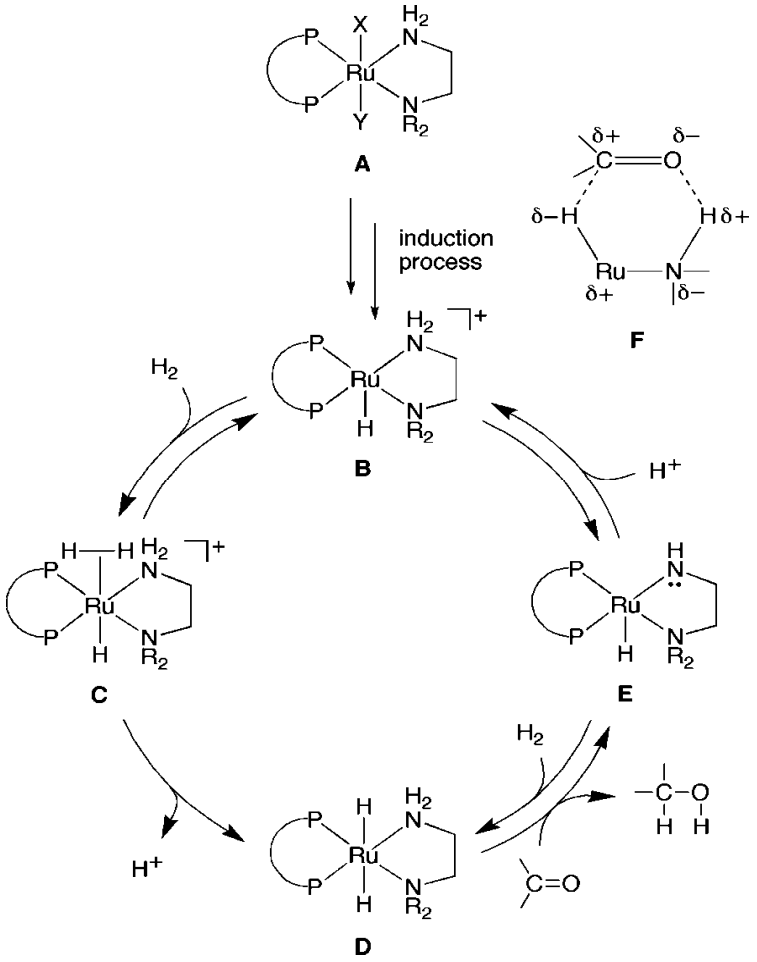

Scheme 2.5: A catalytic cycle for the hydrogenation of ketones catalysed by the *trans*-Ru(II)H_2(TolBINAP)(1,2-diamine) complex[25] (X and Y can both be Cl or η^1-BH_4 and H; P-P is (*S*)-TolBINAP; NH_2-NR_2 is 1,2-diamine and R is H[(*S*,*S*)-DPEN] or CH_3[(*R*)-DMAPEN]).

2.4.2 Earlier computational studies

The aforementioned examples show that the *ee* varies significantly even with minor changes on the ligands. Therefore, it is desirable to establish an *in silico* method to understand and predict the most suitable choice of ligands for such an important asymmetric hydrogenation. Computational approaches have previously proved to be a powerful tool for investigation of the mechanism and origin of enantioselectivity in asymmetric reactions without using vibrational calculations[1617,33]. These studies used density functional theory (DFT) of the type which will be employed in the thesis.

A simplified model has been used for investigating the metal-ligand bifunctional mechanism in the asymmetric H_2 hydrogenation or hydrogen transfer, using Noyori-type catalyts at different levels of theory[30d,30f,34]. However, different theoretical methods afford different calculated activation energies. For example, as reported by Yamakawa *et al.* for the hydrogenation transfer reaction between formaldehyde and methanol, catalysed by the $RuH(NH_2CH_2CH_2Y)(\eta_6$-benzene) (Y = O or NH), the calculated activation energy (E_a) at the MP4 level (15.8 kcal/mol) is approximately 11 kcal/mol higher than the E_a at the B3LYP level (4.7 kcal/mol)[30f]. For the same reaction, a pseudopotential/plane-wave DFT study by Handgraaf *et al.* gives the E_a as 2.0 kcal/mol at the BLYP level of theory[33b]. Likewise, for the hydrogen transfer in the formaldehyde/methanol reaction catalysed by the Ru-arene complexes, the E_a calculated at the MP4 (6.9 kcal/mol) and B3LYP (1.5 kcal/mol) levels are obviously different. These inconsistencies imply a sensitivity of the activation energy to the level of theory used. To enhance the degree of reliablility of computational investigation and predictions in the asymmetric hydrogenation using Noyori-type catalysts, it is necessary to make a careful choice of the most appropriate computational technique.

Di Tommaso *et al.* presented a systematic and comparative DFT study on a simplified Ru(diphosphine)(diamine)-catalysed hydrogen transfer ketone/alcohol reaction, employing a selected set of generalized-gradient-corrected (GGA), hybrid meta-GGA and hybrid DFT (HDFT) exchange-correlation functionals — a detailed discussion of these approaches is given in Chapter 3. The results show that all of these methods agree in predicting that the forward hydrogen transfer acetone/i-Propyl alcohol reaction *via* the metal-ligand bifunctional mechanism has a low energy barrier (≤4 kcal/mol). The DFT

results also agree with higher level MP2 calculations. For the hydride transfer step, the results show that the transition states are sensitive to the exchange-correlation functional and basis set employed, in particular, the (Ru-)H···C(=O) internuclear distance.

Balancing computing time and accuracy, this work concluded that, for this catalytic system [ketone + RuH_2(diphosphine)(diamine)], the calculated activation energy in the hydrogen transfer step in the acetone/*i*-propyl alcohol reaction catalysed by the *trans*-$RuH_2(PH_3)_2$(en) complex at the PBE/DNP level (at 2.15 kcal/mol) is sufficiently reliable, giving a result that is similar to the activation energy at the B3LYP/6-311++G(2df,2pd) and LANL2/(4s,4p,3d,1f) levels (at 2.55 kcal/mol).

One of the very important contributions from the previous work is the establishment of four possible reaction pathways (Q1, Q2, Q3 and Q4) based on the metal-ligand bifunctional mechanism (Scheme 2.6), which can have different stereochemical consequences. This mechanism suggests that the carbonyl carbon of the ketone interacts with the hydride bonded to the central metal and the oxygen of the ketone interacts with the proton bonded to the nitrogen. As the ketone approaches the complex, there are four proposed pathways. (Figures 2.4 and 2.5 illustrate the Q1 and Q2 pathways, and the Q3 and Q4 pathways respectively with the subsequent stereochemical configurations of the alcohol product, phenylethanol.)

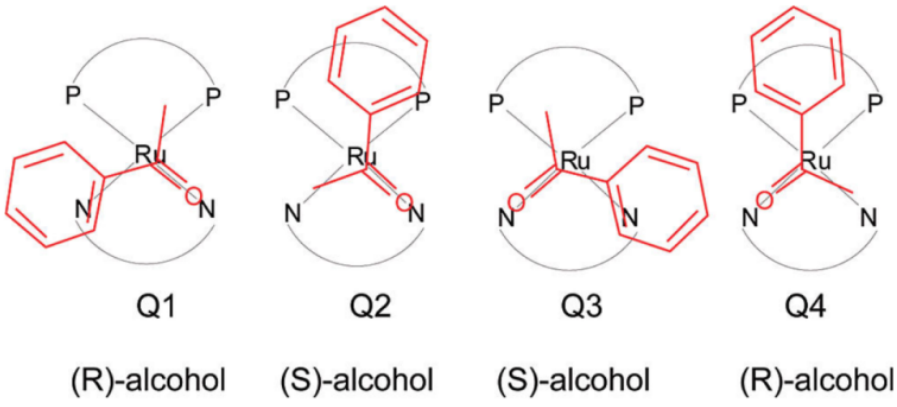

Scheme 2.6: Definition of four possible reaction pathways with the subsequent stereochemical (*R*)- or (*S*)-configurations of the alcohol product in ketone hydrogenation using the Noyori-type catalysts, based on the metal-ligand bifunctional mechanism[28a,28b].

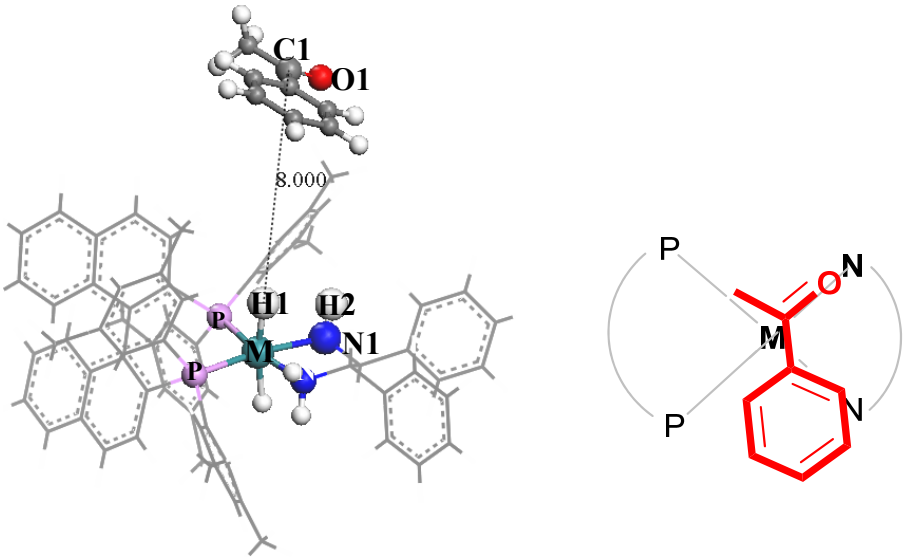

Q1 Approach: (*R*)-phenylethanol

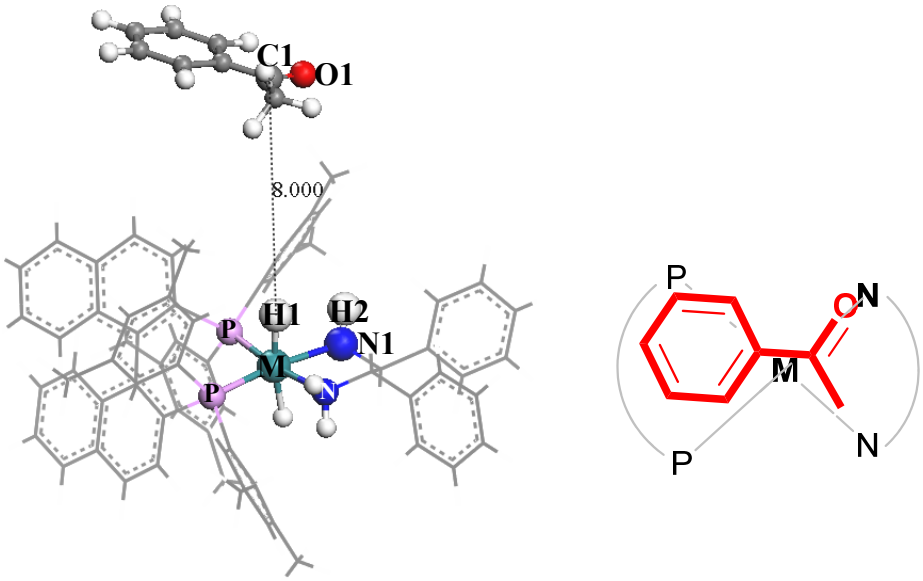

Q2 Approach: (*S*)-phenylethanol

Figure 2.4: Definition of two of the possible reaction pathways, Q1 and Q2, with the subsequent stereochemical (*R*)- or (*S*)-configurations of the alcohol product, phenylethanol.

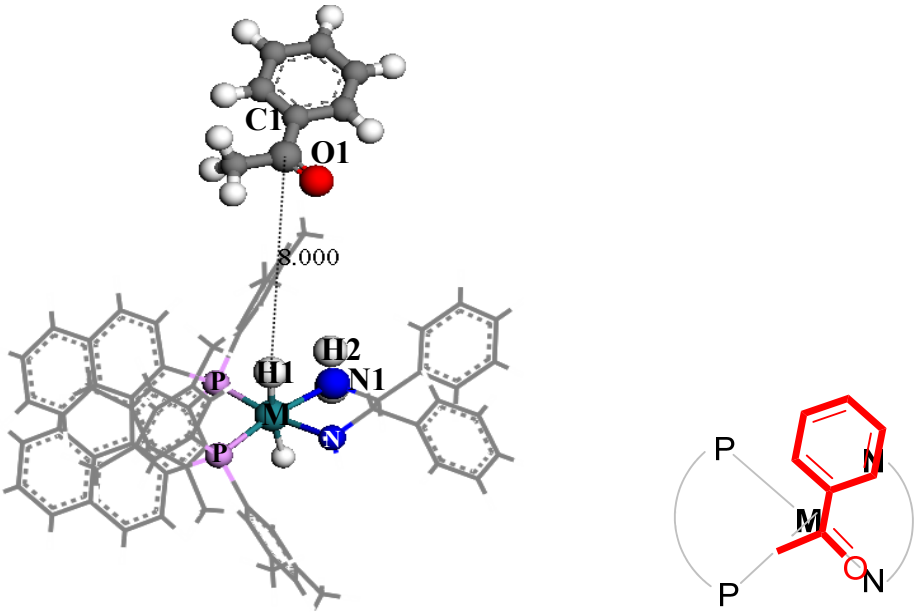

Q3 Approach: (*S*)-phenylethanol

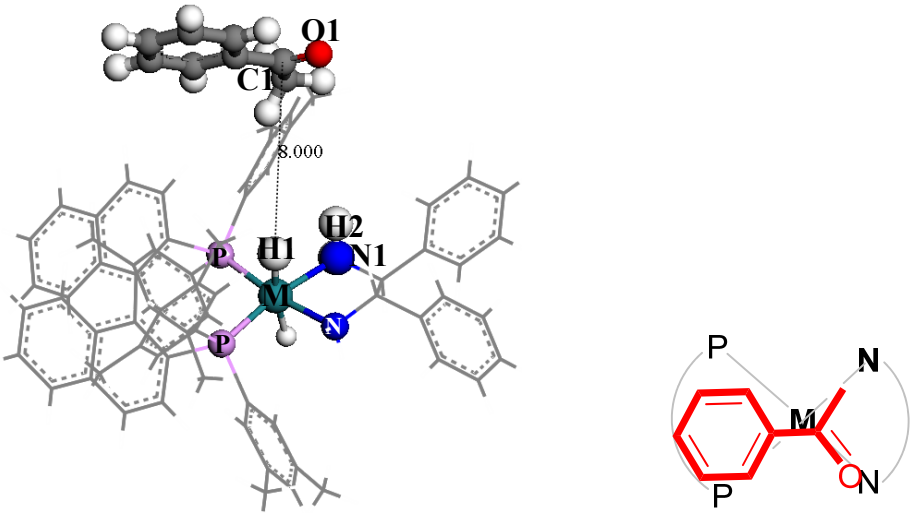

Q4 Approach: (*R*)-phenylethanol

Figure 2.5: Definition of two of the possible reaction pathways, Q3 and Q4, with the subsequent stereochemical (*R*)- or (*S*)-configurations of the alcohol product, phenylethanol.

In addition, a specific reaction with a very high *ee* (99%) in enantioselective hydrogenation of acetophenone (ACP) catalysed by RuH_2[(*S*)-XylBINAP)][(*S*,*S*)-DPEN] was selected to explore the factors controlling enantioselectivity. Based on the metal-ligand bifunctional mechanism, the ketone should approach the complex along the Q1, Q2, Q3 and Q4 pathways, and their energy profiles were computed[28a,28b]. These are shown in Figure 2.6[28a], which illustrates the variation in the calculated energy of system [ACP + {(*S*)-XylBINAP}{(*S*,*S*)-DPEN}] with respect to the pseudo reaction coordinate (Ru-)H···C(=O) distance. The energies of the transition states relative to that at a (Ru-)H···C(=O) distance of 9 Å are –7.61 kJ/mol for Q1, 9.58 kJ/mol for Q2, 25.70 kJ/mol for Q3 and 35.36 kJ/mol for Q4. The four pathways reveal very different energetic trends. Because the reaction must proceed along the lowest energy saddle point, it is evident that Q1, producing the (*R*)-alcohol, is the most favourable pathway, which is in agreement with experiment. For the Q3 and Q4 pathways, the energies of transition states are much higher than those along Q1 and Q2; moreover, no obvious energy minima along the reaction coordinates are observed. In contrast, two distinct minima at 3.75 Å and 2.5 Å are observed in the case of Q1 and a single minimum at 3.75 Å is observed in the case of Q2. A rationalisation of the differences in *ee* in the hydrogenation of ACP catalysed by the RuH_2(diphosphine)(diamine) complexes has been proposed in terms of steric repulsion, electronic effects and CH/π and NH/π interactions[17,28a,28b]. These interations will be discussed in more detail in Chapter 4.

These earlier computational studies focused only on the effect of diphosphine on enantioselectivity, whilst the present study systematically investigates the effect of structural changes in both the diphosphine and diamine ligands. We aim to establish a relationship between enantioselectivity and calculated activation energy on the basis of the metal-ligand bifunctional mechanism in the asymmetric hydrogenation catalysed by the ruthenium complexes with varying substituents on either the phosphine or amine ligand. We will also attempt to clarify the origin of the first peak before the occurrence of the transition state along Q1 shown in Figure 2.5; this aspect will be discussed in Section 4.3.2.

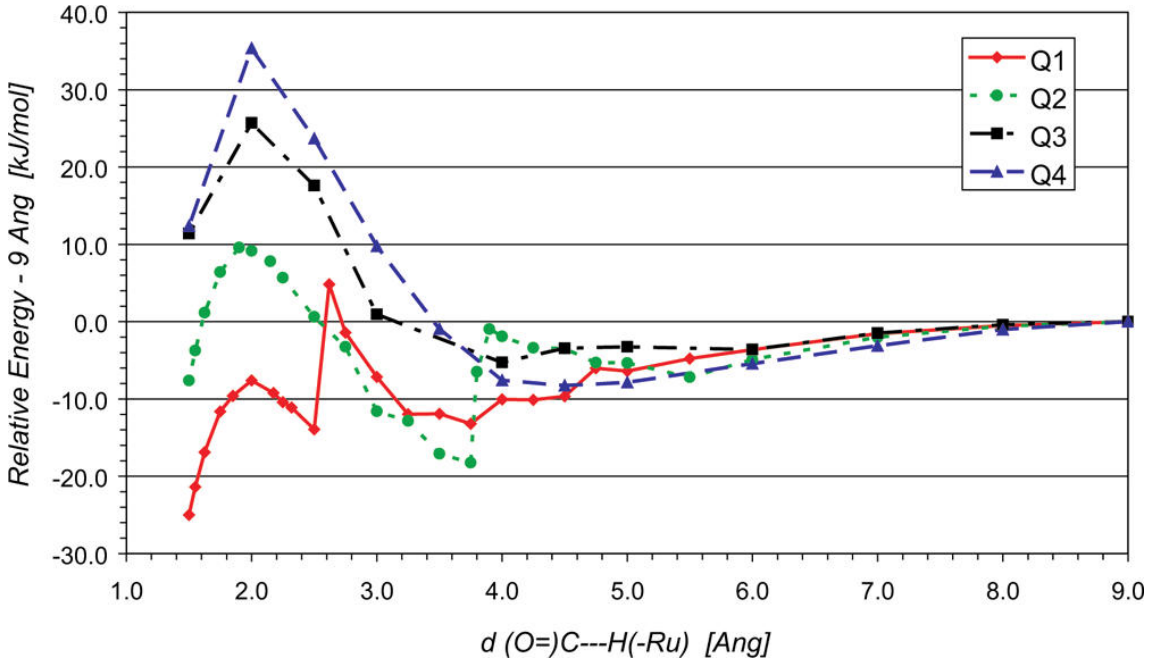

Figure 2.6: Reaction coordinate diagram of system [ACP + RuH_2\{(*S*)-XylBINAP\}\{(*S*,*S*)-DPEN\}] along the pseudo coordinate (Ru-)H···C(=O) internuclear distance for each possible pathway (Q1, Q2, Q3 and Q4), computed at the DFT-PBE level of theory[28a,28b].

2.5 Asymmetric Reduction of C=N Bonds

We now turn to discuss the asymmetric reduction of C=N bonds. Chiral amines are very important and useful intermediates in synthesising new pharmaceuticals, some of which are illustrated in Scheme 2.7, but this field has not been as intensively studied as asymmetric reduction of C=O bonds and there are still many challenges to overcome. In this study, we only focus on the mechanistic aspects of producing achiral amine products.

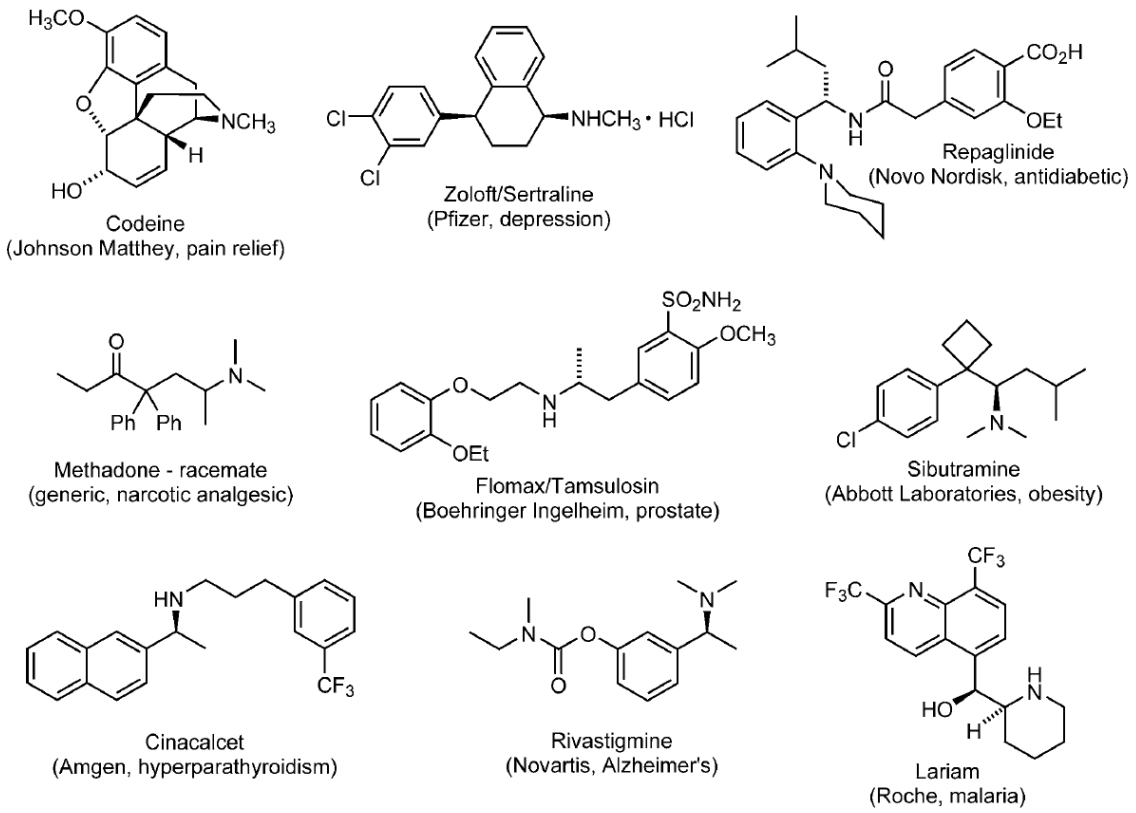

Scheme 2.7: Examples of chiral amine pharmaceutical drugs[35].

2.5.1 Reductive Amination

To produce amines, reductive amination[36] — the conversion of carbonyl groups, i.e., ketones or aldehydes, to amines *via* an imine with a reductant in a one-pot fashion (Scheme 2.8) — is one of the most practical green syntheses applied widely in biotechnology, materials science, agrochemicals, and pharmaceuticals[1b,37].

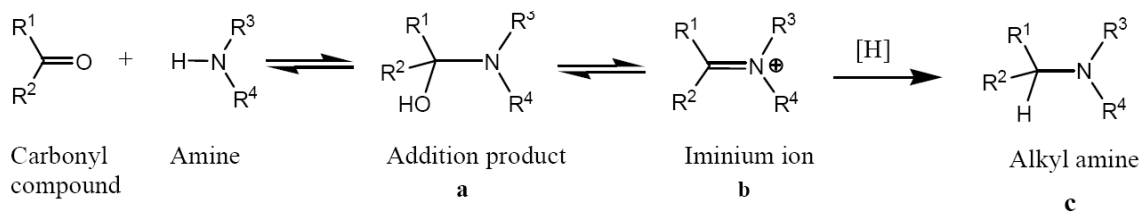

Scheme 2.8: Reductive amination.

In classical syntheses, reductive amination usually involves heterogeneous hydrogenation reactions using toxic hydrogen sources, such as $NaBH_3CN$, and involving the generation of excessive waste[36,38]. The asymmetric reductive amination, although a very important reaction, is still under-developed. Even the reduction of the imine intermediate by transfer hydrogenation is still rare. Over the past decade, only a small number of homogeneous catalysts and enzymes that allow for enantioselective reductive amination have been developed and these can only be applied to limited substrates[39].

2.5.2 Iridium(III) cyclometalated complexes applied to reductive amination

The asymmetric transfer hydrogenation of imines has begun to attract attention. However, until now, only a few combinations of ligands with the catalyst perform well for the asymmetric transfer hydrogenation of C=N double bonds. Cyclic imines can be reduced by M-TsDPEN-type complexes with high *ee*s[40]. In contrast, the methods of producing acyclic imines seem to be more challenging in transition metal catalysis and most acyclic ketimines are difficult to synthesise, which therefore enhances the attraction of reductive amination.

In 2011, Xiao and co-workers developed a set of air-stable cyclometalated imido Ir(III) complexes which are capable of catalysing transfer hydrogenative, reductive amination with safe and inexpensive formate, affording a high chemoselectivity and activity when applied to a broad range of substrates[1b]. Data relating to the reduction of aliphatic ketimines using the cyclometalated iridium complexes and $[Cp^*IrCl_2]_2$ are shown in Figure 2.7. Reactions were conducted on a 1 mmol scale at S/C=4000 with 1 mL F/T in 3 mL CF_3CH_2OH[1b]. These results reveal that complex **1** affords a conversion of greater than 99% in 30 mins in trifluoroethanol, providing a turnover frequency of 1.9×10^4 h^{-1} — the highest activity ever reported in the transfer hydrogenation of imine. The more electron-rich complex **2** shows a slightly lower activity. In contrast, complex **3**, derived from a saturated amine, displays the lowest activity. These results demonstrate a clear relationship between the efficiency of the conversion and the nature of the different electron-donating and withdrawing functionals groups on the iridium(III) cyclometalated complexes. The proposed mechanisms of this catalysis will be discussed in detail in Chapter 6.

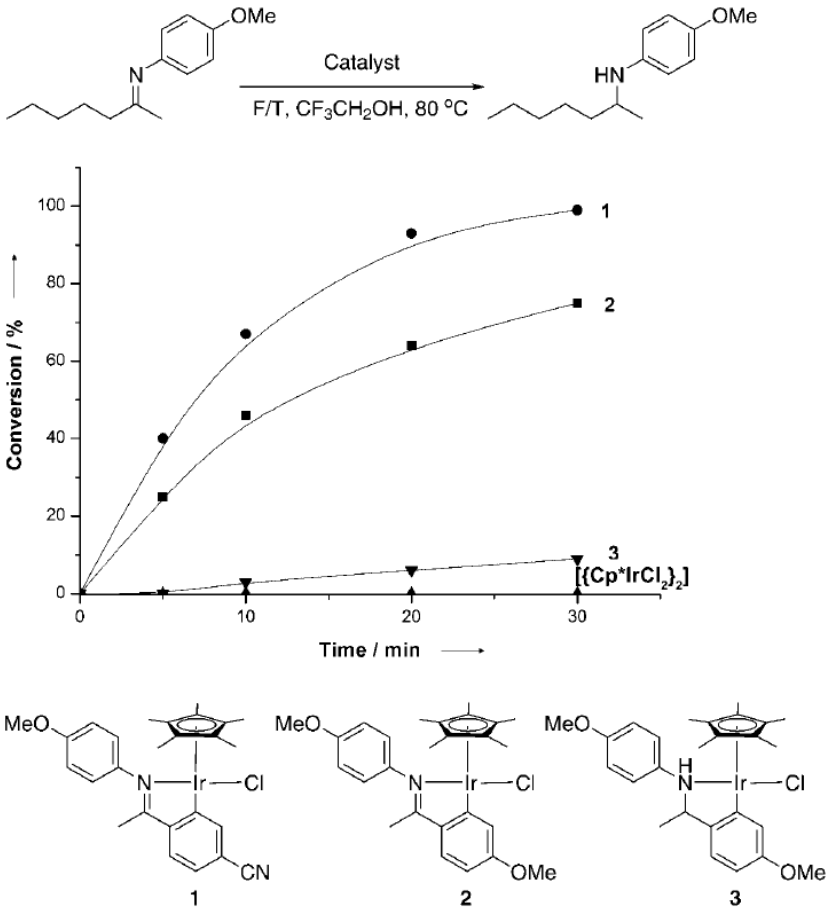

Figure 2.7: Reduction of aliphatic ketimine (above) with the cyclometalated iridium complexes and $[Cp^*IrCl_2]_2$. Reactions were conducted on a 1 mmol scale at S/C=4000 with 1 mL F/T in 3 mL CF_3CH_2OH[1b].

2.6 Summary

It is clear that the fields of asymmetric hydrogenation by ruthenium-based catalysts and reductive amination by iridium complexes pose considerable mechanistic challenges. The main aim of this thesis is to explore these mechanisms using the computational techniques which are discussed in the next chapter.

Chapter 3 **Computational Methodology**

By fusing chemical, physical and mathematical principles, computational modelling is capable of characterising, interpreting and predicting the structures and properties of molecules and materials at the atomic level, and has become an important and commonly-used tool in contemporary scientific research. In this thesis, density functional theory (DFT) has been applied in order to understand the mechanisms of organometallic hydrogenations catalysed by ruthenium-, iron- and iridium-based catalysts. In this chapter, basic electronic structure theory is summarised briefly before introducing DFT, exchange-correlation functionals, pseudopotential methods, techniques for geometry optimisation and locating transition state structures, and details of the computational recipe.

3.1 Electronic structure theory

Electronic structure theory describes electrons in atoms and molecules in terms of quantum mechanics, which postulates that the physical and chemical properties of a system may be obtained by solving the Schrödinger equation. Quantum mechanics explains the wave-particle duality of matter; solution of the Schrödinger equation yields the wavefunction of a system, Ψ. The particle probability density is given by $\Psi^*(\vec{x})\Psi(\vec{x})$ at coordinate $\vec{x}$. The time-dependent Schrödinger equation $i\hbar\frac{\partial\Psi}{\partial t} = \hat{H}\Psi$ gives the time evolution behaviour of the wavefunction. Ignoring relativistic effects, the theory is exact. In most applications, including those in the thesis, the time-independent Schrödinger equation is used:

$$\hat{H}\Psi = E\Psi, \qquad 3.1$$

where $\hat{H}$ is the Hamiltonian operator corresponding to the kinetic and potential energies, and E is the total energy of the system.

For a polyatomic system constituting N_n nuclei and N_e electrons, the many-body time-independent Schrödinger equation in the non-relativistic regime can be written as:

$$\hat{H}\Psi(\vec{r}_1,\vec{r}_2,...,\vec{r}_{Ne},\vec{R}_1,\vec{R}_2,...,\vec{R}_{Nn}) = E\Psi(\vec{r}_1,\vec{r}_2,...,\vec{r}_{Ne},\vec{R}_1,\vec{R}_2,...,\vec{R}_{Nn}), \qquad 3.2$$

where $\vec{r}_i$ stands for the coordinate of the *i*th electron and $\vec{R}_i$ stands for that of the *i*th nucleus. The non-relativistic Hamiltonian operator is the sum of the kinetic and potential operators of all the particles in the system and can be expressed as follows:

$$\begin{aligned}\hat{H} = &-\sum_{i=1}^{N}\frac{\hbar^2}{2m_e}\nabla_{\vec{r}_i}^2 + \frac{1}{2}\sum_{i_1\neq i_2=1}^{N}\frac{1}{4\Pi\varepsilon_0}\frac{e^2}{|\vec{r}_{i_1}-\vec{r}_{i_2}|} \\ &-\sum_{k=1}^{M}\frac{\hbar^2}{2M_k}\nabla_{\vec{R}_k}^2 + \frac{1}{2}\sum_{k_1\neq k_2=1}^{M}\frac{1}{4\Pi\varepsilon_0}\frac{Z_{k1}Z_{k2}e^2}{|\vec{R}_{k_1}-\vec{R}_{k_2}|} \\ &-\sum_{k=1}^{M}\sum_{i=1}^{N}\frac{1}{4\Pi\varepsilon_0}\frac{Z_k e^2}{|\vec{R}_k-\vec{r}_i|} \\ = &\hat{T}_e(\vec{r}) + \hat{V}_{ee}(\vec{r}) + \hat{T}_n(\vec{R}) + \hat{V}_{nn}(\vec{R}) + \hat{V}_{en}(\vec{r},\vec{R}). \end{aligned} \qquad 3.3$$

The first two terms correspond to the electronic kinetic energy and potential energy operators for electron-electron repulsion. The third and fourth terms represent the same physical quantities for the nuclei. The fifth term is the potential energy operator for the electron-nuclear attraction, which couples the dynamics of the nuclear and electronic systems. However, the Schrödinger equation can only be solved exactly for hydrogen atoms and other one-electron systems, while for larger systems, approximations are needed.

3.1.1 The Born-Oppenheimer approximation

The Born-Oppenheimer approximation exploits the fact that the mass of a nucleus is *ca.* 10^3 times larger than that of an electron, which allows us to address the dynamics of the electronic system separately from that of the nuclear system by viewing the latter as static. As a result, electrons adjust to positions of nuclei instantaneously after any change in nuclear positions. The Hamiltonian for the system composed of both nuclei and electrons is thus simplified as below:

$$\hat{H}_e = -\sum_{i=1}^{N} \frac{\hbar^2}{2m_e} \nabla_{\vec{r}_i}^2 + \frac{1}{2} \sum_{i_1 \neq i_2 = 1}^{N} \frac{1}{4\Pi\varepsilon_0} \frac{e^2}{|\vec{r}_{i_1} - \vec{r}_{i_2}|} - \sum_{k=1}^{M} \sum_{i=1}^{N} \frac{1}{4\Pi\varepsilon_0} \frac{Z_k e^2}{|\vec{R}_k - \vec{r}_i|}$$

$$= \hat{T}_e(\vec{r}) + \hat{V}_{ee}(\vec{r}) + \hat{V}_{en}(\vec{r}, \vec{R}) \qquad 3.4$$

This gives an electronic Schrödinger equation:

$$\hat{H}_e(\vec{R}) \Psi_e(\vec{r}, \vec{R}) = E^e(\vec{R}) \Psi_e(\vec{r}, \vec{R}), \qquad 3.5$$

where $\vec{R}$ and $\vec{r}$ are the coordinates of the nucleus and electron respectively. E^e is the electronic energy in the field of the nuclei and Ψ_e is the corresponding electronic wave function.

The above equation shows that both the motion and the energy of the electrons depend on the nuclear coordinates. In determining the lowest energy conformation of the system, the differential of the energy with respect to nuclei coordinates (the force) is used to propagate the nuclei to their new positions. The nuclei are fixed and the electronic problem solved again. This optimisation is carried out iteratively until certain convergence thresholds are reached. As discussed later, second derivatives may also be used in the optimisation process.

Although the Born-Oppenheimer approximation reduces the complexity of the Schrödinger equation, the electron-electron interaction term is complicated. As noted, for most electron systems, there are no analytic solutions. Moreover, the motion of electrons is correlated. According to the Pauli exclusion principle, electrons with parallel spin repel each other more than can be accounted for by Coulomb repulsion. The Hartree-Fock approach seeks to simplify this by introducing a mean field approximation where an external field replaces the effects of all the other electrons. DFT also reduces the dimensionality of the problem by treating the many-body problem in terms of the electron density.

3.2 The Hartree and Hartree-Fock Approximations

In the Hartree equation, the Hamiltonian of a system constituting *N* particles is the sum of one-particle Hamiltonians and the total wavefunction is the product of the wavefunctions of all particles[41]:

$$\hat{H} = \sum_{i}^{N} \hat{h}(i) \ , \tag{3.6}$$

$$\Psi(\vec{r}_1 s_1, \vec{r}_2 s_2, ..., \vec{r}_N s_N) = \Psi(\vec{r}_1 s_1)\Psi(\vec{r}_2 s_2)...\Psi(\vec{r}_N s_N) \, , \tag{3.7}$$

where $\hat{h}$ is the one-particle Hamiltonian and s_i is the spin of the ith electron. Hence, the Schrödinger equation for one particle can be written as below:

$$(-\frac{1}{2}\nabla^2 + V_{\vec{r}})\Psi(\vec{r}\, s) = E\Psi(\vec{r}\, s) \, . \tag{3.8}$$

The Hartree approximation has a major shortcoming — the many-particle wavefunction of the electrons does not obey the Pauli principle, which prohibits two electrons from occupying the same quantum state. By ignoring this principle, the Hartree approximation in general underestimates the average distance between electrons whilst overestimating the average repulsion between them, thus overestimating the total energy. To obey the Pauli principle, the many-particle wavefunction must be antisymmetric with respect to the exchange of electrons with the same spin; this can be formulated using the Slater Determinant. This approach was proposed by V. Fock, and is known as the Hartree-Fock approximation[42].

As noted, the electron-electron interaction is described using a mean field theory. The Hartree-Fock theory provides an inadequate treatment of the correlation between the motions of the electrons within a molecular system, particularly interactions arising between electrons of opposite spin. The major correlation effects arise from pairs of electrons with the same spin, which is termed the exchange interaction, but the motion of electrons of opposite spin remains uncorrelated under the Hartree-Fock theory. Any method which goes beyond the Hartree-Fock theory in attempting to treat this phenomenon properly is known as an electron correlation method or a post-Hartree-Fock method, e.g., the Configuration Interaction (CI)[43], the Møller-Plesset (MP) perturbation theory[44] and the Coupled-Cluster (CC) method[45].

3.3 Density functional theory (DFT)

3.3.1 Thomas-Fermi theory

DFT is a method based on the concept of using electron density instead of the wavefunction to determine properties of the system. In the late 1920s[46], the Hartree approximation was reformulated in terms of electron density, proposed independently by Thomas and Fermi, and named Thomas-Fermi theory[90,91], which was the first primitive quantum mechanical approach applied to many-body electronic structure calculations of molecular and condensed matter systems. In this theory, the kinetic energy is locally approximated by that of a non-interacting homogeneous electron gas with the same density. Later, using the same approximation, Dirac introduced the exchange term into this model[47]. However, a breakthrough was made by P. Hohenberg and W. Kohn in 1964[48], who showed that the ground-state energy and all other ground-state electronic properties were uniquely defined by the electron density. Basing the energy on the total electron density means that there are fewer degrees of freedom to consider in the DFT method. This approach has become popular because of the favourable compromise between accuracy and computational cost, allowing the treatment of large many-electron systems.

3.3.2 Hohenberg-Kohn theorems

In 1964, Hohenberg and Kohn proposed two theorems that used the density as the basic variable in determining the total energy of an interacting many-body system[49]. The first theorem demonstrated a one-to-one correspondence between the many-body wavefunction $\Psi(\vec{r})$ in the ground state and the electron density $\rho(\vec{r})$ in the ground state. The total energy of a system can be written as a functional of electron density, $\rho(\vec{r})$:

$$E[\rho(\vec{r})] = \int V_{ext}(\vec{r})\rho(\vec{r})dr + F[\rho(\vec{r})] \quad 3.9$$

The first term, $\int V_{ext}(\vec{r})\rho(\vec{r})dr$, arises from the interaction of the electrons with an external potential. In the Born-Oppenheimer approximation, $V_{ext}(\vec{r})$ represents the Coulomb interaction between the electrons and nuclei. The second term, $F[\rho(\vec{r})]$, is the sum of the kinetic energy of the electrons and the potential energy of the electron-electron

interactions. However, the exact form is unknown. Because the expression for the Hartree energy as a functional of the density is known, $F[\rho(\vec{r})]$ then could be written as:

$$F[\rho(\vec{r})] = E_H[\rho(\vec{r})] + E_{unknown}[\rho(\vec{r})], \quad 3.10$$

where $E_H[\rho(\vec{r})]$ is the Hartree energy and $E_{unknown}[\rho(\vec{r})]$ is an unknown universal function of the density independent of the external potential. The total energy can be re-written as:

$$E[\rho(\vec{r})] = \int V_{ext}(\vec{r})\rho(\vec{r})dr + E_H[\rho(\vec{r})] + E_{unknown}[\rho(\vec{r})]. \quad 3.11$$

The second Hohenberg-Kohn theorem proved that the exact ground-state energy of the electronic system corresponds to the global minimum of $E[\rho(\vec{r})]$, and the electron density $\rho(\vec{r})$ which minimises this functional is the exact ground-state electron density $\rho_0(\vec{r})$.

3.3.3 Kohn-Sham equations

The second landmark in the development of DFT was by W. Kohn and L. J. Sham (1965)[50], who suggested a practical method to obtain the ground-state electron density. Kohn and Sham suggested that $F[\rho(\vec{r})]$ can be recast as the sum of the three terms:

$$F[\rho(\vec{r})] = E_{KE}[\rho(\vec{r})] + E_H[\rho(\vec{r})] + E_{XC}[\rho(\vec{r})], \quad 3.12$$

where $E_{KE}[\rho(\vec{r})]$ is the kinetic energy, $E_H[\rho(\vec{r})]$ is the electron-electron Coulomb energy and $E_{XC}[\rho(\vec{r})]$ is the sum of the contributions from the exchange and correlation interactions. The ground-state electron density $\rho(\vec{r})$ is given by:

$$\rho(\vec{r}) = \sum_{i=1}^{n} n_i \left|\varphi_i(\vec{r})\right|^2, \quad 3.13$$

where n_i is the occupation number of the ith state and $\left|\varphi_i(\vec{r})\right|$ is a Kohn-Sham orbital.

The first term in equation 3.12, $E_{KE}[\rho(\vec{r})]$, is defined as the kinetic energy of a system of non-interacting electrons with the same density as the real system:

$$E_{KE}[\rho(\vec{r})] = \sum_{i=1}^{N} \int \psi_i(\vec{r})(-\frac{\vec{v}^2}{2})\psi_i(\vec{r})dr \quad , \qquad 3.14$$

where $\vec{v}_i$ is the velocity of the *i*th electron.

The second term, $E_H[\rho(\vec{r})]$, is the Hartree energy. In the Hartree approach, this electronic energy arises from the classical interactions between two charge densities when summed over all possible pairwise interactions, giving:

$$E_H[\rho(\vec{r})] = \frac{1}{2}\iint \frac{\rho(\vec{r}_1)\rho(\vec{r}_2)}{|\vec{r}_1 - \vec{r}_2|} dr_1 dr_2 \qquad 3.15$$

The last term $E_{XC}[\rho(\vec{r})]$ has contributions from not only exchange and correlation, but also from the difference between the true kinetic energy of the interacting system and the kinetic energy of the non-interacting system. The following section will introduce some commonly used exchange-correlation functionals.

3.4 Exchange-correlation functionals

In the earlier section we introduced the Kohn-Sham equations which in principle allow an exact treatment of the total electronic energy of an atomic or molecular system. Our ignorance of the exact exchange and correlation contributions is expressed in the exchange-correlation term, $E_{XC}[\rho(\vec{r})]$. Appropriate approximations for $E_{XC}[\rho(\vec{r})]$ have been the subject of intense study and development. Indeed, there are now many different types of functionals available that are more or less appropriate for particular systems. In this thesis, we discuss the local density approximation (LDA), the generalised gradient approximation (GGA) and hybrid exchange correlation functionals.

3.4.1 Local Density Approximation (LDA)

The LDA is based on the known exchange-correlation energy of a uniform electron gas. The LDA functional is dependent only on the value of the density $\rho(\vec{r})$ at a specific

point in space $\vec{r}$, emphasising the local nature of this approach. In the LDA, the exchange-correlation potential V_{xc} can be separated into exchange and correlation parts.

The exchange contribution to ε_X can be obtained analytically[95], giving:

$$\varepsilon_X(\rho) = \frac{3}{4}\left(\frac{3n}{\pi}\right)^{1/3} \quad , \tag{3.16}$$

while the correlation contribution is obtained through analytic interpolation of accurate values obtained using quantum Monte Carlo calculations by Ceperley and Alder in 1980[51]. The correlation term of the LDA functionals used at the present depends on the parameterisation of these results, one of the most commonly-used of which was proposed by Perdew and Zunger in 1981[50], and will be discussed later.

The LDA is strictly applicable to the homogeneous electron gas, but may be useful in solid systems, although the LDA functional usually leads to the underestimation of bond lengths and results in a significant error in the cohesive energy under most circumstances. To improve the accuracy for inhomogeneous systems we consider the gradient of the electron density at each point as well as the density; this approach is called the generalised gradient approximation (GGA).

3.4.2 Generalised Gradient Approximation (GGA)

As noted, the GGA adds a dependence on the gradient of the density[52]. The exchange-correlation energy is now written as:

$$E_{XC}^{GGA}\left[\rho(\vec{r})\right] = \int \rho(\vec{r})\varepsilon_{XC}\left[\rho(\vec{r}), \nabla\rho(\vec{r})\right]dr \quad . \tag{3.17}$$

One of the most commonly-used non-empirical GGA functionals is the PBE (Perdew-Burke-Ernzerhof)[53] functional. When using the GGA, many computed properties are improved compared with LDA, such as geometries and the ground-state energy of molecules[5354].

3.4.3 Hybrid Functionals

Hybrid functionals include a proportion of exact exchange from the Hartree-Fock theory. The exact exchange energy functional is expressed in terms of the Kohn-Sham orbitals instead of the electron density. Two of the most commonly-used hybrid functionals are B3LYP (Becke, 3-parameter, Lee-Yang-Parr)[55] and PBE0[56].

The B3LYP hybrid exchange-correlation functional is shown below:

$$E_{XC}^{B3LYP} = E_{XC}^{LDA} + a_0(E_X^{HF} - E_X^{LDA}) + a_x(E_X^{GGA} - E_X^{LDA}) + a_c(E_c^{GGA} - E_c^{LDA}), \quad 3.18$$

where the three empirical parameters a_0=0.20, a_x=0.72 and a_c=0.81 are determined by fitting to a set of measured atomisation energies[55b]. E_X^{HF} is the Hartree-Fock exact exchange energy. E_X^{GGA} and E_c^{GGA} are the exchange functional of Becke 88[57] and the correlation functional of Lee, Yang and Parr[55c] respectively. E_c^{LDA} is the correlation functional of the VWN local-density approximation[58].

In 1996, Adamo[56a] modified the pure Perdew-Burke-Ernzerhof functional with 25% Hartree-Fock exchange and 75% PBE exchange, which is known as PBE0, given below:

$$E_{XC}^{PBE0} = E_{XC}^{GGA} + \frac{1}{4}(E_X^{HF} - E_X^{GGA}) \quad 3.19$$

.

PBE0 affords good accuracy for molecular structures and properties as well as energies[56a].

3.5 Dispersion corrected density functional theory (DFT-D)

DFT is now a very widely-used method for electronic structure calculations in quantum chemistry. However, a general shortcoming of common GGA and hybrid functionals, is that they cannot describe long-range electron correlations that are responsible for van der Waals (vdW) or dispersion forces. DFT-D techniques allow for an effective description of dispersion forces within the framework of DFT by adding a semi-empirical correction term into Kohn-Sham equations[59]. In this model, the long range

dispersion interaction is proportional to C_6/R^6. Further improvement can be achieved by introducing a scaling parameter to fit the contribution of dispersion with the exchange repulsion of the Kohn-Sham term. A damping function is also employed to exclude the correction at short distances where interactions are well-described by DFT. The equation is shown below:

$$E_{DFT-D} = E_{DFT} + E_{disp}$$

$$E_{disp} = -\tfrac{1}{2}\sum_{i,j} C_{6ij}\left[\sum_{\vec{R}} |\vec{r}_{ij}+\vec{R}|^{-6} f_{damp}(|\vec{r}_{ij}+\vec{R}|)\right]$$

$$f_{damp}(|\vec{r}_{ij}+\vec{R}|) = s_6.\left(1+exp\left[-d.\left(\frac{|\vec{r}_{ij}+\vec{R}|}{r_0}-1\right)\right]\right)^{-1}, \qquad 3.20$$

where $\vec{r}_{ij}$ is the atom-atom distance vector, S_6 is a functional-dependent scaling parameter, d is a parameter which tunes the steepness of the damping function and C_6 represents a semi-empirical parameter.

3.6 Basis sets

Although there is no exact analytical solution to the time-independent Schrödinger (equation 3.2) for systems containing more than one electron, approximate solutions can be obtained using standard numerical techniques — building the total wavefunction from a basis set of mathematical functions capable of reproducing critical properties of the system. An individual molecular orbital can be expressed as[60]:

$$\Phi_i = \sum_{\mu} c_{\mu i}\chi_{\mu}, \qquad 3.21$$

where $\chi_{\mu}(\mathrm{r})$ are the basis functions and the $c_{\mu i}$ are the molecular orbital coefficients. Molecular orbitals are therefore expressed as linear combinations of a pre-defined set of one-electron functions commonly centred on the atomic nuclei so they bear some resemblance to atomic orbitals. The basis set can be interpreted as restricting each electron to a particular region of space. Larger basis sets impose fewer restrictions on electrons and more accurately approximate exact molecular orbitals, but more computational resources are required.

3.6.1 Slater-type and Gaussian-type functions

There are two types of basis functions commonly used in electronic structure calculations currently: *Slater-type functions* and *Gaussian-type functions*, which are introduced in the following sections. The Slater-type functional form is expressed as[61]:

$$\chi_{\zeta,n,l,m}(r,\theta,\varphi) = N Y_{l,m}(\theta,\varphi) r^{n-1} e^{-\zeta r} , \qquad 3.22$$

where N is a normalisation constant, $Y_{l,m}(\theta,\varphi)$ are spherical harmonic functions, r is the distance of the electron from the atomic nucleus, n is the principal quantum number and ζ is a constant associated with the effective charge of the nucleus. When considering a very small set of functions per atom, Slater-type functions can give superior energies. However, when the number of functions per atom increases, the time to evaluate molecular integrals is costly. Nowadays, most polyatomic calculations are conducted by using Gaussian-type functions, which can be expressed in terms of polar or Cartesian coordinates:

$$\chi_{\zeta,n,l,m}(r,\theta,\varphi) = N Y_{l,m}(\theta,\varphi) r^{2n-2-l} e^{-\zeta r^2}$$
$$\chi_{\zeta,l_x,l_y,l_z}(x,y,z) = N x^{l_x} y^{l_y} z^{l_z} e^{-\zeta r^2} . \qquad 3.23$$

The sum of l_x, l_y and l_z determines the type of orbital. The r^2 dependence in the exponential makes the Gaussian-type functions inferior to the Slater-type functions in two aspects: firstly, at the nucleus, a Gaussian-type function has a zero slope but a Slater-type function has a cusp; therefore Gaussian-type function cannot describe the behaviour of electrons near the nucleus. Secondly, Gaussian-type functions fall too rapidly as the distance from the nucleus increases; therefore the tail of the wavefunction is a worse approximation. However, increasing the number of Gaussian basis functions can achieve a reasonable accuracy to evaluate integrals within an acceptable time; thus Gaussian basis functions are more widely used in electronic structure calculations. Standard basis sets are usually classified as discussed below[62].

3.6.2 Classification of basis sets

A *minimal basis set* contains the minimum number of basis functions needed to describe all of the electrons in a neutral atom. For example, a single *s*-function (1s) would be required for hydrogen and helium; two *s*-functions (1s and 2s) and one set of *p*-function ($2p_x$, $2p_y$ and $2p_z$) would be required for the first-row elements in the periodic table. Lithium and beryllium only require two *s*-functions, but a set of *p*-functions is usually included. Three *s*-functions (1s, 2s and 3s) and two sets of *p*-functions (2p and 3p) would be required for the second-row elements. Minimal basis sets are usually used to give a quick and rough result in the first place since they are much cheaper than larger basis sets. The most common minimal basis set is STO-*n*G[63] in which a linear combination of *n* Gaussian-type functions is used to represent each orbital. It has been shown that at least three Gaussian-type functions are needed to properly represent one Slater-type function. In general, the results obtained when using STO-3G are only slightly different from those using the larger minimal basis sets with more Gaussian-type functions, although for hydrogen-bonded complexes, STO-4G can perform considerably better.

The next level of accuracy can be achieved by doubling the number of basis functions; this results in the *Double Zeta* (DZ) type basis[64]. (The term "zeta" is derived from the exponent of the Slater-type basis functions.) A DZ basis uses two *s*-functions (1s and 1s) for hydrogen; four *s*-functions (1s, 1s', 2s and 2s') and two sets of *p*-functions (2p and 2p') for the first-row elements; six *s*-functions (1s, 1s', 2s, 2s', 3s and 3s') and four sets of *p*-functions (2p, 2p', 3p and 3p') for the second-row elements. The DZ basis is superior because it better accounts for the anisotropy of the electron distribution.

Chemical bonding occurs between valence orbitals and rarely involves the core orbitals. As such, the double zeta approach can be improved by doubling the number of functions used to describe the valence orbitals but keeping a single function for the core orbitals; this is called *split valence basis*[65], and is abbreviated as VDZ (*valence double zeta*).

Simply increasing the number of functions, such as *triple zeta* (TZ),[64a,66] does not always enhance the level of accuracy. In particular, when atoms are close together, their charge distribution leads to a polarisation effect, in which *s*-orbitals tend to have the characteristics of *p*-orbitals and *p*-orbitals tend to have the characteristics of *d*-orbitals.

Consequently, for molecules with a strongly non-isotropic charge distribution, *triple zeta* or *quadruple zeta* can still yield incorrect results. The most common solution to this charge distribution problem is to incorporate polarisation functions, which have a higher angular quantum number corresponding to *p*-orbitals for hydrogen and *d*-orbitals for the first- and second-row elements.

However, the aforementioned basis sets cannot cope with an atom in anionic or excited states, or molecules consisting of lone pairs, which have an increased amount of electron density away from the nuclear centre. In order to describe the tail of the wavefunction, diffuse functions[62b,67] with spatially extended *s*- and *p*-functions are required.

3.6.3 Numerical basis sets

Here, the basis functions use numerical orbitals and each function corresponds to an atomic orbital. The angular component of each function is the spherical harmonic $Y_{l,m}(\theta,\varphi)$, and the radial component is obtained by solving the atomic DFT equations numerically. Atomic basis sets are restricted within a cutoff value, which balances accuracy and computing time. A reasonable level of accuracy, in general, can be achieved by using about 300 radial points from the nucleus to an outer distance of 10 bohr (5.3 Å). The numerical basis set employed in this thesis is DNP (double numerical polarisation). Polarising *d*-functions are added to all non-hydrogen atoms and a polarising *p*-function to all hydrogen atoms.

3.6.4 Plane-wave basis sets

Plane-wave basis sets provide an alternative way to represent atomic orbital in periodic systems. They are non-local, meaning that plane-waves in a simulation box are not bound to a specific atom but to the entire unit cell. The number of plane-wave functions employed does not depend on the component atoms but on the size of the unit cell. A finite number of plane-wave functions is used by choosing a specific cutoff energy. Furthermore, plane-wave basis sets are usually applied alongside an effective core potential or pseudopotential, which will be discussed in the following section.

3.7 Pseudopotentials

Pseudopotentials, as used in the Hartree-Fock and Kohn-Sham methods, are effective potentials which act upon the valence electrons, and are constructed to represent the potential of the core electrons and nuclei. The idea is derived from the fact that only the valence electrons are involved in the chemical bonding of a system. We are therefore able to simplify the description of the system: the contributions from the nucleus and the core electrons are replaced with an angular dependent pseudopotential formed from the free atom of the corresponding element[68], meaning that only the valence states are considered explicitly, reducing computing costs significantly. Inside the core region, the pseudopotential is designed to be much softer than the ionic one. Outside the core region, it is required that the corresponding pseudo wavefunction is close to its all-electron counterpart to maintain the correct behaviour over a broad range of chemical environments.

3.7.1 Pseudopotentials applied in this thesis

There are several ways to treat the core electrons. In this thesis, we employed the following:

DSPP (The Density functional Semi-core PseudoPotentials)[69]: This approach belongs to the hardness-conserving semilocal family of pseudopotentials, which is based on a minimisation of errors with the norm-conserving conditions — the normalisation of valence wave functions must be preserved upon introducing all pseudopotentials. The errors can be kept at almost the same low level as for a single functional. Since these pseudopotentials are generally designed for use with local orbital methods, semi-core functions may be treated as valence functions, assisting in increasing the accuracy and portability. To further improve portability and numerical stability with GGAs, a nonlinear core correction is used. Furthermore, relativistic corrections to atomic scattering properties can easily be incorporated into this pseudopotential. It has been found that the DSPP performs well compared with expensive all-electron calculations[69b]. This type of pseudopotential is used in the DMol^3 code, described later.

LANL (Los Alamos National Laboratory) ECPs: This type of pseudopotential is available for a variety of elements together with the appropriate double zeta valence basis set. The combination of ECP and a valence basis set is thus referred to as LANL2DZ basis[70]. LANL2 ECPs have not been defined for elements H – Ne; the all-electron valence double zeta basis sets developed by Dunning (D95V) are used for these elements instead. The ECP parameters for elements Na – Kr have been derived from atomic wavefunctions obtained in all-electron non-relativistic Hartree-Fock calculations, while relativistic Hartree-Fock calculations have been used for the heavier elements Rb – Bi. This type of pseudopotential is used in the Gaussian code.

GTH (Goedecker, Teter and Hutter): This type is a separable norm-conserving dual-space Gaussian-type pseudopotential. It can be used in both Gaussian-type and plane-wave basis set codes. It separates into local and non-local parts to reduce the computing time[71] and is used in the CP2K code, discussed later.

3.8 Optimisation

3.8.1 Potential energy surfaces

In accordance with the Born-Oppenheimer approximation mentioned in Section 3.1.1, the energy of a system in its ground electronic state can be regarded as a function of the nuclear coordinates. Thus, changes in the energy of a system can be considered as the movement of species on a multi-dimensional function called the *potential energy surface* (PES). Optimisation refers to finding *stationary points* of a function, where the first derivative (gradient) is zero. At a *minimum*, the first derivative of the energy function with respect to all nuclear coordinates is zero and the second derivative is always positive. At a *maximum*, the first derivative of the energy function with respect to all nuclear coordinates is zero and the second derivative is always negative. A *global minimum* is the lowest point on the potential energy surface. Figure 3.1 illustrates a two-dimensional potential energy surface, on which each point corresponds to a state of the system. In many cases, we wish to identify the global minimum. A local minimum is the lowest point in some limited region of the potential energy surface and can also be of interest. Global minima correspond to equilibrium structures of a system. First-order *saddle points* occur

where the second derivative is negative in one direction and positive in all other directions. They correspond to transition states, (e.g., **C** in Figure 3.2) linking two equilibrium structures (**A** and **B** in Figure 3.2); such saddle points are crucial in determining the reaction mechanism.

Minima and maxima can also be located by employing either analytical or numerical methods that involve gradually changing the coordinates of the systems to produce configurations with lower energies until the minimum is obtained and vice versa for a maximum. An optimiser can be used to search for the ground-state structure as well as locate transition structures corresponding to saddle points; these can also be found by doing a frequency calculation. When only one imaginary frequency is found, the system can be in a transition state. Locating a desired transition state can be challenging; below, we introduce minimisation and some methods of locating transition states used in this thesis.

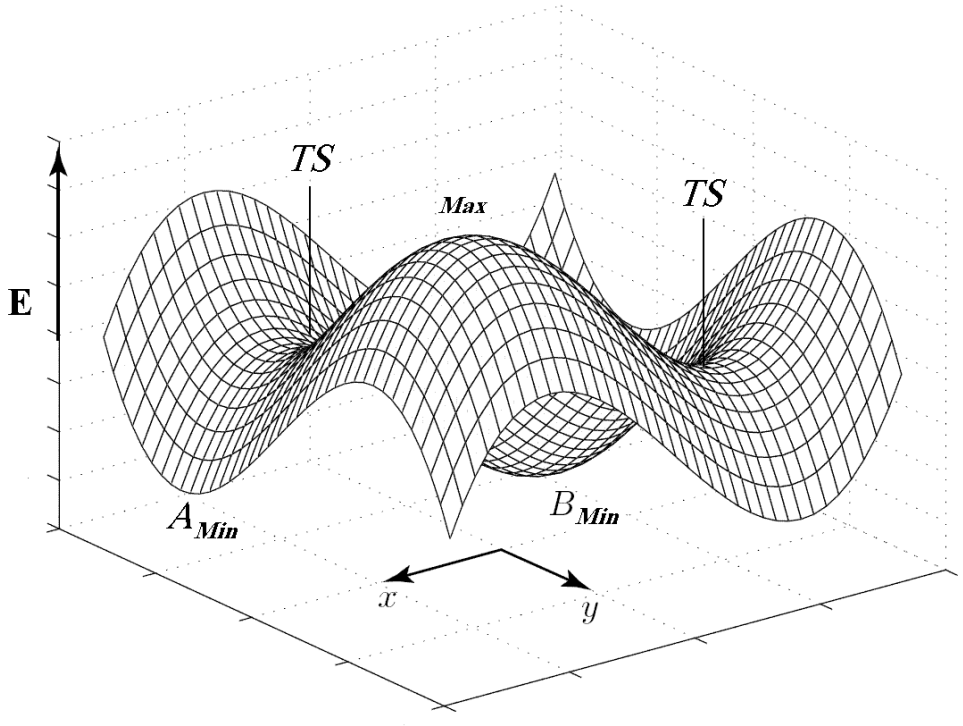

Figure 3.1: Illustration of a two-dimensional potential energy surface. (Taken and modified from reference 168.)

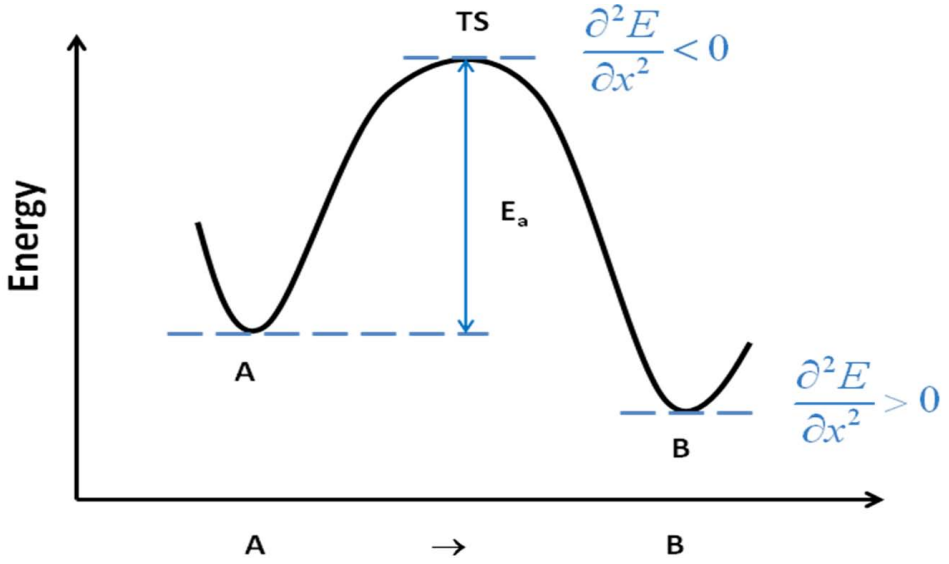

Figure 3.2: One-dimensional reaction coordinate from a simple reaction of reactant A to product B *via* a transition state TS.

3.8.2 Minimisation

Optimisations of structures to their minimum energies are also called minimisations. These methods fall into two categories: (a) first-derivative methods such as the steepest descent[72], giving a quick but rough estimated result, and the conjugate gradients methods[73], which converge more rapidly than the former; (b) second- derivative methods such as the Newton-Raphson and the quasi-Newton approaches[74]. In addition to the gradient, the curvature of the function is also considered. The second derivative is stored in the Hessian matrix. These methods are generally used when the potential energy surface is harmonic close to the extrema; thus the minimum will be located in a single step using a pure quadratic interpolating function; in more complicated real systems, more steps are required. Both the Newton-Raphson and quasi-Newton approaches require the inverse of the Hessian matrix. The quasi-Newton approach builds up the inverse Hessian in successive geometry steps whereas the Newton-Raphson approach requires the inverse Hessian at every point in a geometry search and therefore consumes more computing time.

3.8.3 Methods of locating transition state structures

Constrained optimisation (CO) method

The constrained optimisation (CO) is one of the simplest and most widely-used methods to search for transition states. Reaction pathways and transition states are located with a constrained minimisation technique. We select a pseudo reaction coordinate and fix the distance between the two reactants and minimise the total energy with respect to all remaining degrees of freedom[28b]. Through a series of such constrained structure optimisations, with a different reactant separation in each case, we obtain a reaction coordinate diagram. Since the only constraint is the distance between the reactants, the reactants are free to rotate and translate subject to the above constraint. The transition state is identified when the forces on the atoms vanish and the energy is a maximum along the reaction coordinate but a minimum with respect to all remaining degrees of freedom.

Synchronous transit-guided quasi-Newton (STQN) method

When searching for transition states, a very accurate estimate of the inverse Hessian is necessary at each step because the potential energy surface around the transition state is usually flatter than it is around a minimum. The synchronous transit-guided quasi-Newton (STQN)[75] method uses a linear (LST) or quadratic synchronous transit (QST) approach to locate the quadratic region of the transition states and then uses a quasi-Newton or eigenvalue-following algorithm to complete the optimisation. For the LST approach, the highest point is located by drawing a line between the reactant and product minima on the potential energy surface. The QST approach refines this method by starting at the LST maximum and minimising the energy perpendicular to the LST line. In Gaussian 03, using the QST2 option**,** we require one optimised reactant and one optimised product, followed by the generation of a guess for the transition state which is midway between the reactant and product in terms of redundant internal coordinates. For more complicated systems, one would provide the reactant, the product and a guess for the transition state and use the QST3 option in Gaussian 03 to perform a transition state optimisation.

Nudged elastic band (NEB) method

The nudged elastic band (NEB) method is used to search for reaction pathways when both the initial and final states are known. The NEB algorithm then generates a succession of "images" or a "chain of replicas" along the "band" connecting the initial and final states. The energy of this string of images is then minimised to search for a minimum energy path (MEP) as shown in Figure 3.3[76].

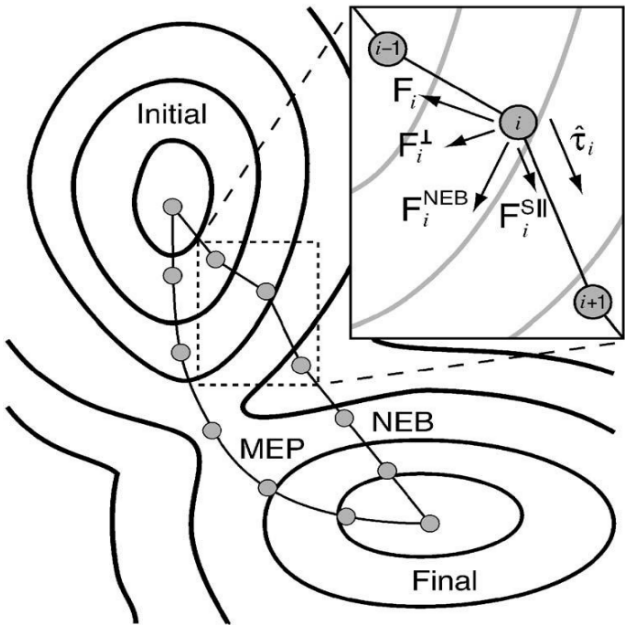

Figure 3.3: Illustration of nudged elastic band method[77].

3.9 Modelling Solvation

Modelling solvation is one of the most challenging issues in computational chemistry. There are several methods currently used[78]; in this thesis we use the PCM (polarisable continuum model) and COSMO (conductor-like screening model) approaches. For the asymmetric hydrogenation of ketones, 1-propanol is used as the solvent and for the reduction of imines, methanol is used.

3.9.1 COSMO Solvation Model

COSMO stands for "COnductor-like Screening MOdel"[79], a continuum solvation model[80] for treating the solvation of molecules by calculating the dielectric screening charges and energies on a van der Waals-like molecular surface in the approximation of a conductor[81]. The dielectric screening calculation can be embedded in self consistent field molecular orbital calculations based on either Hartree-Fock theory or DFT, which is a major strength of this approach.

The COSMO method creates a cavity occupied by the solute. Because of the charge distribution in the solute, a screening charge is generated in the dielectric continuum of permittivity ε. This ideal screening charge is computed in the approximation of an ideal conductor. In such ideal conditions, the total potential on the surface is zero.

In many applications, COSMO has yielded satisfactory results[78,81]. Specifically, this model has proven to calculate solvation energies within 2 kcal/mol of the experimental results for neutral solvent molecules[82].

3.9.2 The Polarisable Continuum Model (PCM)

The PCM, proposed by Tomasi *et al.*[83], is one of the most widely used models to compute a system in a non-aqueous solution, and belongs to the class of self-consistent reaction field (SCRF) methods. These methods all model the solvent as a continuum of uniform dielectric constant ε. The PCM solvation model is available for calculating energies and gradients at the Hartree-Fock and DFT levels of theory. Solvation models based on polarisable continuum dielectrics have been demonstrated to be flexible and accurate, particularly when the solute is situated in a cavity of realistic molecular shape[84].

3.10 Computational details

In this thesis, density functional theory calculations were carried out using the DMol^3[84], Gaussian 03[85] and CP2K[86] codes.

In DMol^3, the electronic wave function is expanded in a localised atom-centred basis set with each basis function defined numerically on a dense radial grid. In this study, we employ the double-numeric-polarised (DNP) basis set, which is comparable to the 6-31G** basis set. However, this numerical basis set is more accurate than 6-31G**[84b]. Due to the high quality of these orbitals, basis set superposition effects are minimised[87]. Furthermore, the numerical basis set is more spatially extended than 6-31G** and is therefore better equipped for describing the tail of the wavefunction caused by long-range interactions. Indeed, it has been shown that the DNP basis set gives values of energies of reaction that are very close to those obtained using the aug-cc-pVTZ basis set[88]. Each basis function was restricted to within a cutoff radius of 4.7 Å. The electron density was approximated using a multipolar expansion up to octupole. For total energies and geometry optimisations, the gradient-corrected PBE exchange-correlation functional was applied[53]. The inner core–electrons for ruthenium were represented using a DFT semi-local pseudopotential, which was generated by fitting all-electron relativistic DFT results, and specifically developed to improve the accuracy of DMol^3 calculations. This methodology employing DMol^3/PBE/DNP has been thoroughly tested by Di Tommaso *et al.*[28c] for the case of H_2-hydrogenation of ketones catalysed by the Ru(diphosphine)(diamine) hydride complexes, by comparing the structures, energies of reaction and activation energies computed at the PBE/DNP level with the results obtained using several other exchange-correlation functionals (BLYP[55c,57], B3LYP[55,58,89], B97-2[90], BB1K[57,91]), MP2 calculations and different basis sets — 6-31G(d,p), 6-31++G(d,p), 6-311++G(d,p), 6-311++G(2d,2p) and 6-311++G(2df,2pd)[28c]. In the optimisation procedure, the geometry was considered to be converged when the energy change was less than 10^{-5} Hartree and the gradient was less than 2×10^{-3} Hartree Å^{-1}, or when a tighter gradient convergence criterion was required, 2×10^{-4} Hartree Å^{-1}.

In Gaussian 03, the hybrid exchange-correlation functionals PBE0[56a], B3LYP[55,89,92], and MPW1PW91[93] were employed. We also compared different basis sets — 6-31G(d,p), 6-311G(d,p), 6-31+G(d,p), 6-311+G(d,p), 6-31++G(d,p) and 6-311++G(d,p) — for hydrogen, carbon, nitrogen and oxygen; for ruthenium, iron and iridium, we used the SDD and LANL2DZ basis sets coupled with the SDD[94] and LANL2[70] pseudopotentials respectively.

In CP2K, the PBE exchange functional was employed, together with the TZV2P-MOLOPT-GTH basis set[95] which was applied on the hydrogen, carbon, nitrogen and oxygen, and the DZVP-MOLOPT-SR-GTH basis set[95] together with the Goedecker, Teter, and Hutter (GTH) pseudopotentials for the heavier iridium.

Different codes offer different methods to locate transition states. In this study, the constrained optimisation method in DMol^3, the synchronous transit-guided quasi-Newton (STQN)[75] method in Gaussian 03 and the nudged elastic band (NEB)[76a,76b,76d,96] method in CP2K were employed.

We have also considered solvent effects with COSMO[81] *via* DMol^3 and PCM[97] *via* Gaussian 03.

The semi-empirical dispersion correction to density functional theory (DFT-D)[59] was applied using Grimme's D3 method without and with the C9 three-body term (DFT_D3[59a] and DFT_D3_C9[59a]) at the PBE and PBE0 level of theory using the CP2K code.

Chapter 4 Effects of Ligand Variation on Enantioselective Hydrogenation Catalysed by Noyori-Type Ruthenium Complexes

4.1 Introduction

In this chapter, we investigate the effects of changing the diphosphine and diamine ligands on the enantiomeric excess (*ee*) in the hydrogenation of acetophenone (ACP) and aim at establishing a relationship between the *ee* and activation energy. The reactions considered in the present study are summarised in Scheme 4.1. From experimental results mentioned in Chapter 2, we recall that [**1a/2a**] is able to reduce ACP to (*R*)-phenylethanol with an *ee* of 99%[22b], whereas when the reaction is catalysed by either [**1b/2a**] or [**1c/2a**] the *ee* decreases to 82%[23] and 83%[24] respectively, the ligands differing only in the position of the methyl group on the aryl rings. However, upon alteration of the diamine, the reaction catalysed by [**1b/2b**] affords the (*R*)-phenylethanol an *ee* of only 22%[25], whilst the reaction catalysed by [**1b/2c**] and [**1b/2d**] generates (*S*)-phenylethanol in 43% and 91% *ee* respectively[25]. We also recall from Chapter 2 that the metal-ligand bifunctional mechanism is widely accepted to be responsible for the high enantioselectivity in the hydrogenation of prochiral ketones catalysed by the *trans*-[RuH_2(diphosphine)(diamine)] complexes[30a30e].

The previously mentioned examples show that the *ee* varies significantly even with minor changes to the ligands as discussed in Chapter 2. A rationalisation of the differences in *ee* in the hydrogenation of ACP catalysed by the *trans*-[RuH_2(diphosphine)(diamine)] complexes has been proposed in terms of steric and electronic effects[17,28a,28b].

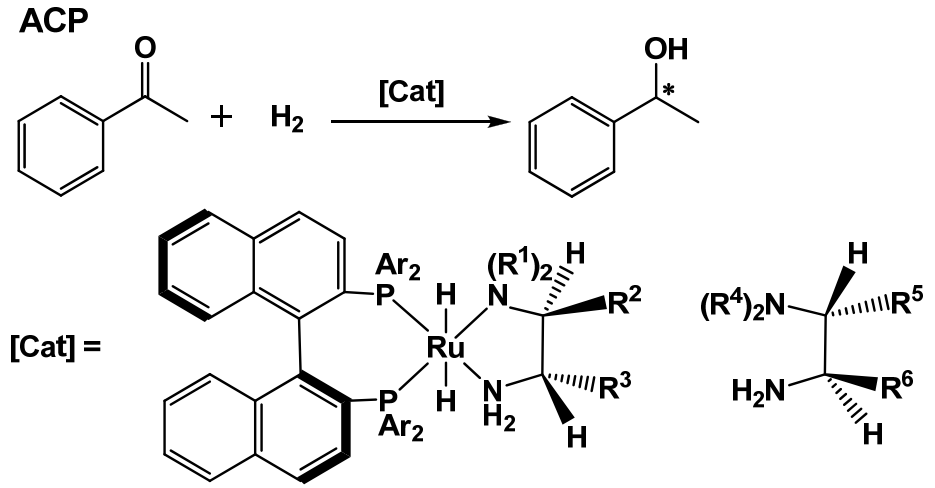

Ar = 3,5-$(CH_3)_2C_6H_3$; (*S*)-XylBINAP **1a**	R^1=H,	R^2=R^3=Ph;	(*S*,*S*)-DPEN **2a**
Ar = 4-$(CH_3)C_6H_4$; (*S*)-TolBINAP **1b**	R^1=CH_3,	R^2=R^3=Ph;	(*S*,*S*)-DMDPEN **2b**
Ar = C_6H_5; (*S*)-BINAP **1c**	R^1=CH_3,	R^2=H, R^3=Ph;	(*S*)-DMAPEN **2c**
	R^4=CH_3,	R^5=H, R^6=Ph;	(*R*)-DMAPEN **2d**

Scheme 4.1: Asymmetric hydrogenation of acetophenone catalysed by the *trans*-[RuH_2(diphosphine)(diamine)] complexes considered in the present study.

However, these computational studies only focused on the effect of diphosphine on the enantioselectivity. In this chapter, we systematically investigate the effect of structural changes in both the diphosphine and diamine ligands. We aim to establish a relationship between enantioselectivity and energy profiles based on the metal-ligand bifunctional mechanism in asymmetric hydrogenation catalysed by catalysts with varying substituents on either the phosphine or amine ligand.

4.2 Methodology

The computational techniques employed in this chapter were discussed in detail in Chapter 3. The DFT calculations were carried out using the DMol^3 code. The PBE exchange-correlation functional, DNP basis set and semi-local pseudopotential were applied. Each basis function was restricted to within a cutoff radius of 4.7 Å.

With respect to the DFT-D calculations, the CP2K and Quantum-Espresso codes were applied. In CP2K, the PBE exchange functionals were employed, together with the TZV2P-MOLOPT-GTH basis set in the case of the hydrogen, carbon, nitrogen and oxygen atoms, and the DZVP-MOLOPT-SR-GTH basis set with the GTH pseudopotentials in the case of the heavier ruthenium atom. In order to locate transition states, the constrained optimisation method in DMol^3 and the nudged elastic band (NEB) method in CP2K were employed.

To treat solvent effects, we have considered the propanol solvent using the COSMO polarisable solvation model[81], which provides a simple but useful estimate of solvation energies. However, the differences between the activation energies of competitive pathways computed in the COSMO solvent model and in the gas phase were only *ca.*1 kcal/mol. Therefore, in this study, we will present the results obtained from gas-phase calculations.

4.3 Results and Discussion

Acetophenone (ACP), the simplest aromatic ketone, has been selected as the substrate in this study to investigate the performance of the ruthenium catalysts with different substituents on the diphosphine and 1,2-diamine ligands. We first explore the intrinsic aspects of the reactivity in terms of the four possible pathways, discussed in Chapter 2, for ACP approaching the active sites of the catalysts based on the metal-ligand bifunctional mechanism in Section 4.3.1. Next, in Section 4.3.2, we explain the origin of the sharp peak occurring before the transition state along the most favourable pathway (Q1), as shown in Figure 2.6 (page 41)[28a]. We then investigate the effect of changing the substituents on both diphosphine (Section 4.3.3) and diamine ligands (Sections 4.3.4 and

4.3.5) and correlate the *ee* with the differences in activation energies and the structural changes in the supporting ligands of the ruthenium catalysts (Section 4.3.6). Finally, we briefly discuss the results of including the effect of the dispersion correction in Section 4.3.7, details of which are given in the Appendix.

4.3.1 Determination of favourable pathways in the hydrogenation of acetophenone using RuH_2[(*S*)-XylBINAP][(*S*,*S*)-DPEN]

Scheme 4.1 summarises the hydrogenation of ACP catalysed by the *trans*-[RuH_2(diphosphine)(diamine)] complexes. Based on the metal-ligand bifunctional mechanism, the active sites (Ru-H, N-H) restrict the pathway of the substrate as it approaches the ruthenium catalyst. The four possible pathways discussed previously in Chapter 2 are illustrated in Scheme 4.2. The Q1 and Q4 pathways give the (*R*)-product and Q2 and Q3 give the (*S*)-product. Regarding the energetic variation, in this study we only consider the electronic energy without taking account of thermal and entropic effects. In this respect, we note that a computational study of the reaction of acetophenone with RuH_2[(*S*)-BINAP][(*S*,*S*)-CYDN] has shown that the difference in the calculated energies of activation is similar to the difference in the free energies of activation[17]. Figure 4.1 shows the reaction coordinate diagram of system [ACP + **1a/2a**] along the four possible pathways (mentioned in Section 2.4), which reveals two things. Firstly, the energy of the intermediate (INT) in Q1 (–5.49 kcal/mol) is lower than that in Q2 (–4.18 kcal/mol), Q3 (–3.60 kcal/mol), and Q4 (–1.97 kcal/mol). Secondly, the activation energies (TS-INT) along different pathways are 3.68 kcal/mol for Q1, 6.47 kcal/mol for Q2, 8.48 kcal/mol for Q3, and 10.28 kcal/mol for Q4, implying that Q1 is the most favourable pathway and the difference in activation energies between Q1 and Q2, Q3, as well as Q4, leads to the substrate interacting with the ruthenium catalyst predominantly along Q1, resulting in high enantioselectivity. Figures 4.2 (A) and 4.2 (B) shows the configurations when ACP approaches the ruthenium catalyst in the two intermediates (Pre-INT and INT, discussed later), transition state (TS) and PRO (Phenylethanol + $16e^-$ species) along the four pathways. There are two intermediates along the Q1 and Q3 pathways.

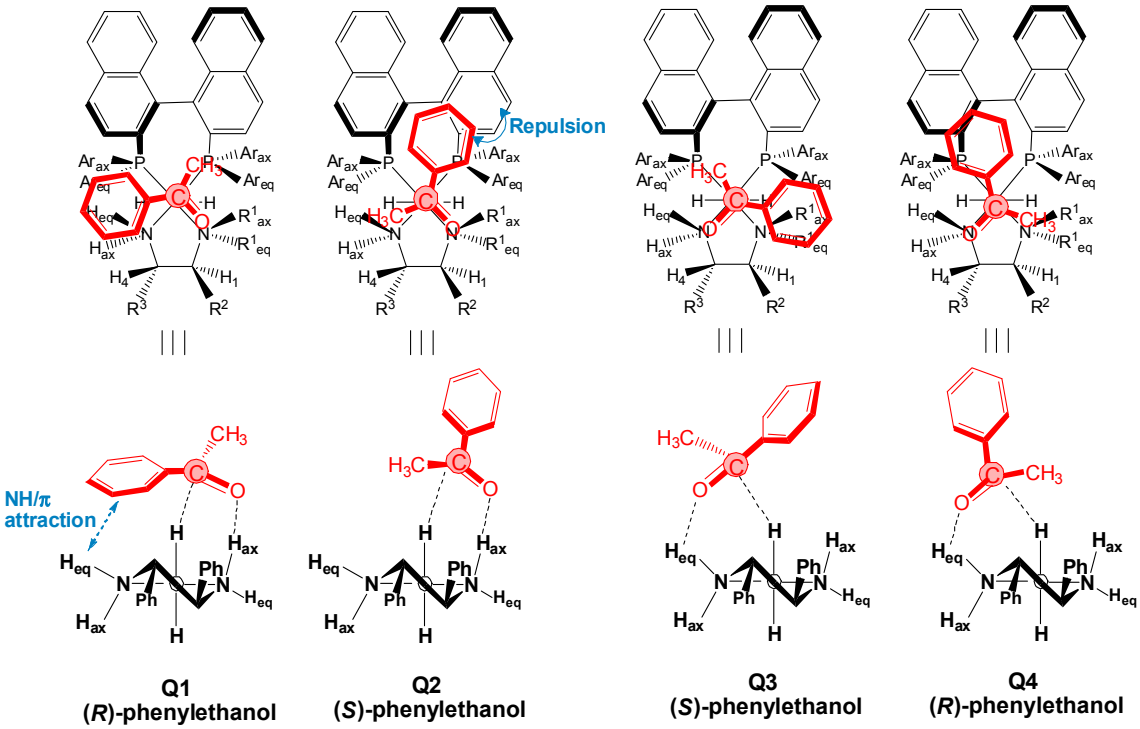

Scheme 4.2: Possible pathways with the subsequent stereochemical configurations of the phenylethanol product.

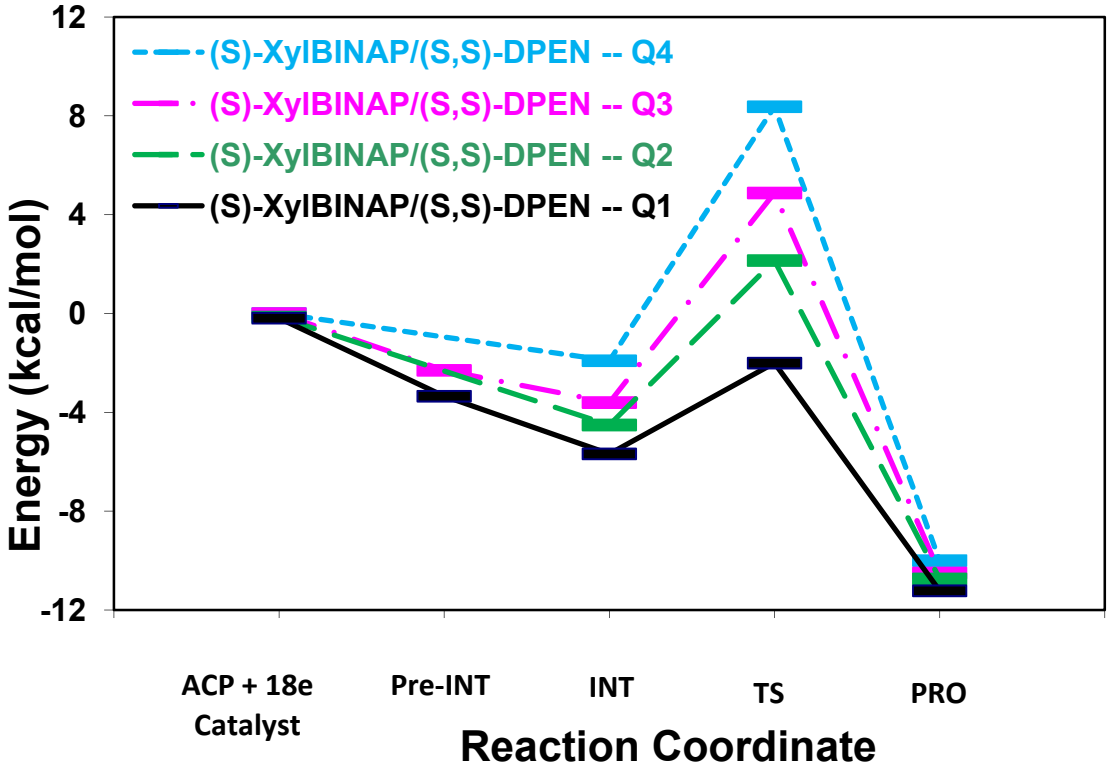

Figure 4.1: Reaction coordinate diagram for the hydrogenation of acetophenone catalysed by RuH_2[(*S*)-XylBINAP][(*S*,*S*)-DPEN] along each possible pathway (Q1, Q2, Q3 and Q4). (PRO is Phenylethanol + $16e^-$ species.)

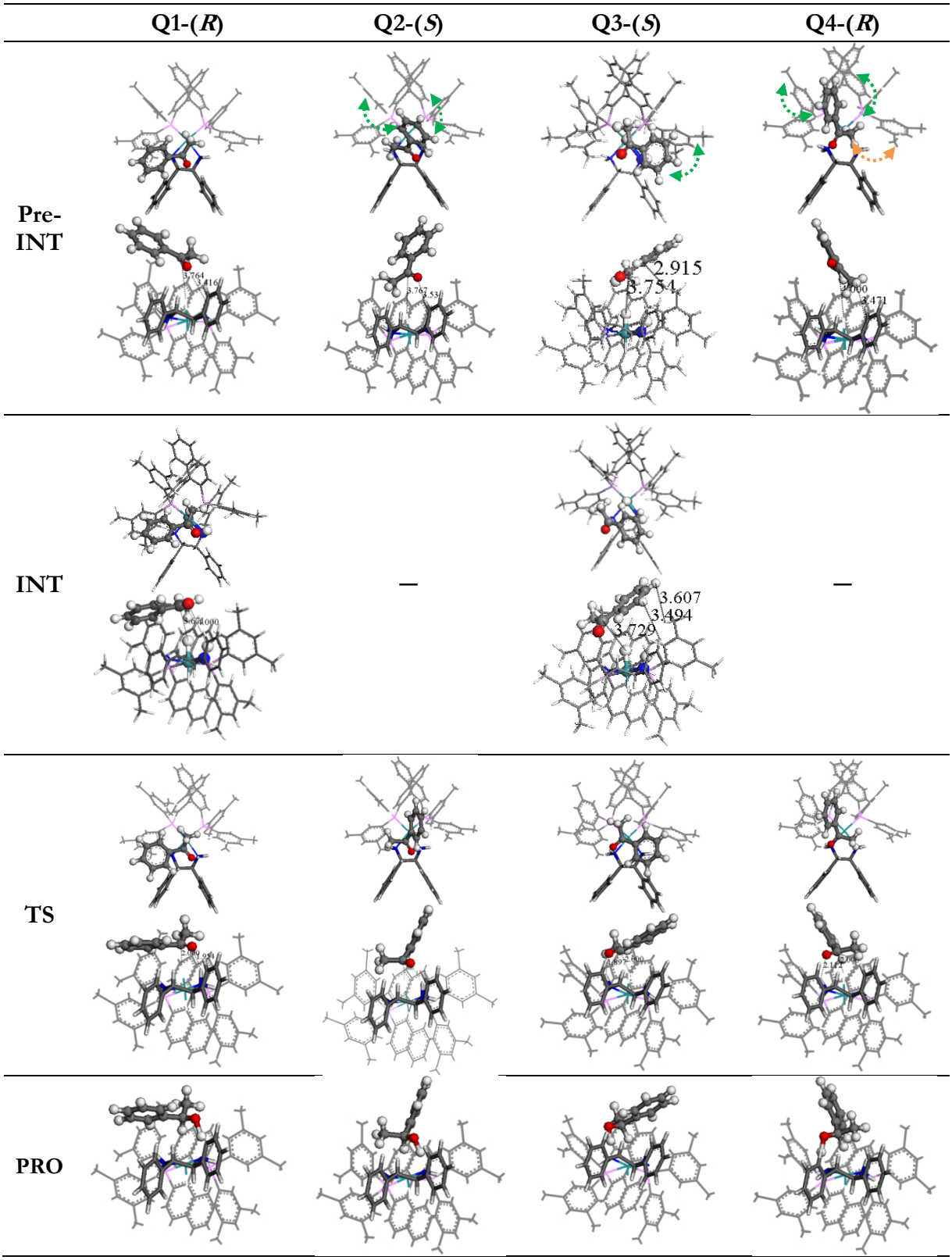

Figure 4.2 (A): Illustration for the asymmetric hydrogenation of acetophenone catalysed by the RuH_2[(*S*)-XylBINAP][(*S,S*)-DPEN] along the Q1, Q2, Q3, and Q4 pathways.

	Pre-INT	INT
Q1-(*R*)	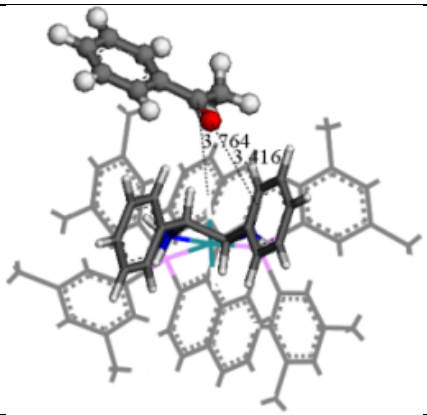	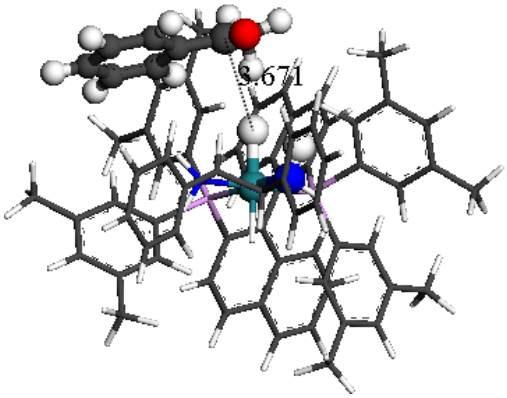
Q2-(*S*)	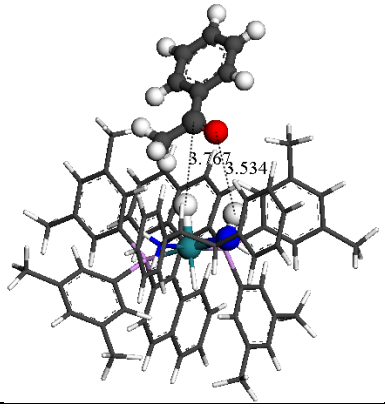	
Q3-(*S*)	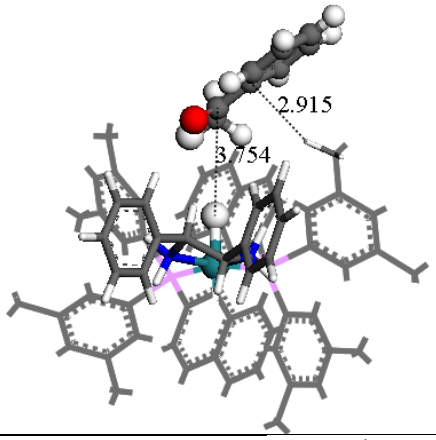	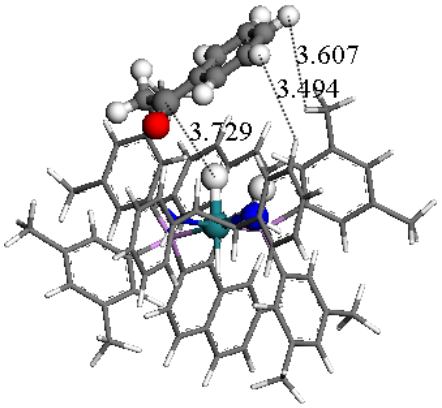
Q4-(*R*)	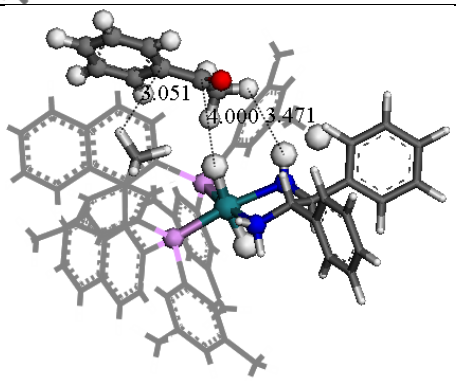	

Figure 4.2 (B): Illustration for the asymmetric hydrogenation of acetophenone catalysed by the RuH_2[(*S*)-XylBINAP][(*S,S*)-DPEN] along the Q1, Q2, Q3, and Q4 pathways.

Q1 is the most favourable reaction pathway. There is no steric hindrance between the intermediate and the transition state to stop ACP from rotating and entering into the "pocket" made by the bulky groups. In addition, the approach of ACP towards the catalyst is driven by an attractive *X*H (*X*= N and C)/π hydrogen bond interaction when the *X*H hydrogen-donor and the aromatic π moiety hydrogen-acceptor come into close contact. In contrast, along Q2, the phenyl group of ACP rotates and becomes upright before forming the intermediates, being stabilised by steric repulsions between one of the aryl rings and the naphthyl groups on the diphosphine, increasing the energy of the whole system. From the intermediate to the transition state, there is no hindering preventing the ACP from entering the pocket. For Q3, in both intermediates, ACP is repelled by the *m*-xylyl groups and the phenyl group on the diamine, thus obstructing the formation of the transition state. For Q4, from the intermediate to the transition state, the phenyl group of ACP is restrained by the one of the aryl groups and the naphthyl group; meanwhile, the methyl group of ACP, from the intermediate to the transition state, is restrained by one of the aryl groups on the diphosphine, which creates a strong steric repulsion when forming the transition state and leads to Q4 being a particularly unfavourable pathway.

Thus, we can conclude that there is a lower activation energy when the interaction between ACP and the catalyst is dominated by the non-bonding NH/π attraction in the intermediate. Most importantly, the primary factor in determining the energy of the transition state is the steric repulsion from the intermediate to the transition state, but not the nature of the intermediate.

4.3.2 Influence on the transition state from different intermediates in acetophenone hydrogenation using RuH_2[(*S*)-XylBINAP][(*S*,*S*)-DPEN]

In the enantioselective hydrogenation catalysed by the RuH_2[(*S*)-XylBINAP][(*S*,*S*)-DPEN] complex along the Q1 pathway, three stable intermediates, denoted as INT-A, INT-B and INT-C (Figure 4.3), are found using constrained optimisation by reducing the pseudo coordinate, (Ru-)H···C(=O), from 9 Å to 1.1 Å. The (Ru-)H···C(=O) distances of the three intermediates are all approximately 3.75 Å. The results in Figure 4.3 show that INT-A and INT-B have similar relative energies (–3.34 kcal/mol and –3.51 kcal/mol respectively) and orientations. The acetophenone (ACP) in INT-B and INT-C are slightly further away from the naphthyl group on the catalyst. The (Ru-)H···C(=O) distances in INT-A, INT-B and INT-C are 3.76 Å, 3.75 Å and 3.66 Å respectively. The phenyl group of ACP is closest to the catalyst in INT-C; thus the energy is reduced to –6.03 kcal/mol.

The influence of the different intermediates on activation energy (E_a) and transition state (TS) structures is now considered. The variations in energy on going from the intermediates INT-A, INT-B and INT-C to the transition state, and to the product, are reported in

Figure **4.**, 4.5 and 4.6 respectively. Although the configurations of INT-A and INT-B are similar, one of the methyl groups on *m*-xylene in INT-A hinders the phenyl group of ACP from rotating into the bulky pocket until the distance of (Ru-)H···C(=O) reaches 2.5 Å, which explains the high peak (4 kcal/mol higher than in the TS) before forming the TS. Nevertheless, the activation energy for the H_2-splitting is *ca.* 10 kcal/mol higher than that in the hydride transfer step from INT-A[28a]. Hence, although one peak prior to the TS is observed for INT-A, it does not affect the overall reaction. It is, however, important to notice that the structure of the transition state and the activation energy are unaffected by the intermediate, and therefore by the way in which ACP approaches the catalyst.

Q1	INT-A	INT-B	INT-C
top view	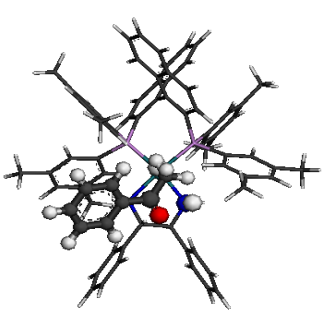	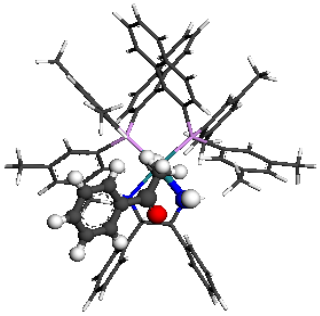	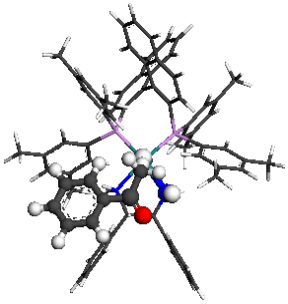
side view	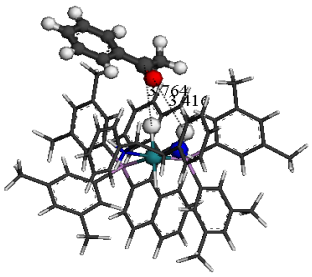	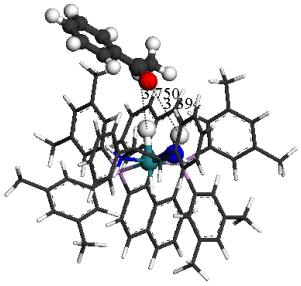	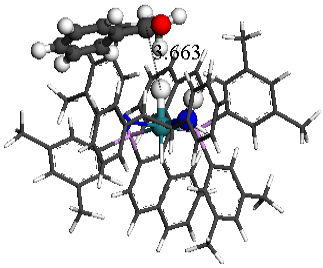
side view	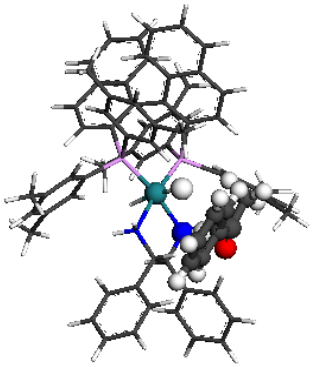	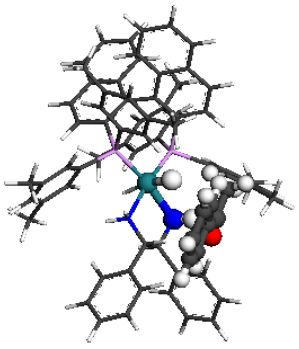	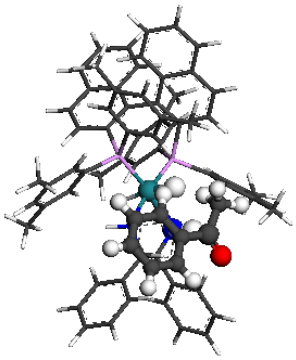
side view	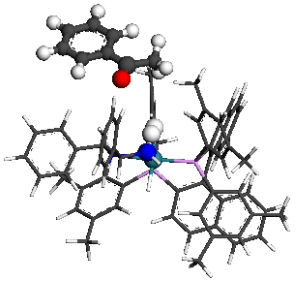	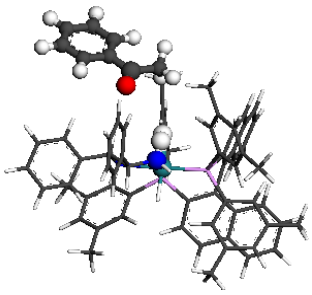	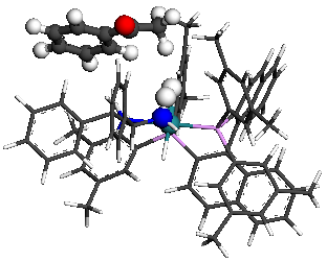
Energy	–3.34 kcal/mol	–3.51 kcal/mol	–6.03 kcal/mol

Figure 4.3: Snapshots from four different angles and relative energies of INT-A, INT-B and INT-C in the hydrogenation of acetophenone catalysed by the RuH_2[(*S*)-XylBINAP)][(*S,S*)-DPEN)] complex along the Q1 pathway.

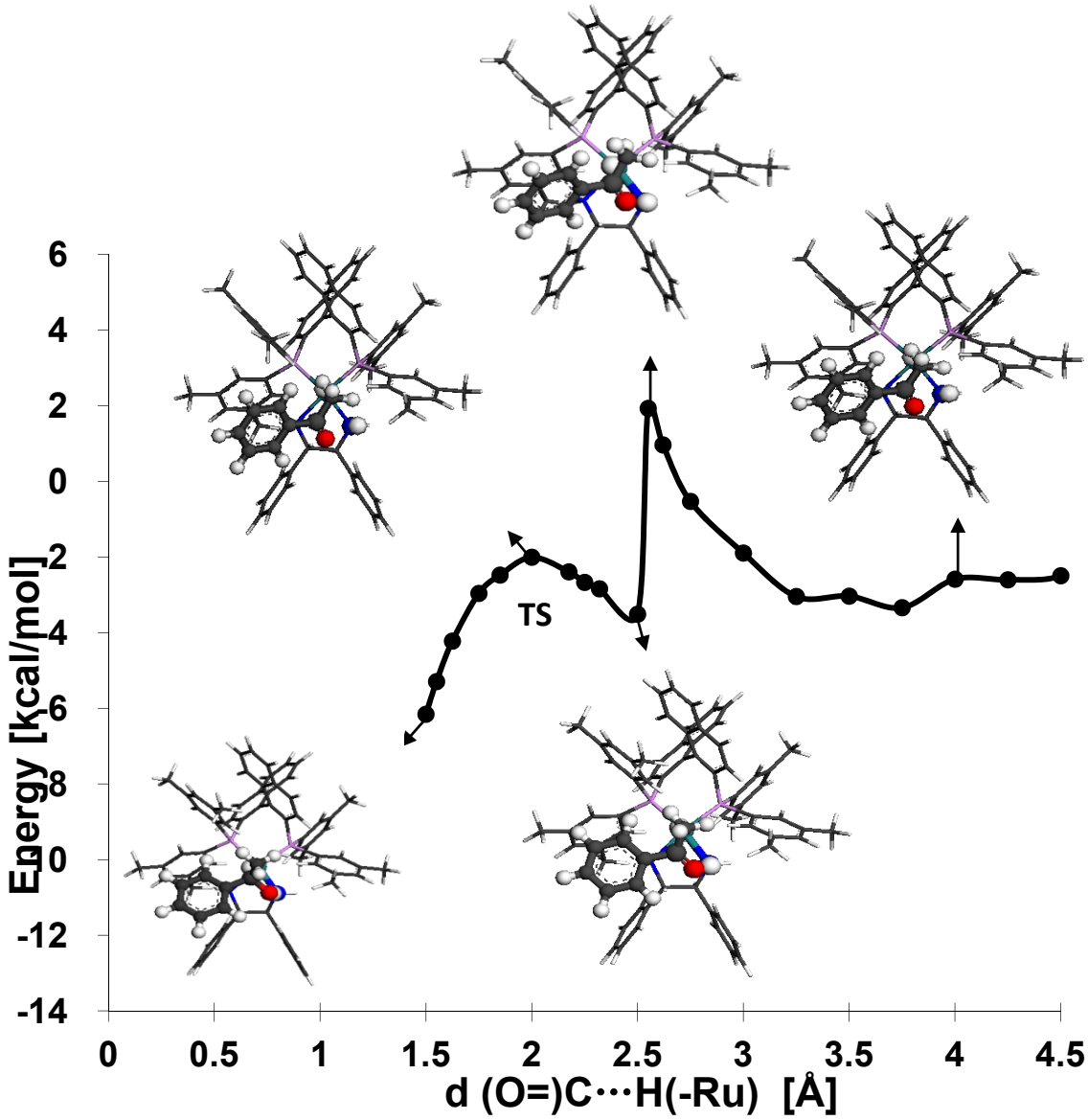

Figure 4.4 (A): Reaction coordinate diagram and structures of the hydrogenation of acetophenone catalysed by the RuH_2[(*S*)-XylBINAP][(*S*,*S*)-DPEN] complex along Q1 from INT-A at the DFT/PBE level of theory.

From INT-A			
d(C-H)	Structure	d(C-H)	Structure
3.76	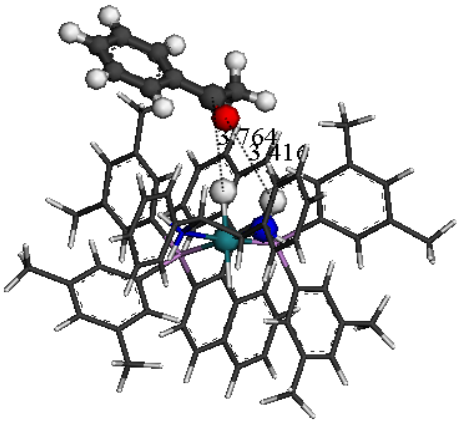	2.55	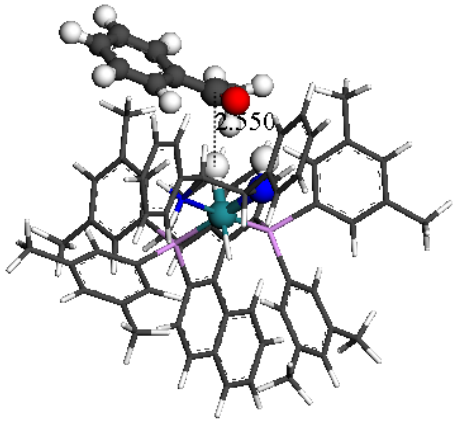
2.50	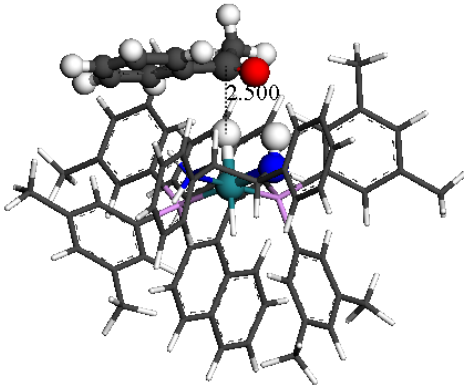	2 (TS)	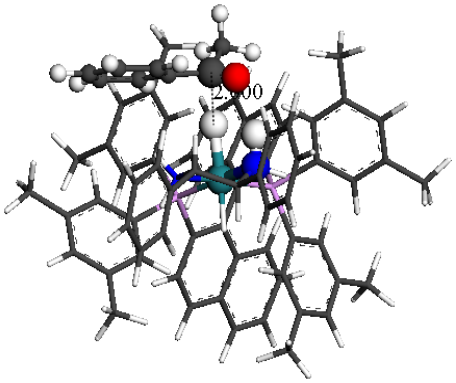
1.50	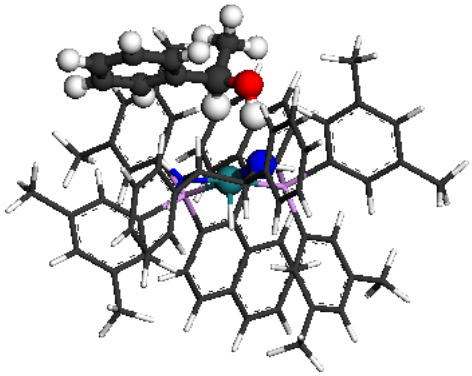		

Figure 4.4 (B): Structures of the hydrogenation of acetophenone catalysed by RuH_2[(*S*)-XylBINAP][(*S*,*S*)-DPEN] when the (Ru-)H···C(=O) distances are at 3.76, 2.55, 2.5, 2 and 1.5 Å along Q1 from INT-A.

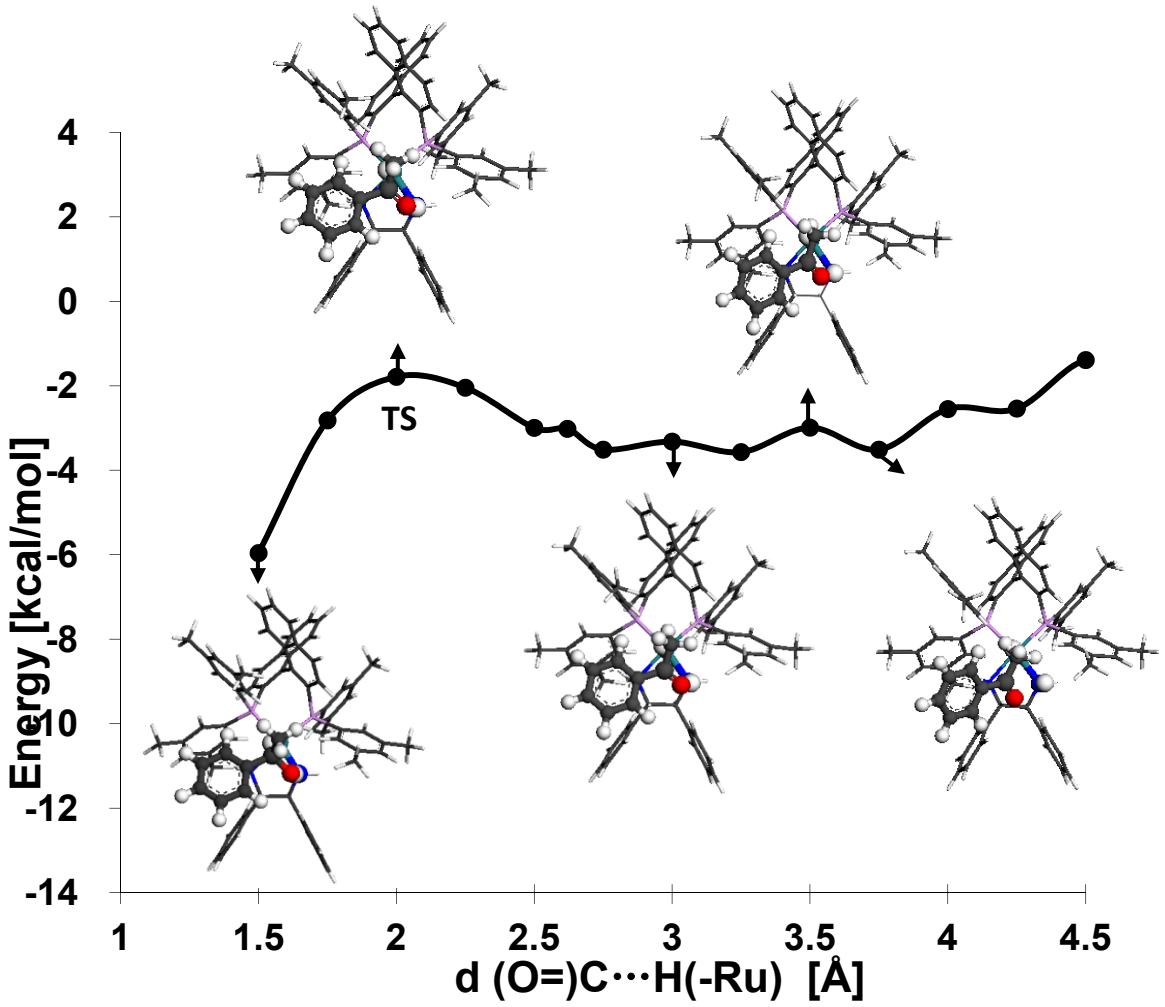

Figure 4.5 (A): Reaction coordinate diagram and structures of the hydrogenation of acetophenone by the RuH_2[(*S*)-XylBINAP][(*S*,*S*)-DPEN] complex along Q1 from INT-B at the DFT/PBE level of theory.

From INT-A			
d(C-H)	Structure	d(C-H)	Structure
3.75	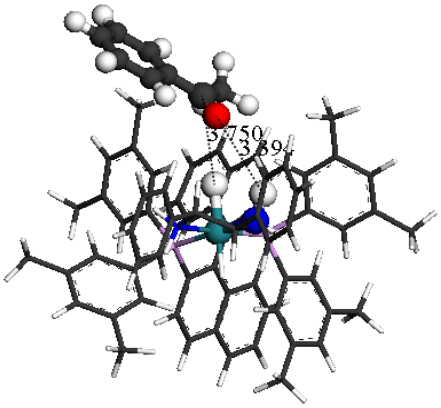	3	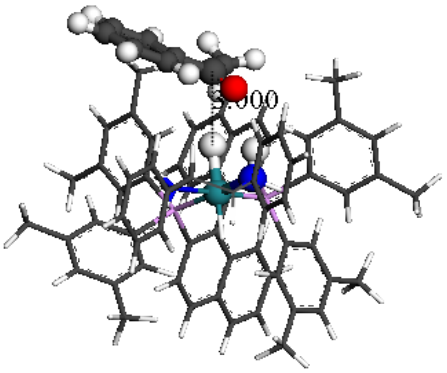
2.75	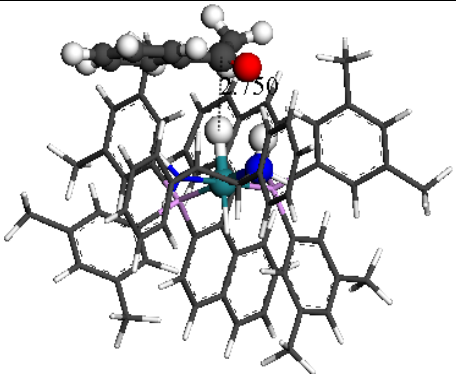	2 (TS)	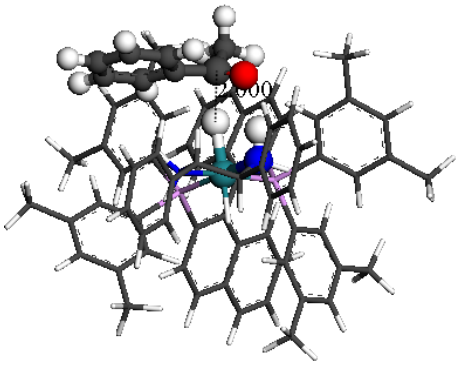
1.50	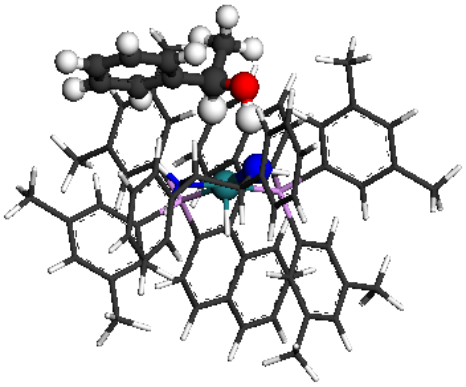		

Figure 4.5 (B): Structures of the hydrogenation of acetophenone catalysed by RuH_2[(*S*)-XylBINAP][(*S*,*S*)-DPEN] when the (Ru-)H···C(=O) distances are at 3.75, 3, 2.75, , 2 and 1.5 Å along Q1 from INT-B.

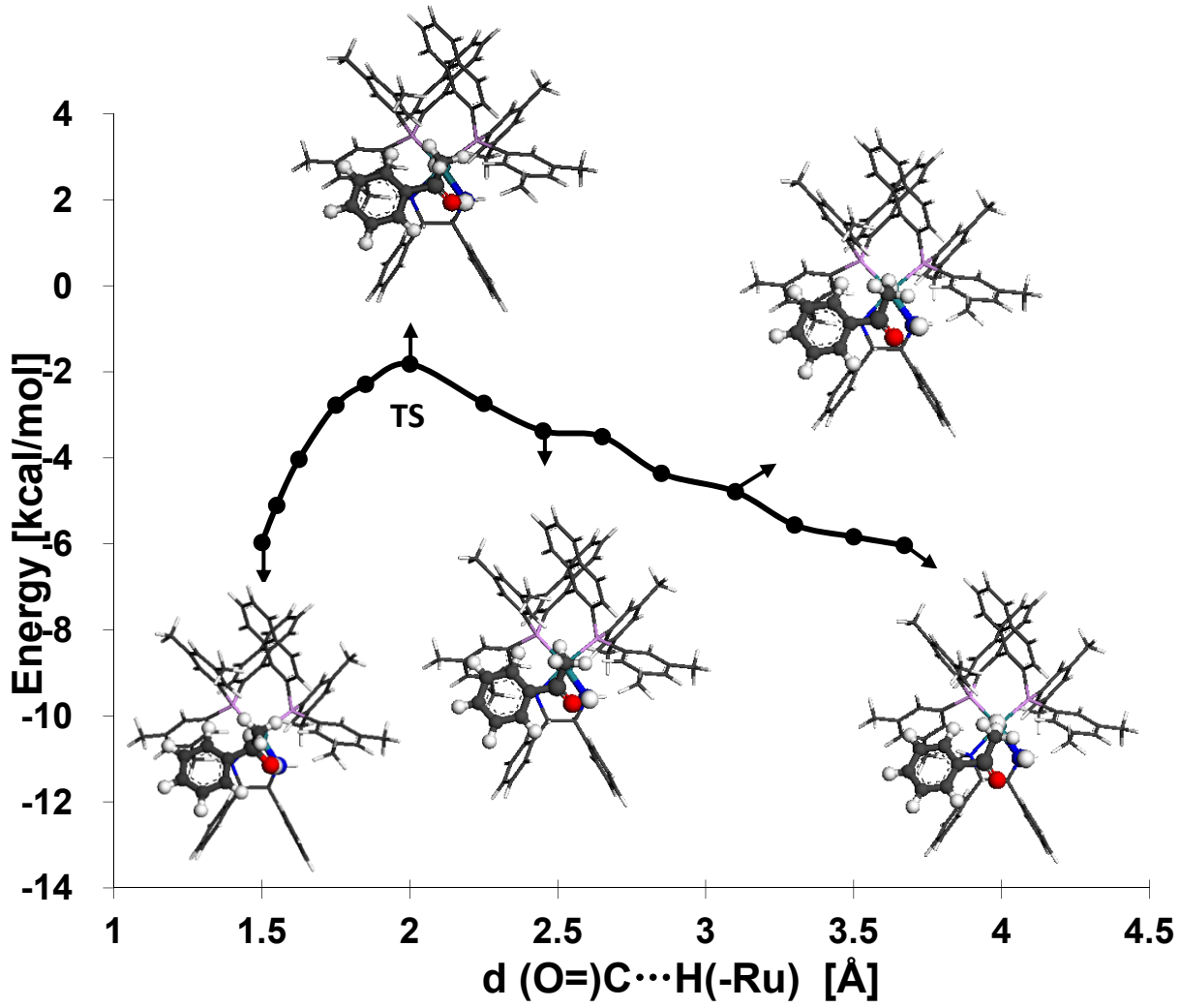

Figure 4.6 (A): Reaction coordinate diagram and structures of the hydrogenation of acetophenone by the RuH_2[(*S*)-XylBINAP][(*S*,*S*)-DPEN] complex along Q1 from INT-C at the DFT/PBE level of theory.

From INT-A			
d(C-H)	Structure	d(C-H)	Structure
3.75	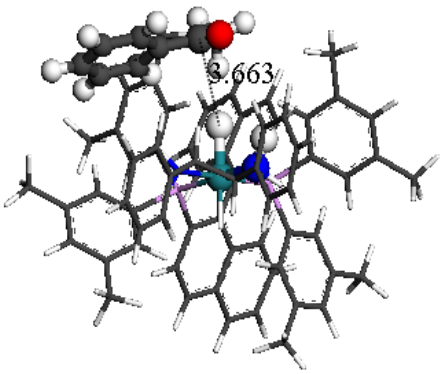	3	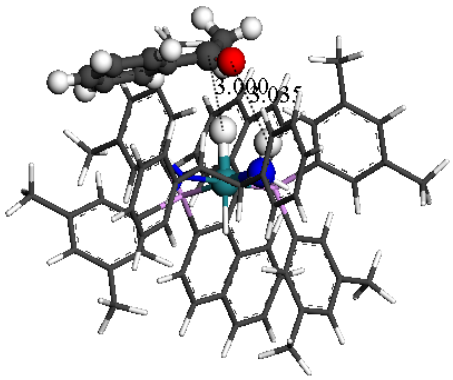
2.50	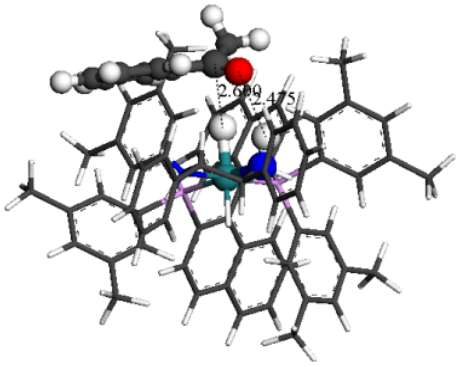	2 (TS)	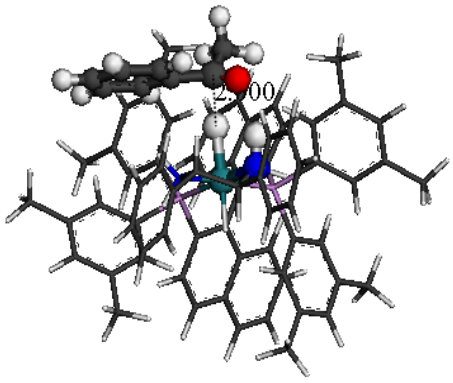
1.50	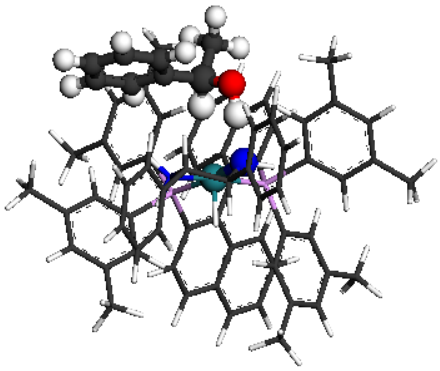		

Figure 4.6 (B): Structures of the hydrogenation of acetophenone catalysed by RuH_2[(*S*)-XylBINAP][(*S*,*S*)-DPEN] when the (Ru-)H···C(=O) distances are at 3.75, 3, 2.5, 2 and 1.5 Å along Q1 from INT-C.

4.3.3 Acetophenone hydrogenation catalysed by RuH_2[(*S*)-diphosphine][(*S*,*S*)-DPEN]

In this section, we investigate the effect of structural variations in the diphosphine ligands on the *ee*; on the basis of the results summarised in the previous section, only the two most favourable pathways, Q1 and Q2, are analysed.

We examine the following (*S*)-diphosphine ligands: Ar = XylBINAP, TolBINAP and BINAP, while keeping the diamine ligand as (*S*,*S*)-DPEN. The reaction coordinate diagrams for the hydrogenation reaction of ACP catalysed by [**1a/2a**], [**1b/2a**] and [**1c/2a**] are presented in Figure 4.7. They reveal, firstly, that for all three systems there are two intermediates, Pre-INT and INT, along Q1; secondly, that the activation energy along Q2 in each system is higher than that along Q1; thirdly, that the energy of the TS in [**1a/2a**] along Q2 increases more than with the other two systems. Figure 4.8 compares the structures of the first intermediate (Pre-INT) and the intermediates with the lowest energy (INT), transition states (TS) and products (PRO) along Q1 and Q2. For all three systems, when ACP approaches the active sites of the RuH_2(*S*-diphosphine)(*S*,*S*-DPEN) complex along Q1, the phenyl group of ACP enters the "pocket" created by the bulky groups of the ligands and forms the second, more stable intermediate INT, which is attracted by the XH/π (X=C and N) interaction and stabilises the motion of the phenyl group of ACP (See Figure 4.8 (B)). Then, formation of the TS mainly involves rotation of the methyl group of ACP. The formation of the TS in Q2 is constrained by the steric repulsion between one of the aryl groups and the naphthyl group on the diphosphine. From Table 4.1, we note that for Q1, the energy of Pre-INT in [ACP + **1a/2a**] (–5.49 kcal/mol) is lower than that in the other two systems (–4.93 kcal/mol and –4.70 kcal/mol for [ACP + **1b/2a**] and [ACP + **1c/2a**] respectively), which indicates that the strength of the non-bonding attraction increases with the number of methyl groups on the aryl group of the catalyst. The E_a in [ACP + **1a/2a**] along Q2 (6.65 kcal/mol) is *ca.* 1.5 kcal/mol higher than that in the other two systems (5.14 kcal/mol and 5.35 kcal/mol). The main cause of this effect is probably the presence of two methyl groups on the xylyl group, which are closer to the phenyl group of ACP and therefore cause a greater steric repulsion. Moreover, the two methyl groups at the *meta*-position create a smaller dihedral angle, thus reducing the degree of freedom of ACP when it enters the pocket, which in turn constrains the formation of the product in a particular

direction and therefore increases selectivity. We therefore see that from the intermediate to the transition state, although there is no hindrance along both pathways in the three systems, the formation of a second, more stable intermediate (INT) along Q1 assists the formation of the TS and thus lowers the activation energy. Furthermore, the methyl group on the *m*-xylene group restrains the motion of ACP along Q2 and elevates the energy of the TS, thereby facilitating the reaction through the Q1 pathway. Hence, the system with a 3,5-dimethyl xylene group gives the highest *ee*, whereas systems with a tolyl group do not differ significantly in enantioselectivity from those with only a phenyl group.

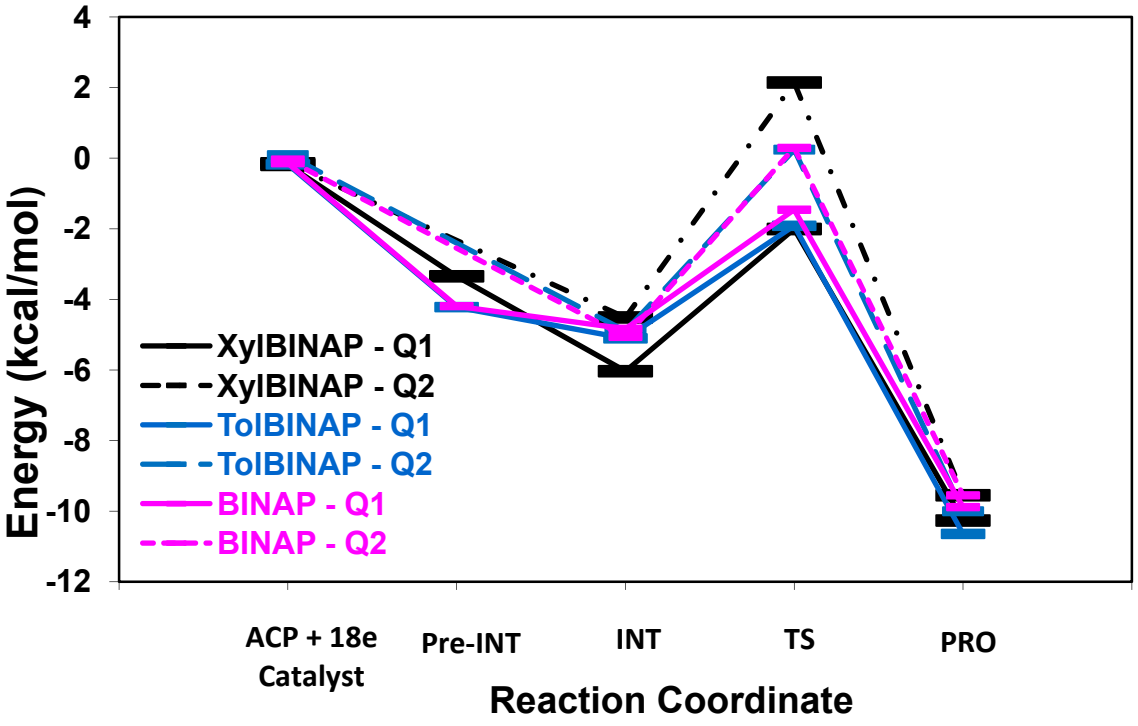

Figure 4.7: Reaction coordinate diagram of the hydrogenation of acetophenone catalysed by the [**1a**], [**1b**], and [**1c**]/[(*S*,*S*)-DPEN] ruthenium complexes along the Q1 and Q2 pathways. (Pre-INT is the first intermediate before forming the intermediate with the lowest energy, INT).

Path		Pre-INT	INT	TS	PRO
1a / 2a	**Q 1**	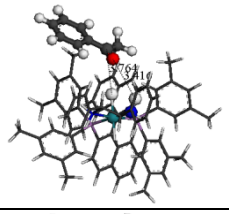	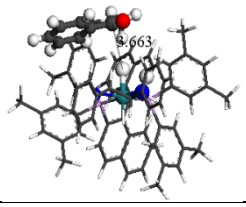	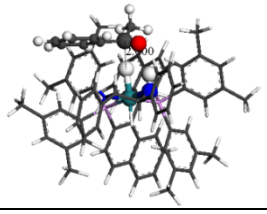	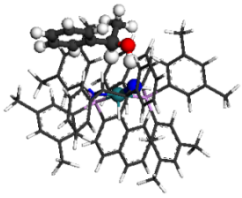
1b / 2a	**Q 1**	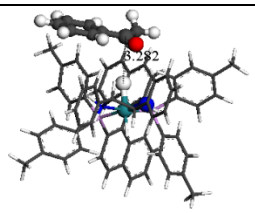	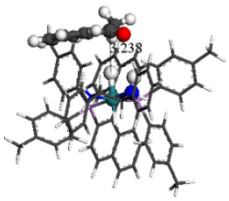	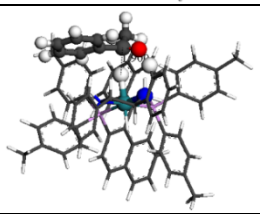	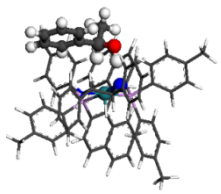
1c / 2a	**Q 1**	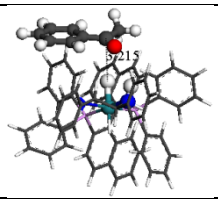	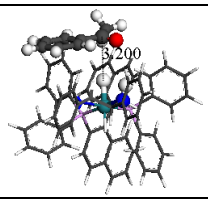	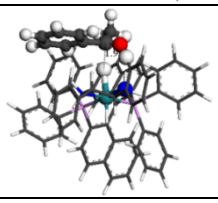	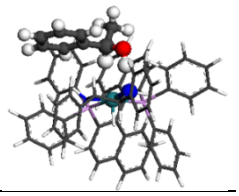
1a / 2a	**Q 2**	—	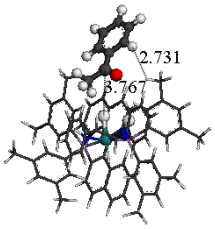	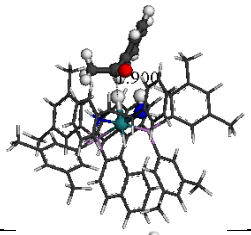	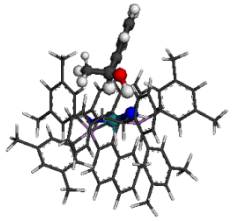
1b / 2a	**Q 2**	—	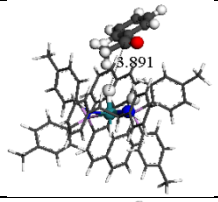	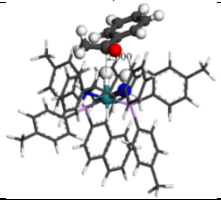	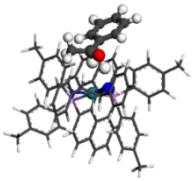
1c / 2a	**Q 2**	—	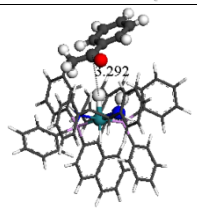	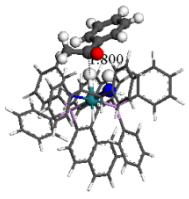	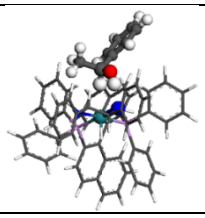

Figure 4.8 (A): Structures in the Pre-INT (the first intermediate), INT (the most stable intermediate), TS (transition state) and PRO (product + 16 e^- species) states in systems [ACP + **1a/2a**], [ACP + 1**b/2a**] and [ACP + **1c/2a**] along the Q1 and Q2 pathways.

Pre-INT

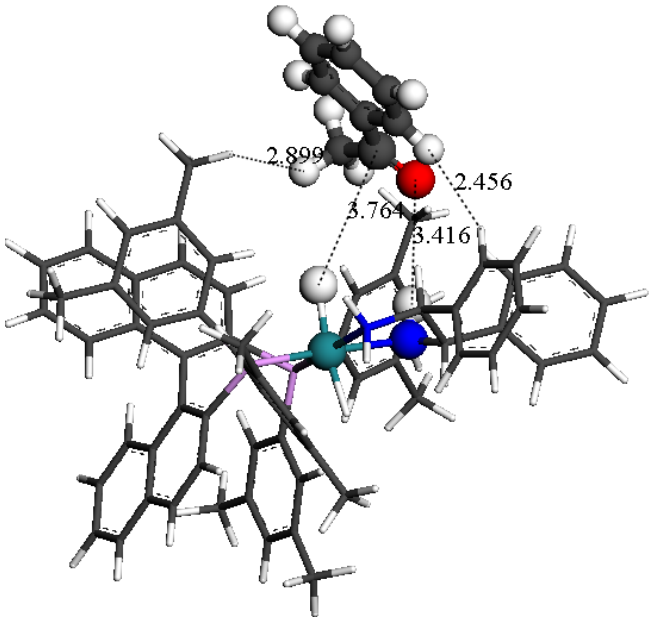

INT

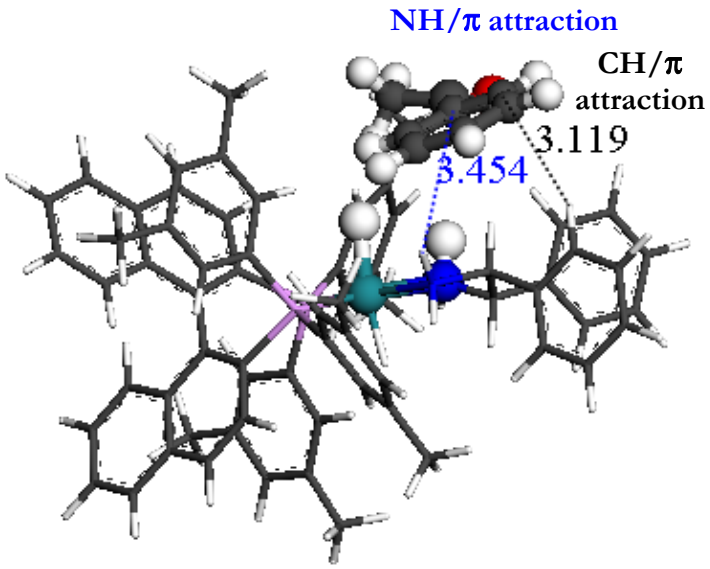

Figure 4.8 (B): Structures in the Pre-INT (the first intermediate) and INT (the most stable intermediate) in system [ACP + RuH_2\{(*S*)-XylBINAP\}\{(*S*,*S*)-DPEN\}] along Q1.

Table 4.1: Energetic characteristics in the hydrogenation of acetophenone catalysed by the RuH_2[(*S*)-diphosphine)][(*S*,*S*)-DPEN] complex along the Q1 and Q2 pathways.

System	Path	Pre-INT	INT	TS	E_a	ΔEa	*ee*
		[kcal/mol]					[%]
1a/2a	Q1	–3.16	–5.49	–1.82	1.34	5.31	97-99
	Q2		–4.37	2.29	6.65		
1b/2a	Q1	–4.05	–4.93	–1.74	2.30	2.83	80-82
	Q2		–4.98	0.16	5.14		
1c/2a	Q1	–3.82	–4.69	–1.32	2.50	2.85	83
	Q2		–5.02	0.33	5.35		

4.3.4 Acetophenone hydrogenation catalysed by RuH_2[(*S*)-TolBINAP][diamine]

We now compare the reaction of ACP hydrogenation catalysed by ruthenium complexes with the same diphosphine, (*S*)-TolBINAP (**1b**), combined with three different diamines: (*S*,*S*)-DPEN (**2a**), (*S*,*S*)-DMDPEN (**2b**) and (*R*)-DMAPEN (**2d**). First we determine the two most energetically preferable pathways associated with the (*R*)- and (*S*)-alcohols. Scheme 4.3 illustrates the possible pathways — Q1, Q2, Q3 and Q4 — with the subsequent stereochemical (*R*)- and (*S*)-configurations of the phenylethanol product in [ACP + **1b/2a**], [ACP + **1b/2b**] and [ACP + **1b/2d**].

Comparing Q1 and Q3 for [ACP + **1b/2b**], one of the aryl groups hampers the approach of ACP as with [ACP + **1b/2a**]; therefore Q1 is a more energetically favourable pathway than Q3. Comparing Q2 and Q4, the phenyl group of ACP is constrained by the aryl group and naphthyl group on the diphosphine, and the methyl group of ACP is constrained by the two methyl groups of the diamine. Moreover, for Q4, the methyl group of ACP is also restrained by one aryl group of the diphosphine, which indicates that the Q2 pathway is energetically more favourable than Q4. Hence, it is likely that Q1 and Q2 are the two most favourable pathways. Nevertheless, for the systems [ACP + **1b/2b**] and [ACP + **1b/2d**], the absence of one phenyl group on the diamine enhances the freedom of ACP. It is therefore not completely clear from Scheme 4.3 as to which are the most favourable pathways for these systems. Thus, we have computed the reaction coordinate diagram of [ACP + **1b/2d**] along each reaction pathway (Figure 4.9).

Figure 4.9 reveals that Q3 and Q4 are the two preferred pathways for [ACP + **1b/2d**]. For [**1a/2a**] and [**1b/2a**] generating the (*R*)-alcohol product, we would expect that the energy profile along Q1 would be lower than that along Q4; conversely, for [**1a/2d**] generating the (*S*)-alcohol, the energy profile along Q3 would be lower than that for Q2.

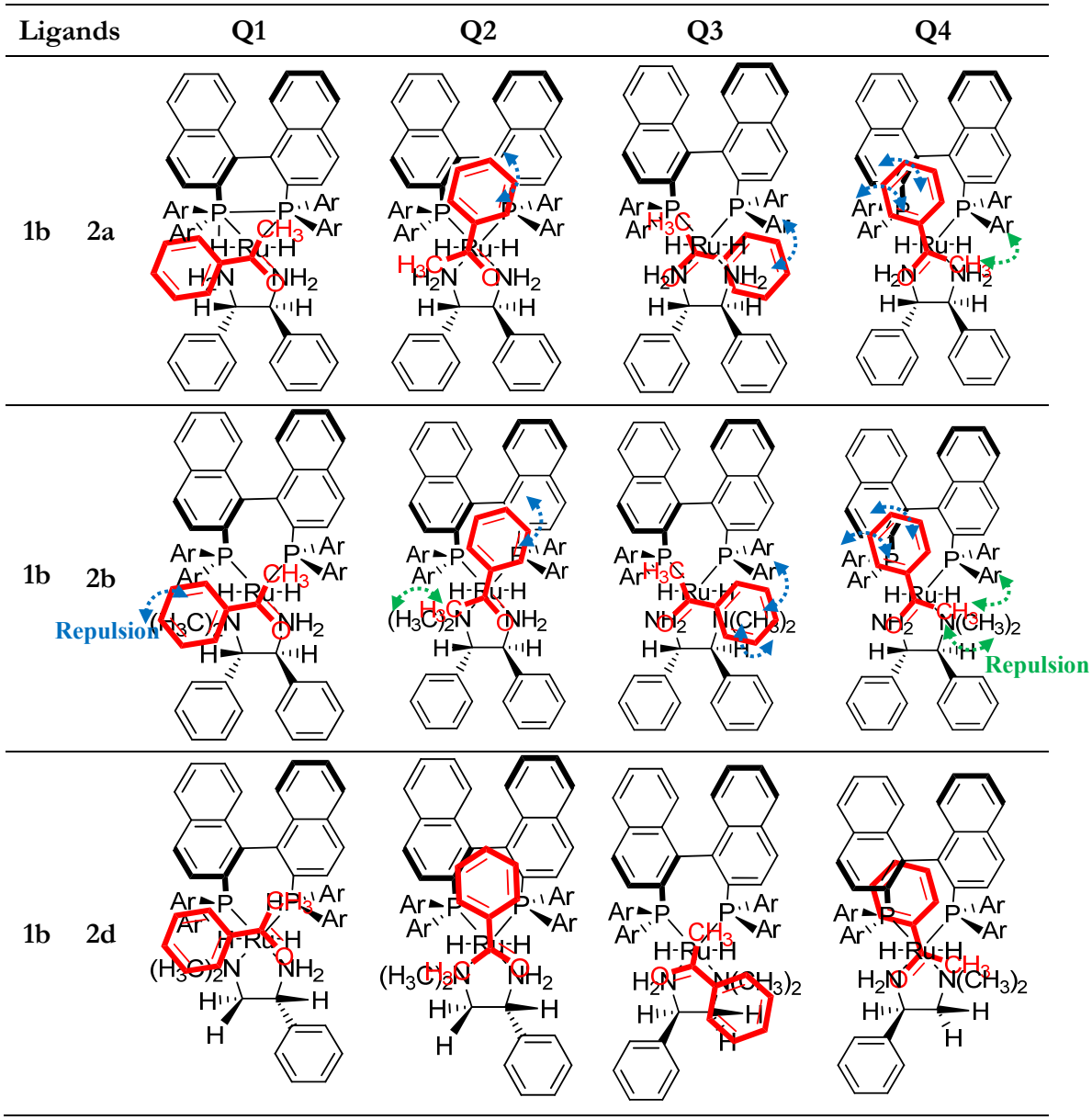

Scheme 4.3: Four possible pathways with the subsequent stereochemical configuration of the phenylethanol in [ACP + **1b/2a**], [ACP + **1b/2b**] and [ACP + **1b/2d**]. Blue and green arrows represent the repulsion between the phenyl group of ACP and the ligand, and between the methyl group of ACP and the ligand respectively.

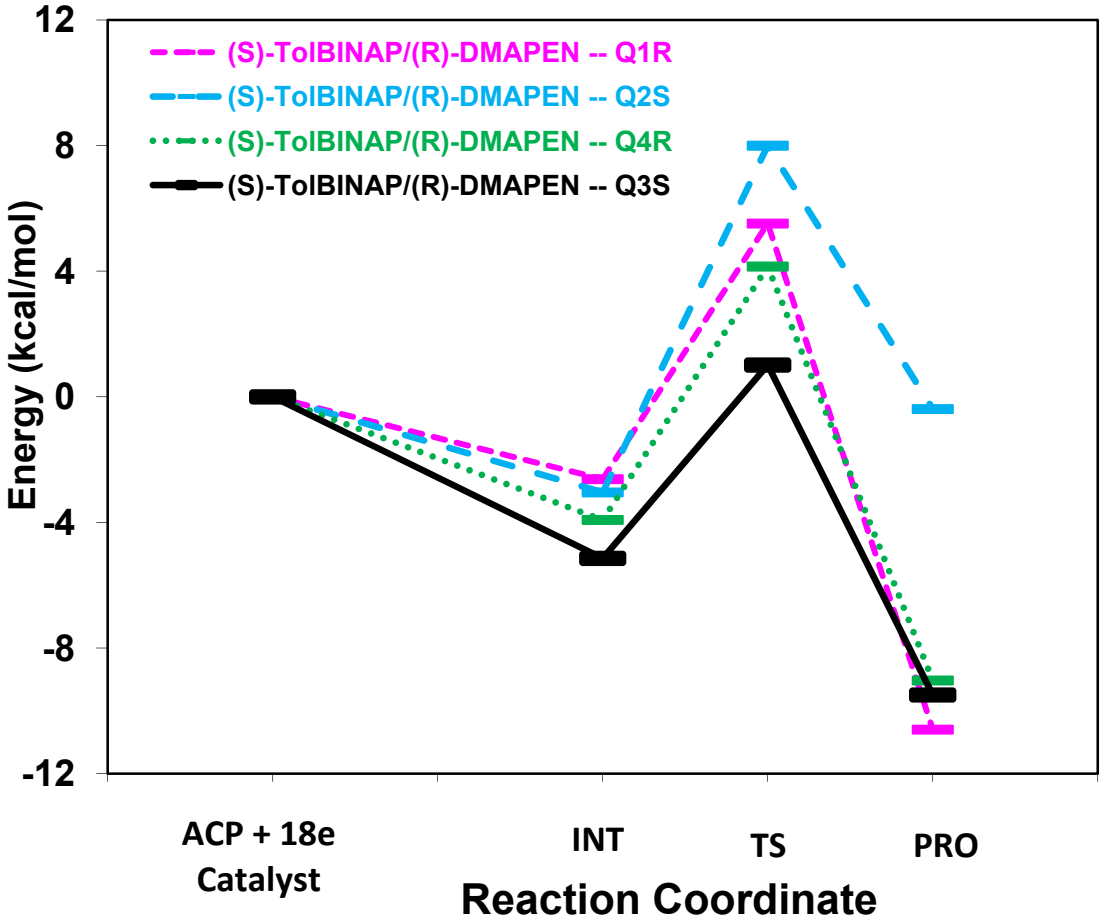

Figure 4.9: Reaction coordinate diagram of the hydrogenation of acetophenone catalysed by the RuH_2[(*S*)-TolBINAP][(*R*)-DMAPEN] complex ([**1b/2d**]) for each possible pathway (Q1, Q2, Q3 and Q4), computed at the DFT/PBE level of theory.

Figure 4.9 illustrates the configurations of Pre-INT, INT, TS and PRO when ACP approaches [**1b/2d**] along Q1, Q2, Q3 and Q4. Turning to Pre-INT and INT, a comparison of Q3 (*S*-configuration) and Q2 (*S*-configuration) reveals that for Q3 in Figure 4.10 (B-I), Ar1 (pointing out of the plane of the paper) pushes the larger phenyl group of ACP away from the two methyl groups on the diamine and reduces the steric repulsion from the two methyl groups when ACP is close enough to the ruthenium catalyst to form the transition state; for Q2 in Figure 4.10 (B-II), Ar3 cannot repel the phenyl group of ACP away from the naphthyl group because Ar3 point into the plane of the paper, away from the ACP and therefore when ACP is closer to the catalyst, the steric repulsion increases. Hence, Q3 is a more energetically favourable pathway. In a comparison between Q4 (*R*-configuration) and Q1 (*R*-configuration), for Q4 in Figure 4.10 (B-III), Ar2 repels the phenyl group of ACP moving towards the space vacated by a phenyl group on the diamine and thus moving away from the naphthyl group — which consequently reduces the steric hindrance in Q4; for Q1 in Figure 4.10 (B-IV), Ar2 is further from the two methyl groups on the diamine and therefore cannot push the phenyl group of ACP across the two methyl groups on the diamine. Hence, from the intermediate to the transition state, the phenyl group of ACP would be hindered by the two methyl groups on the diamine. Thus, Q4 is a more energetically favourable pathway. Comparing Q3 and Q4, there is steric repulsion from the aromatic ring of the diphosphine along Q4 but not along Q3. Hence, Q3 is a more energetically favourable pathway. As with the most favourable Q1 pathway in [**1a/2a**], [**1b/2a**] and [**1c/2b**], two intermediates, Pre-INT and INT, are observed in the most favourable pathway in [**1b/2d**]. We found that the orientations of the structure do not change obviously from INT to Pro *via* the TS. Comparing Q1 and Q2, the phenyl group of ACP is blocked by the stronger steric hindrance from the naphthyl group along Q2 and by the two methyl groups bonded to the nitrogen along Q1. Hence, Q1 is a more energetically favourable pathway.

In conclusion, it is reasonable to suggest that for system [ACP + **1b/2d**] the energy of the transition state follows this ranking: Q3 < Q4 < Q1 < Q2.

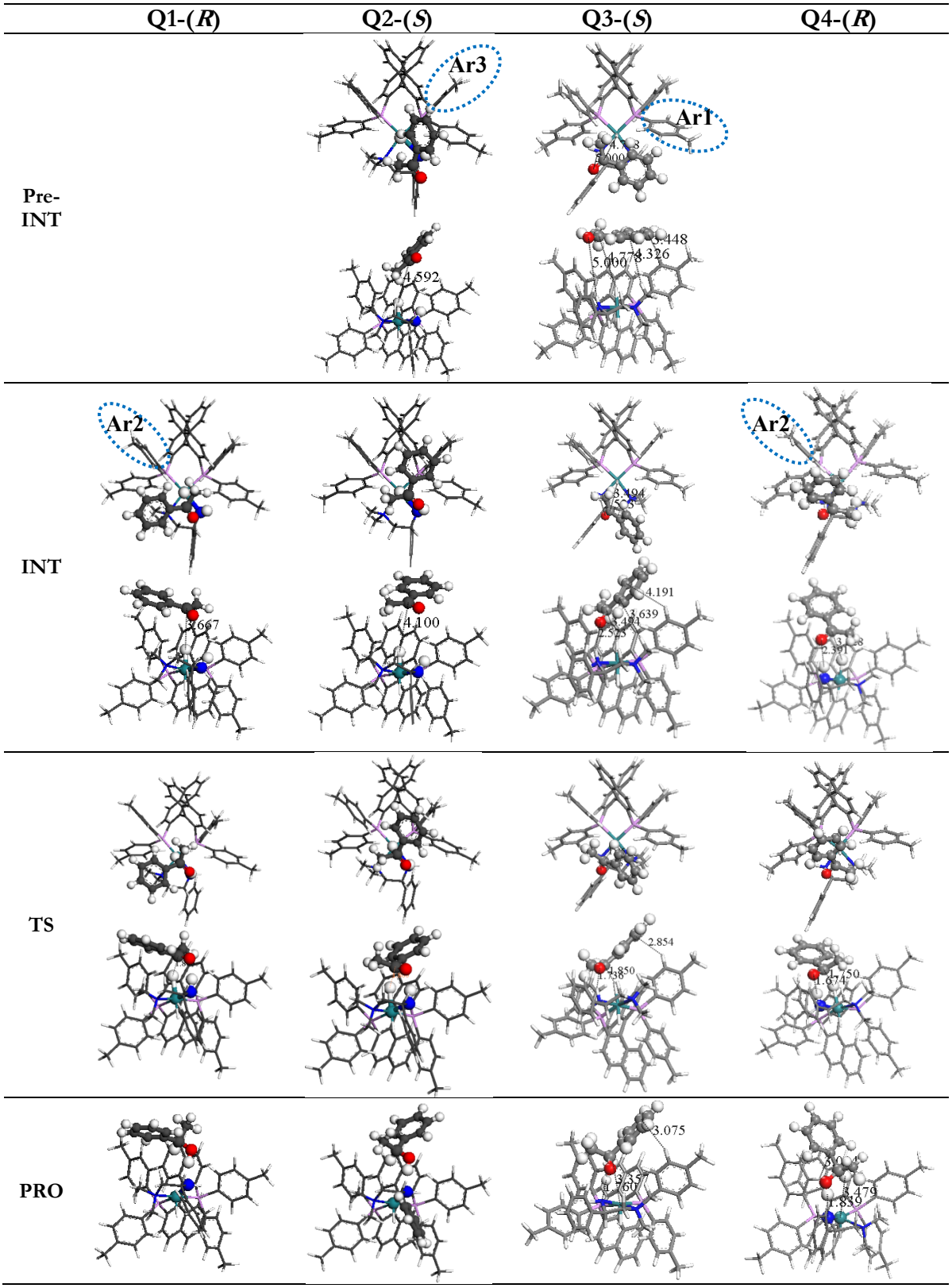

Figure 4.9 (A): Structures when acetophenone approaches [**1b/2d**], RuH_2[(*S*)-TolBINAP][(*R*)-DMAPEN], in the INT, TS and PRO states along Q1, Q2, Q3 and Q4. Ar1, Ar2 and Ar3 are three different tolyl groups on the diphosphine.

Path	State	Structure
I. Q3 (*S*)	**Pre-INT**	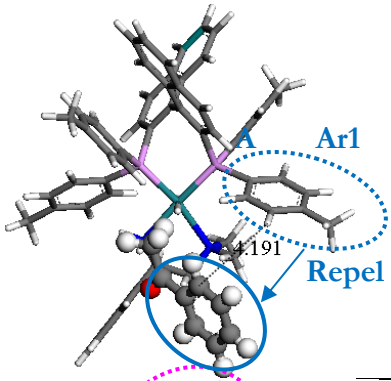
II. Q2 (*S*)	**Pre-INT**	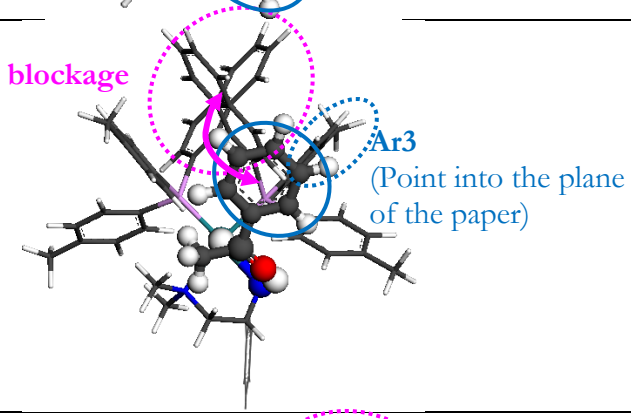
III. Q4 (*R*)	**INT**	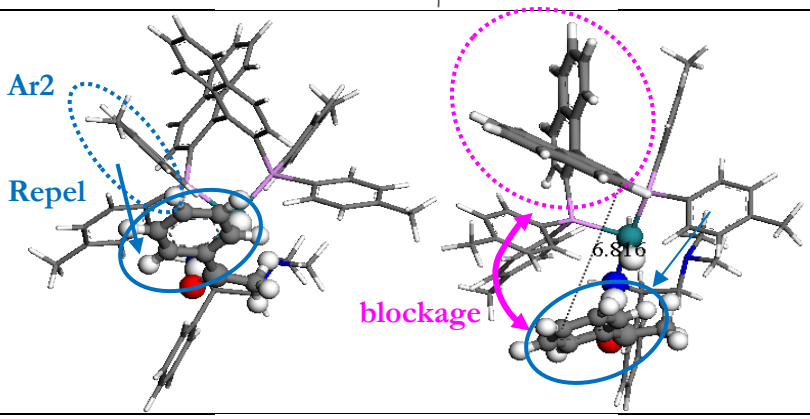
IV. Q1 (*R*)	**INT**	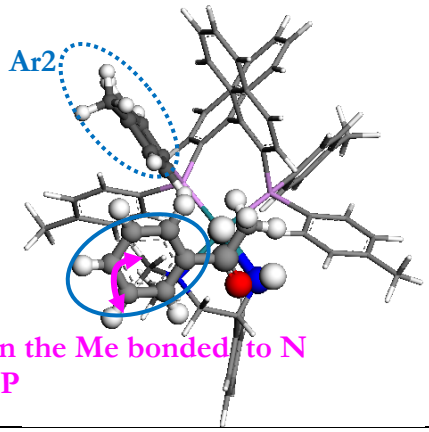

Figure 4.10 (B): Representative structures when acetophenone approaches [**1b/2d**], RuH_2[(*S*)-TolBINAP][(*R*)-DMAPEN], in the intermediate states along Q3, Q2, Q4 and Q1.

Figure 4.11 illustrates the structural characteristics of INT, TS and PRO of system [ACP + **1b/2d**] along Q3. When the (Ru-)H···C(=O) distance is *ca.* 5 Å (System **I**) the CH/π interaction between the phenyl group of ACP and the hydrogen of the toluene, drives ACP towards the catalyst. When the (Ru-)H···C(=O) distance is close to 3.5 Å (System **II**), the (N-)H···O(=C) distance is *ca.* 2.5 Å, which presumably generates a stronger NH/π attraction between ACP and the catalyst. Meanwhile, the phenyl group of ACP is so close to the methyl group bonded to the nitrogen (3.64 Å) that the phenyl group of ACP is repelled and moves further away from the catalyst centre, but this repulsion does not affect the stability of this state. We note that the (N-)H···O(=C) attraction strongly stabilises both ACP and [**1b/2d**]; therefore the structures with a (Ru-)H···C(=O) distance shorter than 3.5 Å and those where the transition state and product occur are all very similar. Clearly, the non-bonding CH/π attraction in System **I** is weaker than the repulsion between the phenyl group of ACP and the methyl of the catalyst, but the NH/π attraction in System **II** is sufficiently strong to be able to overcome the steric repulsion and form a stable intermediate.

This line of reasoning is further supported by an analysis of molecular orbitals and charge distributions. Diagrams of HOMO and LUMO orbitals (Figure 4.12) show that the size of the *d*-orbital of ruthenium shrinks from system **I** to **II**, indicating that hydride bonded to ruthenium is weaker. The charges on Ru(-H), (C=)O, (O=)C, and N(-H) are –0.182, +0.146, –0.226 and +0.113 respectively for system **I** and –0.131, +0.323, –1.455 and +0.272 respectively for **II**. Furthermore, the (Ru-)H···C(=O) and (N-)H···O(=C) distances are 5.00 Å and 5.63 Å for **I** and 3.50 Å and 2.52 Å for **II**. These results indicate that the attraction between ACP which drives its approach to the ruthenium centre is stronger in **II**, which is caused by the NH/π attraction. They also reveal that electron transfer to the carbonyl carbon of the ACP is greater when the (Ru-)H···C(=O) distances are at 3.75 Å (System **II**).

When comparing the structural changes in the asymmetric hydrogenation catalysed by [**1a/2a**] and [**1b/2d**] along Q3 (Figure 4.13), we find that the absence of a phenyl group on the diamine reduces the repulsion from the naphthyl group and the phenyl group on the diamine and facilitates the shift of ACP driven by the electrostatic attraction. Therefore Q3 is the favourable pathway.

Q3	top view	side view	side view
5 Å (Sys I)	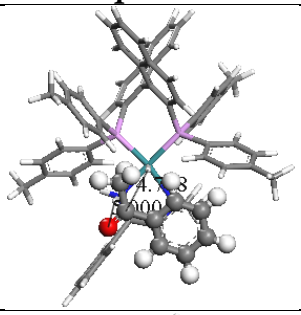	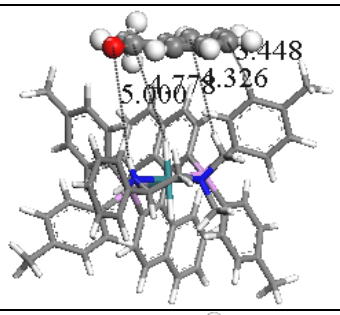	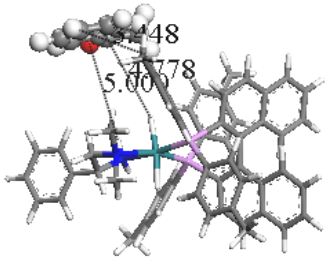
3.5 Å (Sys II)	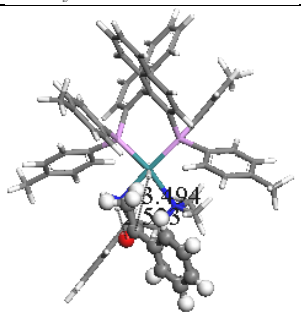	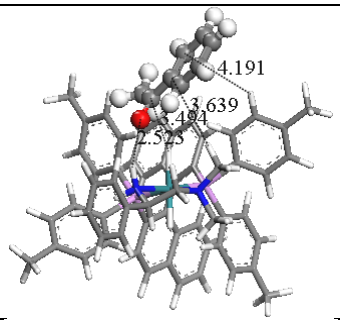	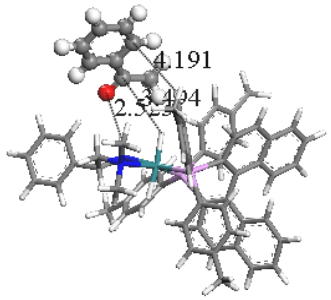
TS	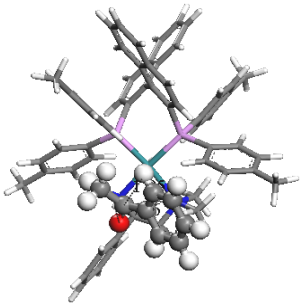	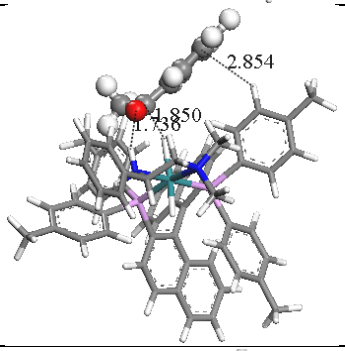	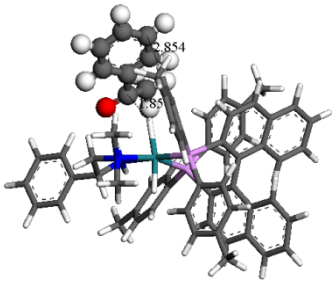
PRO	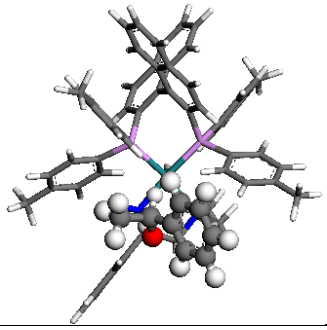	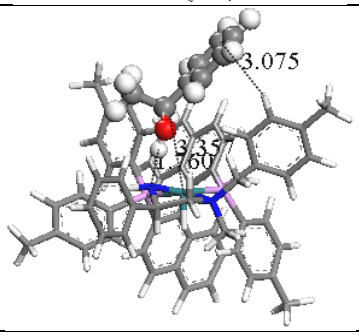	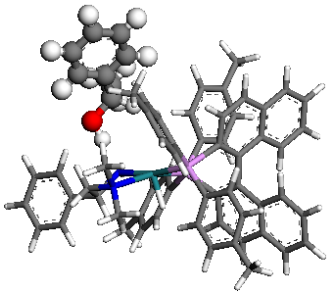

Figure 4.11: Snapshots in the hydrogenation of acetophenone catalysed by RuH_2[(*S*)-TolBINAP][(*R*)-DMAPEN] along the Q3 pathway when the (Ru-)H···C(=O) distances are 5 Å (System **I**) and 3.75 Å (System **II**), and in the TS and PRO states.

Q3	**5 Å (System I)**	**3.5 Å (System II)**
	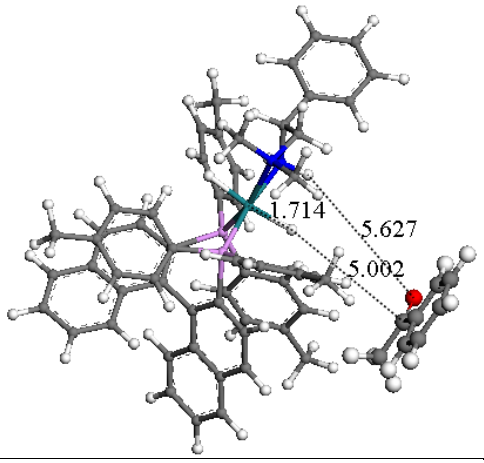	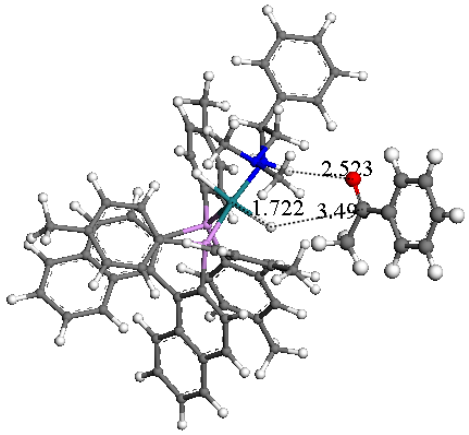
HOMO	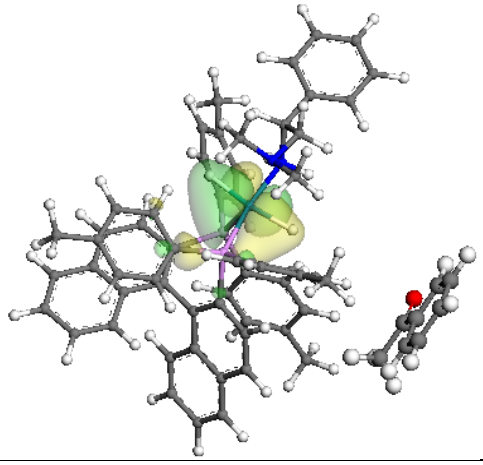	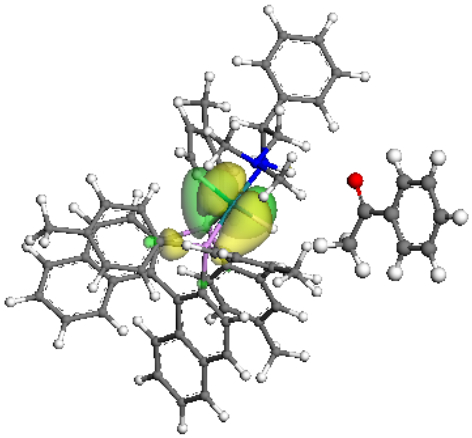

Figure 4.10: Diagrams of the structures and HOMOs of systems (**I**) and (**II**) in the hydrogenation of acetophenone catalysed by RuH_2[(*S*)-TolBINAP][(*R*)-DMAPEN] along the Q3 pathway.

Q3	1b/2d	1b/2d	1a/2a	1a/2a
	top view	side view	top view	**side view**
5 Å	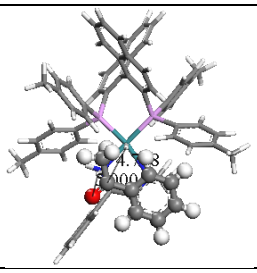	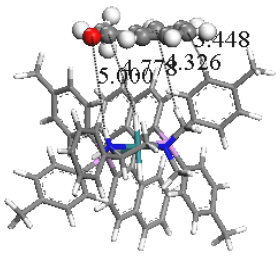	—	—
3.5 Å	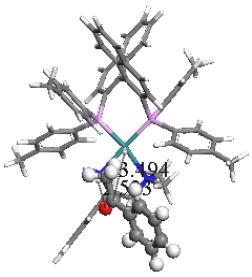	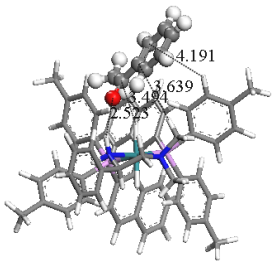	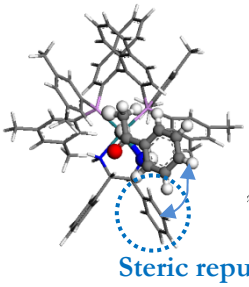	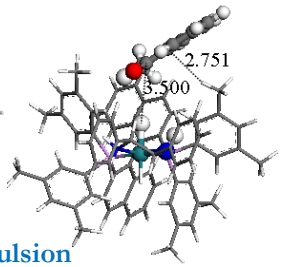
1.85 Å TS	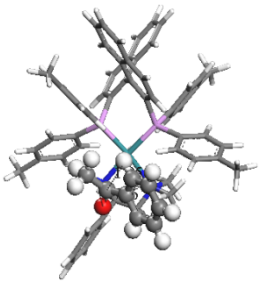	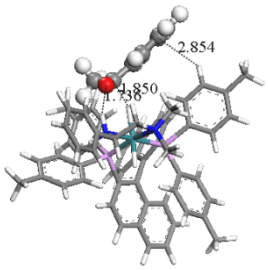		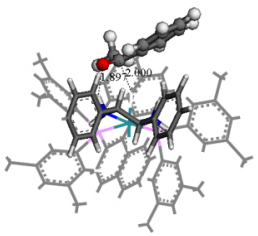
PRO	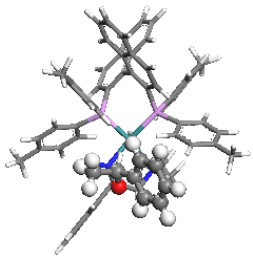	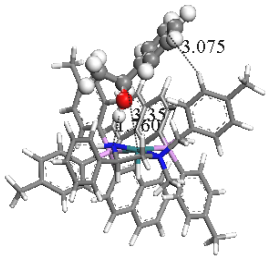	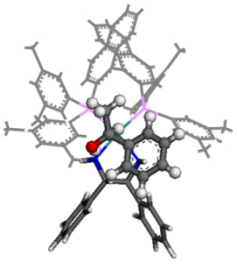	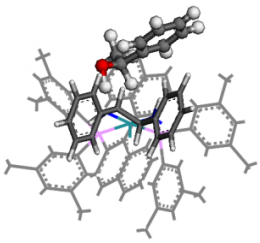

Figure 4.11: A comparison of structural changes in acetophenone hydrogenation by RuH_2[(*S*)-TolBINAP][(*R*)-DMAPEN] and RuH_2[(*S*)-XylBINAP][(*S*,*S*)-DPEN] along Q3.

In Figure 4.14, we now turn to the structural changes in the asymmetric hydrogenation catalysed by [**1b/2d**] along the Q4 pathway. When the (Ru-)H…C(=O) distance is *ca.* 3.3 Å, the CH/π interaction between the phenyl group of ACP and the hydrogen on the tolyl group drives the approach of ACP to the catalyst, while the (Ru-)H···C(=O) distance is close to 2.4 Å, the methyl group of ACP rotates by 9.4º, which makes the energy increase. In the transition state, the (Ru-)H···C(=O) distance is *ca.* 1.75 Å, and the energy of this system reaches the highest point, which may result from the steric repulsion between the phenyl group of ACP and the aryl group on the diphosphine, and from the rotation of the methyl group (from –10.53º to –23.65º). In contrast with Q3, the aryl group on the diphosphine blocks the entrance of the phenyl group of ACP, and therefore Q4 is a less favourable pathway than Q3. When comparing the structural changes in the asymmetric hydrogenation catalysed by [**1b/2d**] and [**1a/2a**] along the Q4 pathway (Figure 4.15), we find that the absence of the phenyl group on the diamine reduces the repulsion. Therefore, the Q4 pathway in the system with DMAPEN has a lower activation energy than that in the system with DPEN.

Next, we consider the effect of the 1,2-diamine substituent on the enantioselectivity whilst fixing the diphosphine ligand as (*S*)-TolBINAP (**1b**). Figure 4.16 shows the reaction coordinate diagram in [ACP + **1b/2a**], [ACP + **1b/2b**] and [ACP + **1b/2d**]. As mentioned earlier, naphthyl rings and methyl groups play an important role in offering strong steric repulsion between the substrate and catalyst; therefore in [ACP + **1b/2b**], ACP is expected to be repelled in either pathway, which leads to a low *ee*. Comparing the latter two systems, in which two protons bonded to the nitrogen are replaced by two methyl groups, a higher *ee* can only be achieved by substituting one of the phenyl groups for a hydrogen on the diamine ligand, thus reducing the steric hindrance between the phenyl group of ACP and the methyl group on the diamine ligand.

In summary, the diphosphine with only one methyl on the tolyl group needs a methyl group on the diamine to limit the available space, enabling the Q3 pathway (*S*-product), and the absence of the phenyl group on the diamine reduces steric repulsion when ACP enters into the pocket which is created by the bulky ligands of the complex.

Q4	top view	side view	side view	τ(C–MeOPh) φ (OCPhC´)
3.3 Å INT	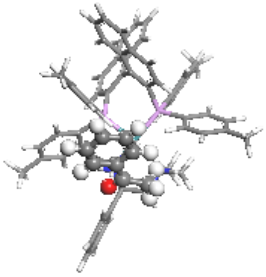	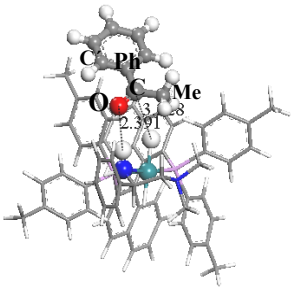	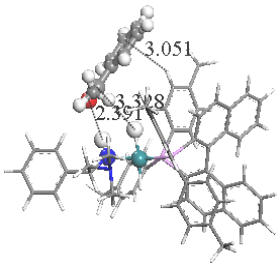	–0.07° 11.16°
2.4 Å	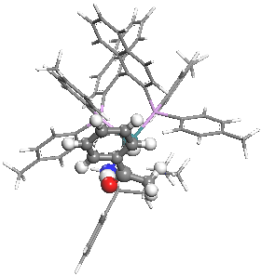	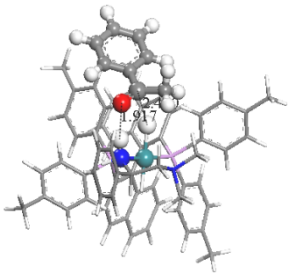	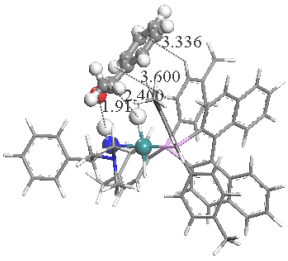	–10.53° 9.34°
1.75 Å TS	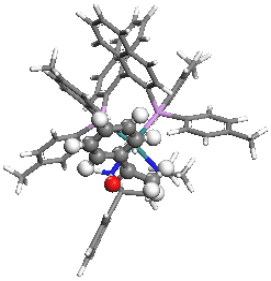	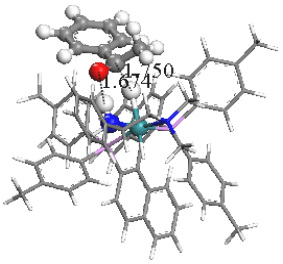	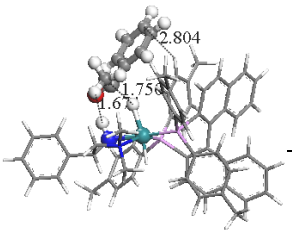	–23.65° 5.73°
PRO	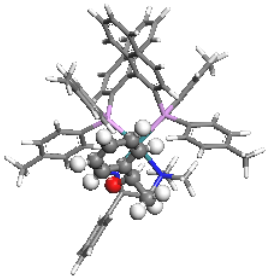	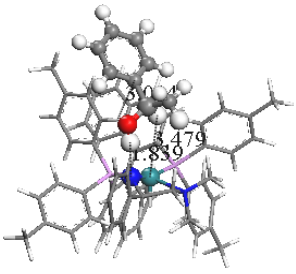	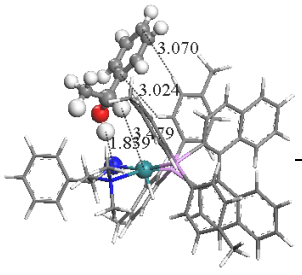	–34.04° 23.87°

Figure 4.12: Illustration of representative snapshots, torsion angles and out-of-plane angles in the asymmetric hydrogenation of acetophenone catalysed by RuH_2[(*S*)-TolBINAP][(*R*)-DMAPEN] along Q4.

Q4	1b/2d	1b/2d	1a/2a	1a/2b
	top view	side view	top view	side view
3.3 Å	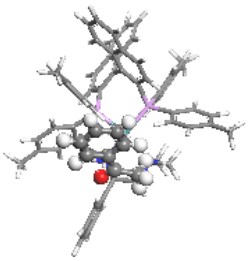	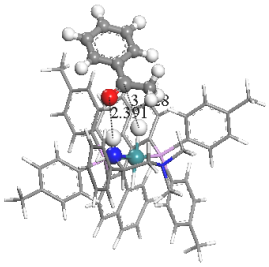	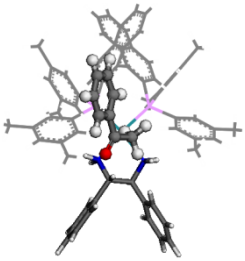	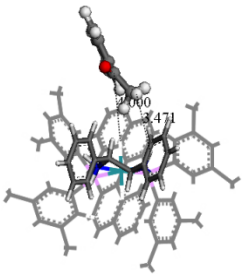
1.85 Å TS	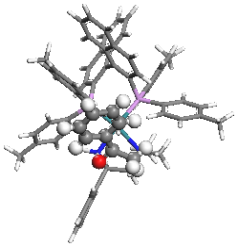	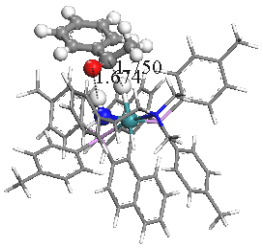	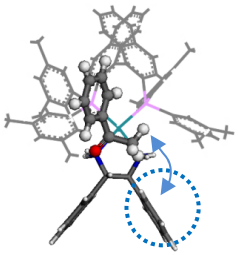 Steric repulsion	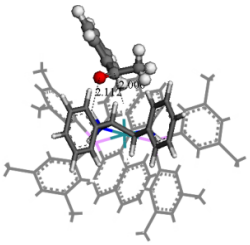
PRO	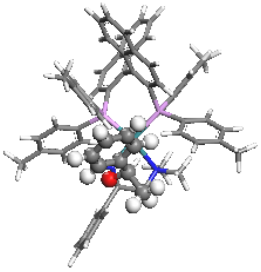	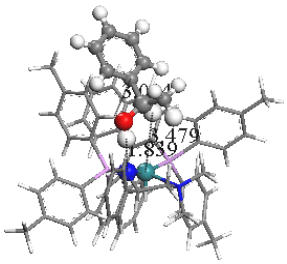	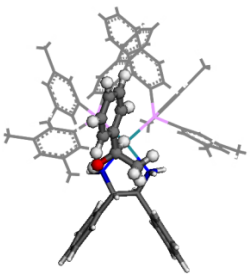	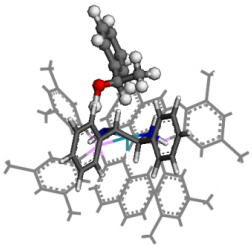

Figure 4.13: A comparison of structural changes in the asymmetric hydrogenation of acetophenone catalysed by RuH_2[(*S*)-TolBINAP][(*R*)-DMAPEN] (**1b/2d**) and RuH_2[(*S*)-XylBINAP][(*S*,*S*)-DPEN] (**1a/2a**) along Q4 when the (Ru-)H···C(=O) distance is 3.3 Å, in the transition (1.85 Å) and PRO (product + 16e$^-$ species) states.

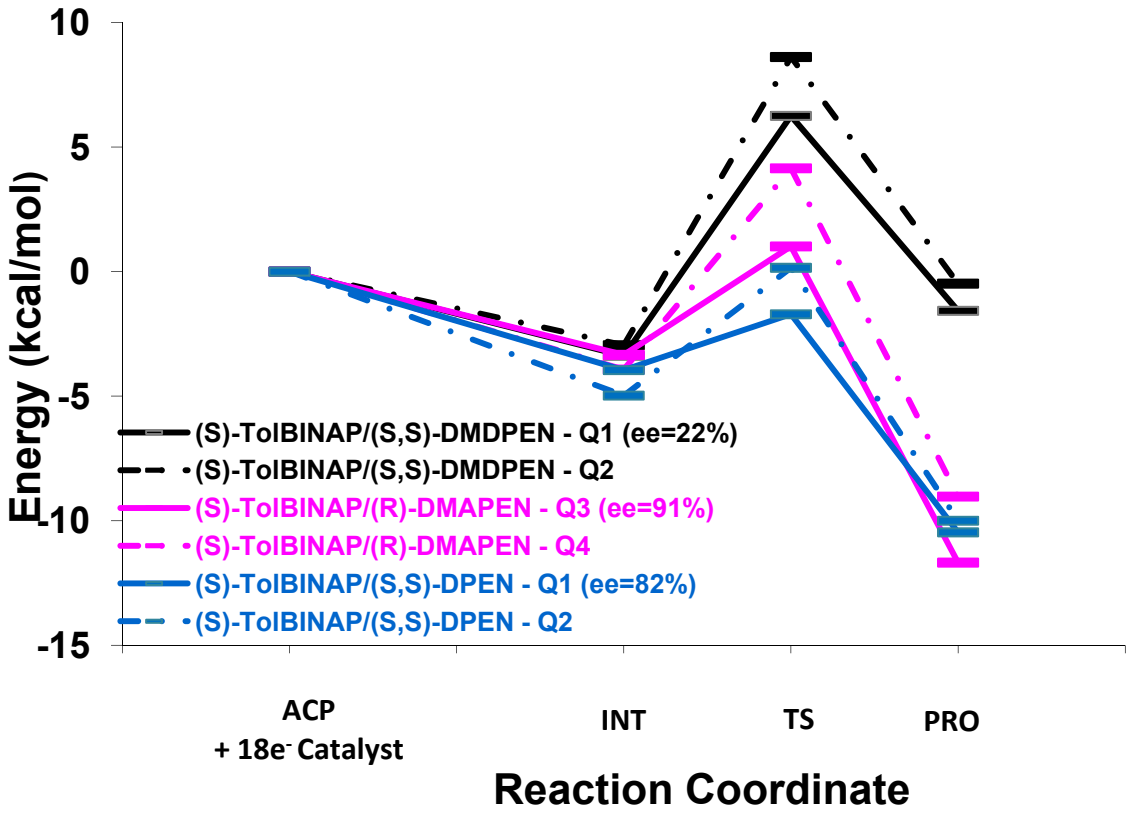

Figure 4.14: Reaction coordinate diagram for the hydrogenation of acetophenone catalysed by the [(*S*)-TolBINAP]/[**2a**], [**2b**] and [**2d**] ruthenium complexes along the two most favourable pathways.

4.3.5 Acetophenone hydrogenation catalysed by RuH_2[(*S*)-XylBINAP][diamine] complexes

As in the earlier section, we probe the impact on enantiomeric selection by changing different functional groups on the diamine while fixing the diphosphine ligand (*S*)-XylBINAP (**1a**): [ACP + **1a/2a**], [ACP + **1a/2b**] and [ACP + **1a/2c**] (see Scheme 4.1). Figure 4.15 shows the reaction coordinate diagram for the hydrogenation of ACP catalysed by these ruthenium complexes along the Q1 and Q2 pathways. Table 4.2 displays their energetic characteristics. Figure 4.15 reveals that along both Q1 and Q2, the energies of the INT, TS and PRO in [ACP + **1a/2a**] are *ca.* 3 kcal/mol, 8 kcal/mol and 9 kcal/mol lower than the energies of the same states in the systems [ACP + **1a/2b**] and [ACP + **1a/2c**] respectively. In addition, the differences in activation energies along Q1 and Q2 — $\Delta E_{a,Q2-Q1}$— are 5.31 kcal/mol for [ACP + **1a/2a**], 1.71 kcal/mol for [ACP + **1a/2b**] and 1.86 kcal/mol for [ACP + **1a/2c**] respectively, indicating that the XylBINAP combined with DMDPEN and DMAPEN gives energetically unfavourable reactions. Comparing a top view (Figure 4.18) and a side view (Figure 4.19), we note that the phenyl group of ACP can only rotate further into the bulky pocket driven by the CH/π and NH/π attraction along Q1 in [ACP + **1a/2a**] (see Figure 4.19 (B)). The two methyl groups on the diamine and those on the xylyl moiety (3,5-dimethylphenyl) cause a large steric repulsion when ACP approaches the catalyst. Even replacing the two phenyl groups on the diamine with two hydrogen atoms does not decrease this repulsion (see Figures 4.18 (B) and 4.19 (B)).

Overall, the performance of XylBINAP depends on the amount of space within the bulky pocket, which is influenced by the functional group on the diamine. (*S*)-XylBINAP/(*S*,*S*)-DPEN ruthenium complexes exhibit the best combination, forming a low-energy intermediate along Q1 and a relatively high-energy transition state along Q2. Nevertheless, the combinations of XylBINAP with DMDPEN and DMAPEN both reduce the enantiomeric selection in the asymmetric hydrogenation of ACP.

Having discussed the effects on the *ee* of changing the diphosphine and diamine ligands, we now turn to discuss the correlation between *ee* and activation energy.

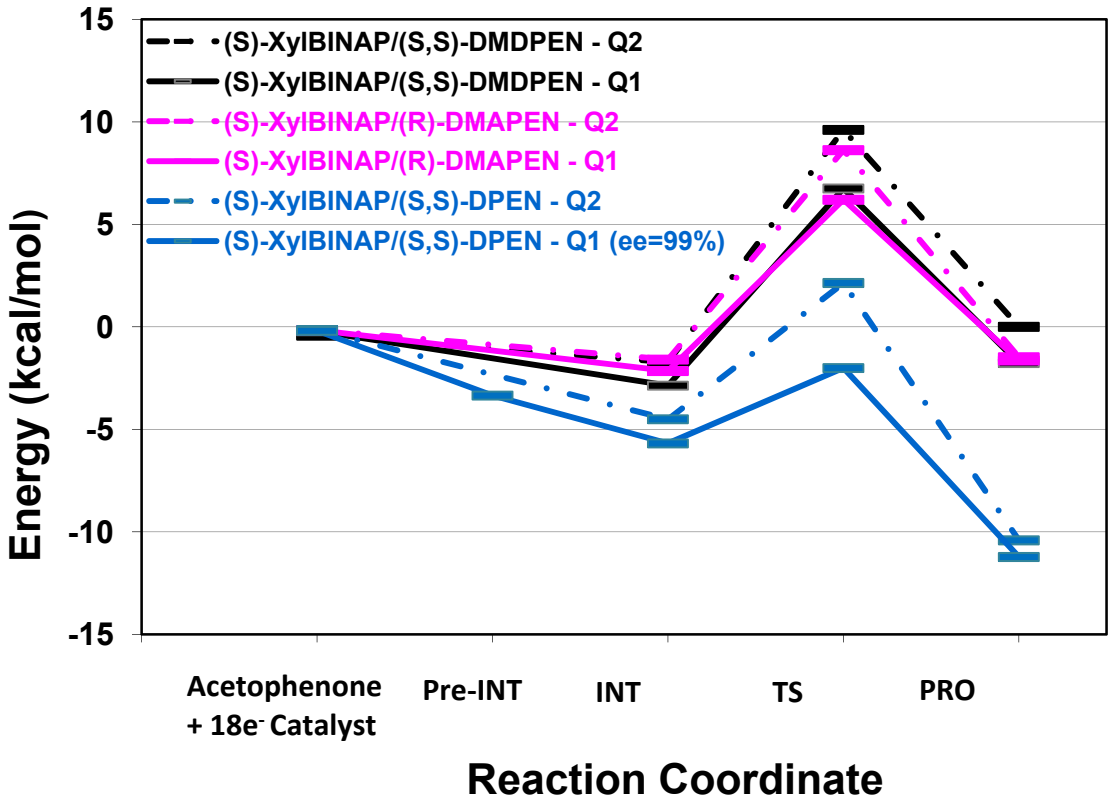

Figure 4.15: Reaction coordinate diagram of the hydrogenation of acetophenone catalysed by the [(*S*)-XylBINAP]/[**2a**], [**2b**] and [**2d**] ruthenium complexes along Q1 and Q2.

Table 4.2: Energetic values of INT, TS and PRO in [**1a**/**2a**], [**1a**/**2b**] and [**1a**/**2c**].

System	Path	INT	TS	E_a	ΔE_a	*ee*
			[kcal/mol]			[%]
1a/2a	**Q1**	-3.16	-1.82	1.34	5.31	97-99
	Q2	-4.37	2.29	6.65		
1a/2b	**Q1**	-2.66	6.96	9.62	1.71	—
	Q2	-1.30	10.04	11.33		
1a/2c	**Q1**	-2.15	6.10	8.35	1.86	—
	Q2	-1.59	8.62	10.21		

- E_a represents the activation energy
- ΔE_a represents the difference in activation energy (here, $\Delta E_a = E_{a,\,Q2} - E_{a,\,Q1}$)

Path		Pre-INT	INT	TS	PRO
1a / 2a	**Q 1**	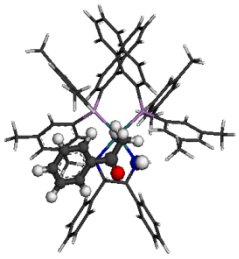	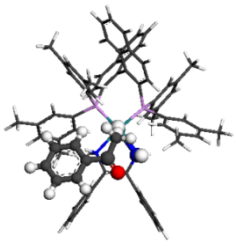	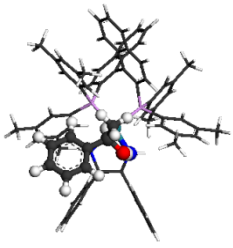	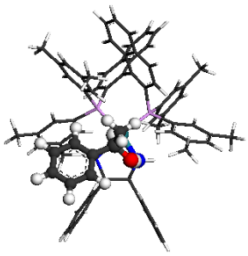
1a / 2b	**Q 1**	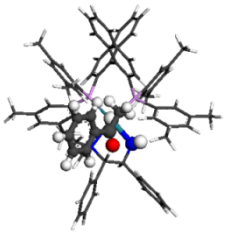	–	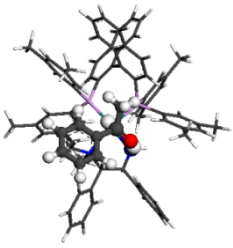	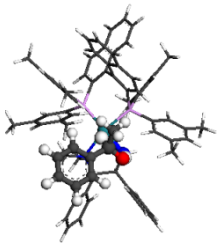
1a / 2c	**Q 1**	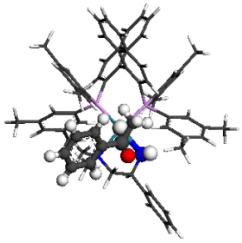	–	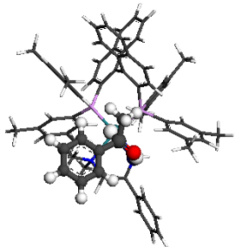	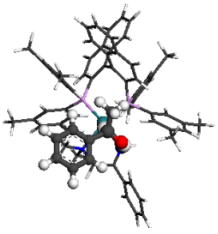
1a / 2a	**Q 2**	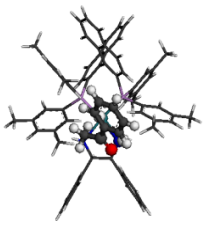	–	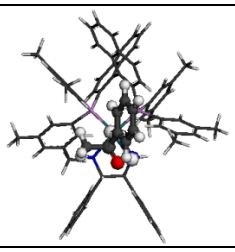	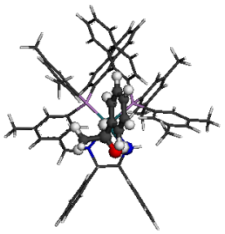
1a / 2b	**Q 2**	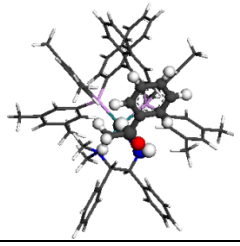	–	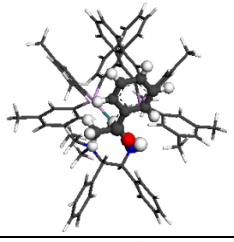	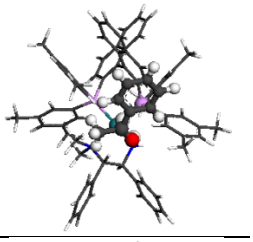
1a / 2c	**Q 2**	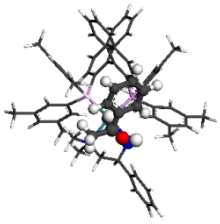	–	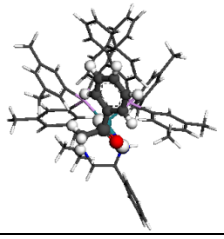	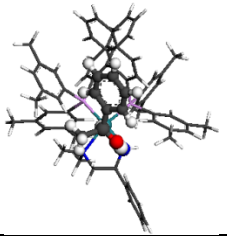

Figure 4.16 (A): Structures of Pre-INT, INT, TS and PRO in the acetophenone hydrogenation using [**1a/2a**], [**1a/2b**] and [**1a/2c**] along Q1 and Q2 (top view).

System	Intermediate
XylBINAP/ DPEN [1a/2a]	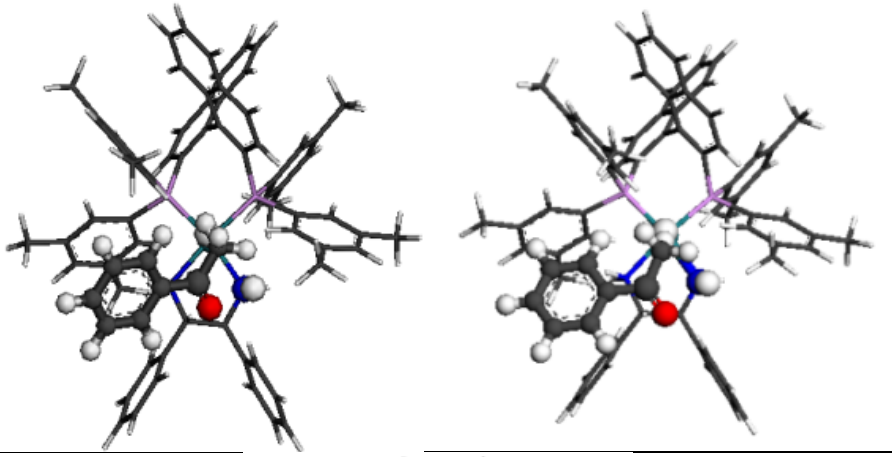
XylBINAP/ DMDPEN [1a/2b]	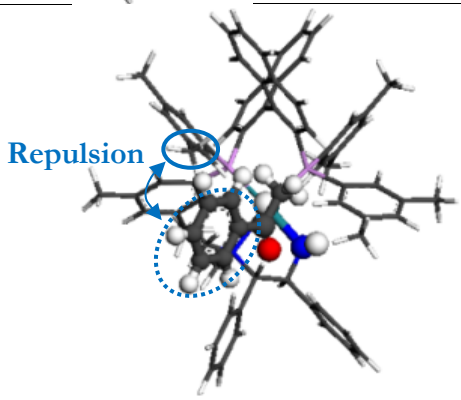
XylBINAP/ DMAPEN [1a/2c]	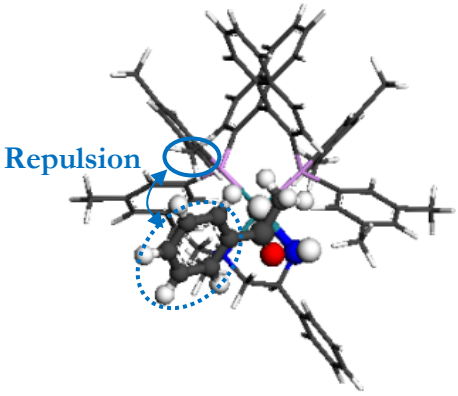

Figure 4. 18 (B): Structures of intermediates in the acetophenone hydrogenation using [**1a/2a**], [**1a/2b**] and [**1a/2c**] along Q1 (top view).

Path		Pre-INT	INT	TS	PRO
1a / 2a	**Q 1**	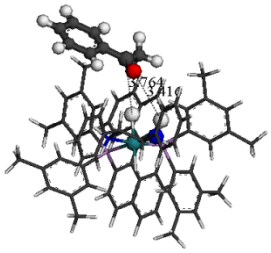	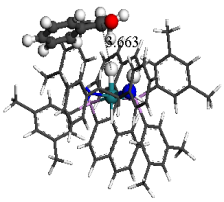	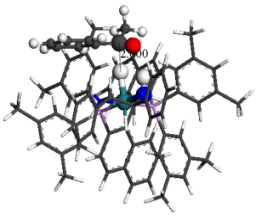	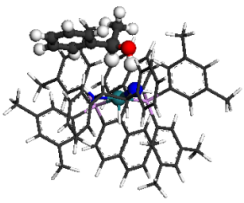
1a / 2b	**Q 1**	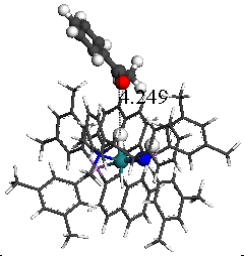	–	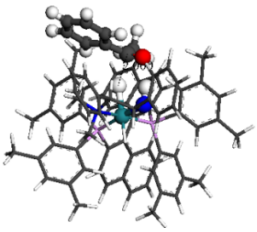	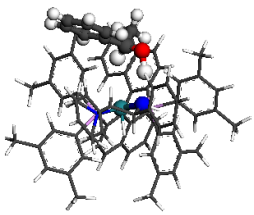
1a / 2c	**Q 1**	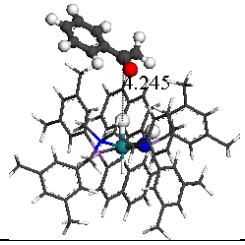	–	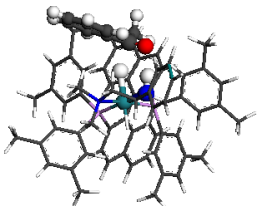	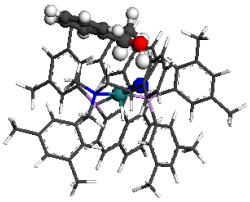
1a / 2a	**Q 2**	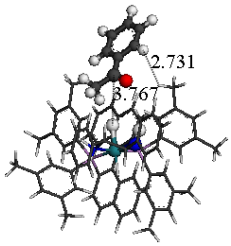	–	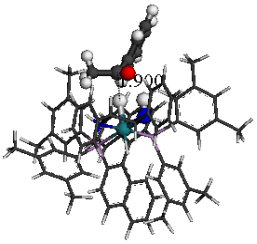	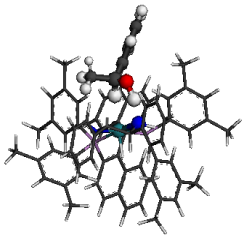
1a / 2b	**Q 2**	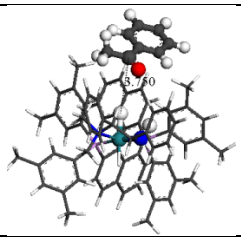	–	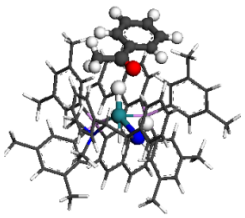	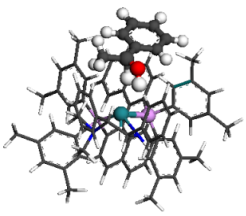
1a / 2c	**Q 2**	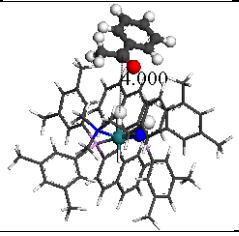	–	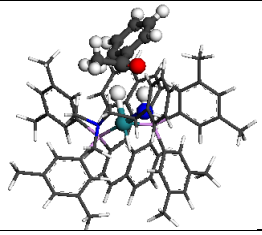	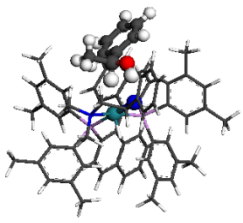

Figure 4.19 (A): Structures of Pre-INT, INT, TS and PRO in the acetophenone hydrogenation catalysed by [**1a/2a**], [**1a/2b**] and [**1a/2c**] along Q1 and Q2 (side view).

System	Intermediate
XylBINAP/ DPEN [1a/2a]	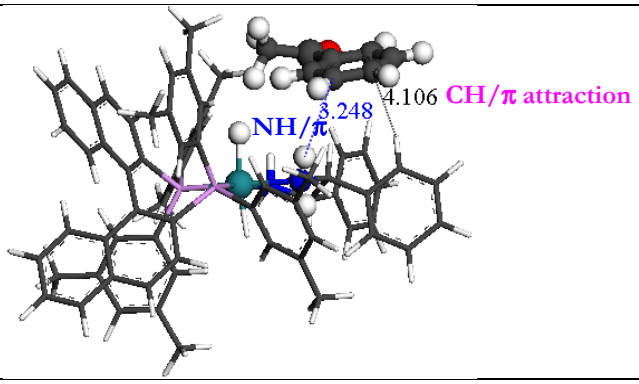
XylBINAP/ DMDPEN [1a/2b]	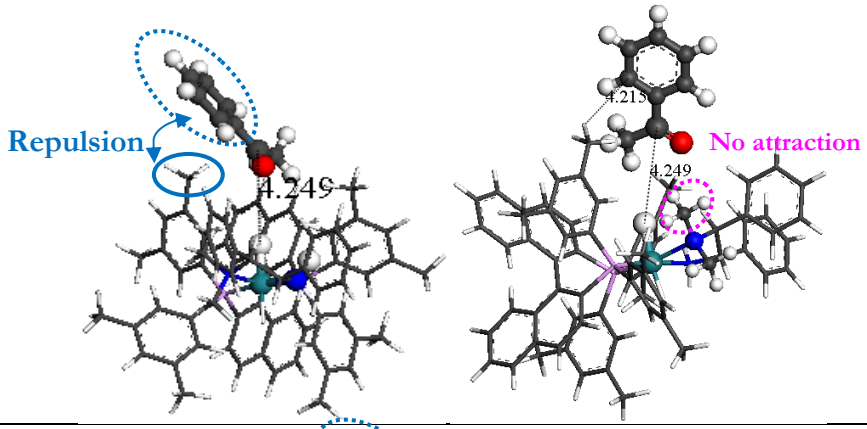
XylBINAP/ DMAPEN [1a/2c]	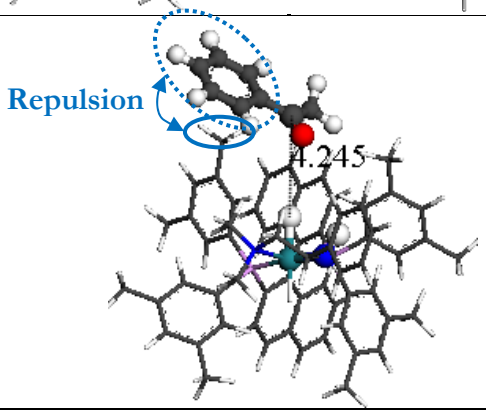

Figure 4.19 (B): Structures of intermediates in the acetophenone hydrogenation catalysed by [**1a/2a**], [**1a/2b**] and [**1a/2c**] along Q1 (side view).

4.3.6 Correlation between enantiomeric excess and activation energy

Table 4.3 shows the relationship between the difference in activation energies (ΔE_a) and the enantiomeric excess (*ee*) along the two most favourable pathways. It is clear that larger values of ΔE_a correspond to a greater *ee*. Theoretically, *ee* could be calculated according to the following equation[16] (discussed in Section 2.3.2) when considering the free energy in a one-step transition state:

$$\%ee_{theory}\left(\Delta\Delta G\right)=\frac{1-e^{-\Delta\Delta G_{S-R}/RT}}{1+e^{-\Delta\Delta G_{S-R}/RT}}\times 100 \quad ,$$

where $\Delta\Delta G$ is the difference in free energies of activation for the (*S*)- and (*R*)-products respectively. Comparing our computational results and the theoretical curve in Figure 4.20, there is indeed a clear correlation between the *ee* and difference in activation energies whilst changing the substituent on both the diphosphine and diamine ligands, with a shift of 1.7 kcal/mol from the theoretical curve (Figure 4.17). Furthermore, the configurations of the product do not affect this correlation. The computational procedure presented can thus be used to predict the *ee* of ketone hydrogenation reactions catalysed by Noyori-type catalysts, and assist in the choice of ligand in optimising the *ee*. This process could potentially save time and effort in matching substrates of interest with appropriate catalysts. For example, for the systems [**1a/2b**] and [**1a/2c**] (for which there are no experimental values of *ee*), we can predict that the *ee* in the hydrogenation of acetophenone should be lower than 15%.

Table 4.3: Energetic characteristics in the hydrogenation of acetophenone catalysed by the RuH_2[(*S*)-diphosphine][(*S*,*S*)-diamine] complexes along the two most favourable pathways.

System	1a-2a	1a-2b	1a-2c	1b-2a	1b-2b	1b-2d	1c-2a
ΔE_a [kcal/mol]	5.31	1.17	1.86	2.83	1.93	3.72	2.85
***ee* [%] (exp.)**	97-99[22b]			80-82[23]	22[25]	91[25]	80-83[24]
Configuration	*R*	–	–	*R*	*R*	*S*	*R*

- E_a stands for the activation energy
- ΔE_a stands for the difference in activation energy between the two most favourable pathways.

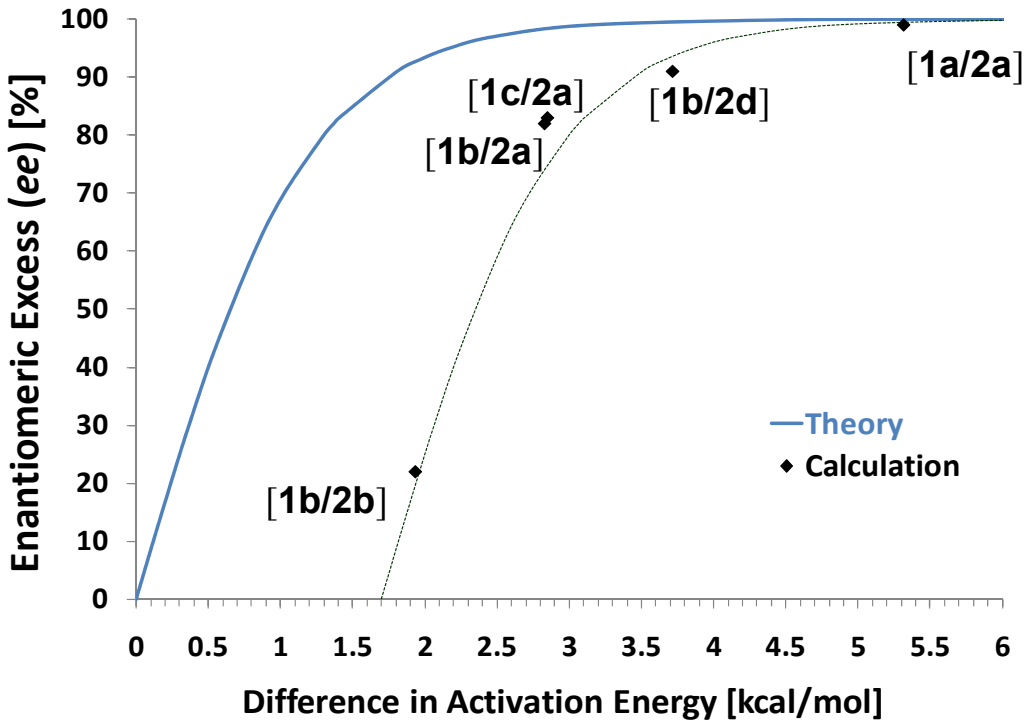

Figure 4.17: Correlation between the *ee* and difference in activation energy (ΔE_a) in the hydrogenation of acetophenone catalysed by the RuH_2(diphosphine)(diamine) complexes whilst changing the substituents on the diphosphine or diamine.

4.3.7 Dispersion correction effect

One would expect the DFT-D dispersion correction to improve accuracy in systems with non-bonding long-range interactions. To test this hypothesis, single point energy calculations were performed at the PBE-D level of theory on the intermediates of the ACP hydrogenation catalysed by the RuH_2[(*S*)-XylBINAP)][(*S,S*)-DPEN] complex. Next, the energies of the transition states associated with the hydride formation and hydride transfer reactions in acetone hydrogenation catalysed by $RuH_2(PH_3)_2$(en) were computed at the DFT-D level of theory using the nudged elastic band method. The calculations, performed using the CP2K code, indicate no major differences (*ca.* 2 kcal/mol difference) compared with the results without the correction. The details are given in the Appendix.

4.3.8 Summary

The overall conclusion of this chapter is summarised in Figure 4.17 which demonstrates a correlation between the difference in activation energy and enantiomeric excess in the two sets of systems. A clear correlation is observed in the acetophenone hydrogenation catalysed by the Noyori-type ruthenium-based complexes on changing the substituents on both diphosphine and diamine ligands. Furthermore, the configuration of the product does not affect this correlation. Calculations of this type could, we suggest, be used to assist the choice of ligand when optimising *ee*. Indeed, the correlation between ΔE_a and *ee* could assist the development of new Noyori-type catalysts by tuning functional groups on ligands.

The work reported in this chapter has been published[98].

Chapter 5 FeH_2(diphosphine)(diamine) Complexes as Alternative Catalysts for Asymmetric Hydrogenation of Ketones?

5.1 Introduction

From the previous chapters, it is clear that the Noyori-type ruthenium catalysts have been a very significant development and have been applied in a variety of fields. Nevertheless, catalysts containing noble metals like ruthenium have the disadvantage of being expensive and toxic. Thus, the development of iron-based catalysts for the hydrogenation of ketones with activities and selectivities comparable to those of ruthenium-based complexes would be a considerable advantage because of the lower cost, toxicity, and environmental impact of iron[99]. The first effective H_2-hydrogenation of ketones catalysed by an iron analogue of the active Shvo-type ruthenium catalyst was reported by Casey *et al.* in 2007[100]. Recently, iron complexes containing P–N–N–P ligands[101] have displayed reasonable activities, but their enantiomeric excess (*ee*) in the H_2-hydrogenation of ketones is, however, not comparable to the *ee* that can be obtained with the ternary ruthenium complexes, comprising diphosphine, diamine and a ruthenium(II) centre[3a,18a]. It would therefore be beneficial to develop the *trans*-[Fe(II)H_2(diphosphine)(diamine)] complexes with an efficiency which could be comparable to the *trans*-[Ru(II)H_2(diphosphine)(diamine)] complexes.

Studies comparing the catalytic mechanisms of the simplified $RuH(II)_2(PH_3)_2(en)$[17,28a28c,30d] and $Fe(II)H_2(PH_3)_2(en)$[101b,102]complexes have been reported, but there is a clear need to investigate the issue of enantioselectivity in iron diamine diphosphine complexes. In Chapter 4, we investigated the effects on enantioselectivity catalysed by the RuH_2(diphosphine)(diamine) complexes and found a correlation between the activation energy and the enantiomeric excess, which could be used in predicting new catalysts. In the present chapter, we apply the same techniques and report a theoretical study of the structural and electronic properties of the simplified and real

Ru(II)H_2(diphosphine)(diamine), and Fe(II)H_2(diphosphine)(diamine) complexes, and of the mechanism of the ketone/alcohol hydrogen transfer reaction catalysed by the ruthenium and iron complexes.

5.2 Methodology

The DFT calculations in this chapter were carried out using the DMol^3 [84] and Gaussian 03 codes as discussed in Chapter 3. In DMol^3, the PBE/DNP level of theory and density functional semi-core pseudopotentials (DSPP) were applied. Each basis function was restricted to within a cutoff radius of 4.7 Å. Calculations with Gaussian 03 employed the PBE[53], PBE0[56a], B3LYP[55,92] and MPW1PW91[93] functionals, together with the 6-31G(d,p) basis set for hydrogen, carbon, nitrogen, oxygen and phosphorus, and the small-core quasi-relativistic LANL2[70] and SDD[94c,94d] effective core potential (ECP)/DZ for ruthenium and iron.

The constrained optimisation (CO) method was applied using DMol^3 and the synchronous transit-guided quasi-Newton (STQN) method was employed using Gaussian 03 to locate transition states.

5.3 Results and Discussion

We first consider the structural and electronic properties of M(II) H_2(diphosphine)(diamine), where M = Ru or Fe, and then discuss the mechanisms and key features controlling the enantioselectivity in the hydrogenation of ketones by both catalysts. In this chapter, the M in "M"(II) will always represent either Ru or Fe.

5.3.1 Stability of Fe(II)H_2(diphosphine)(diamine) isomers

Scheme 5.1 illustrates a proposed catalytic cycle for the hydrogenation of acetophenone by M(II)H_2(diphosphine)(DPEN) complexes involving hydrogen transfer from *trans*- or *cis*-M(II)H_2(diphosphine)(diamine) complexes, as discussed in Section 2.4.1.

The catalyst precursor M(II)Cl_2(diphosphine)(DPEN) **A** is converted to [M(II)H_2(diphosphine)(DPEN)]$^+$ **B** in 2-propanol with or without an alkaline base. Then H_2 reacts with **B** to form three possible cationic complexes **C1** (H_2 *trans* to H), **C2** (H_2 *trans* to P) and **C3** (H_2 *trans* to N), followed by deprotonation of the complex generating two possible active M(II)H_2(diphosphine)(DPEN) complexes **D1** (*trans*-hydride) and **D2** (*cis*-hydride). Then a ketone is reduced by **D1** or **D2** to form an alcohol and a 16-electron amide species **F** *via* a transition state **E**. Protonation of **F** by an alcoholic solvent regenerates complex **B**, while **F** partially returns to **D** by reacting with H_2. We first explore the most stable conformational isomers assuming they are stabilised in the singlet spin state, after which the spin state of the more stable isomer is examined.

The dihydride metal M(II)H_2(diphosphine)(diamine) complexes can adopt both *trans*- and *cis*-conformations with respect to the hydrogen atoms (Scheme 5.2), and the dominant *trans*-[Ru(II)H_2{(*S*)-XylBINAP}{(*S*,*S*)-DPEN}] **1** complex (see Figure 5.1) has been successfully used as a catalyst in the enantioselective hydrogenation of acetophenone with exceedingly high *ee* (99%). For the analogue Fe(II)H_2[(*S*)-XylBINAP)](*S*,*S*)-DPEN], we first of all need to determine which of the isomers is more stable. The electronic energy difference between the *trans*-[Fe(II)H_2{(*S*)-XylBINAP}{(*S*,*S*)-DPEN}] **2** and *cis*-[Fe(II)H_2{(*S*)-XylBINAP}{(*S*,*S*)-DPEN}] **3** complexes, as well as between the *trans*-[Fe(II)H_2{(*S*)-BINAP}{(*S*,*S*)-DPEN}] **4** and *cis*-[Fe(II)H_2{(*S*)-BINAP}{(*S*,*S*)-DPEN}] **5** complexes, computed at the PBE, PBE0, and B3LYP levels of theory, are reported in Table 5.1. The results show that the energy of the *trans*-isomer is 3.7 - 8.4 kcal/mol lower than the *cis*-isomer for XylBINAP and 3.6 - 8.3 kcal/mol for BINAP. In Table 5.1, we also report the relative electronic energies of the *trans*- and *cis*-isomers of the Ru(II)H_2[(*S*)-XylBINAP)][(*S*,*S*)-DPEN] and Ru(II)H_2[(*S*)-BINAP)][(*S*,*S*)-DPEN] complexes, and find that the *trans*-isomer is about 2.2 - 4.5 kcal/mol for XylBINAP and 2.0 - 4.0 kcal/mol lower in energy than the *cis*-isomer for BINAP. Our results agree with the experimental evidence that the *trans*-dihydride ruthenium complex is the observed species in the solution[30c,103], and show that the *trans*-[Fe(II)H_2(diphosphine)(diamine)] complex is the more stable isomer for the iron complex.

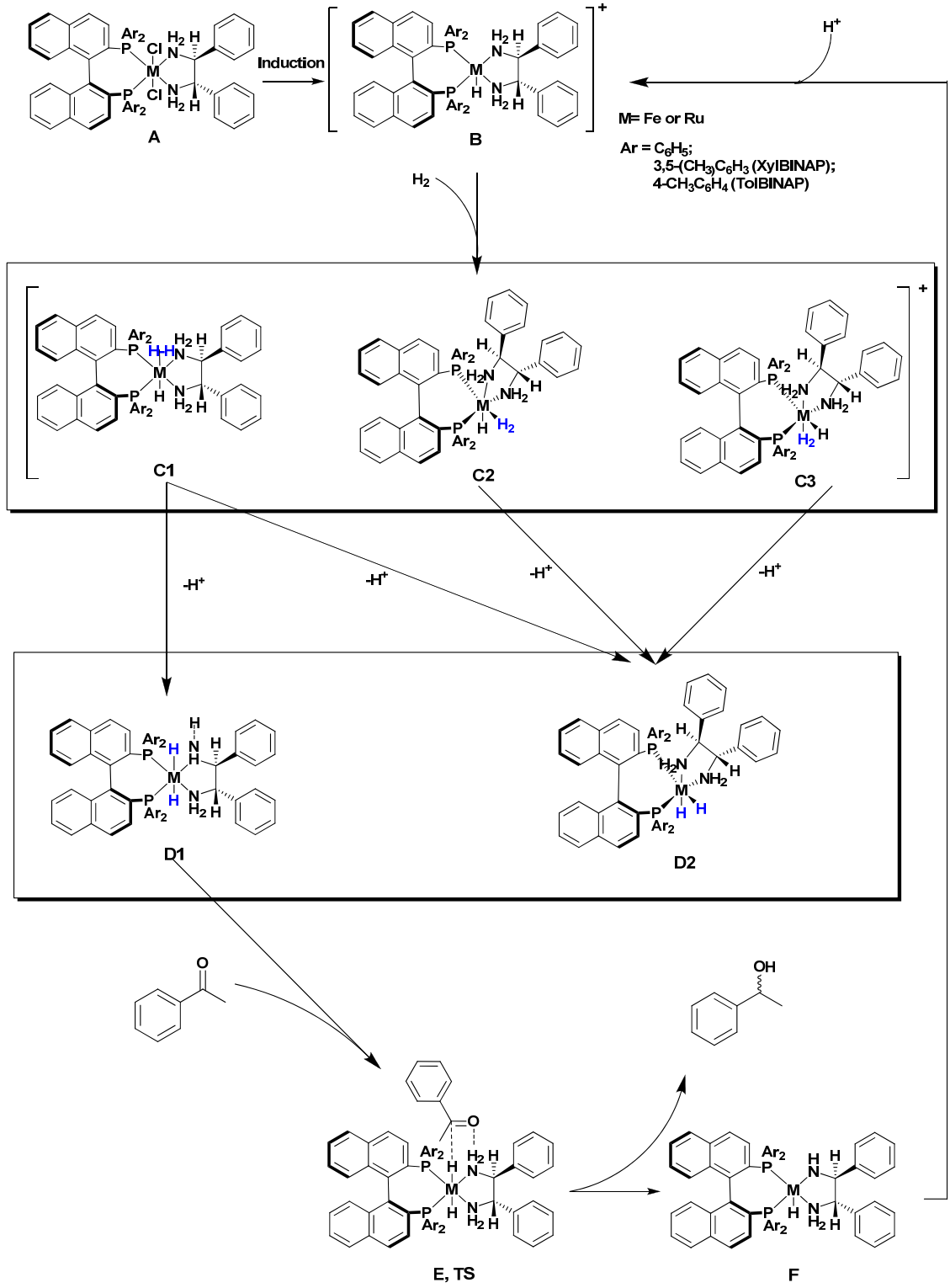

Scheme 5.1: Proposed catalytic cycle for the hydrogenation of acetophenone catalysed by the diphosphine/1,2-diamine ruthenium complexes.

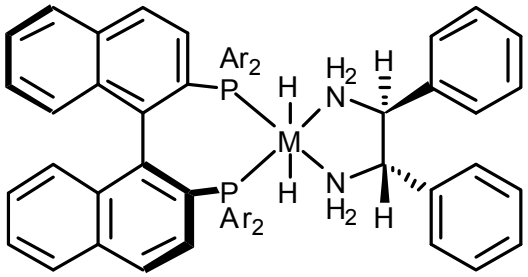

trans-[M(II)H_2(diphosphine)(diamine)]

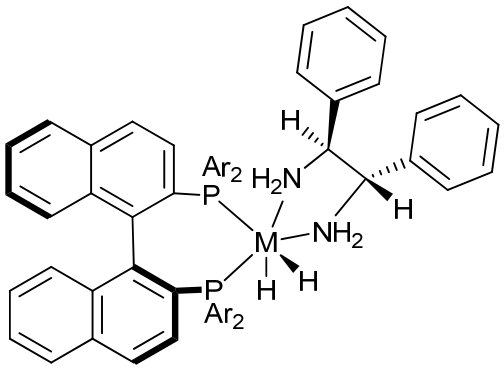

cis-[M(II)H_2(diphosphine)(diamine)]

M = Ru or Fe

(*S*)-Xyl BINAP: Ar = 3,5-$(CH_3)_2C_6H_3$

(*S*)-BINAP: Ar = C_6H_5

Scheme 5.2: Structures of *trans*- and *cis*-[M(II)H_2(diphosphine)(diamine)] complexes, where Ar = 3,5-$(CH_3)_2C_6H_3$ or C_6H_5.

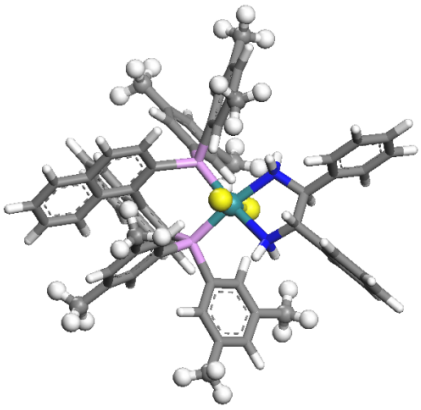

trans-[Ru(II)H_2\{(*S*)-XylBINAP\}\{(*S*,*S*)-DPEN\}] **1**

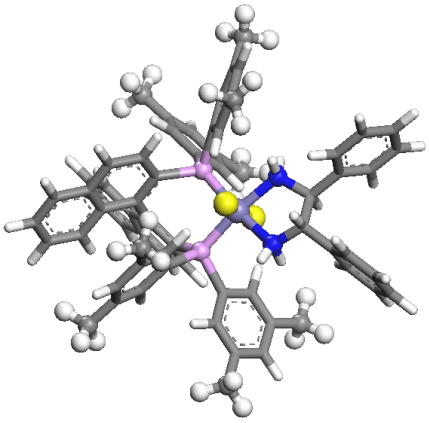

trans-[Fe(II)H_2\{(*S*)-XylBINAP\}\{(*S*,*S*)-DPEN\}] **2**

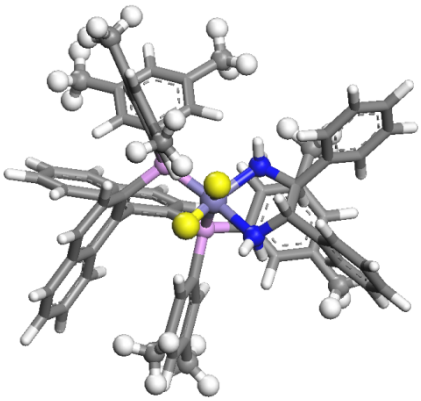

cis-[Fe(II)H_2\{(*S*)-XylBINAP\}\{(*S*,*S*)-DPEN\}] **3**

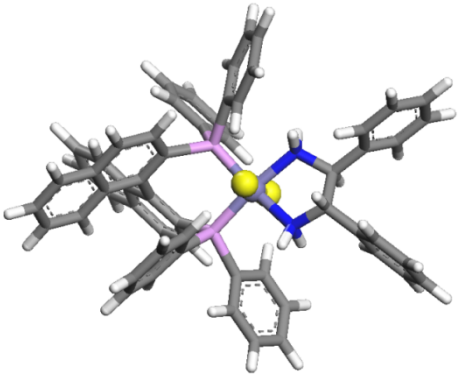

trans-[Fe(II)H_2\{(*S*)-BINAP\}\{(*S*,*S*)-DPEN\}] **4**

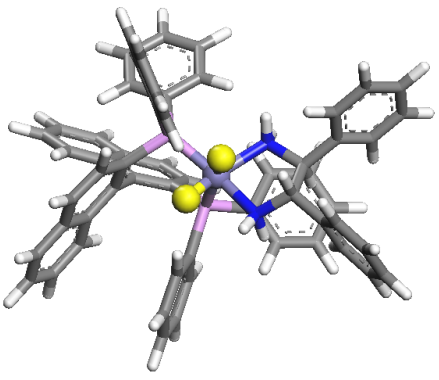

cis-[Fe(II)H_2\{(*S*)-BINAP\}\{(*S*,*S*)-DPEN\}] **5**

Figure 5.1: Structures of *trans*- and *cis*-[M(II)H_2(diphosphine)(diamine)], and Ar = 3,5-$(CH_3)_2C_6H_3$ or C_6H_5.

Table 5.1: Electronic energy differences between the *trans*- and *cis*-isomers of the M(II)H_2(diphosphine)[(*S*,*S*)-DPEN] complexes.

Level of Theory	Basis Set	Ru(II)H_2(diphosphine) (*S*,*S*-DPEN)		Fe(II)H_2(diphosphine) (*S*,S-DPEN)	
		XylBINAP	BINAP	XylBINAP	BINAP
		ΔE (*trans*–*cis*) [kcal/mol]			
PBE	DNP	-4.50	-4.04	-8.09	-7.15
PBE	6-31G **/LANL2DZ	-2.21	-2.02	-3.70	-3.61
PBE0	6-31G **/LANL2DZ	-3.95	-3.75	-8.41	-8.28
B3LYP	6-31G **/LANL2DZ	-2.98	-2.60	-8.21	-7.91

5.3.2 Spin state of *trans*-[Fe(II)H_2(diphosphine)(diamine)] complexes

Turning now to the electronic properties of the iron and ruthenium complexes, the former are often paramagnetic with high spin states, whereas the latter are diamagnetic with low-spin states. It is likely that for *trans*-[Fe(II)H_2(diphosphine)(diamine)] complexes, the presence of a strong field ligand such as diphosphine assists the formation of low-spin metal complexes, owing to their greater *d-d* splitting[104]. To investigate further, we have optimised the ruthenium and iron complexes **1** and **2** (see Figure 5.1) by imposing the spin multiplicity on the singlet, triplet and quintet states. The results in Table 5.2 reveal that for the ruthenium complex **1**, the singlet state is 42.2 kcal/mol and 98.0 kcal/mol more stable than the triplet and quintet states respectively, whereas for the iron complex **2**, the singlet state is more stable than the triplet and quintet states by 27.3 kcal/mol and 57.5 kcal/mol respectively. These energy differences are still large enough to result in the *trans*-[Fe(II)H_2(diphosphine)(diamine)] complexes having a singlet ground state as with the *trans*-[Ru(II)H_2(diphosphine)(diamine)] complexes. This trend is consistent with recent results reported by Chen *et al.*[102] and Sui-Seng *et al.*[101b] for the simplified Fe(II)$H_2(PH_3)_2$(en) complex.

Table 5.2: Relative energies of *trans*-[Ru(II)H_2{(*S*)-XylBINAP)}{(*S*,*S*)-DPEN}] and *trans*-[Fe(II)H_2{(*S*)-XylBINAP}{(*S*,*S*)-DPEN]}] with S=0, 2 or 4.

Spin Multiplicity	RuH_2[(*S*)-XylBINAP][(*S*,*S*)-DPEN]	FeH_2[(*S*)-XylBINAP][(*S*,*S*)-DPEN]
	ΔE [kcal/mol]	
Singlet	0	0
Triplet	42.21	27.25
Quintet	97.98	57.48

5.3.3 Mechanism of ketone hydrogenation using M(II)$H_2(PH_3)_2$(en)

The results from the previous section confirm that the conformation and spin state of the Fe(II)H_2(diphosphine)(diamine) complexes are the same as those of Ru(II)H_2(diphosphine)(diamine)] complexes, i.e., *trans*-[M(II)H_2(diphosphine)(diamine)] is the most stable isomer and this complex is in the singlet spin state. We can therefore propose that *trans*-[$Fe^{II}H_2$(diphosphine)(diamine)] catalyses the hydrogenation of ketones *via* the same mechanism as the ruthenium-amine-based complexes, i.e., the metal-ligand bifunctional mechanism[30].

In order to probe the mechanism of ketone hydrogenation catalysed by the Ru- and FeH_2(diphosphine)(diamine) complexes and exclude the influence of the two bidentate ligands, we have considered a simplified catalytic system composed of one ethylenediamine and two PH_3 ligands, i.e., *trans*-[M(II)$H_2(PH_3)_2$(en)]. As in the case of the *trans*-[M(II)H_2{(*S*)-XylBINAP}{(*S*,*S*)-DPEN}] complexes, the two *trans*-[M(II)$H_2(PH_3)_2$(en)] complexes are also stabilised in the singlet state[101b,102].

The proposed catalytic cycle is composed of two parts[30c30e] (see Scheme 5.3): (a) hydrogenation from the ketone to the alcohol through the metal-ligand bifunctional mechanism, where the hydridic Ru-H and protic N-H are transferred to the C=O bond *via* a six-membered pericyclic transition state (TS), and the 18-electron hydride-amino metal complex becomes a 16-electron hydrido-amido metal species; (b) regeneration of the catalyst through heterolytic splitting of dihydrogen across the Ru=N bond.

In order to search for the transition state in the simplified system, we attempted the synchronous transit-guided quasi-Newton (STQN) and the constrained optimisation (CO) methods, discussed in detail below.

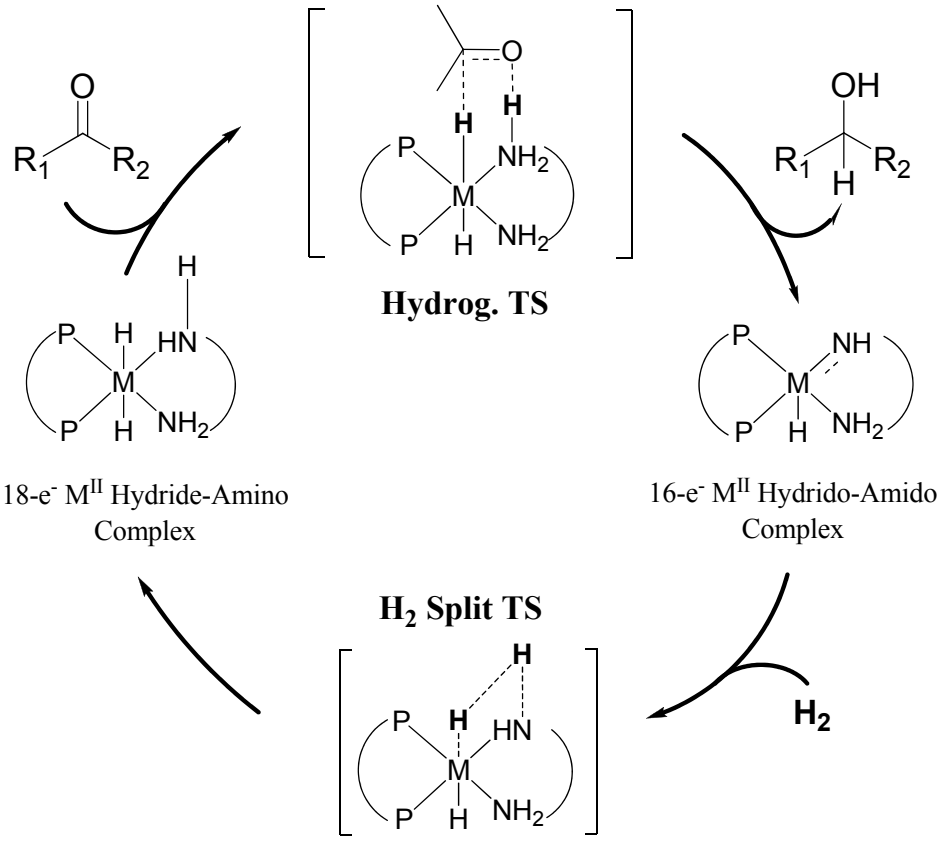

Scheme 5.3: Catalytic cycle for the hydrogenation of ketones using the *trans*-[M(II)H_2(diphosphine)(diamine)] complexes.

5.3.3.1 Locating the transition state using the synchronous transit-guided quasi-Newton (STQN) method

First, we attempted using the STQN method (discussed in Chapter 3) to search for the transition states. In Table 5.3, we report the activation energies for the H_2-hydrogenation of acetone catalysed by Ru(II)$H_2(PH_3)_2$(en) and Fe(II)$H_2(PH_3)_2$(en)[102]. The values of the energy barriers of the hydrogen-transfer process are 2.2 - 3.4 kcal/mol and 2.0 - 3.2 kcal/mol for the ruthenium and iron system, respectively. For H_2-splitting, the activation energies are 8.4 - 13.8 kcal/mol and 8.2 - 12.8 kcal/mol for the ruthenium and iron systems respectively. These figures indicate that different exchange-correlation functionals give similar energy barriers in both systems, and that the energy barriers for the reactions of hydrogen-transfer and H_2-splitting catalysed by Ru(II)$H_2(PH_3)_2$(en) are close to those calculated for Fe(II)$H_2(PH_3)_2$(en).

The reaction coordinate diagram (Figure 5.2) shows the relative energy of the intermediates and transition states involved in the catalytic cycle (Scheme 5.3), with respect to the energies of the acetone, the H_2 molecule and the *trans*-[M(II)$H_2(PH_3)_2$(en)] complex. The energies and structures of the minima and saddle point have been computed at the B3LYP/6-31G** level of theory. Figure 5.2 shows that the mechanism of the reaction, as well as the activation energies for the catalytic steps involved in the hydrogenation of acetone catalysed by Fe(II)$H_2(PH_3)_2$(en) and Ru(II)$H_2(PH_3)_2$(en) are very similar, suggesting that the ketone/alcohol hydrogen transfer reaction in the presence of the *trans*-[Fe(II)H_2(diphosphine)(diamine)] complexes could have an activity comparable to that of the *trans*-[Ru(II)H_2(diphosphine)(diamine)] catalysed processes. Moreover, the rate-determining step in the catalysis of both systems is dependent on the H_2-splitting, and we can deduce that the mechanism of the ketone hydrogenation catalysed by this type of iron-based complex would go through the metal-ligand bifunctional mechanism.

Table 5.3: Energy barriers (in kcal/mol) for the H_2-hydrogenation of acetone catalysed by the *trans*-[M(II)H_2(PH_3)$_2$(en)] model catalysts.

Reference	Chen[11]	This Thesis				
Functional	B3LYP	PBE	PBE	PBE0	B3LYP	mPW1PW91
Basis Set	6-31G ** LAND2DZ	DNP N/A	6-31G ** LAND2DZ	6-31G ** LAND2DZ	6-31G ** LAND2DZ	6-31G** SDD
$\Delta E_{Ru,\ Hydrog.\ TS}$	2.85	2.15	2.20	2.77	3.40	2.68
$\Delta E_{Fe,\ Hydrog.\ TS}$	2.37	2.02	2.00	2.41	3.17	2.32
$\Delta E_{Ru,\ H2\text{-}Splitting\ TS}$	12.48	8.36	9.74	8.42	13.76	8.69
$\Delta E_{Fe,\ H2\text{-}Splitting\ TS}$	10.86	8.16	9.24	8.07	12.79	8.54

- $\Delta E_{M,\ Hydrog.\ TS}$ is the energy barrier for the hydrogen transfer in the acetone/isopropanol reaction catalysed by the 18-electron hydride-amino metal complex;
- $\Delta E_{M,\ H2\text{-}Splitting\ TS}$ is the energy barrier for the heterolytic dihydrogen splitting on the 16-electron hydrido-amido metal complex.

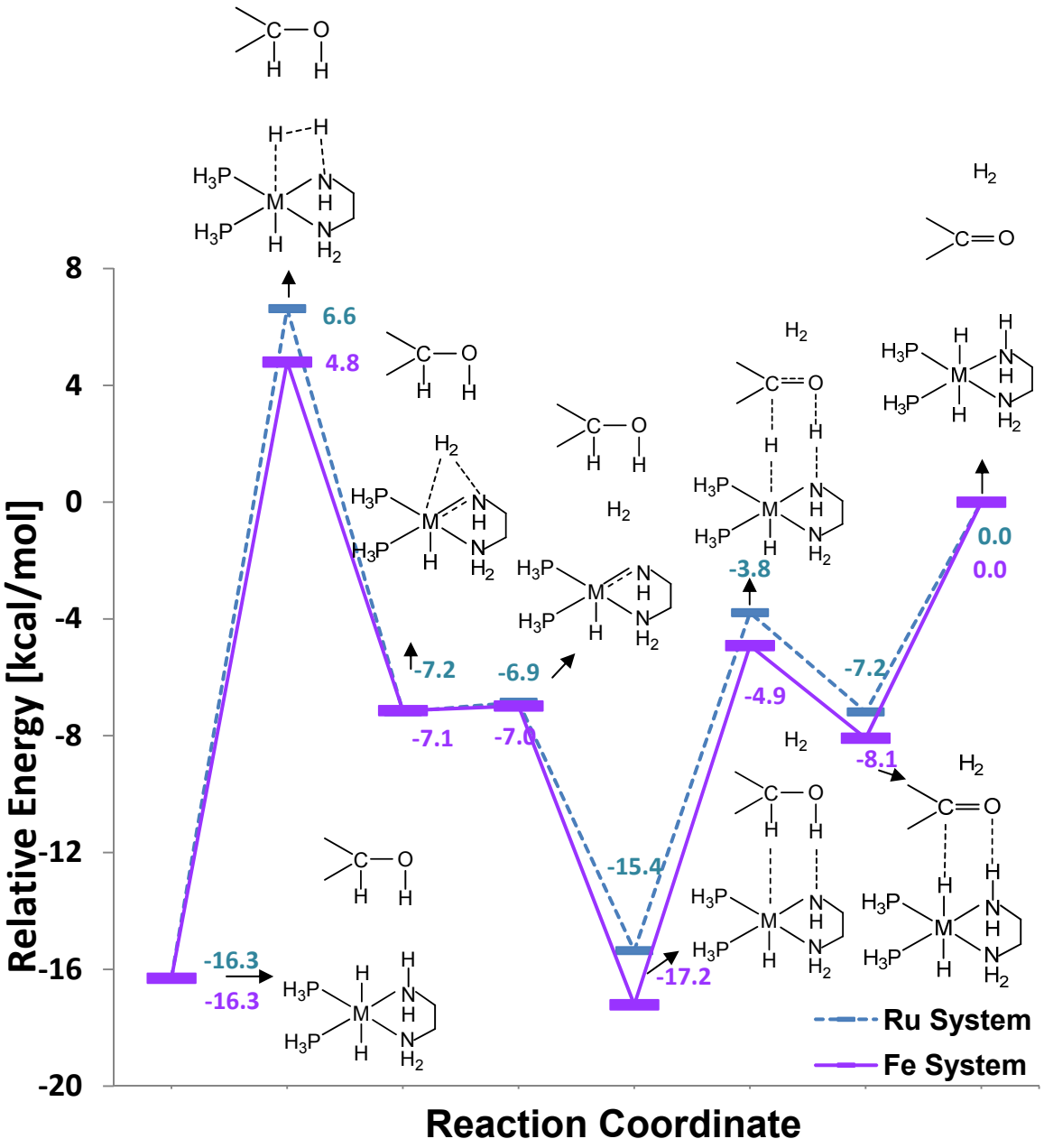

Figure 5.2: Reaction coordinate diagram for the H_2-splitting and hydrogenation of acetone catalysed by the *trans*-[M(II)H_2(PH_3)$_2$(en)] complexes at the B3LYP/6-31G** level of theory using Gaussian 03.

5.3.3.2 Locating the transition state using the constrained optimisation method

The aforementioned synchronous transit-guided quasi-Newton (STQN) method can only describe the reaction from the most stable intermediate to the product *via* the transition state. In this section, we use the constrained optimisation (CO) method following the same technique as in Chapter 4 by optimising with respect to a pseudo coordinate, (M-)H···C(=O), allowing us to explore the structural changes prior to the intermediate state. Figure 5.3 displays the reaction coordinate diagrams in the hydrogenation of acetone catalysed by the Ru(II)$H_2(PH_3)_2$(en) and Fe(II)$H_2(PH_3)_2$(en) complexes whilst gradually reducing the (M-)H···C(=O) distance from 8 Å to 1.1 Å with the representative structures shown alongside the diagram. Interestingly, we note that the energy drops when the (Ru-)H···C(=O) distance is 4 Å, and the acetone rotates to an upright position and moves away from Ru(II)$H_2(PH_3)_2$(en). In contrast, the energy in the iron system changes more smoothly. We magnify the region of Figure 5.3 containing the range of (M-)H···C(=O) distances from 4 Å to 1.75 Å and plot it in Figure 5.4, which shows that in [acetone + Ru(II)$H_2(PH_3)_2$(en)], the minima and transition state occur when the (Ru-)H···C(=O) distances are 3.5 Å and 2 Å; in [acetone + Fe(II)$H_2(PH_3)_2$(en)], the minima and transition state occur at 2.75 Å and 2.25 Å. Figure 5.4 also reveals that the difference in activation energies of the ruthenium and iron systems is *ca.* 1.5 kcal/mol. The structural changes in [Acetone + Ru(II)$H_2(PH_3)_2$(en)] while the (Ru-)H···C(=O) distance is reduced from 8 Å to 1.2 Å are illustrated in Figure 5.5. When the (Ru-)H···C(=O) distance is between 4 Å and 3.25 Å, the acetone expands as a result of the two methyl groups repelling each other. When the (Ru-)H···C(=O) distance is 3 Å, the attraction between acetone and Ru(II)$H_2(PH_3)_2$(en) is greater than the repulsion and therefore the acetone does not expand in the subsequent structures. The structural changes in [Acetone + Fe(II)$H_2(PH_3)_2$(en)] while the (Fe-)H···C(=O) distance is reduced from 8 Å to 1.1 Å are illustrated in Figure 5.6, which shows that there is no dramatic repulsion when the acetone approaches Fe(II)$H_2(PH_3)_2$(en). The structural changes in an iron-based system are smooth. Comparing Figures 5.5 and 5.6, their structures from 8 Å to 1.1 Å are similar for the two systems apart from those in the range, 4 Å to 3.25 Å.

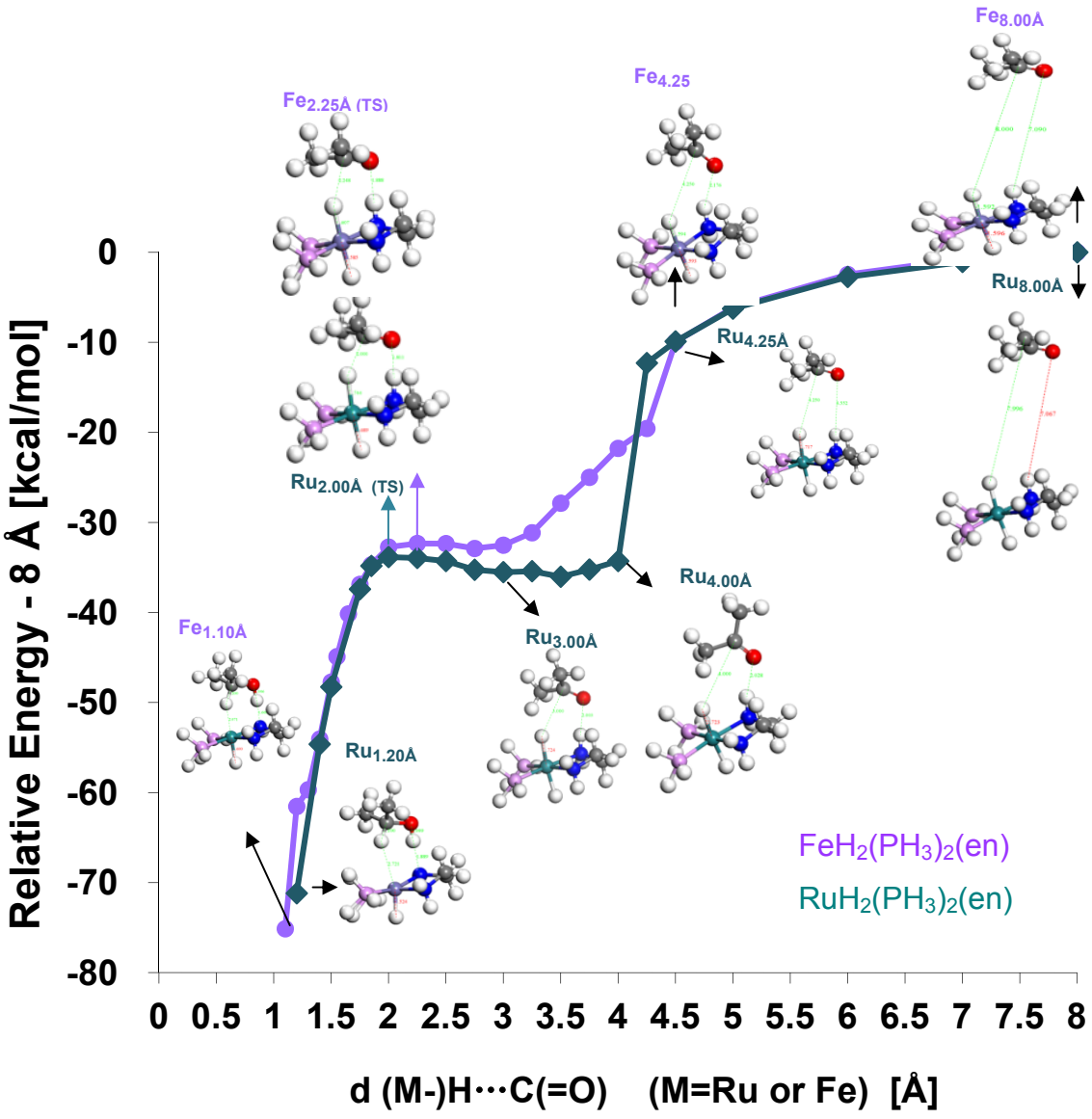

Figure 5.3: Reaction coordinate diagram for the hydrogenation of acetone catalysed by Ru(II)$H_2(PH_3)_2$(en) and Fe(II)$H_2(PH_3)_2$(en) as the (M-)H···C(=O) distance is gradually reduced from 8 Å to 1.1 Å at the PBE/DNP level of theory using DMol[3].

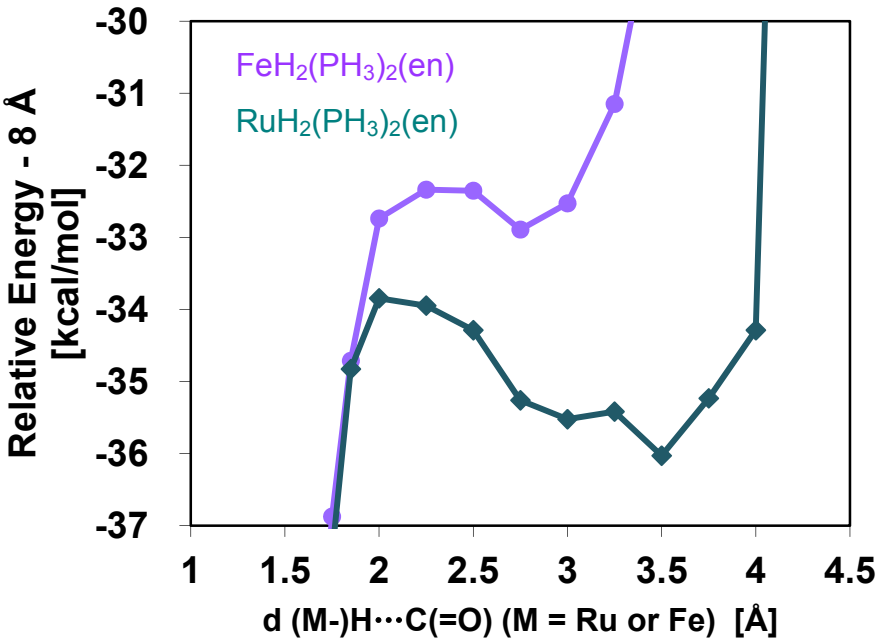

Figure 5.4: Reaction coordinate diagram of the hydrogenation of acetone catalysed by Ru(II)$H_2(PH_3)_2$(en) and Fe(II)$H_2(PH_3)_2$(en) as the (M-)H···C(=O) distance is gradually reduced from 4 Å to 1.75 Å.

[Å]	Acetone + $RuH_2(PH_3)_2$(en)		[Å]	Acetone + $RuH_2(PH_3)_2$(en)	
8.00	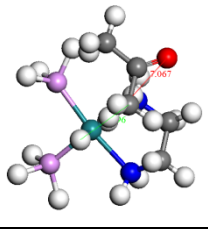	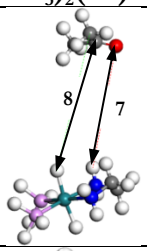	2.75	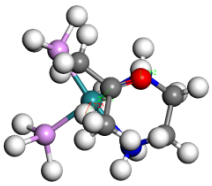	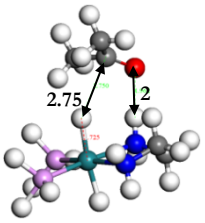
4.25	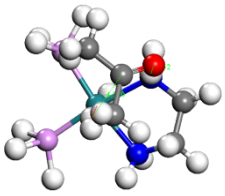	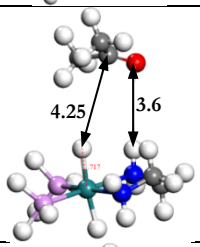	2.50	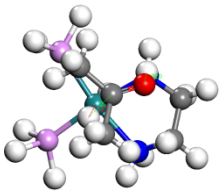	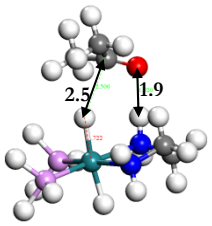
4.00	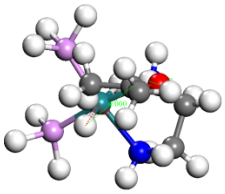	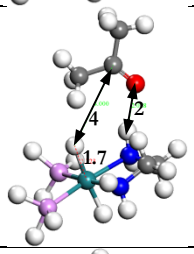	2.25	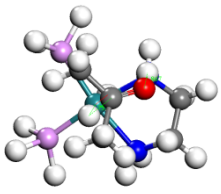	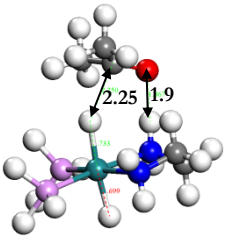
3.50	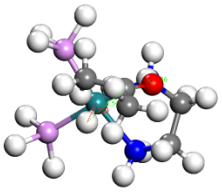	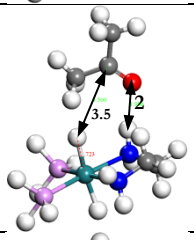	2.00	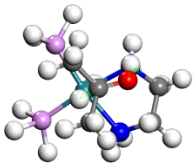	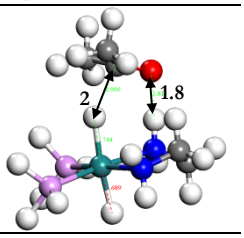
3.25	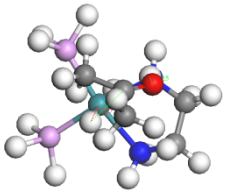	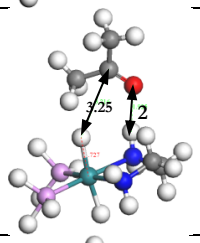	1.75	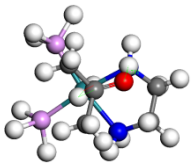	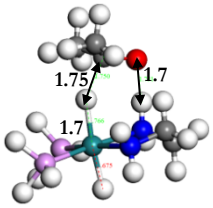
3.00	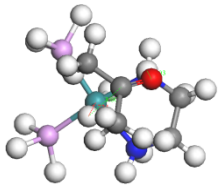	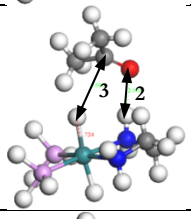	1.50	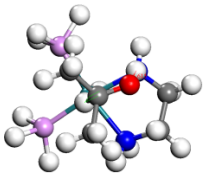	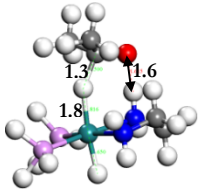
2.75	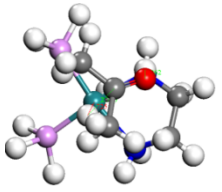	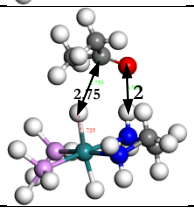	1.20	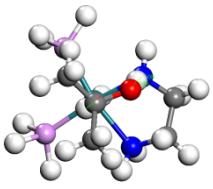	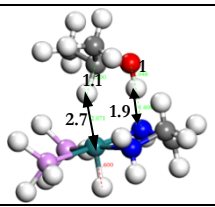

Figure 5.5: Snapshots of the hydrogenation of acetone catalysed by Ru(II)$H_2(PH_3)_2$(en) as the (Ru-)H···C(=O) distance is gradually reduced from 8 Å to 1.2 Å.

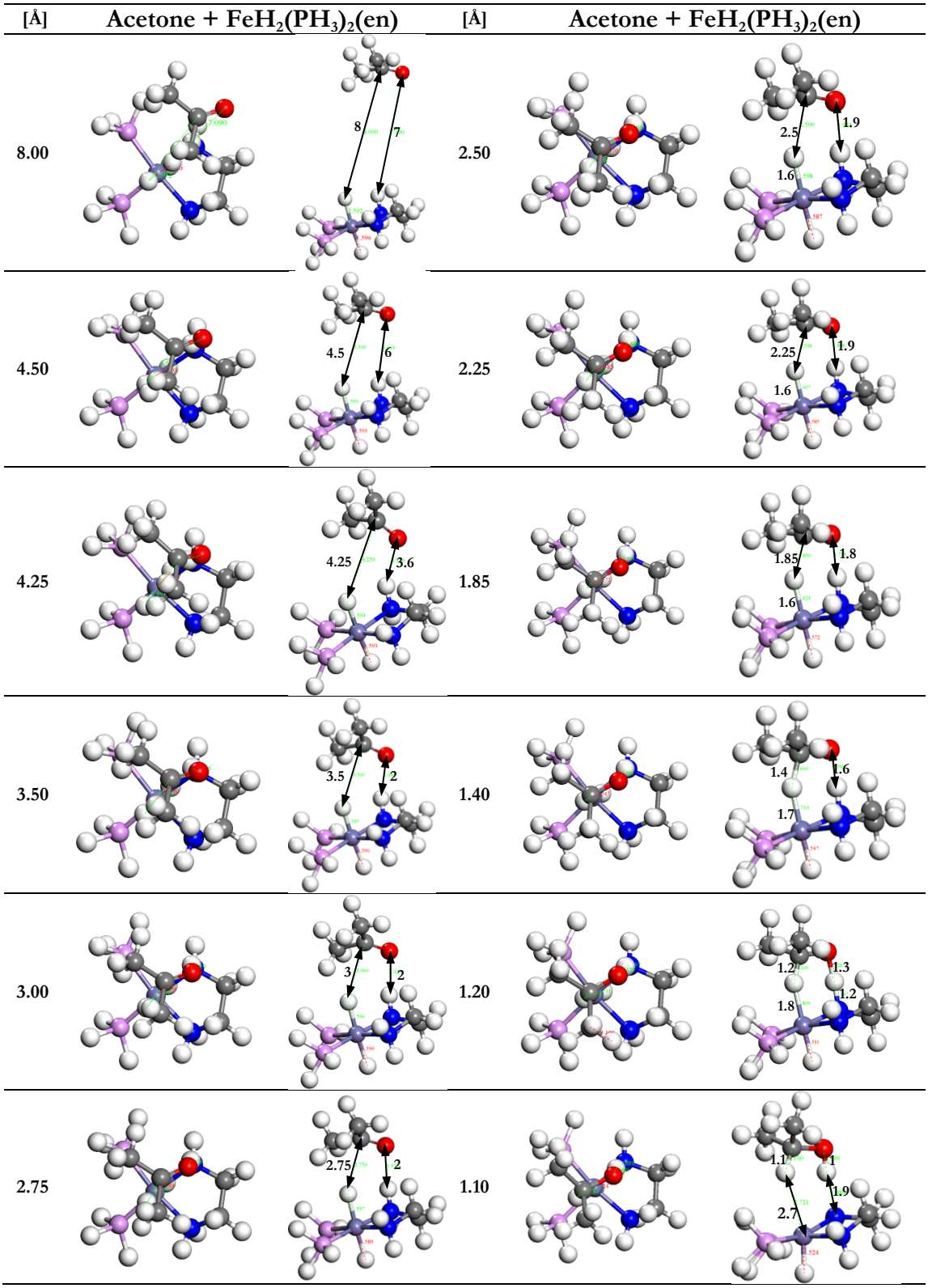

Figure 5.6: Structural changes of the hydrogenation of acetone catalysed by Fe(II)$H_2(PH_3)_2$(en) as the (Fe-)H···C(=O) distance is gradually reduced from 8 Å to 1.1 Å.

5.3.4 Enantioselectivity of acetophenone hydrogenation by *trans*-[M(II)H_2{(*S*)-XylBINAP}{(*S*,*S*)-DPEN}]

As noted earlier, acetophenone is reduced to (*R*)-phenylethanol with an outstanding *ee* of 99% when the reaction is catalysed by *trans*-[Ru(II)H_2{(*S*)-XylBINAP}{(*S*,*S*)-DPEN}] **1** (Scheme 5.4)[22b]. This high enantioselectivity has been explained by comparing the energy differences of all the possible pathways by which acetophenone can approach the active sites of the ruthenium catalyst. A stable intermediate forms when the reactant enters the pocket made by the bulky groups of the ruthenium catalyst along the reaction pathway associated with the (*R*)-product[28a,28b]. For catalytic systems like Ru(II)H_2(diphosphine)(diamine), the enantioselectivity in the hydrogenation of pro-chiral ketones is therefore controlled by the formation of the ketone/ruthenium-complex intermediates. The stability of these intermediates depends on the interaction between the bulky diphosphine and/or diamine ligands, and the pro-chiral ketone, but not on the H-transfer process.

In the previous section, we have shown the strong similarities between the mechanism of the ketone/alcohol hydrogen-transfer reaction catalysed by the ruthenium and iron (diphosphine)(diamine) complexes. We now turn our investigation to the reduction of acetophenone (ACP) to (*R*)- and (*S*)-phenylethanol catalysed by the hypothetical iron-based catalyst *trans*-[Fe(II)H_2{(*S*)-XylBINAP}{(*S*,*S*)-DPEN}] **2**, analogous to the highly successful **1**. Our calculations aim to answer the following question: can a high enantioselectivity be achieved when using Fe(II)H_2(diphosphine)(diamine) complexes? To this end, we have applied a constrained optimisation technique to model the approach of the acetophenone to the active M-H and N-H sites of the two catalysts along the two most favourable pathways[28a,28b]. The Q1 pathway illustrated in Figure 5.7 gives the (*R*)-product and Q2 gives the *(S)*-product.

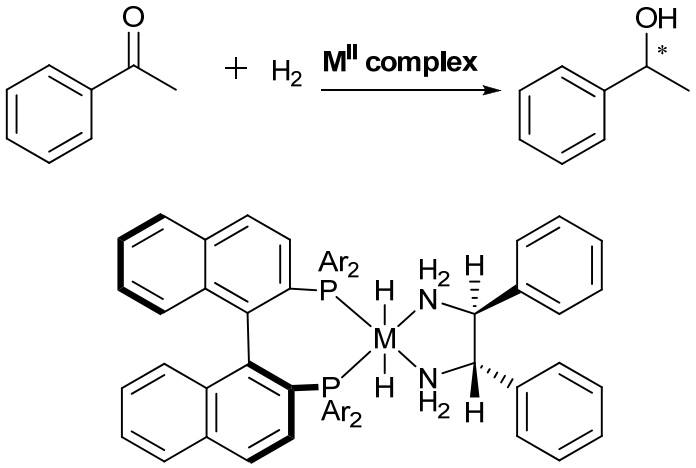

M = Ru or Fe

Ar = 3,5-$(CH_3)_2C_6H_3$; (*S*)-XylBINAP

XylBINAP = 2,2'-bis-(di-3,5-xylylphosphino)-1,1'-binaphthyl.

DPEN = 1,2-diphenylethylenediamine.

Scheme 5.4: Asymmetric H_2-hydrogenation of acetophenone (ACP) catalysed by the *trans*-[{M(II)H_2(*S*)-XylBINAP)}{(*S*,*S*)-DPEN)}] catalysts. (**1** represents*trans*-[Ru(II)H_2}{(*S*)-XylBINAP}{(*S*,*S*)-DPEN}] and **2** represents *trans*-[Fe(II)H_2}{(*S*)-XylBINAP}{(*S*,*S*)-DPEN}].)

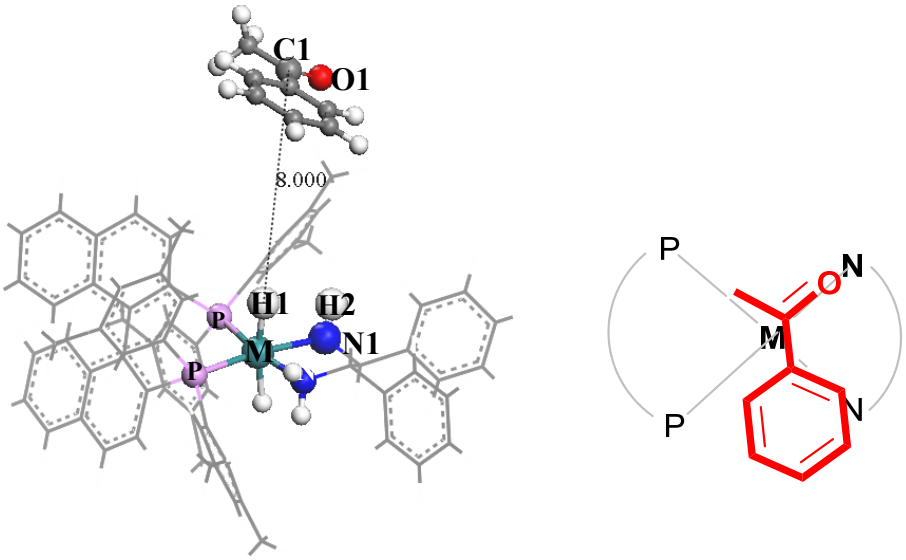

Q1 Approach: (*R*)-phenylethanol

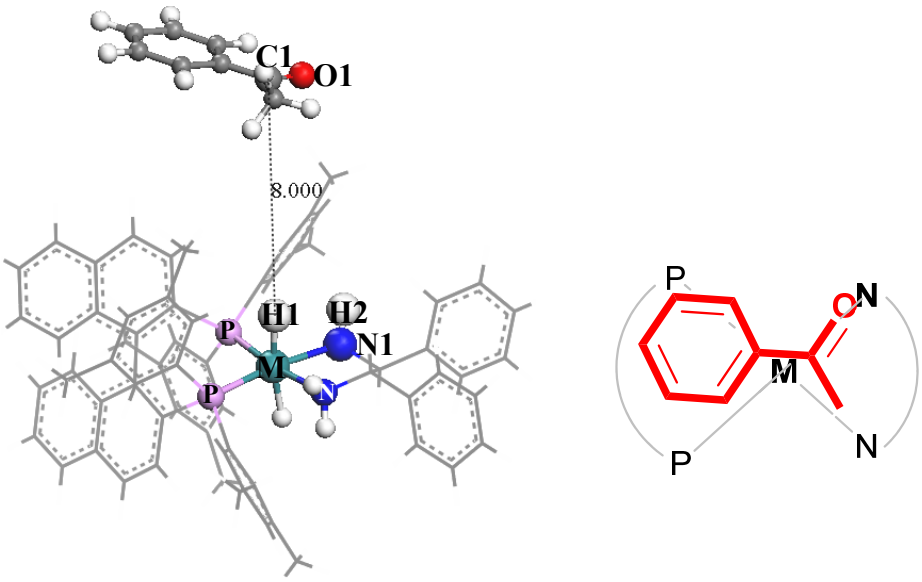

Q2 Approach: (*S*)-phenylethanol

Figure 5.7: Definition of two of the possible reaction pathways, Q1 and Q2, with the subsequent stereochemical configurations of the alcohol product, phenylethanol, in the asymmetric hydrogenation of acetophenone.

Figure 5.8 displays the variation in the relative energy of the systems [ACP + **1**] and [ACP + **2**] calculated at the DFT/PBE level with respect to the internuclear distances, (M-)H···C(=O), for the Q1 and Q2 pathways. A detailed analysis of the transition state structure involved in the ketone/alcohol hydrogen transfer reaction *via* the metal-ligand bifunctional mechanism has shown that the (Ru-)H···C(=O) distance can safely be taken as the pseudo reaction coordinate[28a,28b].

Here, as in the previous chapter, we only consider the electronic energy without taking into account thermal and entropic effects. We define the relative energy as $\Delta E_i = E_i - E_{ref}$, where E_i is the electronic energy of the structure at a specified (M-)H···C(=O) distance, and E_{ref} is the sum of the electronic energy of isolated ACP and the ruthenium or iron catalyst. The reaction coordinate diagrams in Figure 5.8 are characterised by a maximum at approximately 2 Å, which corresponds to a good approximation to the structure of the transition state for the hydrogen transfer ACP/phenylethanol reaction (Hydrog. TS) *via* the metal-ligand mechanism. The Q1 reaction pathway is the most energetically favourable for both [ACP + **1**] and [ACP + **2**], with the Hydrog. TS of Q1 being 4.2 kcal/mol and 6.7 kcal/mol more stable than the Hydrog. TS of Q2 for the ruthenium and iron systems respectively. The high energy difference between Q1 and Q2 for the iron system indicates that the ACP will react with the catalyst along the Q1 pathway, and that an *ee* comparable to the one obtained using the ruthenium catalyst can be expected. Since Q1 is the lowest energy approach, the features of the reaction coordinate diagram along Q1 in the ruthenium and iron catalytic systems are of more interest. Figure 5.9 shows that both the ruthenium and iron systems, [ACP + **1**] and [ACP + **2**], are characterised by two minima located at approximately 2.5 Å (Pre-INT) and 3.75 Å (INT), separated by a peak at approximately 2.6 Å with respect to the (M-)H···C(=O) distance. This peak is caused by the constraints on the (M-)H···C(=O) and is therefore not the transition state structure between the intermediates Pre-INT and INT[28a]. It is important to note that there is a similar trend along Q1 for the reaction coordinate diagrams in [ACP + **1**] and [ACP + **2**]. Therefore, in order to understand if the occurrence of the two intermediates in the Q1 pathway offers the same type of stabilisation of the Hydrog. TS structure as occurs in the ruthenium catalytic system when ACP approaches the iron catalyst, we have fully optimised the structures with (M-)H···C(=O) distances of 3.75 Å and 2.5 Å.

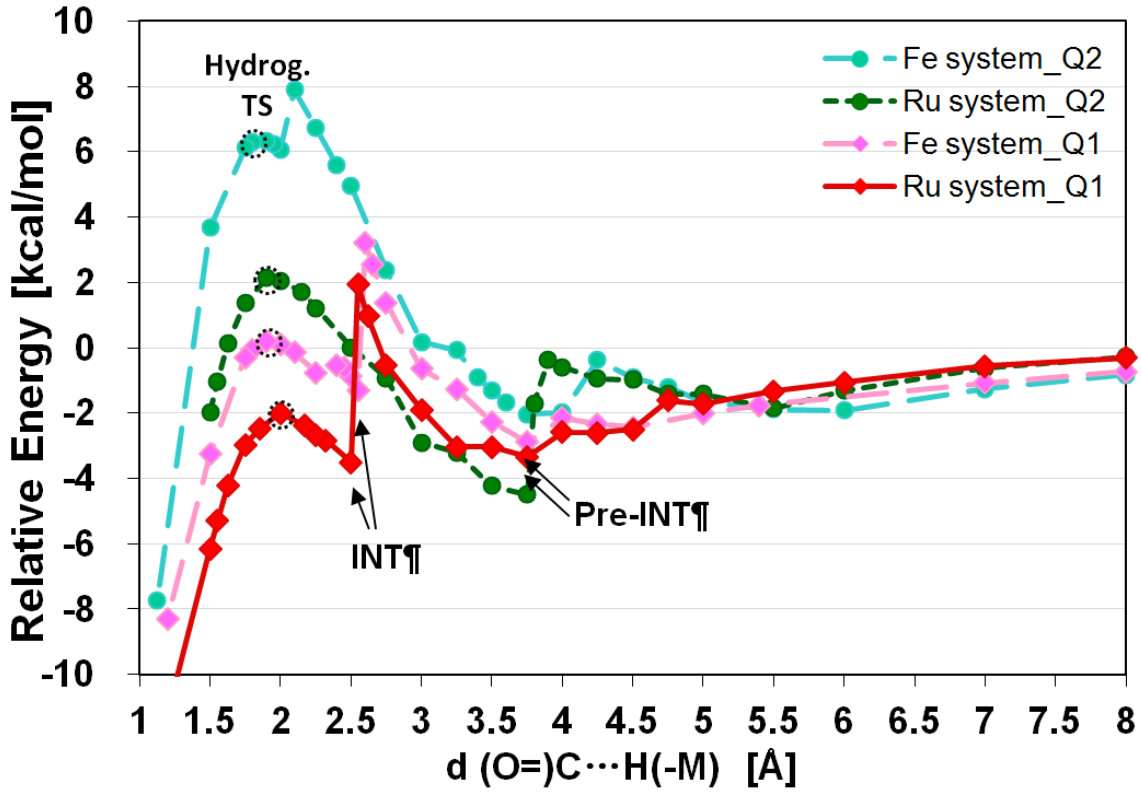

Figure 5.8: Reaction coordinate diagram for [ACP + *trans*- $M^{II}H_2$(*S*-XylBINAP)(*S*,*S*-DPEN)] with respect to the (M-)H···C(=O) distance along Q1 and Q2.

The structural characteristics of the fully optimised ruthenium and iron minima (Pre-INT_{Ru}, INT_{Ru}, Pre-INT_{Fe}, and INT_{Fe}) and of the transition state structure (Hydrog. TS), along the Q1 pathway, are shown in Figure 5.9 and Figure 5.10, and described in Table 5.4. The reaction coordinate diagram in Figure 5.9 shows that Pre-INT_{Ru} and Pre-INT_{Fe} are stable structures when the ACP and the catalyst are brought together by non-bonding interactions at a (M-)H···C(=O) bond distance of 3.76 Å for Pre-INT_{Ru} and 4.32 Å for Pre-INT_{Fe} before ACP enters into the pocket in the bulky group of the catalyst. When ACP approaches the catalyst to within a (M-)H···C(=O) distance of 3.6 – 3.7 Å, with a separation of *ca.* 3 Å between the aromatic ring of ACP and the nearest atoms on the complex, it appears that there is an appreciable attractive interaction between the NH/CH and the aromatic rings[28a,105], which drives the rotation of the phenyl group of ACP (the angle φ_{OCPhC}, changes from –4.5° in Pre-INT_{Ru} to 19.8° in INT_{Ru} and from –3.5° in Pre-INT_{Fe} to 17.8° INT_{Fe}) forming the stable intermediates INT_{Ru} and INT_{Fe}. In both systems, we also notice that from Pre-INT_{Ru} to INT_{Ru} and from Pre-INT_{Fe} to INT_{Fe}, the $\tau_{C\text{-}PhOMe}$ angle for ACP rotates by only 0.1° and 1.3° in the ruthenium and iron systems respectively.

Additionally, the angles θ_{OCMe}, θ_{OCPh} and θ_{MeCPh} (where Me refers to the carbon of the methyl group and Ph to the carbon of the phenyl group of ACP) are all approximately 120º. These results show that the methyl group of ACP does not rotate significantly and the carbonyl carbon still keeps its sp^2 hybridisation. As for the change from INT to Hydrog. TS, the phenyl group of the ACP does not rotate significantly, as $\varphi_{OCPhC'}$ changes by only 0.6º and 5.1º from INT_{Ru} to Hydrog. TS_{Ru}, and from INT_{Fe} to Hydrog. TS_{Fe} respectively. The methyl group of ACP rotates further away from the catalyst as shown in Figure 5.9 and Table 5.4 ($\tau_{C\text{-}PhOMe}$ changes from 1.1º in INT_{Ru} to –16.2º in Hydrog. TS_{Ru} and from 1.5º in INT_{Fe} to –18.9º Hydrog. TS_{Fe}). Furthermore, the carbonyl carbon starts to transform from a planar sp^2 to a tetrahedral sp^3 hybridisation (θ_{MeCPh} rotates from 118.3º in INT_{Ru} to 115.8º in Hydrog. TS_{Ru} and from 118.6º in INT_{Fe} to 114.5º in Hydrog. TS_{Fe}). We consider, for comparative purposes, two adducts (ADDUCT-I and ADDUCT-II) that appear after the transition state; these are not discussed in Chapter 4. The two adducts comprise the species formed after the hydride bonded to the metal centre has been transferred to the carbonyl carbon and the species created by the subsequent proton transfer to the oxygen. Since the hydridicity of Ru-H is greater than that of Fe-H, the hydride transfer in the ruthenium system may slightly precede the transfer in the iron system, but when considering the entire process, we envisage that the hydride and proton transfer simultaneously, as demonstrated in Figures 5.11 and 5.12. Finally, when ACP is completely reduced to the phenylethanol, the carbonyl carbon is fully sp^3 hybridised ($\theta_{O\text{-}C\text{-}Me} \sim \theta_{O\text{-}C\text{-}Ph} \sim \theta_{Me\text{-}C\text{-}Ph} \sim 110º$). The calculations above clearly demonstrate the strong similarity in the hydrogenation of ketones catalysed by **1** and **2**.

In the iron system, a small rise in energy is observed at 2.4 Å for Q1 and 2.1 Å for Q2 (see Figure 5.8). In addition, the energy barriers of the hydrogen-transfer process are 2.22 kcal/mol and 5.75 kcal/mol higher than those in the ruthenium system for Q1 and Q2 respectively. These increases in energy may be attributable to the 30% smaller ionic volume of iron compared to ruthenium, which brings the ligands closer together and gives rise to more hindrance in the iron system. Figures 5.11 and 5.12 show the variation in the bond length of d(M-H1), d(H1-C1) d(N1-H2), and d(H2-O1) (the labels of the atoms are shown in Figure 5.7) in the hydrogenation of ACP catalysed by **1** and **2.** When focusing on the curves of d(Ru-H) and d(N-H), we note that the occurrence of hydride transfer and proton transfer overlap in Figure 5.11 as well in Figure 5.12. These results suggest that in both systems, the hydride and proton transfer occur simultaneously, which is consistent with experiment.

Overall, a comparison of the hydrogen-transfer in the hydrogenation of ruthenium and iron systems shows that the formation of the Hydrog. TS and two stable intermediates is similar. Thus, we expect that a high *ee* can be achieved by controlling the ligand-metal interaction.

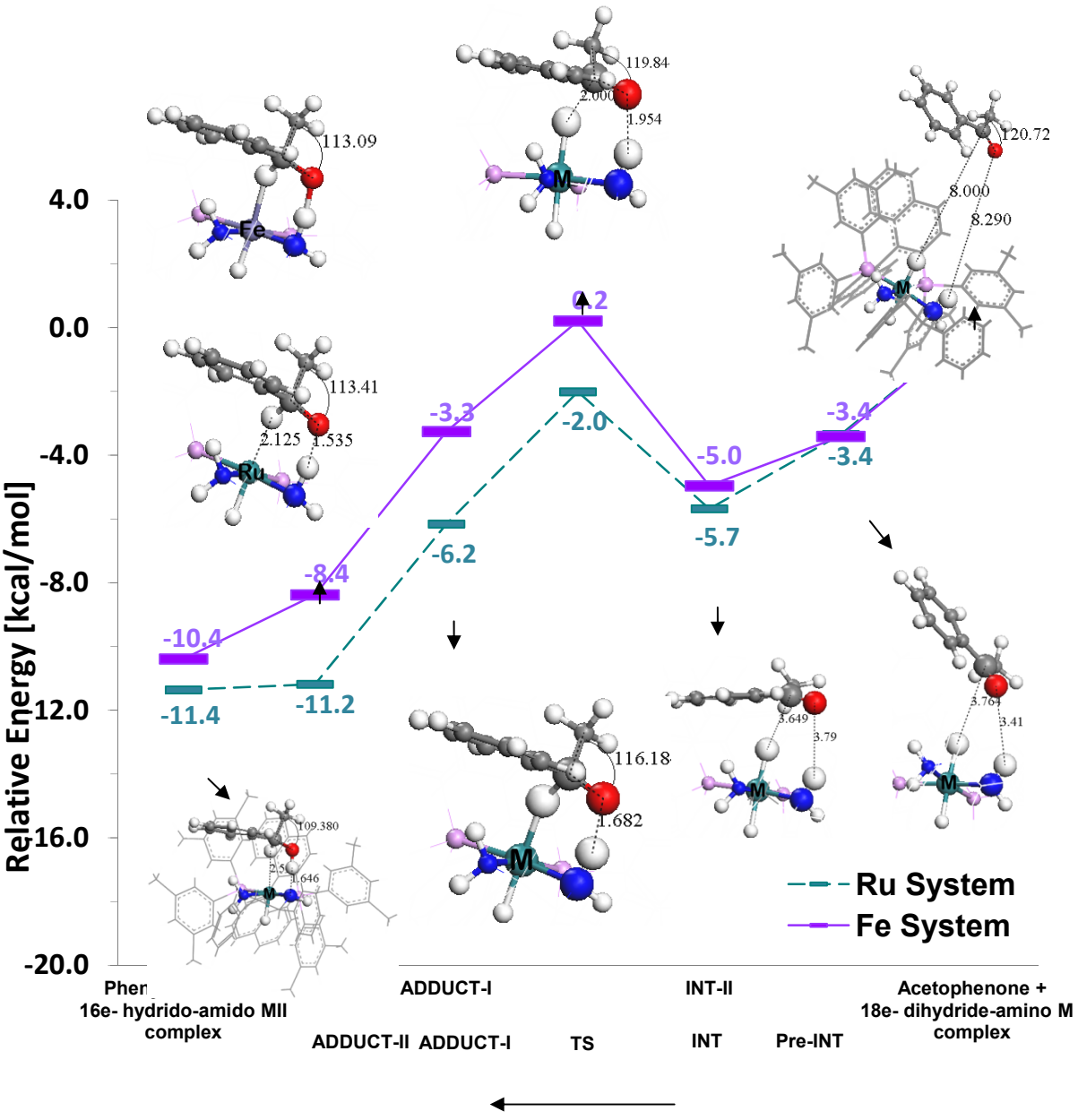

Figure 5.9: Reaction coordinate diagram for the hydrogenation of acetophenone to phenylethanol catalysed by *trans*-[M(II)H_2\{(*S*)-XylBINAP\}\{(*S*,*S*)-DPEN\}] at the PBE/DNP level of theory. Energies are reported relative to free acetophenone and free catalysts **1** and **2** respectively. (The ligands bound on the P and N atoms are removed for clarity in Pre-INT ~ ADDUCT-II.)

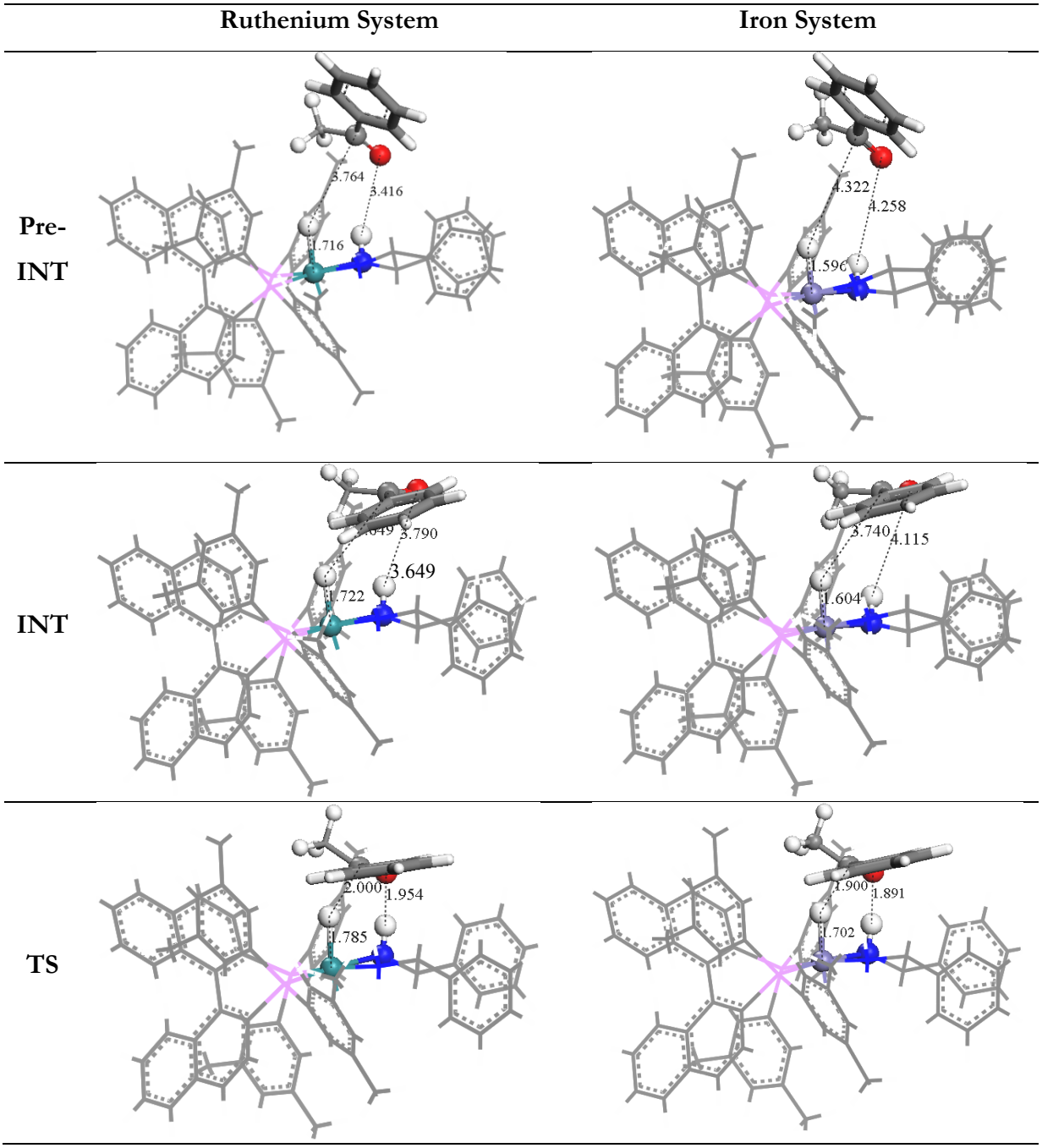

Figure 5.10: Structures of the minima (Pre-INT and INT) and transition state-like structure (Hydrog. TS) corresponding to the entrance of the acetophenone into the active sites of *trans*-{[$M^{II}H_2$(*S*)-XylBINAP][(*S*,*S*)-DPEN]} along Q1, computed at the PBE/DNP level of theory.

Table 5.4: Energetic and geometric characteristics associated with the entrance of ACP into the active sites of *trans*-{[$M^{II}H_2$(*S*)-XylBINAP][(*S*,*S*)-DPEN]} along Q1.

Ru System	Bonding	Relative Energy	d(H1-C)	d(H3-O)	d(M-H1)	d(N-H3)	φ(OCPhC')	τ(C-PhOMe)	θ(MeCO)	θ(OCPh)	θ(PhCM)
		[kcal/mol]	[Å]	[Å]	[Å]	[Å]	[°]	[°]	[°]	[°]	[°]
Phenylethanol + 16e⁻ hydrido-amido Ru^{II}complex	C-H, H-O	-11.4	1.1	1.0	2.5	1.6	26.6	-32.8	109.4	112.9	110.3
ADDUCT-II	C-H, H-N	-11.2	1.2	1.5	2.1	1.1	24.7	-32.5	113.4	114.5	108.2
ADDUCT-I	C-H-Ru, H-N	-6.2	1.5	1.7	1.9	1.1	22.1	-27.4	116.2	116.3	111.2
Hydrog. TS	H-Ru, H-N	-2.0	2.0	2.0	1.8	1.0	20.4	-16.2	119.8	119.0	115.8
INT-II	H-Ru, H-N	-5.7	3.6	3.8	1.7	1.0	19.8	1.1	121.6	120.1	118.3
INT-I	H-Ru, H-N	-3.4	3.8	3.4	1.7	1.0	-4.5	1.0	120.6	120.2	119.1
Acetophenone + 18e⁻ dihydride-amino Ru^{II} complex	H-Ru, H-N	-0.3	8.0	8.3	1.7	1.0	-0.4	0.3	120.7	120.5	118.7

Fe System	Bonding	Relative Energy	d(H1-C)	d(H3-O)	d(M-H1)	d(N-H3)	φ(OCPhC')	τ(C-PhOMe)	θ(MeCO)	θ(OCPh)	θ(PhCM)
		[kcal/mol]	[Å]	[Å]	[Å]	[Å]	[°]	[°]	[°]	[°]	[°]
Phenylethanol + 16e⁻ hydrido-amido Fe^{II} complex	C-H, H-O	-10.4	1.1	1.0	2.8	1.8	31.5	-33.0	108.9	112.7	110.5
ADDUCT-II	C-H-Fe, O-H-N	-8.4	1.2	1.5	2.1	1.1	22.3	-32.8	113.1	114.1	108.3
ADDUCT-I	C-H-Fe, H-N	-3.3	1.5	1.7	1.8	1.1	22.2	-28.0	116.1	166.4	110.4
Hydrog. TS	H-Fe, H-N	0.2	1.9	1.9	1.7	1.0	22.9	-18.9	119.3	118.8	114.5
INT-II	H-Fe, H-N	-5.0	3.7	4.1	1.6	1.0	17.8	1.5	121.2	120.1	118.6
INT-I	H-Fe, H-N	-3.4	4.3	4.3	1.6	1.0	-3.5	0.2	120.8	120.7	118.4
Acetophenone + 18e⁻ dihydride-amino Fe^{II} complex	H-Fe, H-N	-0.8	8.1	8.4	1.6	1.0	-0.1	0.1	120.6	120.6	118.8

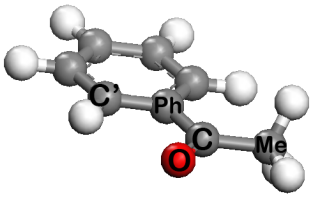

Acetophenone

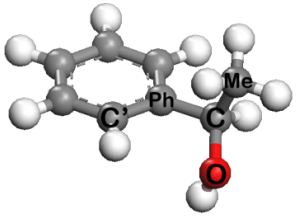

Phenylethanol

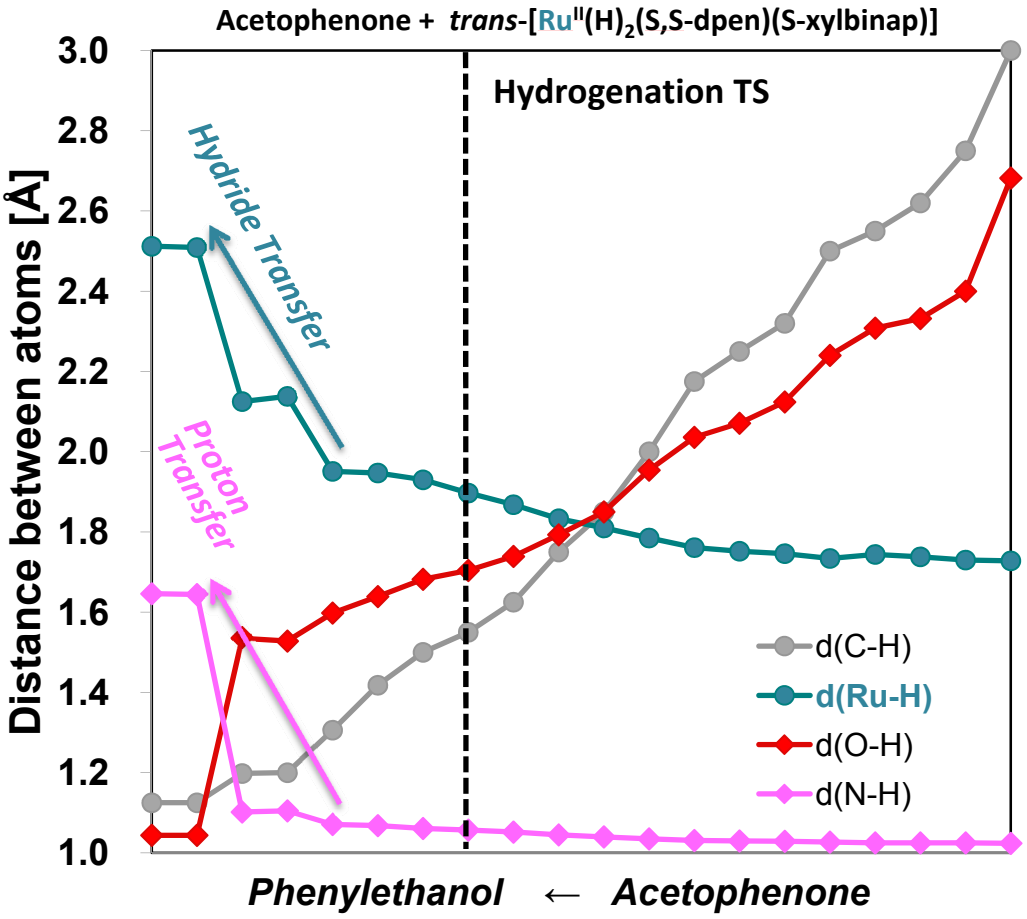

Figure 5.11: The variation of bond lengths of d(carbonyl-hydride), d(iron-hydride), d(oxygen-proton), and d(nitrogen-proton) in the reaction between ACP and *trans*-[Ru(H)$_2${(*S*)-XylBINAP}{(*S*,*S*)-DPEN}].

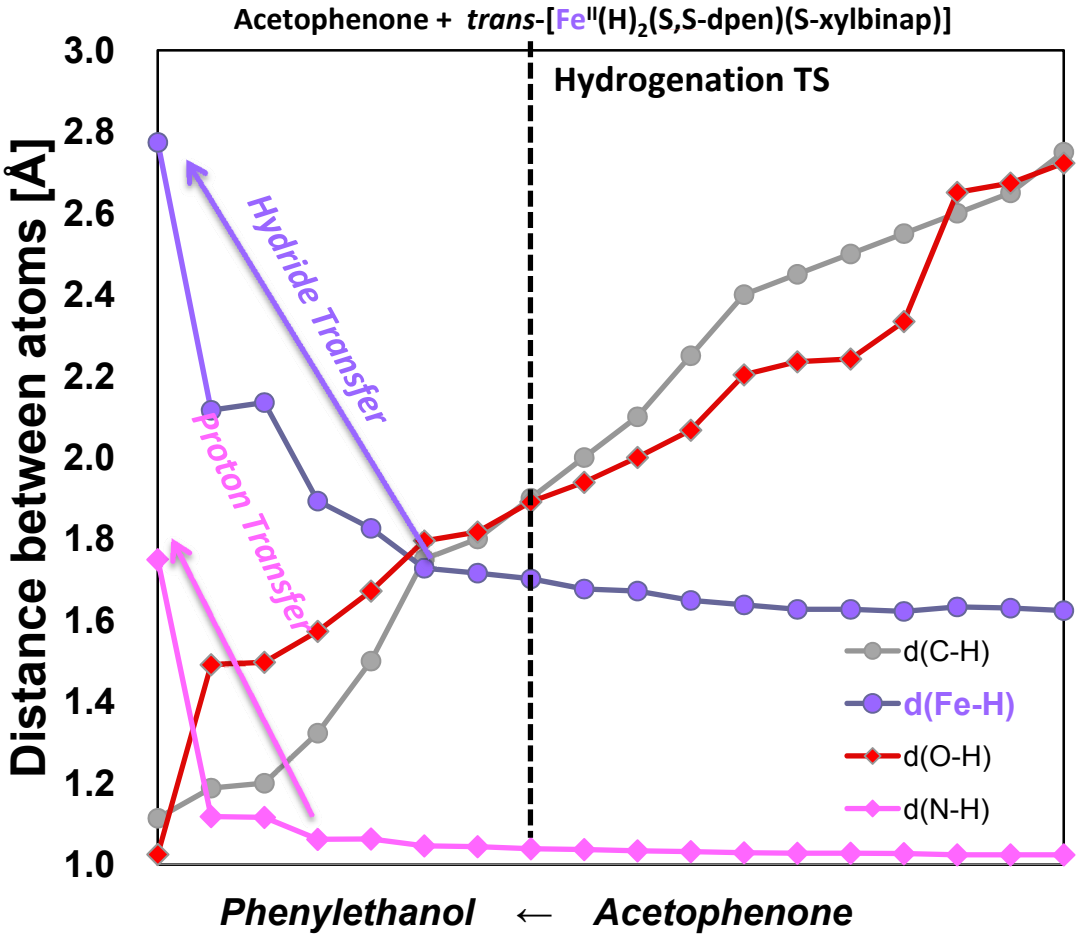

Figure 5.12: The variation of bond lengths of d(carbonyl-hydride), d(iron-hydride), d(oxygen-proton), and d(nitrogen-proton) in the reaction between ACP and *trans*-[Fe(H)$_2${(*S*)-XylBINAP}{(*S*,*S*)-DPEN}].

5.4 Summary and Conclusions

The results of our calculations clearly indicate that both the Fe(II)H_2(diphosphine)(diamine) and Ru(II)H_2(diphosphine)(diamine) complexes are stabilised in the *trans*-conformation with respect to the position of the hydride. Moreover, we find that for both the *trans*-[Fe(II)H_2(diphosphine)(diamine)] and *trans*-[Ru(II)H_2(diphosphine)(diamine)] complexes, the electronic ground states have zero spin, indicating that the FeH_2(diphosphine)(diamine) complexes have similar electronic and structural properties to the highly successful ruthenium Noyori-type catalysts for the hydrogenation of ketones.

The catalytic cycles for the H_2-hydrogenation of acetone *via* the simplified M(II)H_2(PH_3)$_2$(en) catalysts have also been computed. The results show that the activation energy for the hydrogen-transfer and H_2-splitting processes are similar for the two metal complexes, suggesting that the mechanism of the hydrogenation of ketones catalysed by the *trans*-[Fe(II)(H)$_2$(diphosphine)(diamine)] complexes should be the same as the mechanism for the ruthenium system.

As for enantioselectivity, we have constructed the reaction coordinate diagrams associated with the entrance of the acetophenone into the active sites of the *trans*-[Ru(II)H_2{(*S*)-XylBINAP}{(*S*,*S*)-DPEN}] and *trans*-[Fe(II)H_2{(*S*)-XylBINAP}{(*S*,*S*)-DPEN}] catalysts. In both cases, the energy profile associated with the (*R*)-alcohol (Q1) is the most favourable. The enantioselectivity of the iron and ruthenium complexes is related to the occurrence of a similar type of intermediate along the Q1 pathway which fixes the molecular orientation of the acetophenone before the actual hydrogen-transfer process occurs.

We therefore suggest that iron complexes, like the important Ru(II)H_2(diphosphine)(diamine), could be active in the hydrogenation of ketones and could produce enantiomeric excesses similar to those obtained using Noyori-type catalysts.

The work reported in this chapter has been published[106].

Chapter 6 **Imine Reduction Catalysed by Cyclometalated Iridium(III) Complexes**

6.1 Introduction

In imine reduction catalysed by transition-metal complexes, the substrates are usually limited to cyclic imines[107]; thus reductive amination of ketones to produce acyclic ketimines would be desirable. Xiao and co-workers have recently developed a type of air-stable cyclometalated imino iridium(III) complex that can catalyse the transfer hydrogenative reductive amination with safe, inexpensive formate ($HCOO^-$) and without the use of a water scavenger. The system has a high activity and can be applied to a wide range of substrates with different functional groups. The imine is a key intermediate for reductive amination and is formed by the condensation of a ketone and an amine, and then reduced to the final amine product by the catalyst. Experimental evidence shows that different functional groups on this type of iridium catalyst lead to different rates of imine conversion. Transfer hydrogenation in the reduction of imines and its key intermediate process have been less well-studied compared to the reduction of ketones. Investigation of the mechanism of imine reduction is, however, crucial for promoting the development of greener reductive amination reactions.

The catalytic reaction cycle in which we are interested is shown in Scheme 6.1. The first step is the mixing of the precatalyst $[Cp^*IrCl_2]_2$ and the additive (NaOAc) with the ligands consisting of different electron-donating and withdrawing functional groups (shown at the bottom of Scheme 6.1) to form the cyclometalated iridium complex, which then reacts with $HCOO^-$ in the solution to form the iridium hydride. The iridium hydride then transfers its hydride to the 'protonated imine' (iminium) to generate the product (amine) and a $16e^-$ iridium intermediate species. This species then reacts with $HCOO^-$ to regenerate the iridium hydride complex.

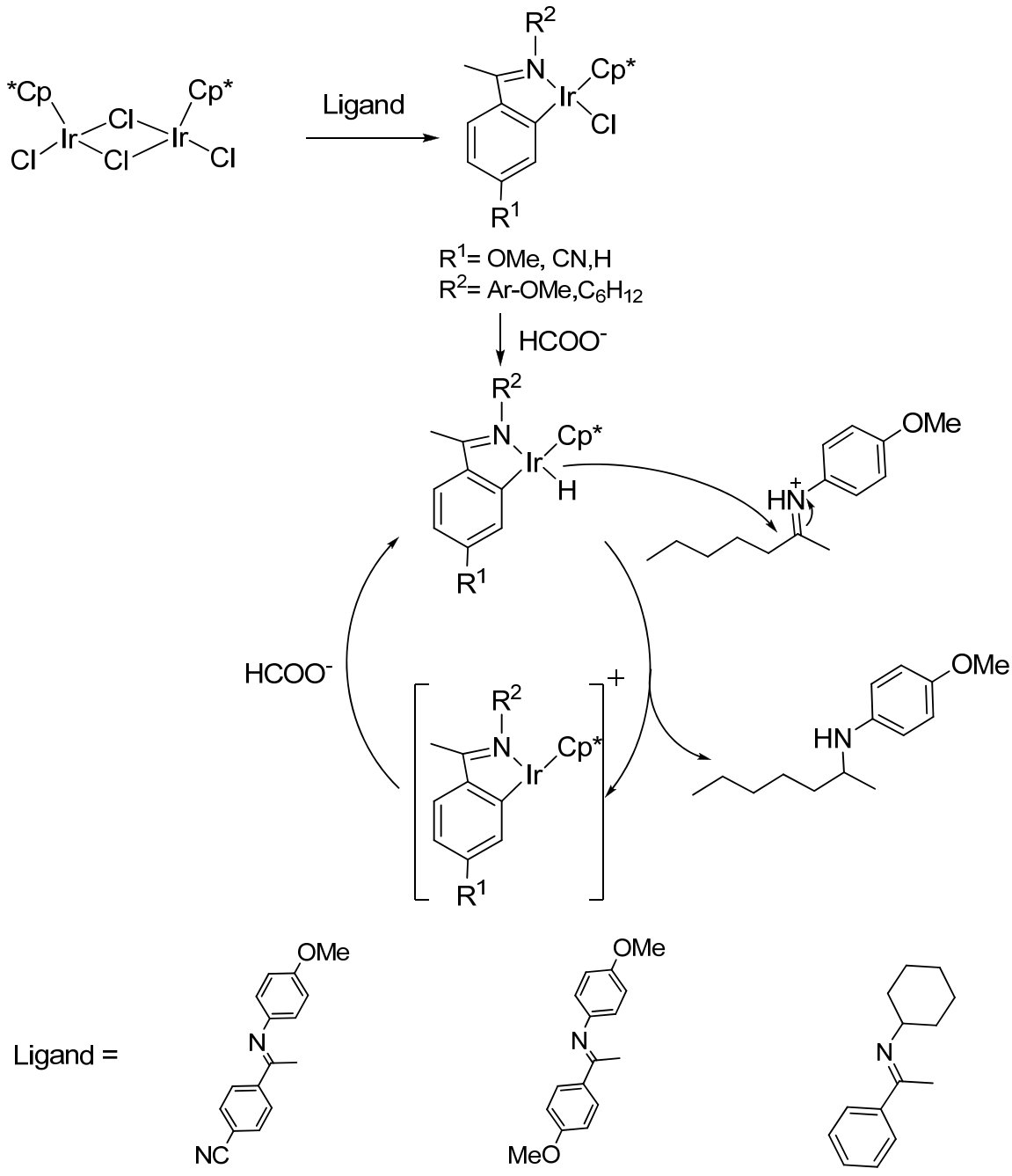

Scheme 6.1: Catalytic cycle for the reduction of imines from the precatalyst ($[Cp^*IrCl_2]_2$) through the reactant (*R*-iminium) to the product (*R*-amine).

One of the challenges of this work is that, as we shall see, in this type of reaction, the system catalysed by the cyclometalated iridium complex with a less negative hydride bonded to the iridium exhibits a higher activity, which is not the expected hydride transfer behaviour. One of the main aims of this study is to clarify this problem. More generally, in this chapter, we aim at gaining a clearer understanding of the mechanism in these reactions using density functional theory (DFT) calculations. In Section 6.2, we report the development of a suitable DFT methodology (exchange-correlation functionals, basis sets, pseudopotentials, closed or open shell configurations and charge analysis) for the investigation of this type of novel reaction by comparing the computed structural properties of the catalysts under investigation with those from X-ray analyses. In Section 6.3.1, we review the effect on the activity of the cyclometalated iridium(III) catalysts with different functional groups from experimental studies. In Section 6.3.2, we compare the molecular orbitals of the isolated catalysts which give different conversions in the imine reduction; we examine the relationship between the HOMO of the catalysts and the LUMO of the iminium. In Section 6.3.3, we focus on the hydride transfer step and try to establish a technique to locate transition state structures using the constrained optimisation method in the DMol^3 code. In Section 6.3.4, we consider both the hydride formation and hydride transfer steps using the synchronous transit-guided quasi-newton (STQN) method in the Gaussian 03 code and nudged elastic band (NEB) method in the CP2K code with and without solvent effects. In order to locate the transition states and understand the reaction mechanisms, two simplified systems **A** and **C,** and one real system **B** were examined. A comparison of the three systems is displayed in Table 6.1.

Table 6.1: A comparison of the three systems **A**, **B** and **C** examined in the imine reduction catalysed by the cyclometalated iridium(III) complexes.

	A (simplified)	**B (real)**	**C (simplified)**
Section	6.3.3.1-2	6.3.3.3	6.3.4
Method of locating TS	CO	CO	STQN & NEB
Reaction	hydride transfer	hydride transfer	hydride formation hydride transfer
Complex	complexes **12–13** 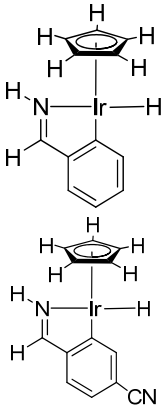	complex **8 – 10** 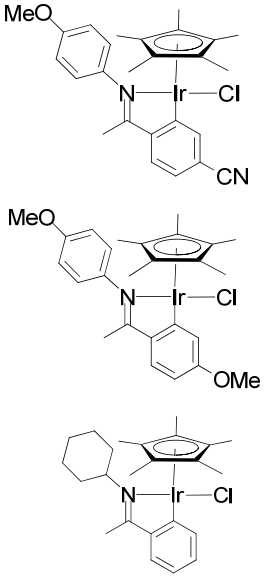	complex **18** 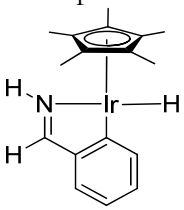
Substrate	iminium **14** 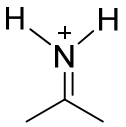	iminium **11** 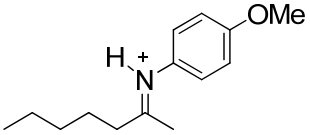 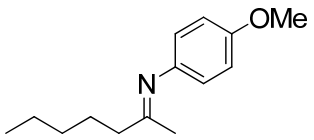	iminium **20** 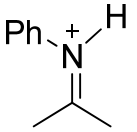 imine **21** 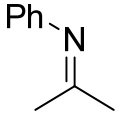
Product	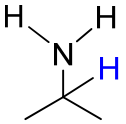	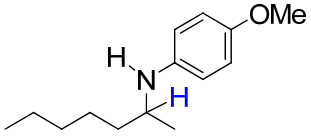	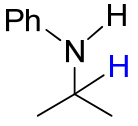

6.2 Methodology

DFT calculations were carried out using the DMol[3], Gaussian 03, and CP2K codes, details of which are given in Chapter 3.

As in the calculations in previous chapters, in DMol[3], the PBE/DNP level of theory and semi-local pseudopotential were applied. Each basis function was restricted to within a cutoff radius of 4.7 Å.

In Gaussian 03, the PBE0, B3LYP and MPW1PW91 hybrid exchange-correlation functionals were employed. We also compared different basis sets — 6-31G(d,p), 6-311G(d,p), 6-31+G(d,p), 6-311+G(d,p), 6-31++G(d,p) and 6-311++G(d,p) — for hydrogen, carbon, nitrogen and oxygen; for iridium, we used the SDD and LANL2DZ basis set coupled with the SDD and LANL2 pseudopotentials respectively. In CP2K, the PBE exchange-correlation functional was employed, together with the TZV2P-MOLOPT-GTH basis set for the hydrogen, carbon, nitrogen and oxygen, and the DZVP-MOLOPT-SR-GTH basis set together with the GTH pseudopotential for the heavier iridium.

We recall that different codes offer different methods to locate transition states. In this study, a constrained optimisation method was employed using DMol[3], the Synchronous Transit-Guided Quasi-Newton (STQN) method was employed using Gaussian 03 and the Nudged Elastic Band (NEB) method was employed using CP2K. The details will be reported in the results section.

Finally, we have also considered solvent effects with the polarisable continuum model (PCM)[97], which provides a simple but useful estimate of solvation energies.

6.2.1 Determination of exchange-correlation functional, basis set and pseudopotential

Since the reaction of imine reduction catalysed by this type of cyclometalated imido complex has not been theoretically investigated before, it is essential to determine the appropriate computational methodology. In the first part, we determine the appropriate exchange-correlation functional, basis set, and pseudopotential for complex **1**. In the following part, we examine the electronic configuration of the simpler complex **2** to

determine if the system adopts the closed or open shell configuration. In the last part, complexes **3**, **4**, **5**, **6** and **7** are examined to determine the charge distributions for systems and establish the relationship between the charge and the hydricity of the iridium-hydride of the complex.

The cyclometalated Ir-Cl complex **1** (Scheme 6.1) was used to select the optimal exchange-correlation functional, basis set and pseudopotential for the investigation of these systems. Table 6.2 gives the bond lengths and angles for the atoms bonded to iridium, and the sum of the deviations from the experimental values. PBE predicts differences of 0.05 – 3.39% for bond lengths and bond angles with respect to the experimental values, whilst BLYP overestimates the values of the structural properties by 0.11 – 6.40%, indicating results computed at the PBE level are closer to the experimental data. The hybrid exchange approximation to density functional theory embodied in the B3LYP, MPW1PW91, and PBE0 functionals exhibits a better agreement with the experimental structure, as shown by the comparison of the sum of the deviations in Table 6.2. The size of the Pople basis set with or without diffuse functions is also considered. In addition, the effective core potentials (ECP) for iridium are of the SDD and LANL2DZ types. Table 6.2 demonstrates that the PBE0 hybrid functional with the SDD/6-31G(d,p) basis sets gives generally a good agreement with X-ray crystallography data in a reasonable execution time. Thus, PBE/DNP with a convergence criterion of 2×10^{-3} Hartree $Å^{-1}$ using DMol^3 and PBE0/SDD (6-31G**) using Gaussian 03 were selected to optimise the geometry and search for the transition states in the following sections.

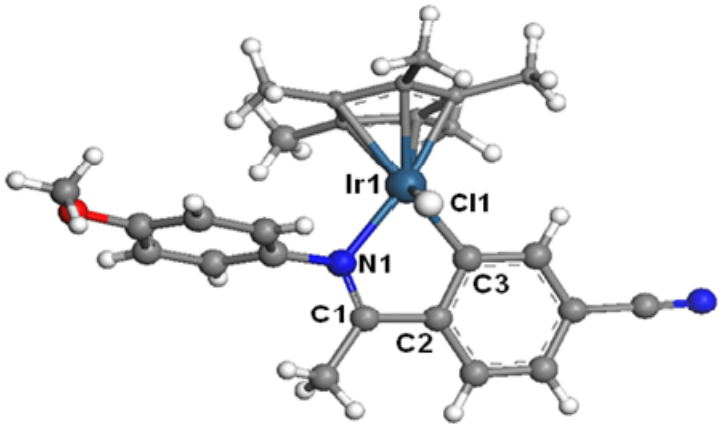

1

Scheme 6.2: Cyclometalated Ir-Cl complex **1**.

6.2.2 Determination of closed or open shell configuration

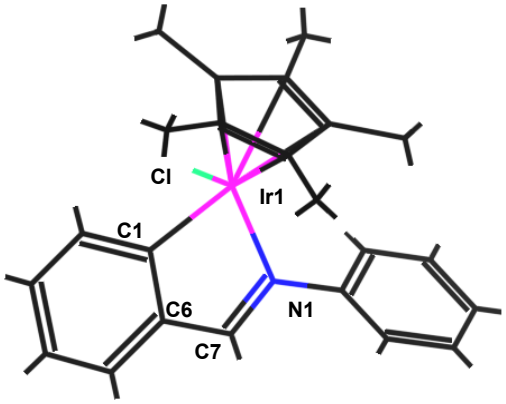

2

Scheme 6.3: Cyclometalated Ir-Cl complex **2**.

Iridium complexes tend to be present in the Ir(I) or Ir(III) oxidation states. Experiments show this type of iridium complex to be Ir(III), which might be expected to have a closed shell configuration. In order to verify this, a slightly simplified Ir-Cl complex **2** was optimised in closed and open shell configurations and the structural properties compared with experimental X-ray data. Table 6.3 shows the comparison between the experimental and computational values of the structural parameters in the closed and open shell configurations, indicating that the computed values in the two configurations are close to the experimental values, but the closed shell Ir(III) is slightly more stable. Exploring both closed and open shell configurations can be very computationally expensive; hence all calculations in the following sections will use the closed shell configuration.

Table 6.2: Structural properties of complex **1** from experimental data and DFT calculations.

	Exp	DMol^3				Gaussian									
XC		**PBE/ E-3**	**PBE/ E-4**	**BLYP/ E-3**	**BLYP/ E-4**	**PBE**	**B3LYP**	**MPW1 PW91**	**MPW1 PW91**	**PBE0**	**PBE0**	**PBE0**	**PBE0**	**PBE0**	**PBE0**
Basis Set		**DNP**	**DNP**	**DNP**	**DNP**	**LANL2DZ/ 6-31G****	**LANL 2DZ/ 6-31G****	**LANL 2DZ/ 6-31G****	**SDD/ 6-31G****	**LANL 2DZ/ 6-31G****	**LANL 2DZ/ 6-31+G****	**LANL 2DZ/ 6-311++G****	**SDD/ 6-31G****	**SDD/ 6-31+G****	**SDD/ 6-311++G****
		Bond Lengths [Å]								**Bond Lengths [Å]**					
Ir1-Cl1	2.40	2.41	2.41	2.45	2.45	2.44	2.46	2.42	2.41	2.42	2.42	2.42	2.41	2.41	2.41
Ir1-C_3	2.02	2.02	2.02	2.04	2.04	2.01	2.02	2.01	2.02	2.01	2.00	2.01	2.01	2.01	2.02
Ir1-N1	2.09	2.09	2.09	2.13	2.13	2.01	2.11	2.08	2.09	2.08	2.08	2.08	2.09	2.09	2.09
C3-C2	1.41	1.43	1.43	1.43	1.43	1.43	1.42	1.42	1.42	1.42	1.42	1.41	1.42	1.42	1.41
$C1_7$-N1	1.31	1.32	1.32	1.32	1.32	1.32	1.31	1.30	1.30	1.30	1.304.	1.30	1.30	1.30	1.30
Ir1-C	2.27	2.34	2.35	2.42	2.42	2.35	2.37	2.31	2.31	2.31	2.31	2.29	2.30	2.30	2.29
(π-ring)	2.16	2.21	2.21	2.26	2.26	2.20	2.21	2.18	2.18	2.18	2.18	2.17	2.18	2.18	2.17
	2.16	2.20	2.20	2.24	2.24	2.18	2.21	2.18	2.18	2.17	2.17	2.16	2.17	2.18	2.17
	2.16	2.21	2.21	2.26	2.26	2.19	2.21	2.17	2.18	2.17	2.17	2.16	2.17	2.18	2.17
	2.28	2.36	2.36	2.43	2.43	2.37	2.38	2.33	2.32	2.32	2.32	2.31	2.32	2.32	2.31
C-N	1.16	1.17	1.17	1.17	1.17	1.18	1.16	1.16	1.16	1.16	1.16	1.16	1.16	1.16	1.16
		Bond Angles [º]								**Bond Angles [º]**					
C1-Ir1-Cl1	86.12	87.63	87.52	88.39	88.16	87.05	87.13	86.45	86.33	86.39	86.24	86.03	86.27	86.32	86.27
Cl1-Ir1-N1	87.39	87.08	87.89	87.49	87.17	86.47	86.46	86.30	86.34	86.34	86.06	85.97	86.38	86.28	86.19
N1-Ir1-Cl1	77.28	77.76	77.77	77.55	77.57	77.94	77.72	77.82	77.59	77.85	77.91	77.63	77.61	77.63	77.45
		Sum of Deviations [%]								**Sum of Deviations [%]**					
		19.33	19.85	36.92	35.47	13.65	20.84	6.6	6.36	5.41	4.66	4.66	5.07	5.28	3.37
		Computing Time/Core [hour]								**Computing Time/Core [hour]**					
		10.47	17.03	10.44	15.05	19.68	33.68	33.68	37.20	29.20	26.0	298.4	37.20	125.6	225.5

- E-3 and E-4 indicate that in the optimisation, the geometry was considered to be converged when the energy change was less than 2×10^{-3} Hartree $Å^{-1}$and 2×10^{-4} Hartree $Å^{-1}$ respectively.

Table 6.3: A comparison of bond lengths and bond angles derived from experimental and computational data of the cyclometalated Ir-Cl complex **2** computed in the closed and open shell configurations.

Complex 2	Exp.	Computed	Diff(%)*	Computed	Diff(%)*
		Closed shell		Open shell	
***Bond length* [Å]**					
Ir-C(1)	2.042	2.031	-0.54	2.016	-1.27
Ir-N(1)	2.088	2.097	0.43	2.080	-0.38
Ir-Cl	2.403	2.411	0.33	2.392	-0.46
C(1)-C(6)	1.412	1.428	1.13	1.414	0.14
C(6)-C(7)	1.433	1.427	-0.42	1.413	-1.40
C(7)-N(1)	1.292	1.312	1.55	1.299	0.54
***Bond angle*[º]**					
C(1)-Ir-N(1)	77.60	78.107	0.65	78.103	0.65
C(1)-Ir-Cl	87.12	88.267	1.32	89.072	2.24
Cl-Ir-N(1)	86.15	88.011	2.16	87.768	1.88
Energy [Hartree]		-1583.42		-1583.40	
ΔE [kcal/mol]		0		8.53	

6.2.3 Hydricity and Charges

One of the motivations of this study is to understand why the iridium catalyst with the less negative hydride exhibits a higher activity. If we assume that the rate-determining step in this catalytic cycle is the hydride transfer, the hydricity of the cyclometalated iridium hydride might be expected to dominate the rate of reaction, although as noted, experiment suggest that the situation is more complex. We are interested in the charge of the hydride because it affects its hydricity. In order to investigate the influence of the functional groups of the catalysts on the iridium hydride, we have examined five cyclometalated imido iridium complexes [Ir-H (**3**), Ir-H-CN (**4**), Ir-H-CN-Me (**5**), Ir-H-OMe (**6**) and Ir-H-OMe-Me (**7**)]

with electron-donating –Me (–CH_3) and –OMe, and electron-withdrawing –CN^- groups by computing Hirshfeld[108] and Electro-Static Potential (ESP)[109] charges. Hirshfeld[108] uses integration of the atomic deformation densities which defines net atomic charges and multipole moments that describe the molecular charge reorganisation. It can be used to calculate the external electrostatic potential and the interaction energy between molecules or within a molecule. ESP[109] is an approach to determine atomic multipole properties by fitting Gaussian functions to reproduce the molecular electrostatic potential.

From Table 6.4, we note that the bond lengths and bond angles among the five catalysts with different functional groups only vary slightly. In addition, the charge on the hydride of **4** and **5** becomes more positive with respect to the charge on the hydride of **3**, as computed in terms of their Hirshfeld[108] and ESP[109] charges, due to the –CN^- group which is electron-withdrawing. If we consider the relationship between **4** and **5**, we note that the charge on the hydride is more negative in **5**, which is due to the –Me group donating electron density to the hydride. However, for **6** and **7**, the charges on the hydride in both of these complexes have become more negative in comparison with the charge on the hydride of **3**, owing to the presence of –OMe, which is a strong electron-donating group. The hydride in **7** is more negative than the hydride in **6** which is caused by the addition of a –Me group in **7**.

In conclusion, by computing the Hirshfeld and ESP charges, a clear charge variation on the iridium hydride is observed when placing electron-withdrawing and donating functional groups on the iridium catalyst. We therefore expect that Hirshfeld and ESP can be reliably used to establish a relationship between hydricity and charge distribution in real systems.

Table 6.4: A comparison of the bond lengths, bond angles and charges of iridium-hydride of the five cyclometalated iridium complexes with different functional groups.

		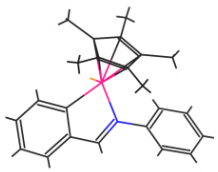 **3**	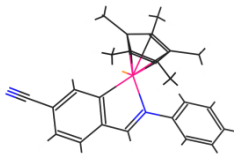 **4**	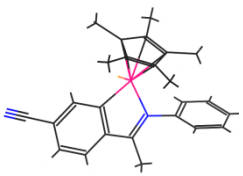 **5**	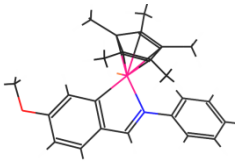 **6**	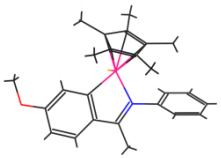 **7**
		Ir-H	**Ir-H-CN**	**Ir-H-CN-Me**	**Ir-H-OMe**	**Ir-H-OMe-Me**
Bond Length [Å]	**Ir-C(1)**	2.022	2.018	2.016	2.021	2.017
	Ir-N(1)	2.077	2.070	2.070	2.088	2.078
	Ir-H(1)	1.602	1.601	1.601	1.600	1.601
	C(1)-C(6)	1.434	1.434	1.432	1.433	1.433
	C(6)-C(7)	1.421	1.422	1.440	1.417	1.436
	C(7)-N(1)	1.321	1.322	1.326	1.322	1.328
Bond Angle [°]	**C(1)-M-N(1)**	78.150	78.039	77.560	78.281	77.678
	C(1)-M-H(1)	81.020	81.650	81.039	81.954	81.373
	H(1)-M-N(1)	85.294	85.503	85.142	86.039	83.926
Charge	**Hirshfeld**	-0.0622	-0.0585	-0.0604	-0.0661	-0.0665
	ESP	-0.857	-0.769	-0.798	-0.973	-0.976

6.3 Results

6.3.1 The influence of different functional groups on the activity of cyclometalated Iridium(III) catalysts

The impact of adding electron-withdrawing or donating functional groups on the reactivity of the cyclometalated catalyst in the imine reduction has been investigated in Prof. Xiao's group at the University of Liverpool using three cyclometalated iridium complexes **8**, **9**, and **10**[1b]. Interestingly, different rate constants and conversions are observed in Table 6.5. It is clear that different functional groups have an effect on the conversion percentage, e.g., **8** with $-CN^-$ gives a much higher rate constant (6.7 s^{-1}) and conversion (98%); **9** with –OME gives 4.6 s^{-1} and 74%; **10** gives 1.4 s^{-1} and 24%. Hence, we can deduce that complexes with groups making the hydride more electron-deficient such as $-CN^-$ will have a higher activity than those with groups that make the hydride more electron-rich, that is, complexes containing groups such as –OMe. We therefore conclude that the charge on the hydride influences the conversion of the imine reduction catalysed by the cyclometalated Ir-H complexes. However, this result confounds the expectation that the more negative hydride would result in a higher activity. One of our main challenges is to explain this observation; first, however, we compare the structural properties from experimental and computational data using the parameters obtained from Section 6.2.

6.3.2 Structural, charge, and molecular orbital properties of cyclometalated iridium catalysts with different functional groups

We now consider the imine reduction catalysed by complexes **8**, **9** and **10** in detail, using the computational parameters and techniques established and tested using complexes **1** to **7** in Section 6.2. We firstly compare the structural properties of **8** and **9** from experimental and computational results; secondly we compute the charges on the iridium hydride of catalysts **8**, **9** and **10**; thirdly, we analyse the properties of their molecular orbitals.

Table 6.5: Cyclometalated iridium complexes **8**, **9** and **10** used in the reduction of the aliphatic ketimine with their rate constants (*k*) [s^{-1}].

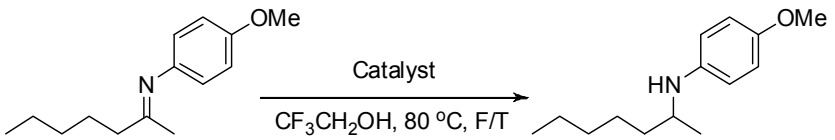

Complex	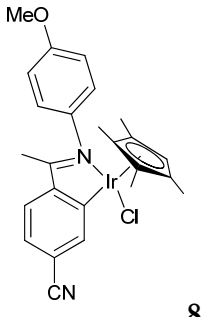 **8**	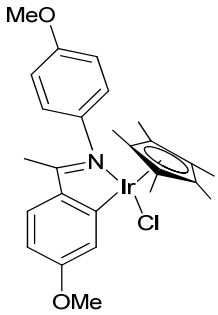 **9**	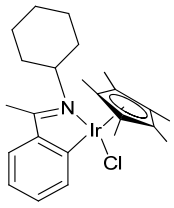 **10**
rate constant (*k*) [s^{-1}]	6.7	4.6	1.4

The structural properties of the catalysts computed at different levels of theory (complexes **8** and **9**), compared with those obtained from experiment before computing their energies, are shown in Scheme 6.4 and Table 6.5. Table 6.5 shows that for both complexes **8** and **9**, the differences between computational and experimental bond lengths and angles are within 2%, indicating our computational settings are reasonable. Furthermore, we can relate the reaction rate with the charge on the hydride, although as noted, the correlation is initially counter-intuitive.

Catalyst **8**, containing $–CN^–$, has a less negative charge (–0.48) on the hydride in comparison with those on **9** (–0.70) and **10** (–0.97). (Their rate constants (*k*) are 6.7, 4.6, and 1.4 s^{-1} respectively in Table 6.5.) Therefore, we can deduce that the catalysts with groups making the hydride more electron-deficient, such as $–CN^–$, will have a higher activity than those with an electron-rich hydride, containing groups such as –OMe. This

computational result is in agreement with the experimental result; the charge on the hydride influences the conversion of this type of catalysis, but in a way that confounds the expectation that the more negative hydride would render a higher conversion. In order to explain this finding, we will consider an analysis of the molecular orbitals of complexes **8**, **9** and **10** in the following section.

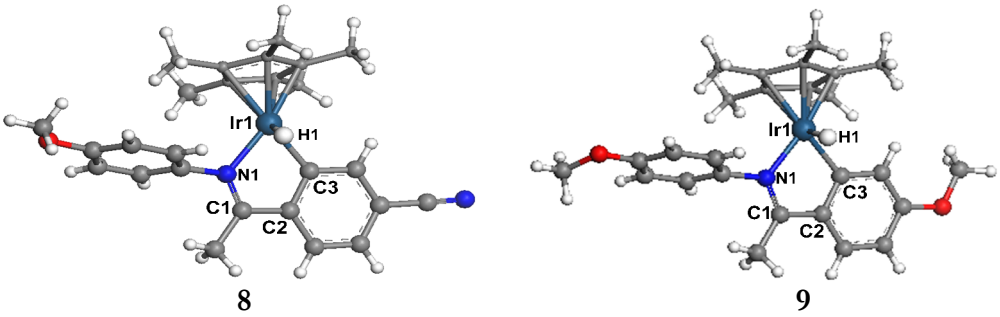

Scheme 6.4: Cyclometalated Ir-H complexes **8** and **9** with labels.

Table 6.6: Structural properties of complexes **8** and **9** from experimental data and DFT calculations. The units are [Å] for bond length and [º] for bond angles.

Catalyst	**8**	**9**	**8**	**9**	**8**	**8**	**9**	**9**
Code	**Exp**	**Exp**	**DMol**	**DMol**	**G03**	**G03**	**G03**	**G03**
XC			**PBE**	**PBE**	**PBE0**	**PBE0**	**PBE0**	**PBE0**
Basis Set	**1**	**2**	**DNP**	**DNP**	**LANL2DZ/ 6-31G****	**SDD/ 6-31G****	**LANL2DZ/ 6-31G****	**SDD/ 6-31G****
Ir_1-N_1	2.09	2.03	2.07	2.08	2.06	2.07	2.06	2.07
Ir_1-H_1	1.75	1.71	1.60	1.60	1.59	1.59	1.59	1.59
Ir_1-C_3	2.04	2.05	2.02	2.02	2.00	2.01	2.00	2.01
N_1-C_1	1.31	1.32	1.33	1.33	1.31	1.31	1.31	1.31
C_2-C_3	1.47	1.44	1.44	1.44	1.44	1.44	1.44	1.44
Ir_1-C	2.26	2.27	2.29	2.29	2.26	2.25	2.26	2.26
(π-ring)	2.29	2.26	2.35	2.35	2.31	2.31	2.31	2.31
[Å]	2.27	2.25	2.33	2.33	2.30	2.30	2.30	2.30
	2.26	2.23	2.27	2.27	2.25	2.25	2.26	2.26
[º]	2.21	2.17	2.22	2.22	2.19	2.19	2.19	2.19
N_1-Ir_1-H_1	81.32	88.77	85.71	85.02	85.04	85.14	84.87	84.95
H_1-Ir_1-C_2	87.10	86.45	81.61	80.45	81.30	81.26	81.37	81.23
C_3-Ir_1-N_1	76.63	77.66	77.65	77.90	77.75	77.56	77.97	77.79

Let us first consider the shape of the molecular orbitals in the vicinity of the hydride as indicated by the arrows in Figure 6.1 which compares the HOMO energy diagrams of catalysts **8** and **9** respectively. We note that the electron density of the two complexes is mainly concentrated around the iridium metal centre. When focusing only on the orbital shapes of the iridium hydride of the two complexes, we find that the HOMOs around the hydride of **8** and **9** are almost indistinguishable. Turning to the LUMO energy diagrams of catalysts **8** and **9** shown in Figure 6.2, we note that the electron density around the iridium hydride decreases, which implies that the electrons transferring to the imine are mainly from the hydride — this is consistent with experimental results. In addition, we note that the LUMO around the hydride of **8** is slightly larger than that of **9**.

We next investigate the interaction of frontier molecular orbitals between the substrate, aliphatic ketimine **11** and catalysts **8**, **9** and **10**. The HOMO of the catalyst interacts with the LUMO of the aliphatic ketimine. Table 6.7 shows that the HOMO of **8** (–4.64 eV) is closer to the LUMO of the substrate (–7.51eV) than that of the other two systems (–4.27 eV for **9** and –4.13 eV for **10**), suggesting **8** would react with the ketimine more easily than would the other two catalysts. Our next step is to locate the transition states in this reaction.

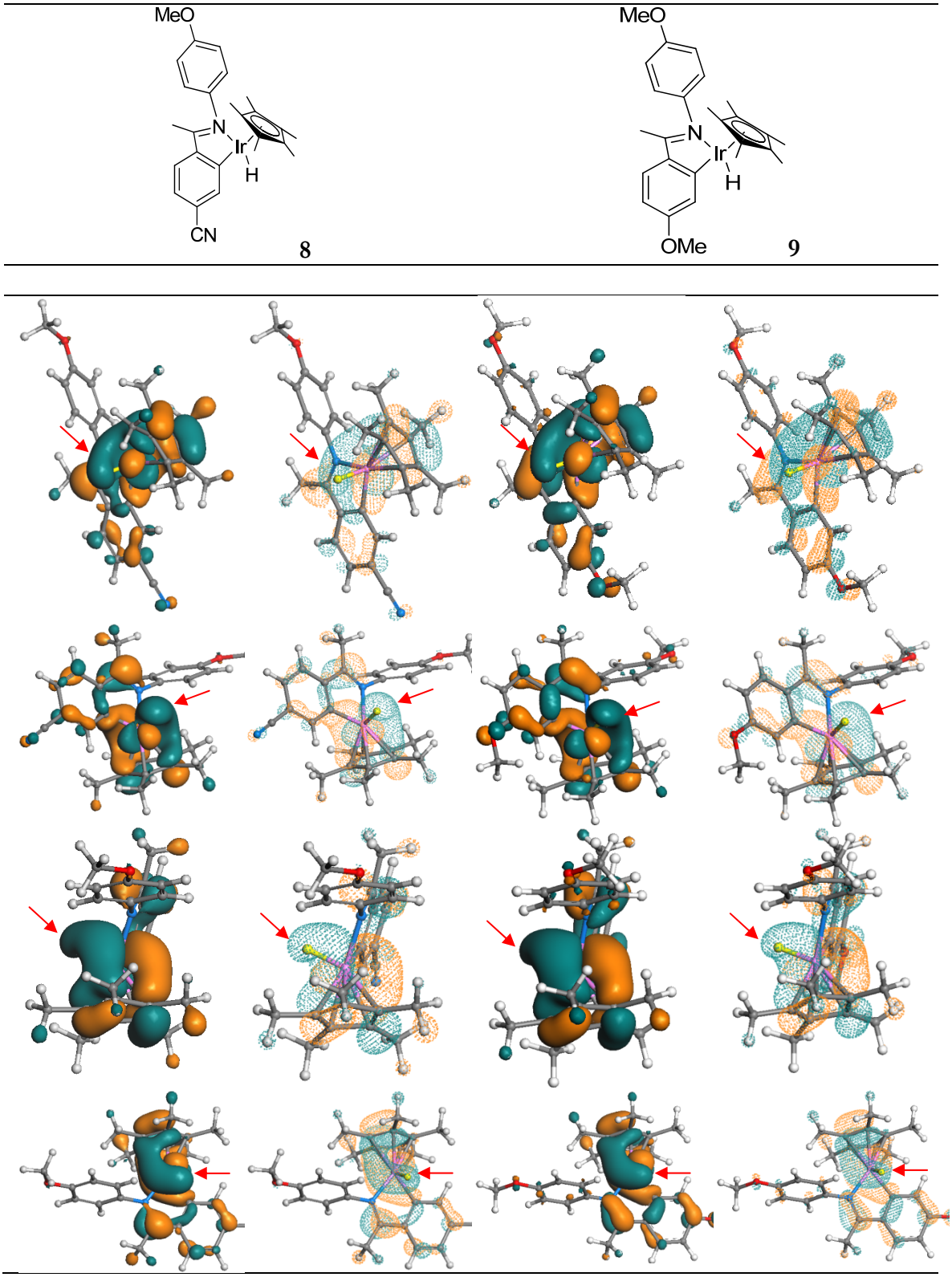

Figure 6.1: A comparison of HOMO energy diagrams of catalysts **8** and **9** in four orientations. (HOMOs are represented by solid and dash dot lines — to show the structure beneath; the hydrides are indicated by arrows.)

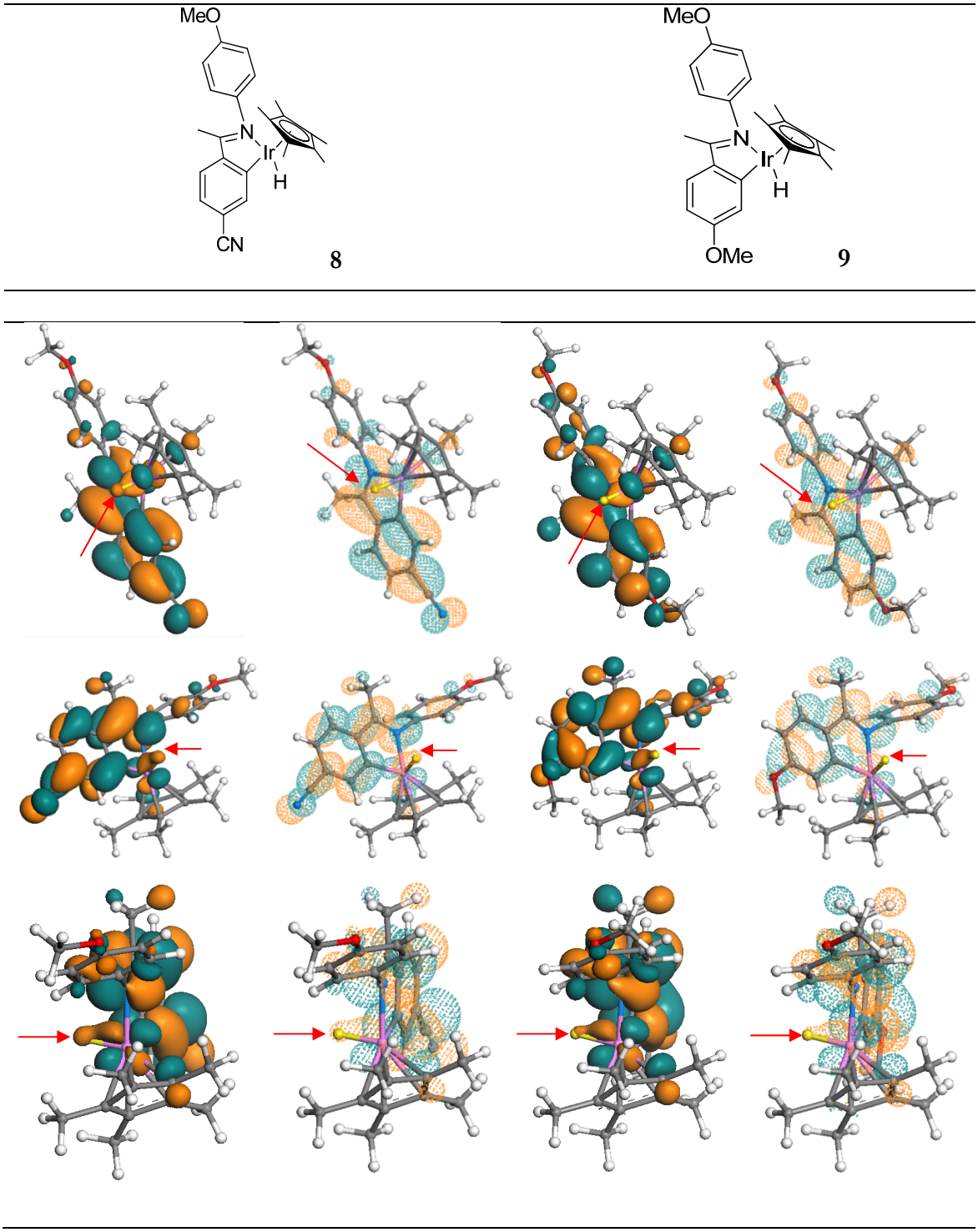

Figure 6.2: A comparison of LUMO energy diagrams of catalysts **8** and **9** in four orientations. (LUMOs are represented by solid and dash dot lines — to show the structure beneath; the hydrides are indicated by arrows.)

Table 6.7: HOMO-LUMO energies of the catalysts **8**, **9** and **10**, and substrate **11**.

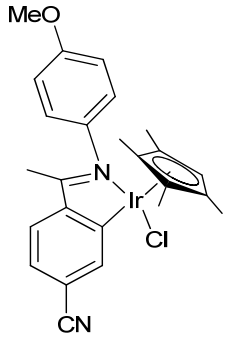

8

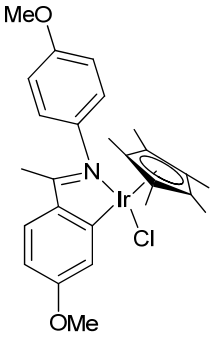

9

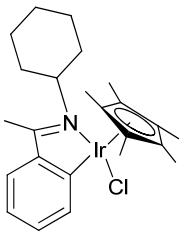

10

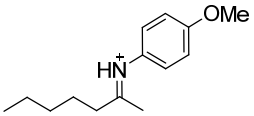

11

Charge on Ir-H	-0.48	-0.70	-0.97	
HOMO [eV]	-4.64	-4.27	-4.13	-9.11
LUMO [eV]	-2.64	-1.99	-1.82	-7.51
Conversion [%]	97	74	24	

6.3.3 Locating the transition state in the hydride transfer step using the constrained optimisation method in systems A1, A2 and B

Our first attempt at locating the transition states in this novel catalysis follows the constrained optimisation (CO) method as in Chapters 4 and 5. In this section, we discuss the search for the transition state structures and activation energies associated with the transfer of the hydride on the cyclometalated iridium complex to the carbon of the imine or iminium. As the reaction condition is acidic, it is reasonable to assume that the actual substrate is the protonated imine (iminium). Simplified systems **A1** and **A2** and one real system **B** (Figure 6.3) have been investigated by using the constrained optimisation method. Before considering the calculation of the transition states, the most stable intermediates are examined.

6.3.3.1 Geometry optimisation of simplified systems A1 and A2

In order to develop the technique of locating the transition state structure, we simplified the real system **B** to systems **A1** and **A2** as shown in Figure 6.3. For the catalyst, the phenyl group of **8** (in system **B**) is replaced by a hydrogen atom; the methyl groups of Cp* of **8** (in system **B**) are replaced by hydrogen atoms to become **12** (in system **A1**) and **13** (in system **A2**) with a cyanide group. For iminium, the aliphatic iminium **11** (in system **B**) is replaced by the simpler aromatic imimium **14** (in systems **A1** and **A2**).

To optimise the geometries of the simplified systems **A1** [**14** + **12**] and **A2** [**14** + **13**], we initialised the configuration of the iridium catalyst and iminium with a pseudo coordinate (Ir-)H···C(-N) distance of 9 Å and computed their energies whilst reducing this reaction coordinate. The only difference between systems **A1** and **A2** is that in system **A1**, there is no $-CN^-$ on catalyst **12**, but in system **A2**, there is one $-CN^-$ on catalyst **13**; this has been considered in order to determine the influence on the hydride transfer activation energy with the addition of one electron-withdrawing group on the catalyst. In the simplified systems **A1** and **A2**, we found that when we shortened the (Ir-)H···C(-N) distance to *ca.* 4 Å, the system started to converge and form two stable intermediates with different orientations (**I**) and (**II**). In Figure 6.3, the energies of orientation (**I**) in system **A1** and orientation (**I**) in system **A2** are both only 0.015 kcal/mol higher than those of

orientation (**II**) in system **A1** and **o**rientation (**II**) in system **A2** respectively. Because of this minor difference, it is necessary to see if the same transition state will result from the two intermediates with different orientations. The four stable intermediates, **A1(I)**, **A1(II)**, **A2(I)** and **A2(II)** — as shown in Figure 6.3, with orientations (**I**) and (**II**) in systems **A1** and **A2** — are regarded as initial structures in the search for the transition states. This is considered in the next section.

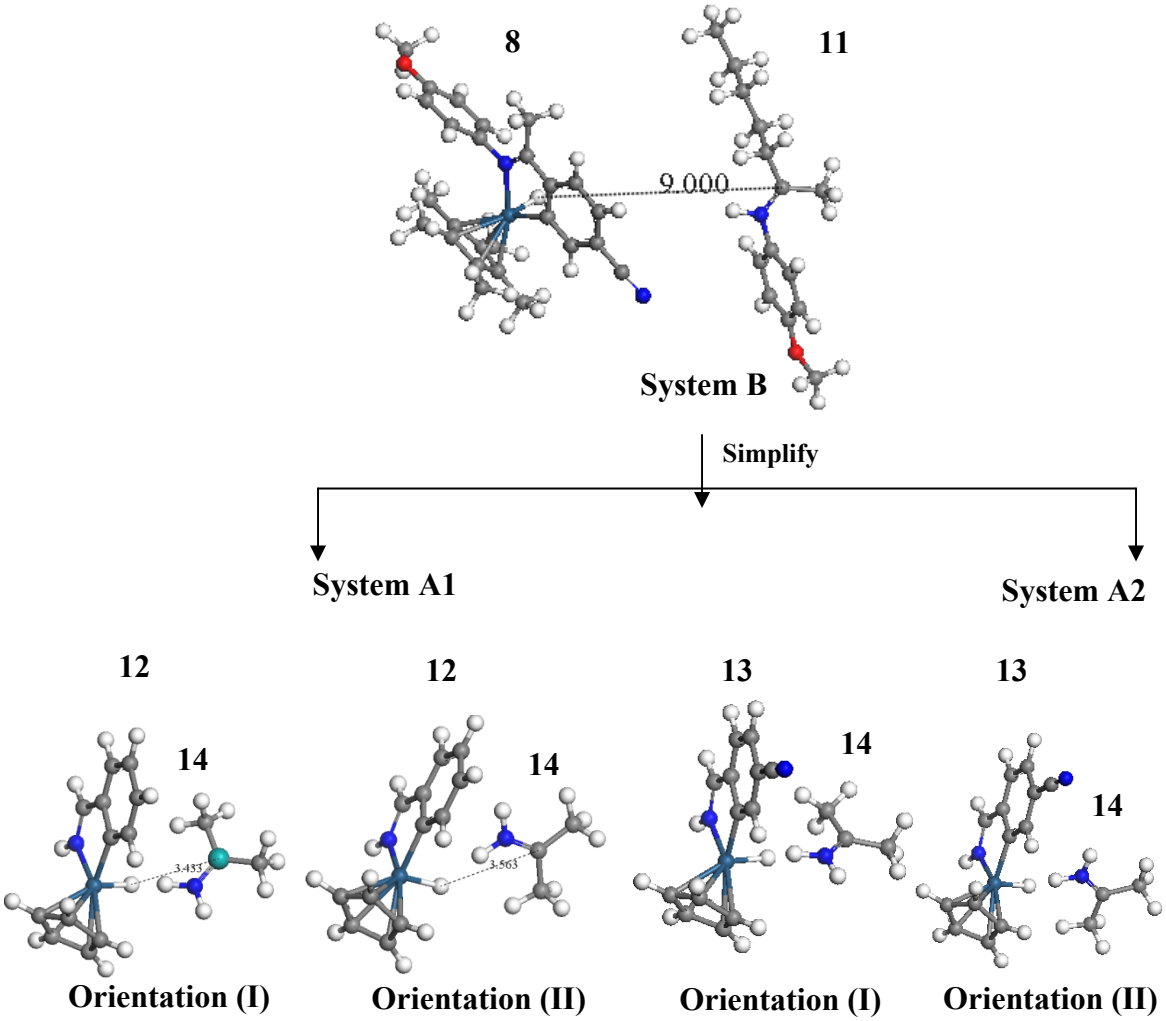

Figure 6.3: Above: real catalytic system **B**. Below: Two stable intermediates with two orientations (**I**) and (**II**) in simplified systems **A1** (without $-CN^-$) and **A2** (with $-CN^-$).

6.3.3.2 Locating the transition state for systems A1 and A2

In this section, the transition state structures are searched by gradually reducing the pseudo coordinate (Ir-)H···C(-N) from 4 Å to 1.1 Å using the constrained optimisation method *via* the DMol^3 code. The reaction coordinate diagram is plotted in Figure 6.4. It shows that the first peaks occurring in **A1(I)** and **A1(II)** are at 2.31 Å whilst those occurring in **A2(I)** and **A2(II)** are at 2.42 Å. We note that the energy variation in **A1(I)** is similar to that in **A1(II)**, and the energy variation in **A2(I)** is similar to that in **A2(II)**. Furthermore, the energy barriers in **A2(I)** and **A2(II)** are both 0.1 kcal/mol higher than those in **A1(I)** and **A1(II)**.

The structural changes on reducing the (Ir-)H···C(-N) distance from 3.5 Å to 1.2 Å in systems **A1(I)** and **A1(II)** are shown in Figure 6.4, which reveals that there is no obvious structural change between the two routes from intermediates with different orientations (**I**) and (**II**). Their final structures are the same, stabilised by the formation of an Ir-N bond, but they do not produce an amine.

In conclusion, these results indicate that initial intermediates with different orientations do not affect the reaction coordinate diagram. In addition, reducing the pseudo reaction coordinate (Ir-)H···C(-N) distance from 3.5 to 1.2 Å in systems does not result in a significant energy difference between **A1** (without $-CN^-$) and **A2** (with $-CN^-$). Most importantly, we did not obtain the expected amine product from this reaction, and the peak observed might not be the transition state, indicating this may not be an appropriate simplified system; we will therefore construct another, slightly larger simplified system **C** in Section 6.3.4. Furthermore, the result reveals that the system starts to converge when the (Ir-)H···C(-N) distance is shorter than 4 Å. In the next section, we will probe the hydride transfer by turning to the real catalysts **8** and **10** using the same constrained optimisation technique to search for the transition state but only investigating an (Ir-)H···C(-N) distance of < 4 Å.

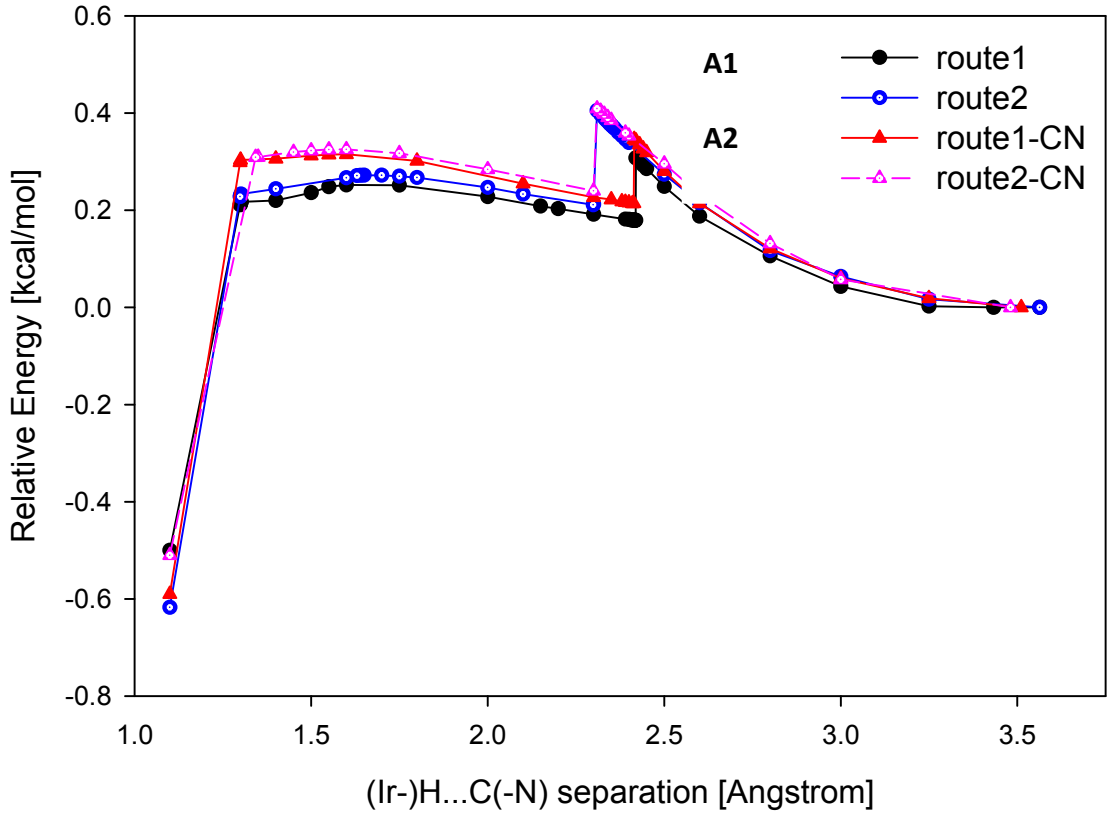

Figure 6.4: Reaction coordinate diagram for the iminium reduction catalysed by the cyclometalated catalysts **12** and **13** whilst reducing the (Ir-)H···C(-N) distance from different intermediates, with orientation s(**I**) and (**II**), in systems **A1** (without $-CN^-$) and **A2** (with $-CN^-$).

(Ir-)H···C(-N) **[Å]**	**A1(I)**	(Ir-)H···C(-N) **[Å]**	**A1(II)**
3.43	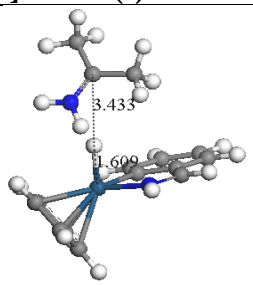	3.56	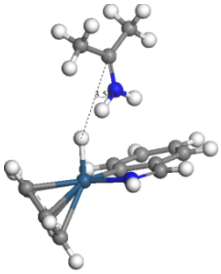
2.42 (1st Peak)	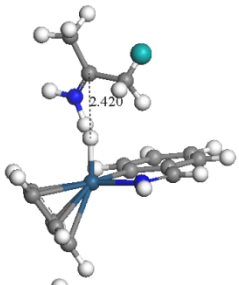	2.31 (1st Peak)	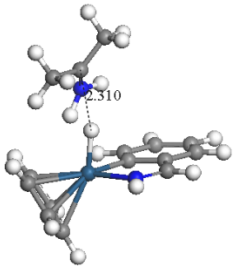
2.42	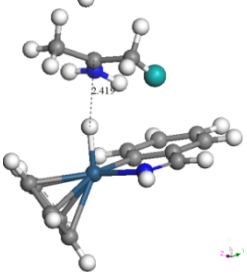	2.30	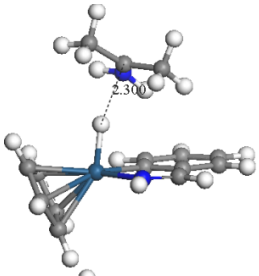
1.60 (2nd little Peak)	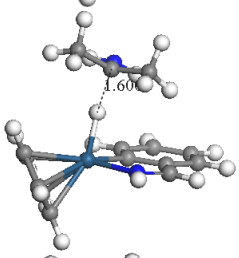	1.65 (2nd little Peak)	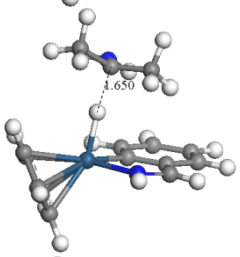
1.30	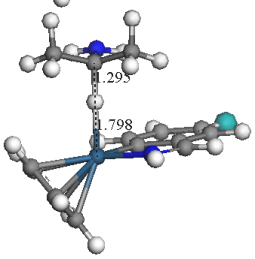	1.30	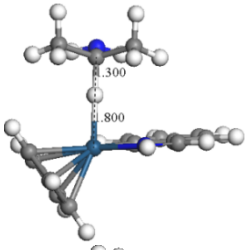
Ir-N=2.16	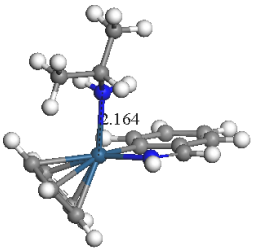	Ir-N=2.16	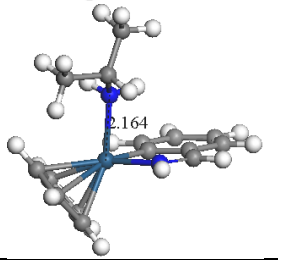

Figure 6.5: Structural changes whilst reducing the (Ir-)H···C(-N) distance from 3.5 Å to 1.2 Å in systems **A1(I)** and **A1(II)**.

6.3.3.3 Locating the transition state for real system B

According to Section 6.3.3.1, there might be more than one stable intermediate. For system **B**, we first established four possible initial configurations of complex **8** with respect to iminium **11** (Figure 6.6) in order to determine which one would be the most stable intermediate. We fixed the orientation of complex **8** and rotated iminium **11** (which gives Initial Configuration **I**), and obtained Initial Configuration **II** by rotating iminium 11 through 180º. Initial Configurations **III** and **IV** were obtained by rotating **11** anti-clockwise 90º and clockwise 90º respectively. Figure 6.7 shows that the most stable intermediate is obtained from Initial Configuration **I**, revealing that the most stable catalysts **8** and **10** are constructed when their (Ir-)H···C(-N) distances are at 3.38 Å and 3.4 Å. Using the same constrained optimisation method as for the previous simplified systems **A1** and **A2**, we optimised the initial structure of system **B.** (The hydrogen of either iridium complex **8** or complex **10** is placed at 4 Å from the carbon of iminium **11**.) However, the calculated activation energies E_a in the iminium reduction catalysed by complexes **8** and **10** are 0.45 kcal/mol and 0.46 kcal/mol; thus we cannot relate the activation energy to the electron-donating/withdrawing power of the functional groups.

We must now consider whether the rate-determining step might not be the hydride transfer step but is instead the hydride formation step. We note that the constrained optimisation method might not be appropriate to locate the transition state in this type of reaction. Our next step is to modify these simplified systems and probe the transition state in the hydride formation step to understand which is the rate-determining step in the whole catalytic cycle by applying the STQN and NEB methods, discussed in Chapter 3.

Initial Configuration I	**Initial Configuration II**
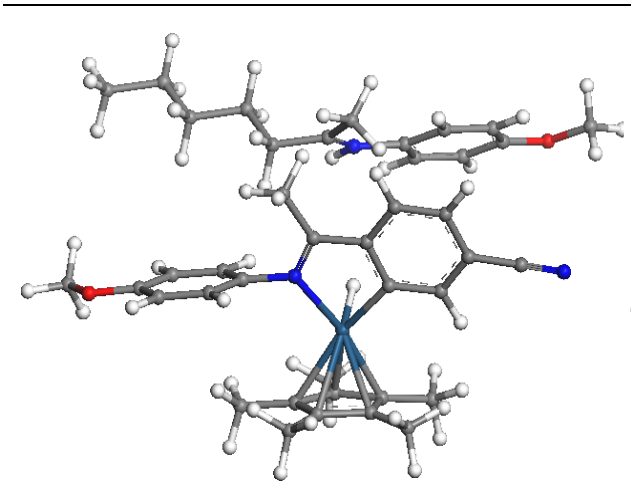	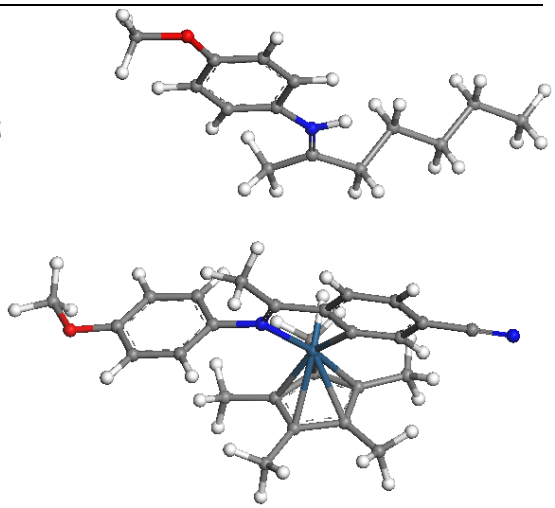
Initial Configuration III	**Initial Configuration IV**
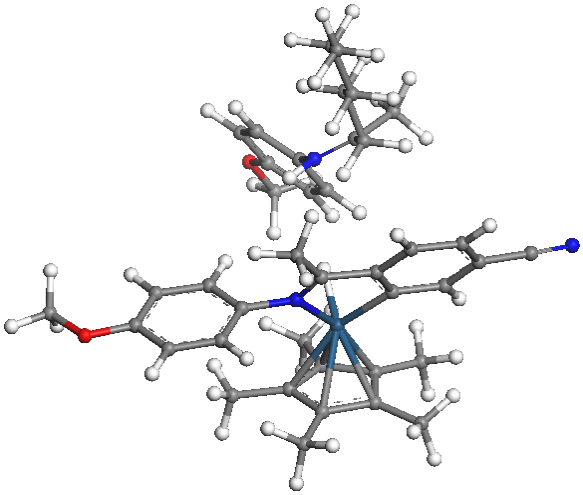	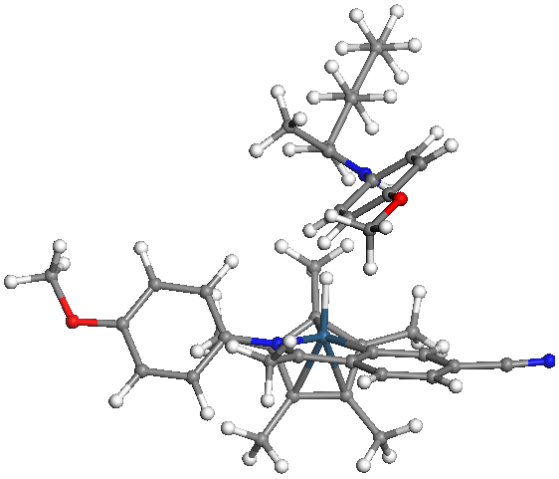

Figure 6.6: Four conjectures for Initial Configurations **I**, **II**, **III** and **IV** of complex **8** with respect to iminium **11** in the real iridium catalytic system **B**.

Optimised Catalysis System (Intermediate) with complex **8**

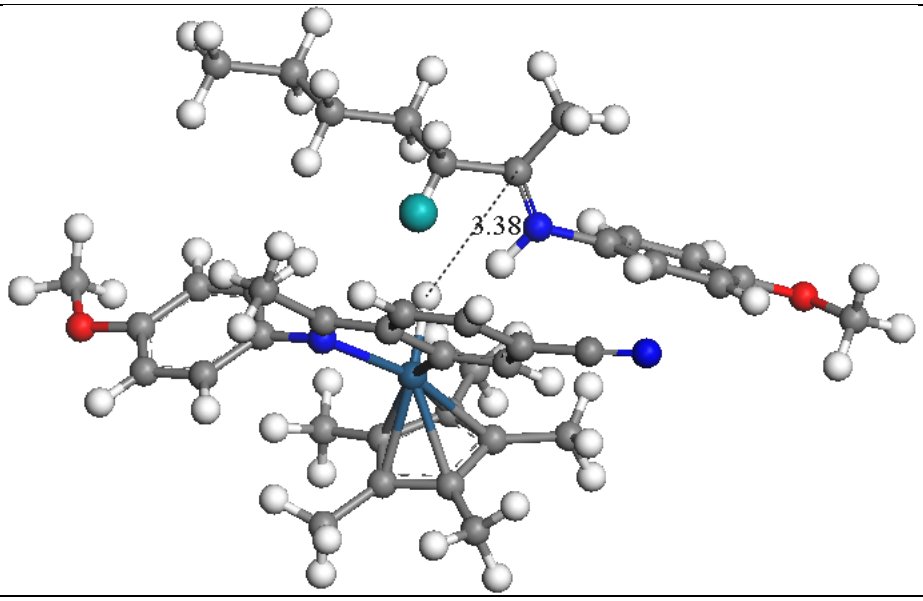

Optimised Catalysis System (Intermediate) with complex **10**

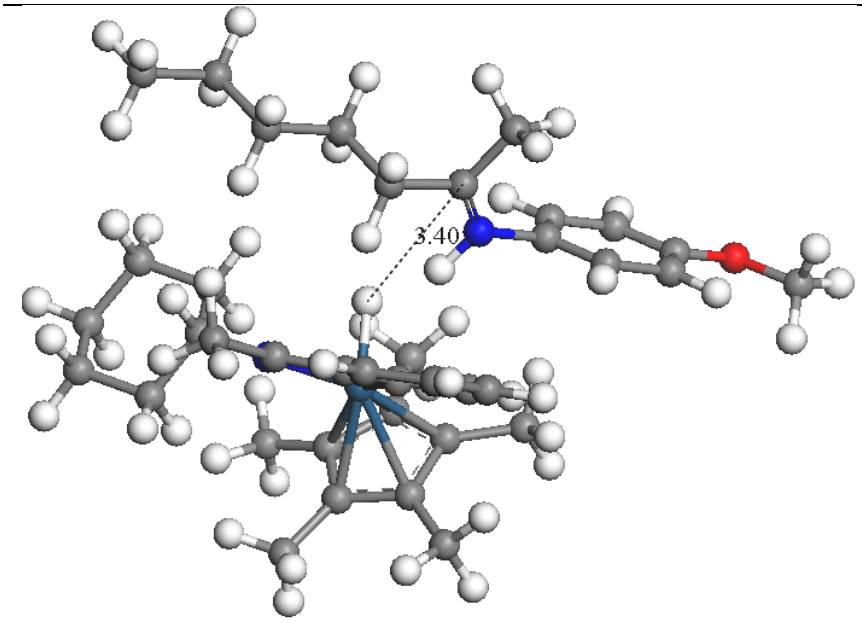

Figure 6.7: Structures of the most stable intermediate in system **B** using complexes **8** and **10**.

6.3.4 Locating the transition state for the simplified system C by the STQN and NEB methods

Since the CO method used in Section 6.3.3 did not locate the expected transition state, in this section we turn to the STQN and NEB methods. We only considered the hydride transfer step in Section 6.3.3, whereas here we begin to include the hydride formation step. The simplified system **A** in Sections 6.3.3.1 and 6.3.3.2 did not yield the results we expected, perhaps because the system was too simple. Regarding the substrate, we assume that the aromatic group bonded to the nitrogen would play an important role in this reaction and thus now replace some of the hydrogen atoms in system **A** by methyl groups to create another simplified system **C** in order to investigate the possible reaction pathways associated with the reaction, but not the effect of the ligands on the activity of the catalyst. The five hydrogen atoms of the Cp* of complexes **12** and **13** in systems **A1** and **A2** are replaced by the five methyl groups to become complex **18**; the hydrogen of iminium **14** in systems **A1** and **A2** are replaced by the phenyl group to become iminium **20**. The complete catalytic cycle is illustrated in

Scheme **6.5**. Firstly, the chloride in **15** is replaced by the formate to form **16**. The subsequent step is hydride formation from **16** to **18** *via* a transition state **17**. Next, this iridium hydride complex **18** reacts with iminium **20** to form **16** and product **22** through a transition state **19**, which is the hydride transfer step. Using system **C**, we first calculated the activation energies in the hydride formation step.

6.3.4.1 Locating the transition state for the hydride formation

The mechanism of formation of hydrides from the cyclometalated iridium formate complexes has never been reported. In collaboration with the group of Prof. Xiao, we have suggested three possible reaction mechanisms for the hydride formation (HF) step, starting from complex **16** to form complex **18** plus one CO_2 molecule *via* a transition state **17**, which are sketched in Scheme 6.6. The following three pathways are associated with the formation of the transition state.

Pathway HF-I: The iridium is assumed always to be five coordinated. The ion pair is formed from the dissociated formate and the cationic iridium: the iridium is concurrently bonded with the oxygen and hydrogen atoms of the formate.

Pathway HF-II: A free coordination site on the iridium is created by changing the hapticity of the Cp* group from η5 to η3 *via* the "ring slippage" mechanism. When a coordinate site on the iridium is available, the iridium is able to interact with the oxygen and hydrogen atoms simultaneously to form the active Ir-H complex **18** and CO_2.

Pathway HF-III: The breakage of the iridium-nitrogen bond offers coordination space for the iridium to react with the hydrogen of the formate and form the Ir-H complex **18** and CO_2.

The results from the calculations on these HF pathways are discussed below.

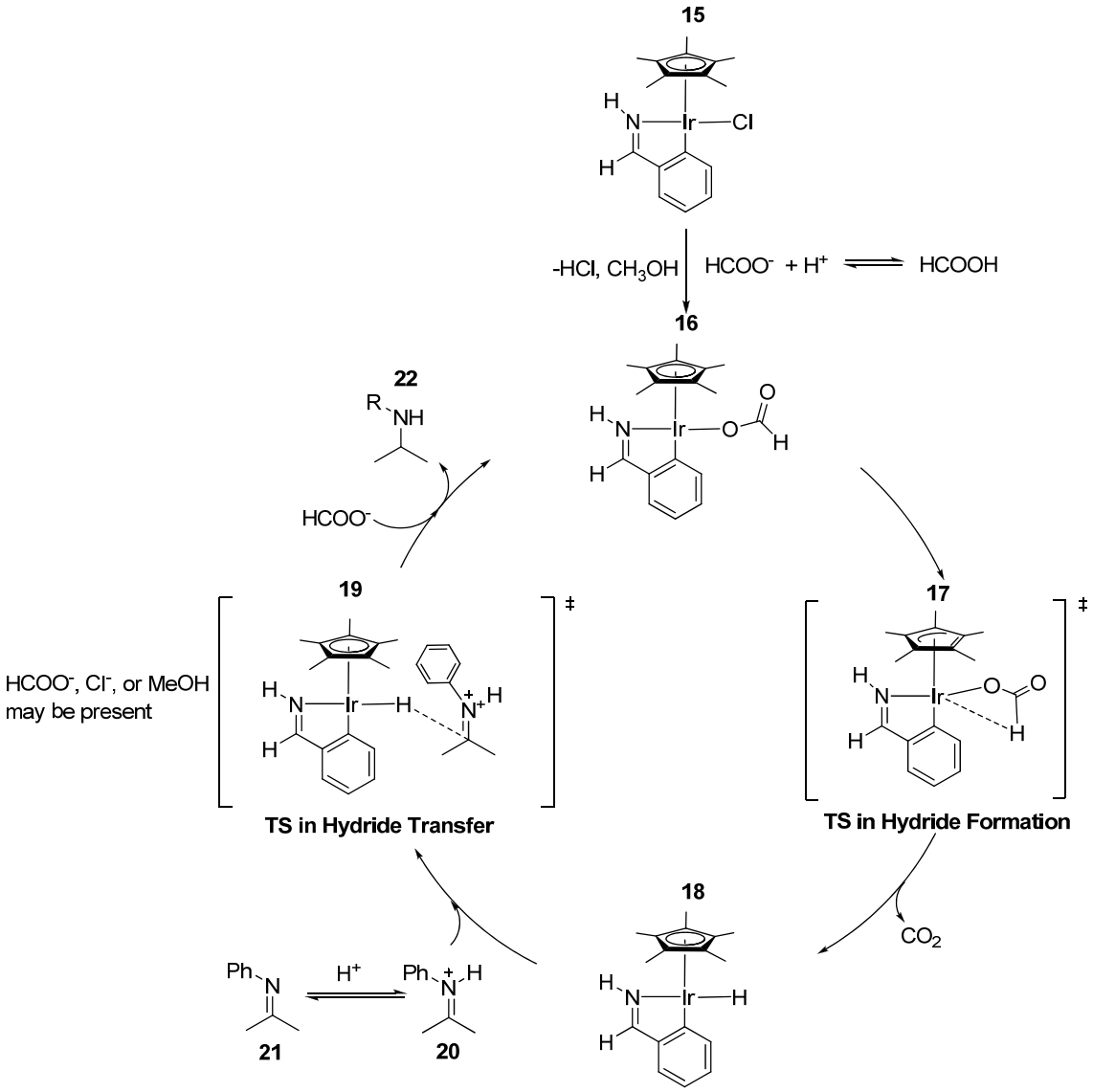

Scheme 6.5: The whole catalytic cycle for the reduction of aromatic ketimines catalysed by the cyclometalated iridium(III) complex.

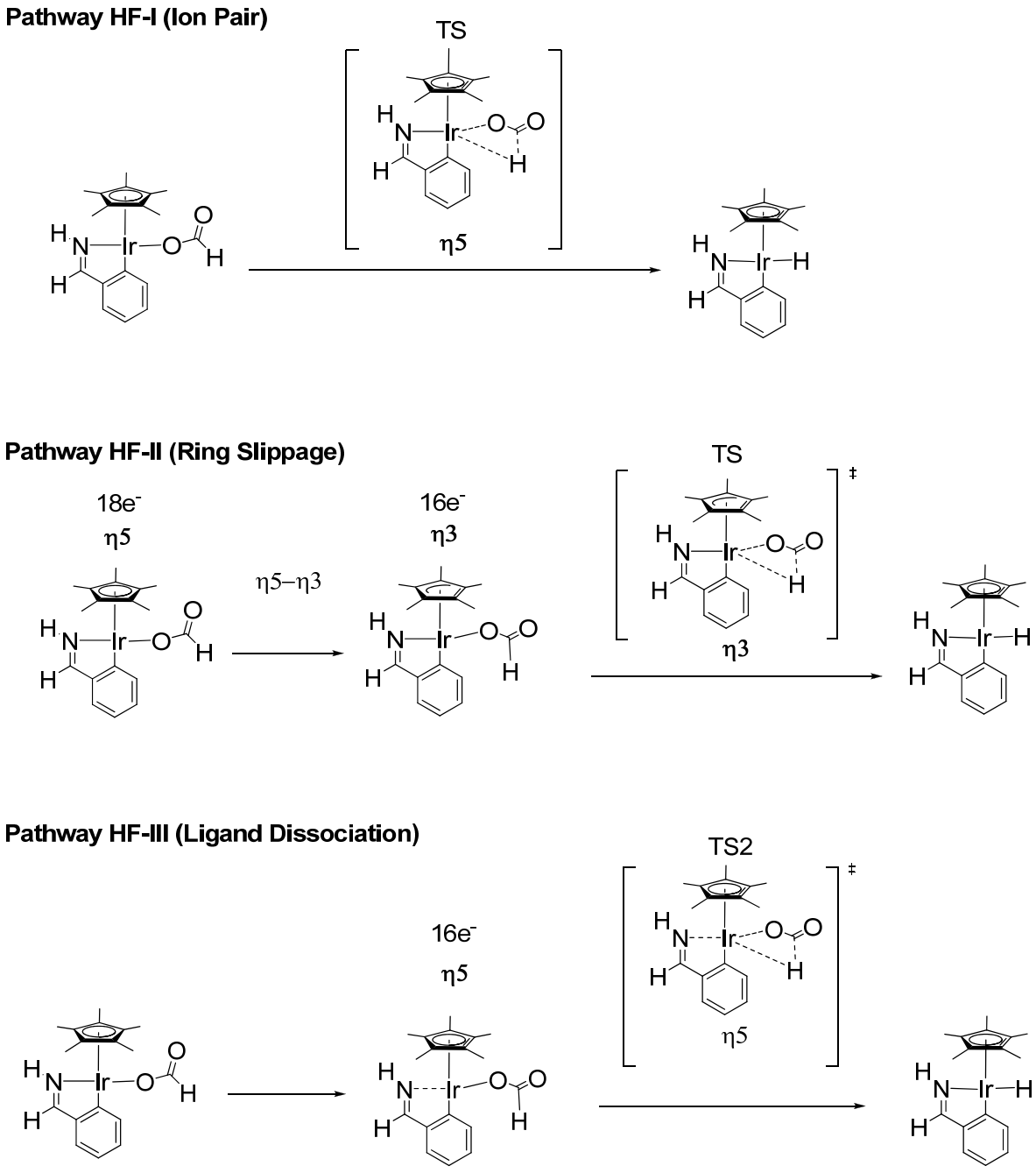

Scheme 6.6: Possible pathways in the hydride formation step in the imine reduction catalysed by the iridium cyclometalated complex.

Hydride formation on pathway HF-I without considering solvent effects

In pathway HF-I (the ion pair mechanism), the configurations and molecular orbital diagrams of the complexes **16** (intermediates/INT), **17** (transition state/TS), and **18** plus CO_2 (which together is the product of hydride formation step PRO) are shown in Figure 6.8. From the investigation of their molecular orbitals, we can understand why iridium formate complex **16** is stabilised with this kind of orientation. For the INT, there is clearly some overlap of the orbitals between the iridium and the hydride in the HOMO diagram, indicating the attraction between them; in the LUMO, there is no molecular orbital distributed on the hydride. In the TS, the orbitals are observed on the hydride in both the HOMO and LUMO diagrams. In the PRO, the molecular orbitals of iridium and the hydride overlap completely in the HOMO diagram, indicating that a covalent Ir-H bond is formed, and there is no orbital overlap between the iridium and CO_2. The orbital of the hydride in the LUMO diagram is more localised than that in the HOMO diagram.

The reaction coordinate diagram for the hydride formation along pathway HF-I is displayed in Figure 6.9, revealing that when the formate bonds with the cationic iridium complex, a very stable complex **16** is formed. We also note that the values of the activation energies (E_a) and reaction energies computed at the PBE0 and B3LYP levels of theory using Gaussian 03 are similar. Table 6.8 shows the activation energies (*ca.* 24 kcal/mol at PBE using NEB *via* CP2K; *ca.* at 27 – 28 kcal/mol at PBE0 and B3LYP using STQN *via* Gaussian 03) and energies of reaction along pathway HF-I computed using different exchange-correlation functionals and basis sets, indicating that the values of E_a are not significantly influenced by the choice of exchange-correlation functionals and basis sets. Furthermore, the 6-31G (d,p) double zeta basis set is shown to be accurate enough, confirming that it is not necessary to use more extended basis sets, such as triple zeta basis sets.

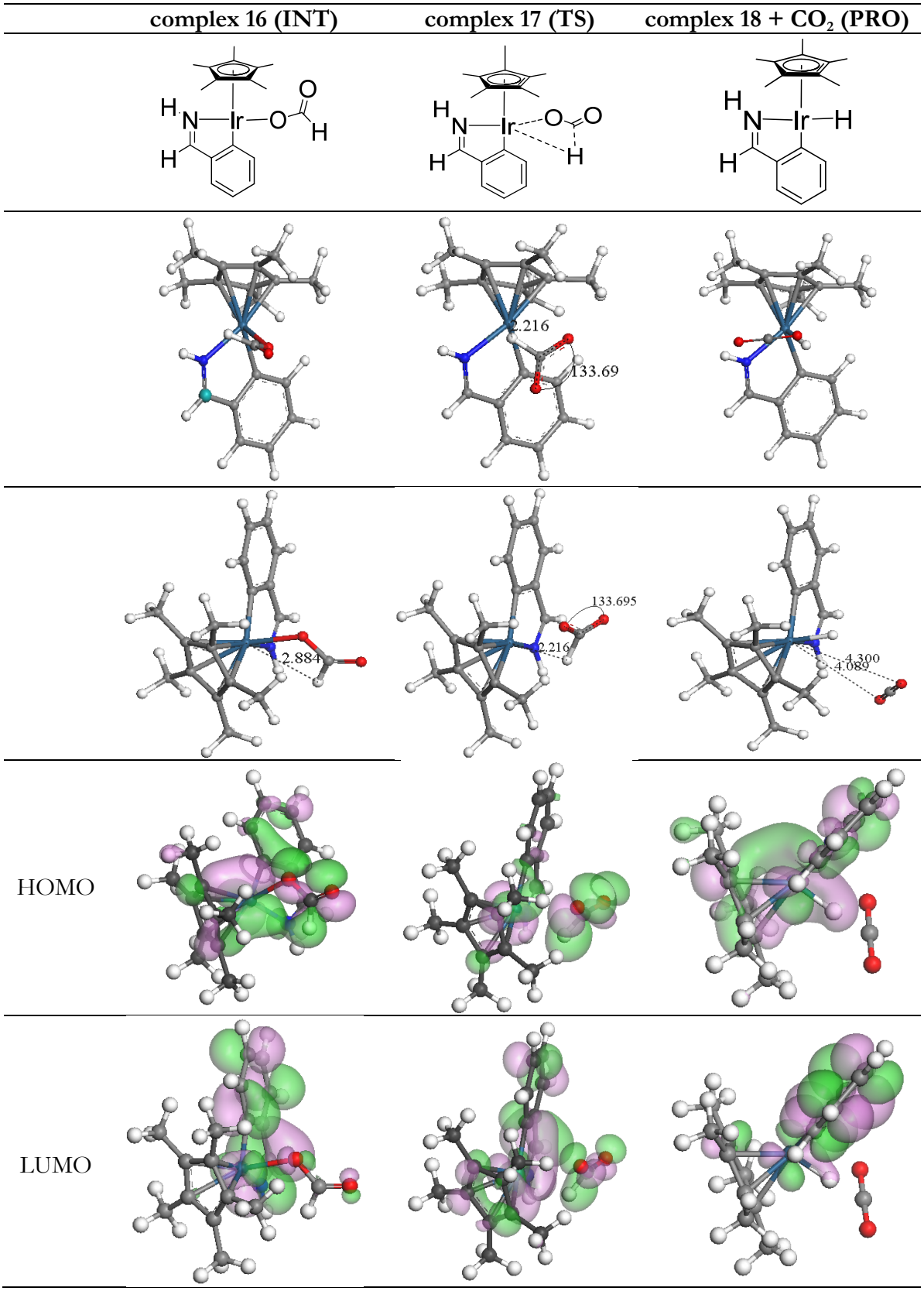

Figure 6.8: Structural properties and molecular orbitals of INT, TS and PRO in the imine reduction.

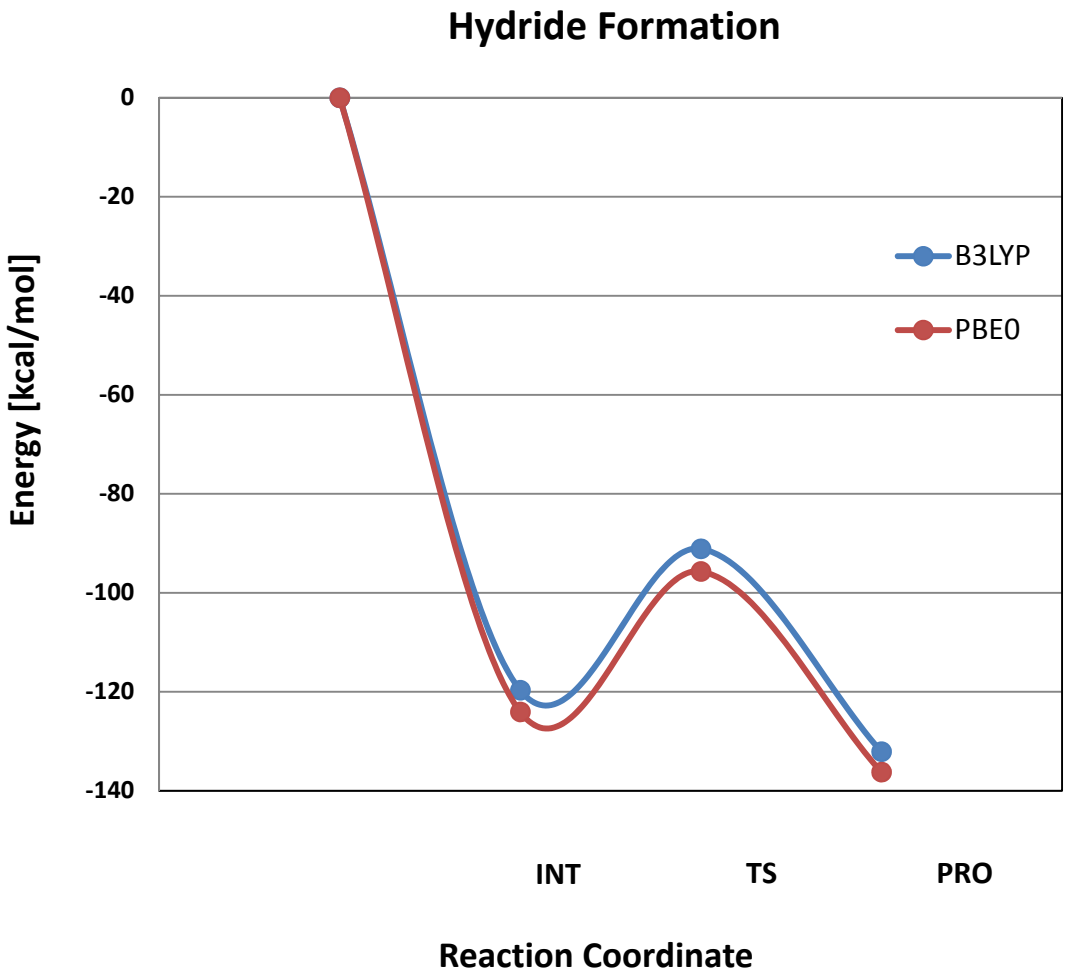

Figure 6.9: Reaction coordinate diagram for the hydride formation step along pathway HF-I in the imine reduction from **16** (INT) to **18** (PRO) *via* **17** (TS) at the PBE0 and B3LYP levels of theory *via* the Gaussian 03 code.

Table 6.8: Activation energies (TS–INT) and energies of reaction (PRO–INT) in the hydride formation step along pathway HF-I in the imine reduction catalysed by the iridium(III) complexes at different levels of theory, using the NEB method in CP2K and the STQN method in Gaussian 03, without and with considering solvent effects.

	Basis Set	E_a(TS-INT) [kcal/mol]	E (PRO-INT) [kcal/mol]
Without Solvent Effect using NEB *via* the CP2K code			
PBE	**TZV2P-MOLOPT-GTH DZVP-MOLOPT-SR-GTH**	24.18	-11.31
Without Solvent Effect using STQN *via* the Gaussian 03 code			
PBE0	**6-31G(d,p)**	28.38	-12.16
B3LYP	**6-31G(d,p)**	28.57	-12.41
BLYP	**6-31G(d,p)**	26.06	-12.86
PBE0	**6-31 G(d,p)**	28.38	-12.16
	6-311 G(d,p)	27.01	-16.08
	6-31+ G(d,p)	28.66	-10.48
	6-311+ G(d,p)	27.58	-14.06
	6-31++ G(d,p)	28.67	-10.48
	6-311++ G(d,p)	27.61	-14.00
B3LYP	**6-31 G(d,p)**	28.57	-12.41
	6-311 G(d,p)	27.35	-16.91
	6-31+ G(d,p)	28.62	-10.79
	6-311+ G(d,p)	27.72	-14.76
	6-31++ G(d,p)	28.62	-10.81
	6-311++ G(d,p)	27.74	-14.72
Consider Methanol *via* using STQN *via* Gaussian 03 with PCM			
PBE0	**6-31 G(d,p)**	26.09	-0.60
	6-311+ G(d,p)	24.83	-1.20
B3LYP	**6-31 G(d,p)**	26.34	-1.29
	6-311+ G(d,p)	25.20	-2.28

Hydride formation on pathway HF-II (The η5 → η3 ring-slippage mechanism)

The STQN method can only locate the transition state along the minimum energy pathway. The transition state located by the STQN method using Gaussian 03 is that along pathway HF-I. To compute the energy barrier along pathway HF-II, we have applied the nudged elastic band (NEB) method at the PBE level of theory as implemented in CP2K. Figure 6.10 displays the reaction coordinate diagram and the structural changes along pathway HF-II. An activation energy of 32 kcal/mol could only be successfully obtained using CP2K/NEB; this was 8 kcal/mol greater than that computed for the ion pair mechanism (pathway HF-I), implying that pathway HF-II is less favourable than pathway HF-I.

Hydride formation on Pathway HF-III (The dissociation of ligand mechanism)

To investigate the viability of the HF-III mechanism, we tried to find a stable intermediate where the nitrogen is dissociated from iridium. However, this structure always reverts to the original complex **16**. We therefore excluded this reaction pathway.

In summary, in the hydride formation step in the imine reduction using the cyclometalated iridium complex, we conclude that pathway HF-I (ion-pair), not the ring-slippage mechanism, is the most favourable pathway.

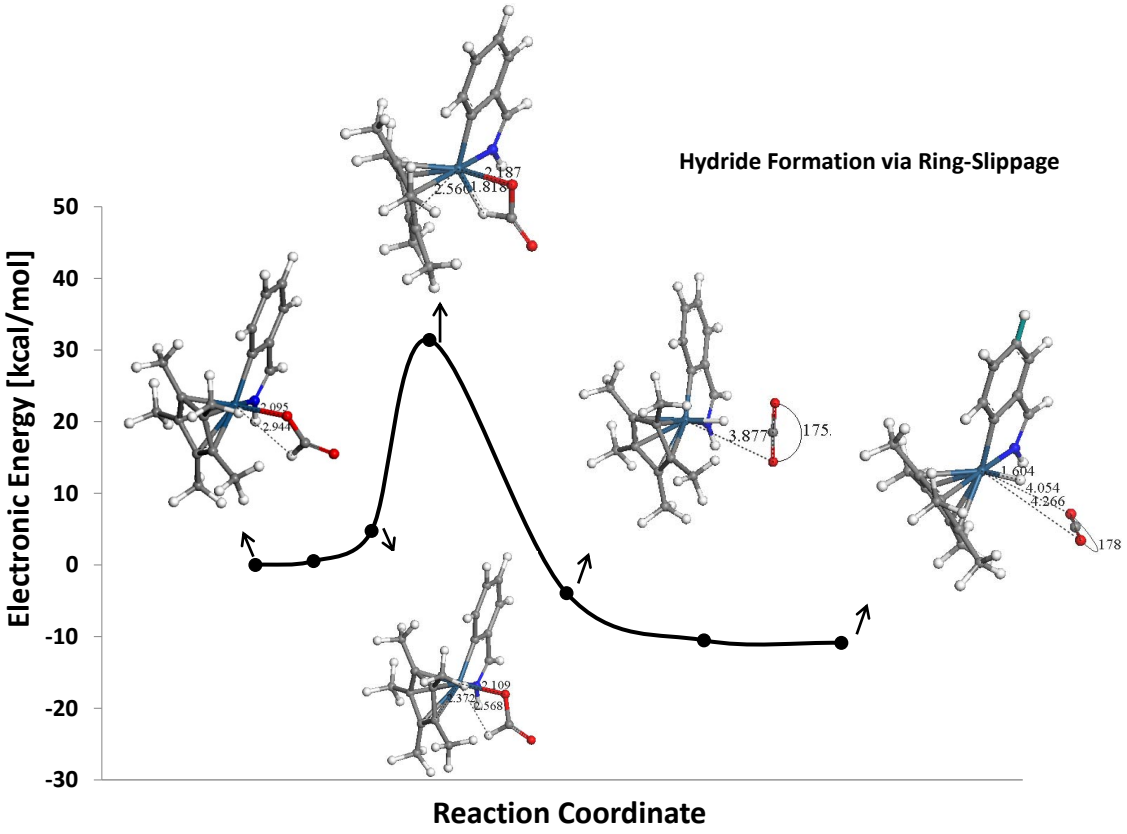

Figure 6.10: Reaction coordinate diagram for the hydride formation in the imine reduction by ring-slippage mechanism (pathway HF-II) using the NEB method implemented at the PBE level of theory *via* the CP2K code.

6.3.4.2 Locating the transition state in the hydride transfer step in system C

In this section we consider the second half of the catalytic cycle for the reduction of imine to amine catalysed by the Cp*-Ir complexes, that is, the hydride transfer (HT) step. We have initially proposed six possible reaction pathways, which are illustrated in Scheme 6.7. The reaction mechanisms along each pathway are described first and then discussed in detail below.

Pathway HT-I: The iminium is stabilised with the formate. In the transition state (TS), the η5→η3 ring slippage occurs between iridium and Cp*. In addition, the breakage of Ir-H with hydrogen approaching the iminium and the formation of Ir-O with oxygen approaching iridium are hypothesised to occur simultaneously. Once the formate has bonded to iridium and the hydride has transferred to the carbon of the iminium, the amine is generated.

Pathway HT-II: It is assumed that formate bonded with iminium does not interact with the catalyst. In the transition state, only the hydride bonded to iridium transfers to the carbon of the substrate. When the cationic iridium complex is formed, the anionic formate will then form a cation-anion pair with it.

Pathway HT-III: Compared with pathway HT-II, the formate in pathway HT-III is not associated with the iminium and therefore the net charge of the whole system is +1. Upon transfer of the hydride to the carbon of the iminium, the formate in solution spontaneously interacts with the cationic iridium complex to form a stable iridium formate complex **16**.

Pathway HT-IV: The only difference between pathways HT-IV and HT-III is the first intermediate. In pathway HT-IV, after the hydride transfers to the carbon of the iminium, the nitrogen of the iminium will bond to the iridium temporarily. Then the formate will break the Ir-N bond and form an amine plus an iridium formate complex **16**.

Pathway HT-V: We assume that the imine, but not the iminium, interacts with **18**, so that the net charge of the whole system is zero. When the hydride transfers to the carbon of imine **21**, a temporary intermediate ─ an imine with a hydride bonded to the carbon ─ is formed. Meanwhile, the nitrogen of the imine bonds to iridium. Then, the formate of formic acid will interact with the iridium and break the Ir-N bond to form an iridium formate complex **16**; in the meantime, the hydrogen of formic acid will react with the intermediate (the imine bonded with a hydride) to form an amine.

Pathway HT-VI: Pathway VI represents a competing side reaction. The protonation of the Ir-H complex **18** will occur to generate a hydrogen molecule, whilst the resulting cationic iridium complex will react with the formate of formic acid to form **16**.

We now consider the results of the calculations for the six pathways listed above.

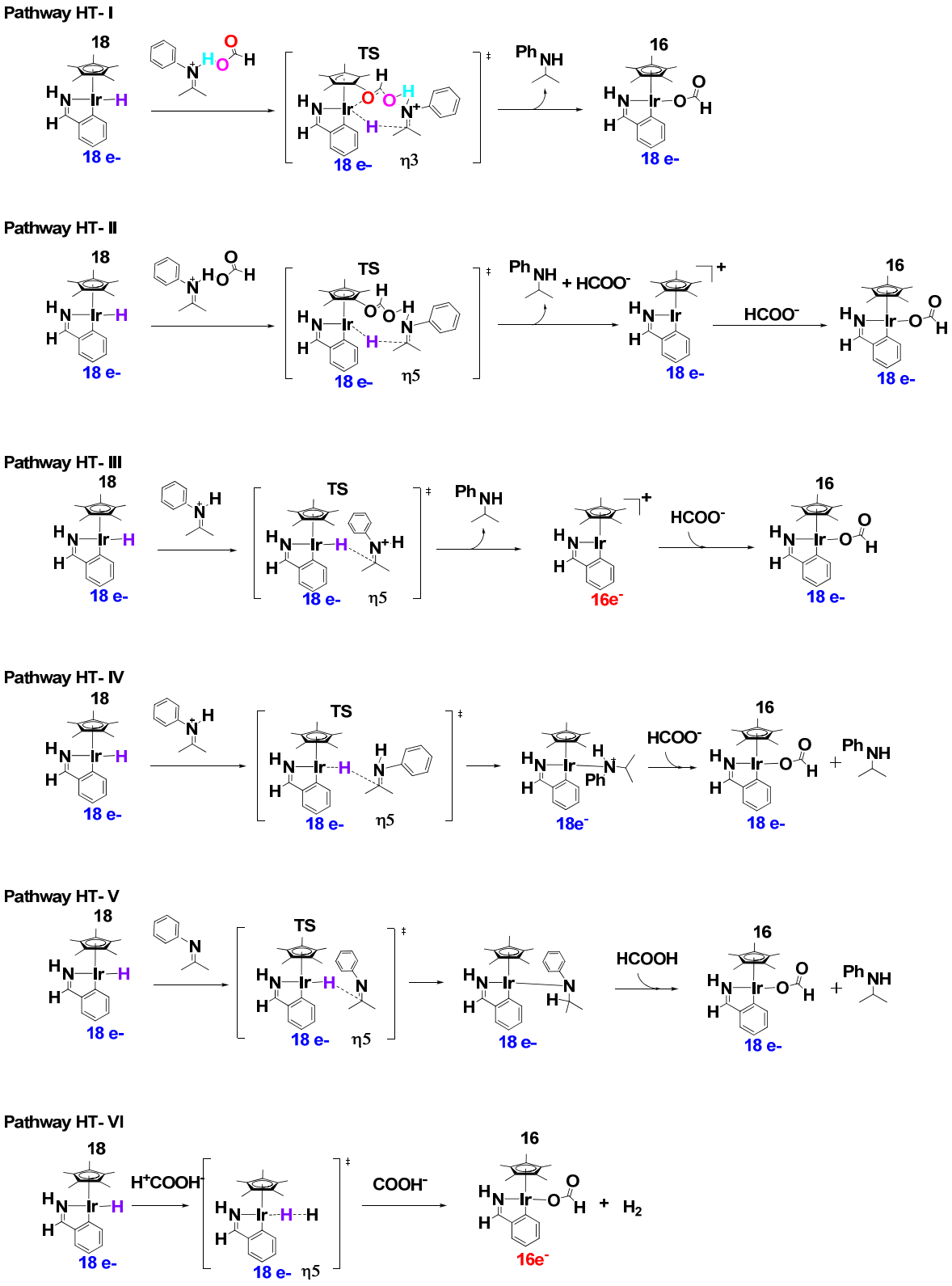

Scheme 6.7: Possible pathways for the hydride transfer in the imine reduction catalysed by the iridium cyclometalated complex.

In pathway HT-I, the formate stabilises the iminium. Four possible configurations for INT and PRO were computed, and their energies and structures are reported in Table 6.9. The most stable configurations of INT and PRO (the top row of Table 6.12) are 1.5 – 6.5 kcal/mol lower than the other three configurations. The most stable INT and PRO were selected to search for the transition state. A transition-state-like structure was found and is shown in Figure 6.11; this structure resembles the transition state in pathway HT-II and not the transition state illustrated for pathway HT-I. We note that from INT to PRO, the iminium rotates by approximately 180º. Moreover, the $\eta 5 \rightarrow \eta 3$ ring slippage should in theory occur between Ir and Cp*. In addition, the breakage of Ir-H with the hydride approaching the iminium and the formation of Ir-O with the oxygen approaching the iridium should happen simultaneously, which might not be possible in a single step. Therefore, pathway HT-I seems to be an unlikely reaction route. Moreover, when we examined this transition-state-like structure *via* a vibrational calculation, it revealed that all of the frequencies were positive, implying that this is not a real transition state. The transition-state-like structure is shown in Figure 6.11 and is not the transition state proposed in the pathway HT-II; it is obvious that the formate is not involved in the hydride transfer step. From these results, it appears that pathways HT-I and HT-II are not favourable.

The configurations and relative energies for INT, TS and PRO for pathway HT-III are shown in Table 6.10. The transition state occurs when the bond length of Ir-H is 1.65 Å and the distance of H-C is 1.85 Å. The E_a in the hydride transfer step is *ca.* 8 kcal/mol, which is 20 kcal/mol lower than the E_a in the hydride formation step.

In pathways HT-IV and HT-V, we cannot find any stable product. As a result, we conclude that the two pathways are unfavourable.

In pathway HT-VI, the activation energy is *ca.* 46 kcal/mol at the PBE level of theory using NEB *via* CP2K; thus this pathway is very unfavourable.

In summary, the hydride transfer step in the imine reduction catalysed by this type of cyclometalated iridium complex follows pathway HT-III.

Table 6.9: Four possible stable configurations with relative energies for INT and PRO in the hydride transfer step of the imine reduction in system **C** along pathway HT-I.

INT	**[kcal/mol]**	**PRO**	**[kcal/mol]**
Configuration	**ΔE**	**Configuraiton**	**ΔE**
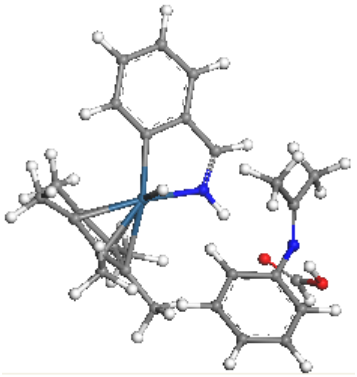	0	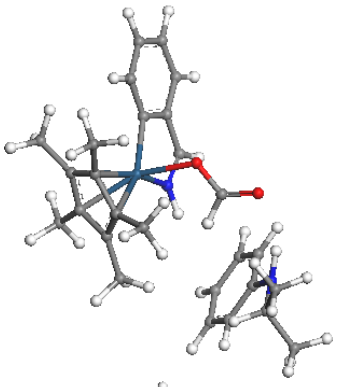	0
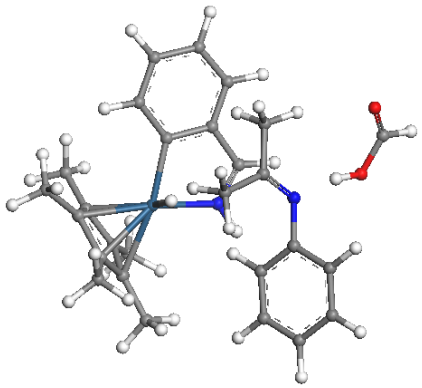	2.77	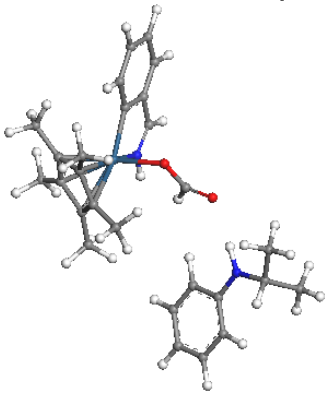	1.5
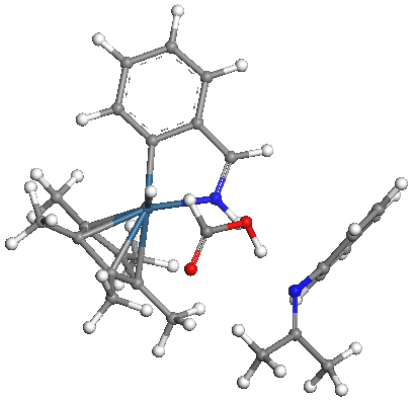	5.32	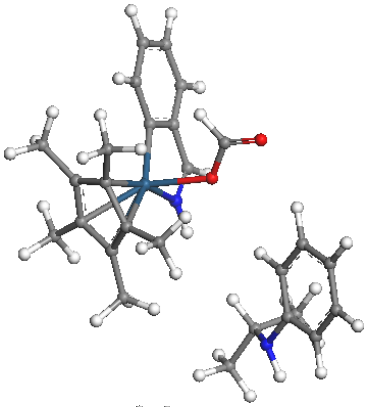	4.36
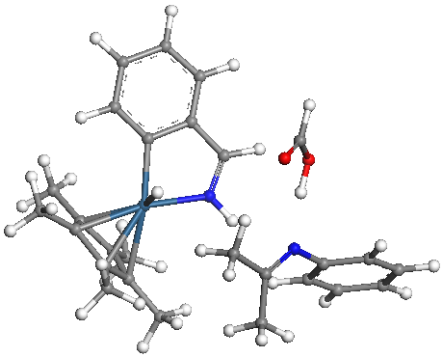	6.54	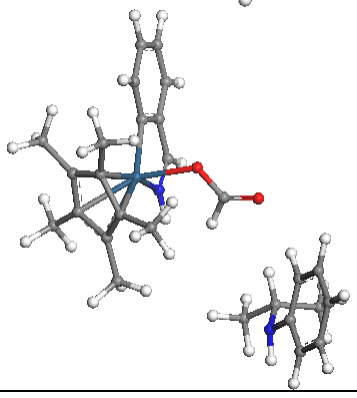	5.69

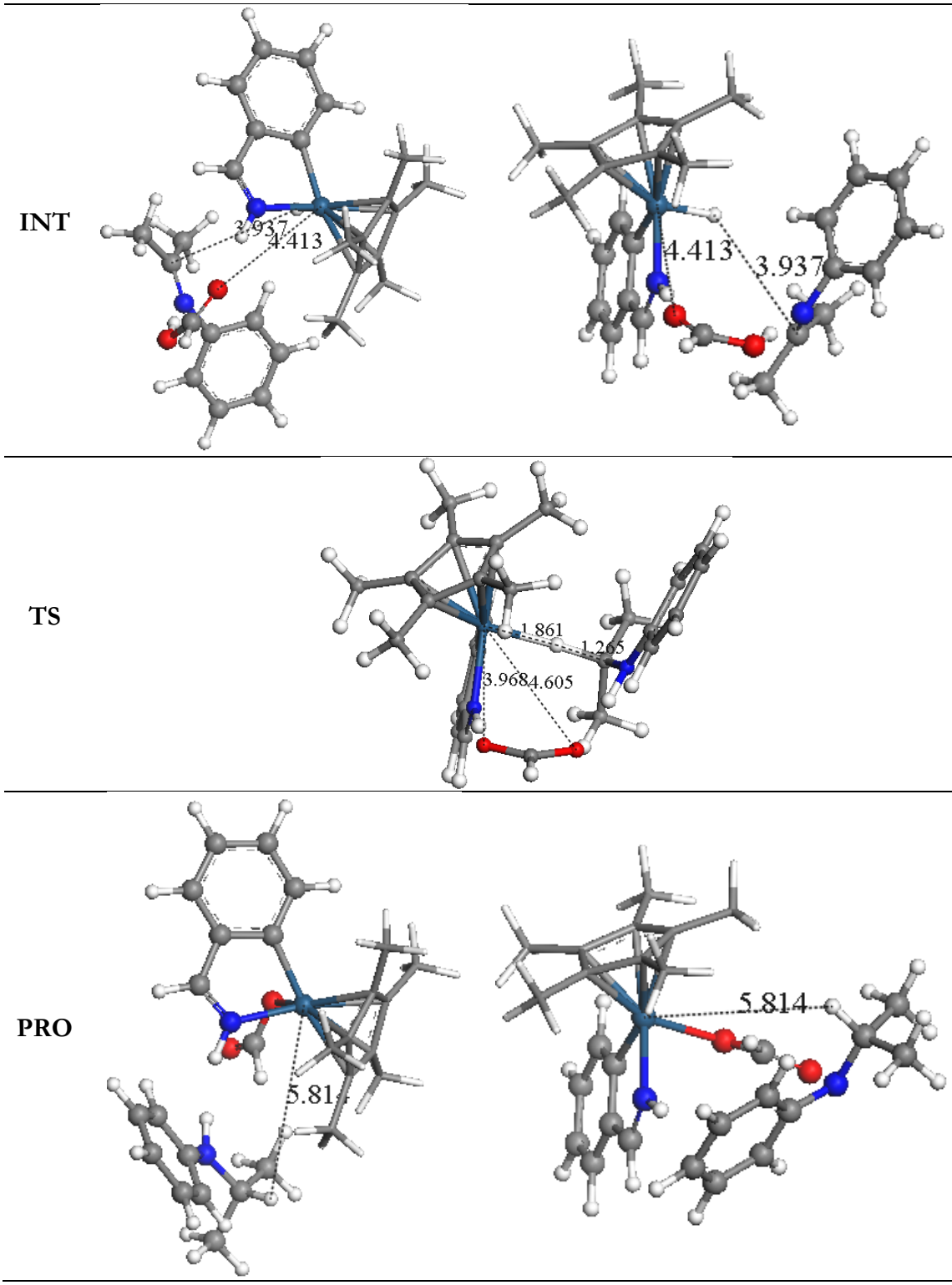

Figure 6.11: Configurations of INT, TS-like structure and PRO in the hydride transfer step in system **C** along pathway HT-I.

Table 6.10: Configurations and relative energies of INT, TS and PRO in the hydride transfer step of the imine reduction using the cyclometalated iridium complex along pathway HT-III. These values are computed at the PBE0 and B3LYP levels of theory.

	Structure	ΔE (B3LYP) [kcal/mol]	ΔE (PBE0) [kcal/mol]
INT	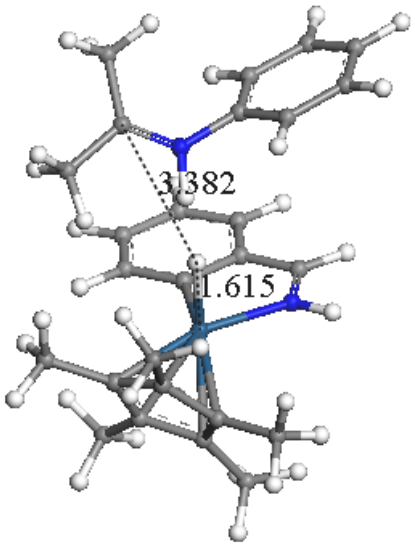	0	0
TS	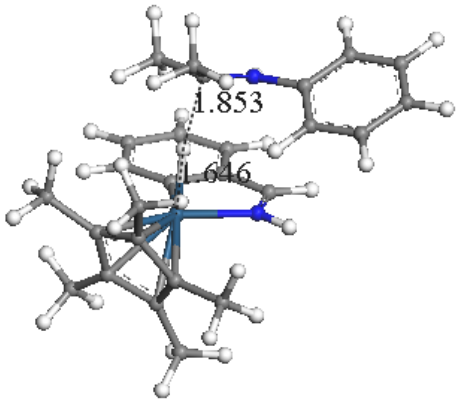	8.71	7.65
PRO	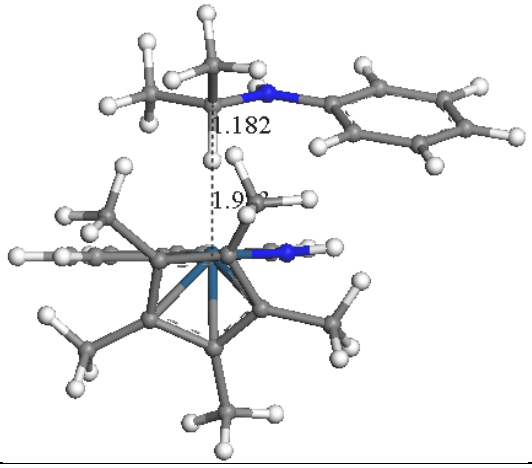	-5.45	-0.53

6.3.4.3 Reaction coordinate diagram of the entire catalytic cycle without solvent effects

Figure 6.12 shows the reaction coordinate diagram for the whole catalytic cycle in the imine reduction, computed at the PBE0 and B3LYP levels of theory using Gaussian 03. The activation energy (E_a) of the hydride formation step is about 20 kcal/mol larger than the E_a of the hydride transfer step, implying that hydride formation is the rate-determining step; this explains why the hydricities of catalysts with different functional groups in the hydride transfer step do not correlate with activity. Furthermore, the activation energy in the hydride formation is high, which we assume is caused by the presence of the formate anion in the transition state. In the following section, this model is modified by adding methanol as a solvent, which is first treated implicitly *via* the PCM approach and then explicitly by adding a single methanol molecule.

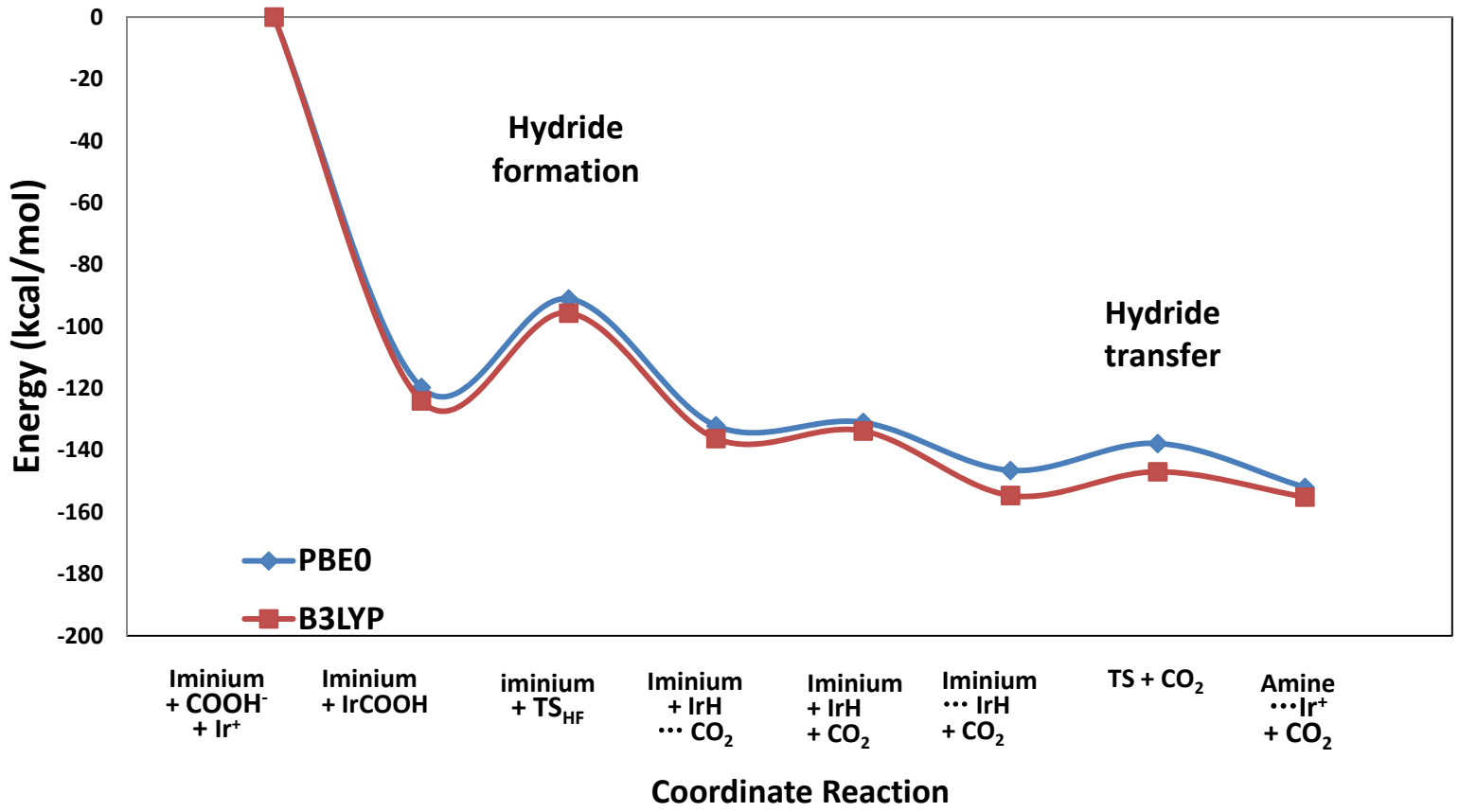

Figure 6.12: Reaction coordinate diagram of the whole catalytic cycle in the imine reduction catalysed by the iridium cyclometalated complex without considering solvent effects, at the PBE0 and B3LYP levels of theory. (The notation Ir^+ here means the cationic iridium(III) species.)

6.3.4.4 Solvent effects: considering implicit and explicit methanol

The methanol solvent, by specific interactions with the catalyst, could affect the mechanism, or the barriers and energies of reaction. In this section we present some calculations aimed at addressing some of these issues.

Considering implicit methanol using PCM

Table 6.8 reports the effect of the solvent on the activation energies and energies of reaction using the Polarisable Continuum Model (PCM) *via* the Gaussian 03 to simulate the alcoholic (methanol) environment. The results show that the activation energies E_a differ by *ca.* 2 kcal/mol and the energies of reaction increase by *ca.* 10 kcal/mol compared with those in the gas phase. The small changes in activation energy computed *via* PCM indicates that solvent treated at this level does not strongly influence the hydride formation step in the imine reduction using the iridium cyclometalated catalyst.

Considering explicit methanol by incorporating one methanol molecule

In this subsection, we add a real methanol molecule in the vicinity of the intermediate (INT), transition state (TS) and PRO in both the hydride formation and transfer steps and then perform geometry optimisations. Several initial configurations had been examined and Table 6.10 illustrates the two stable INTs, TS and PRO in the hydride formation step. The lowest energy intermediate on the left-hand side is selected to search for the transition state. Table **6.11** displays the configurations and the relative energies of INT, TS and PRO in the imine reduction *via* pathway HF-III. Compared with the calculations where no methanol molecule was included in the model, the E_a drops by 10 kcal/mol to 17.78 kcal/mol. Table 6.12 shows the structural configurations and relative energies of the INT, TS and PRO in the hydride transfer step. The activation energies drop by 4 to 3.74 kcal/mol compared with those without the incorporation of a methanol solvent molecule in the gas phase.

The reaction coordinate diagram of the whole catalytic cycle in the imine reduction with and without adding an explicit methanol molecule is shown in Figure 6.13. The values of E_a in the hydride formation step and hydride transfer step are 17.78 and 3.74 kcal/mol respectively when the solvent is incorporated, which implies that the rate-determining step is still the formation of the hydride.

6.4 Summary

We have shown that the constrained optimisation method with the application of a single pseudo-coordinate (Ir-)H···C(-N) fails to locate the transition state, but the synchronous transit-guided quasi-Newton (STQN) and nudged elastic band (NEB) methods work well. The rate-determining step in this imine reduction is in the hydride formation step but not the hydride transfer step, which explains why hydricities of different catalysts with different electron-donating and withdrawing functional groups do not relate to activity. In the gas phase, the activation energies in the hydride formation and transfer steps are 27 – 28 kcal/mol and 7 – 8 kcal/mol. When considering the implicit methanol solvent, the activation energy in the hydride formation is 25 – 26 kcal/mol. When considering an explicit methanol molecule as solvent, the activation energies in the hydride formation and transfer steps are *ca.* 18 kcal/mol and 3.4 kcal/mol respectively. The differences in activation energy between the hydride formation and transfer steps are *ca.* 20 kcal/mol and 14 kcal/mol in the gas phase and incorporate one methanol molecule. We have demonstrated that the ring-slippage mechanism is not a favourable pathway.

To summarise, we have provided useful insights into the mechanisms of these novel catalytic reactions, which help to illuminate some aspects of the experimental studies.

Table 6.11: Configurations and relative energies of INT, TS and PRO in the hydride formation step of the imine reduction using the iridium complexes with methanol as a solvent, computed at the PBE0 level of theory using the Gaussian 03 code.

	Structure	ΔE [kcal/mol]	
INT	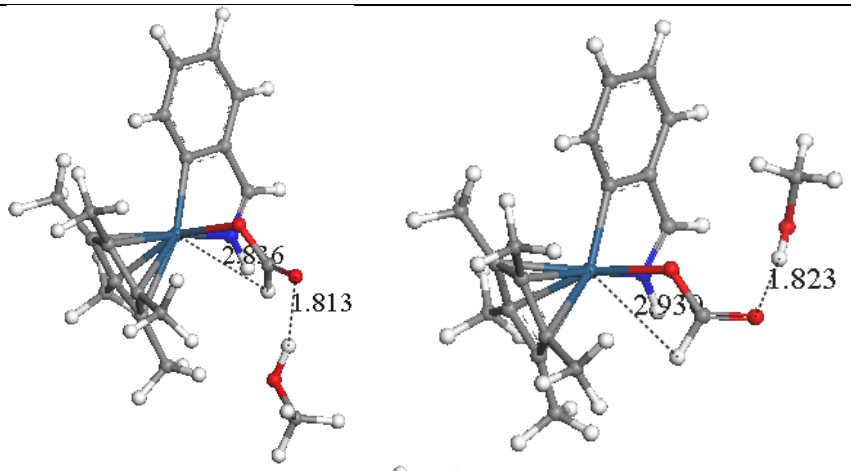	0	1.21
TS	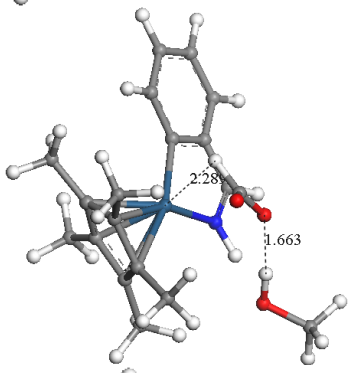		17.78
PRO	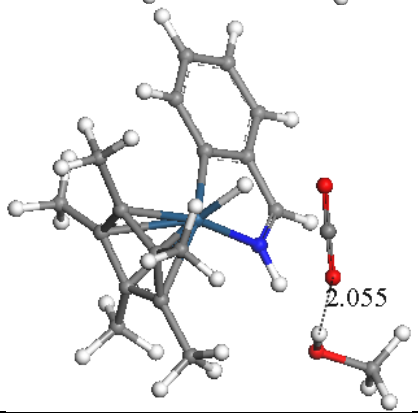		-9.72

Table 6.12: Configurations and relative energies of INT, TS and PRO in the hydride transfer step of the imine reduction using the iridium complexes with methanol as a solvent, computed at the PBE0 level of theory using the Gaussian 03 code.

	Structure	ΔE [kcal/ mol]
INT	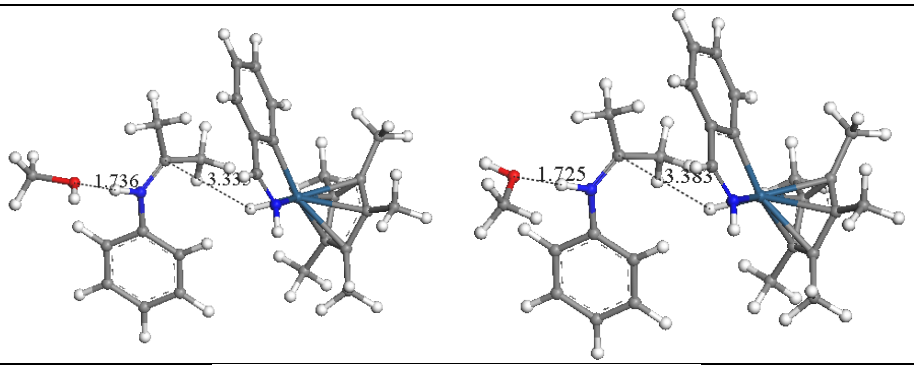	0 0.12
TS	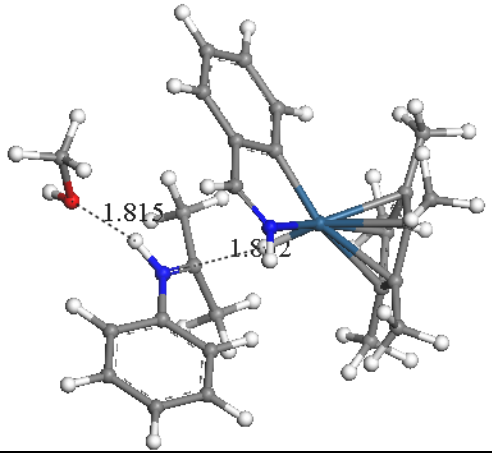	3.79
PRO	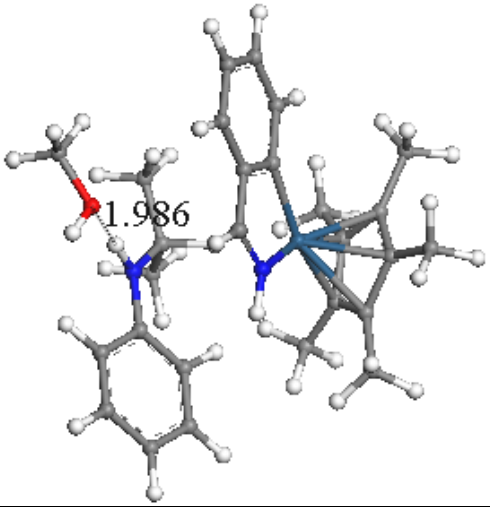	-9.32

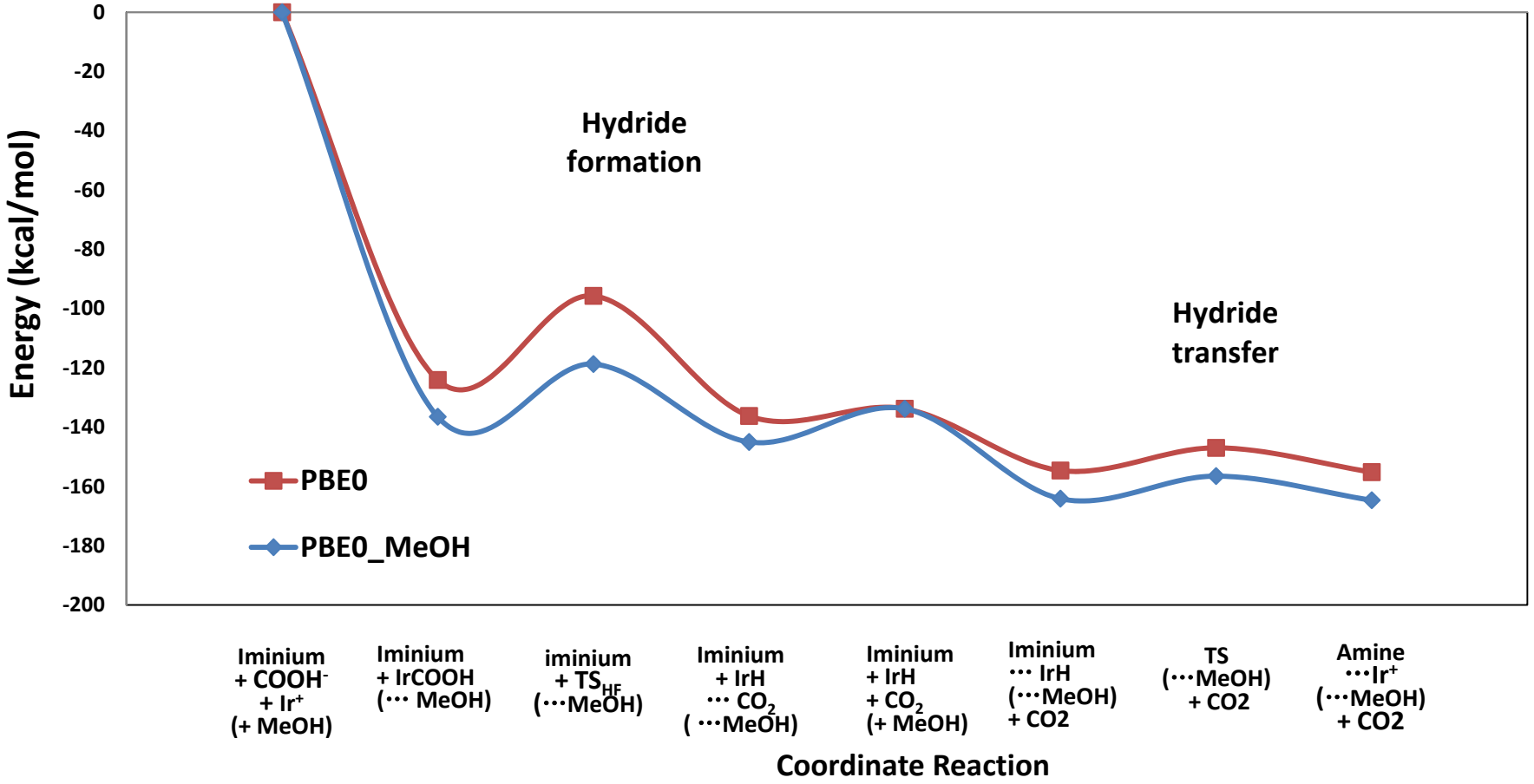

Figure 6.13: Reaction coordinate diagram of the whole catalytic cycle in the imine reduction catalysed by the cyclometalated iridium complex with methanol as a solvent.

Chapter 7 **Summary and Conclusions**

7.1 Summary

This thesis has examined a range of problems associated with asymmetric hydrogenation. First, we considered the hydrogenation of acetophenone (ACP) catalysed by ruthenium diphosphine diamine complexes with different functional groups on ligands, and we found that a lower activation energy could be obtained when the interaction between ACP and the catalyst is dominated by non-bonding NH/π attraction in the intermediate (INT). More importantly, the primary factor in determining the activation energy is the steric repulsion from the intermediate to transition state, not the nature of intermediate(s). Furthermore, the methyl group on the *m*-xylene restrains the motion of ACP along the Q2 pathway and elevates the energy of the transition state that makes the Q1 more facile. Hence, the system with a 3,5-dimethyl xylyl group results in the highest enantiomeric excess (*ee*). The use of TolBINAP, if combined with DPEN, could not compensate for the lack of steric hindrance on the former; if combined with DMDPEN, two methyl groups and one phenyl group on the diamine create excessive steric repulsion; if combined with DMAPEN, it could offer the appropriate compromise to create the most favourable pathway, Q3. The most significant conclusion of the work is the demonstration of a clear correlation between the difference in calculated activation energy (ΔE_a) and the *ee* for the hydrogenation of ACP catalysed by Noyori-type ruthenium-based complexes on changing the substituents on both the diphosphine and diamine. Furthermore, the configuration of the product does not affect this correlation. We suggest that calculations of this type could be used to assist in the choice of the ligand when optimising *ee*.

Regarding the effects of replacing the ruthenium by iron in the hydrogenation of ketones catalysed by Noyori-type catalysts on enantioselectivity, our calculations clearly indicate that both the FeH_2(diphosphine)(diamine) and RuH_2(diphosphine)(diamine) complexes are stabilised in the *trans*-conformation with respect to the position of the hydride atom. Moreover, we found that for both the *trans*-[Fe(II)H_2(diphosphine)(diamine)] and *trans*-[Ru(II)H_2(diphosphine)(diamine)] complexes, the electronic ground states have zero spin, indicating that the FeH_2(diphosphine)(diamine) complexes have similar

electronic and structural properties to the highly successful Noyori-type catalysts for the hydrogenation of ketones.

The catalytic cycles for the H_2-hydrogenation of acetone catalysed by the simplified catalysts M(II)H_2(PH_3)$_2$(en), where M = Ru or Fe, have also been computed. The results show that the activation energies for the H-transfer and H_2-splitting processes are similar for the two metal complexes, suggesting that the mechanism of the hydrogenation of ketones catalysed by the *trans*-[Fe(II)H_2(diphosphine)(diamine)] complexes should be the same as for the ruthenium catalytic system.

As for enantioselectivity, we have computed the reaction coordinate diagrams associated with the entrance of the acetophenone into the active sites of the *trans*-[RuH_2{(*S*)-XylBINAP}{(*S*,*S*)-DPEN}] and *trans*-[FeH_2{(*S*)-XylBINAP}{(*S*,*S*)-DPEN}] catalysts. In both cases, the energy profile associated with the (*R*)-alcohol (Q1) is the most favourable. The enantioselectivity of the ruthenium- and iron-based complexes is related to the occurrence of a similar type of intermediate along the Q1 pathway, which fixes the molecular orientation of the acetophenone before the actual H-transfer process occurs. We therefore suggest that iron complexes, such as the important Ru(II)H_2(diphosphine)(diamine), could be active in the hydrogenation of ketones and could produce an enantiomeric excess similar to those obtained using Noyori-type ruthenium catalysts.

In the imine reduction catalysed by the cyclometalated iridium(III) complexes, we demonstrated that the rate-determining step is in the hydride formation step and not the hydride transfer step, which explains why the hydricities of catalysts with different electron-donating and withdrawing functional groups do not relate to the activity observed in experiment.

For the hydride formation step, we showed that the ring slippage-mechanism is not a favourable pathway.

When using an implicit methanol solvent with PCM, the energy barrier in the hydride formation step drops by only *ca.* 2 kcal/mol compared with the gas phase. However, when considering an explicit methanol molecule in the reaction, the activation

energy drops by *ca.* 10 kcal/mol in the hydride formation step and *ca.* 4 kcal/mol in the hydride transfer step compared with the gas phase.

Our attempt to locate the transition state by the constrained optimisation method using pseudo coordinate (Ir-)H···C(-N) failed, but both the synchronous transit-guided quasi-Newton (STQN) and nudged elastic band (NEB) methods worked well.

Overall, our computations show good agreement with the experimental results and demonstrate the role of these techniques in investigating these catalytic systems.

7.2 Future work

Non-bonding interactions between the substrate and the catalyst's ligands play a key role in affecting the enantioselectivity of the hydrogenation of aromatic ketones catalysed by the ruthenium diphosphine diamine complexes. Therefore, although we have tested DFT methods including corrections to the dispersion forces (DFT-D) for the simplified system [acetone + $RuH_2(PH_3)_2(en)$], we still need to apply such methods to real systems, where dispersion interactions are more significant.

Bergens's group has recently proposed an alternative mechanism to the bifunctional ligand-metal mechanism for the hydrogenation of ketones catalysed by ruthenium catalysts[29a,29c,29d]. In future work we may therefore consider this new mechanism when investigating enantioselectivity. The methods we have used, however, provide a solid methodological framework for better study of these systems.

Our calculations have provided a better understanding of the mechanism of the imine reduction catalysed by the achiral cyclometalated iridium(III) complexes. The molecular orbital diagrams of reactants, transition states and products in both the hydride formation and transfer steps in systems containing iridium complexes with different electron-donating and withdrawing functional groups will be computed and illustrated in order to understand the influences on activity with respect to the molecular orbitals. Our next step will be to investigate asymmetric imine reduction.

Appendix

Single point energy calculations in the hydrogenation of acetophenone catalysed by RuH_2[(*S*)-XylBINAP)][(*S*,*S*)-DPEN] complexes

We performed single point energy calculations on the PBE-relaxed structure using the PBE-D dispersion corrected functional developed by Grimme and co-workers. Calculations were carried out using the CP2K and Quantum-Espresso (QM) codes. Table A.1 shows the energy difference between Pre-INT and INT ($\Delta E_{Pre\text{-}INT-INT}$) and activation energies (ΔE_{TS-INT}) computed at the PBE and PBE-D levels of theory. The DFT-D correction stabilises Pre-INT by 2 – 5 kcal/mol with respect to uncorrected PBE. However, the activation energies computed at PBE-D *via* CP2K and QM are both negative (–4.85 kcal/mol and –3.77 kcal/mol respectively). The results for the transition state were highly inconsistent with those obtained using GGA, hybrid meta-DFT (HMDFT), hybrid DFT (HDFT) and MP2 calculations[28c] and may highlight the inadequacy of this method. To remove this ambiguity, we explored the whole catalytic cycle of acetone hydrogenation catalysed by the simplified $RuH_2(PH_3)_2$(en) catalyst using the dispersion-corrected DFT methodology.

Table A.1: Energy differences between Pre-INT and INT, and activation energies in the hydrogenation of acetophenone catalysed by RuH_2[(*S*)-XylBINAP)][(*S*)-DPEN] computed at the PBE and PBE-D levels of theory.

Code	**DMol^3**	**CP2K**	**CP2K**	**Q-Espresso**
Functional	PBE	PBE	PBE-D	PBE-D
Basis Set	DNP	DZVP-MOLOPT-SR-GTH		PW (E_{cut} = 200 eV)
Pseudopotential	DSPP	GTH	GTH	Ultrasoft
$\Delta E_{(Pre\text{-}INT-INT)}$	-2.34	-3.28	-7.20	-5.05
E_a	3.68	1.38	-4.85	-3.77

- $\Delta E_{(Pre\text{-}INT-INT)}$ stands for the energy difference between the two intermediates, Pre-INT and INT
- $E_a = \Delta E_{(TS\text{-}INT)}$ stands for the activation energy

Catalytic cycle in the hydrogenation of acetone catalysed by $RuH_2(PH_3)_2(en)$ complexes computed at the DFT-D level of theory

Scheme A.1 illustrates the catalytic cycle for the hydrogenation of ketones catalysed by the RuH_2(diphosphine)(diamine) complexes. The reaction coordinate diagrams in the H_2-splitting and hydride transfer using the metal-ligand bifunctional mechanism computed at different levels of theory are plotted in Figure A.1, A.2 and A.3.

Figure A.1 shows the reaction coordinate diagrams in the hydride formation of acetone hydrogenation using the PBE and PBE0 exchange-correlation functionals with and without dispersion correlations (DFT-D3 and DFT-D3_C9); these yield similar results.

Figure A.2 delineates the structural changes in the [H_2 + $16e^-$ Ru species] which form a stable $18e^-$ ruthenium complex when optimised using PBE-D3_C9. Two transition state structures are observed in this step. The structural changes in the other five diagrams at the PBE, PBE0, PBE-D3, PBE0-D3, PBE0-D3_C9 levels of theory are similar to those shown in Figure A.2.

Figure A.3 shows the reaction coordinate diagrams in the hydride transfer of acetone hydrogenation at the PBE, PBE-D3 and PBE-D3_C9 levels of theory, which reveals that the activation energies of the three profiles are similar: 0.37 kcal/mol, 0.43 kcal/mol and 0.67 kcal/mol respectively.

Figure A.4 depicts the structural changes in the [Acetone + $18e^-$ Ru complex] to [2-Propanol + $16e^-$ Ru intermediate species], which are similar to the other two profiles. In Table A.2, we report the activation energies for the hydride transfer and H_2-splitting hydrogenation catalysed by $RuH_2(PH_3)_2(en)$ at different levels of theory. In the hydride transfer process, their activation energies range from 0.37 to 3.40 kcal/mol. For the hydride formation process, they range from 7.80 to 13.76 kcal/mol.

Overall, in this simplified system, accounting for dispersion correction results in no major differences compared with the results at the PBE level of theory for the hydrogenation of acetone catalysed by the $RuH_2(PH_3)_2(en)$ complexes.

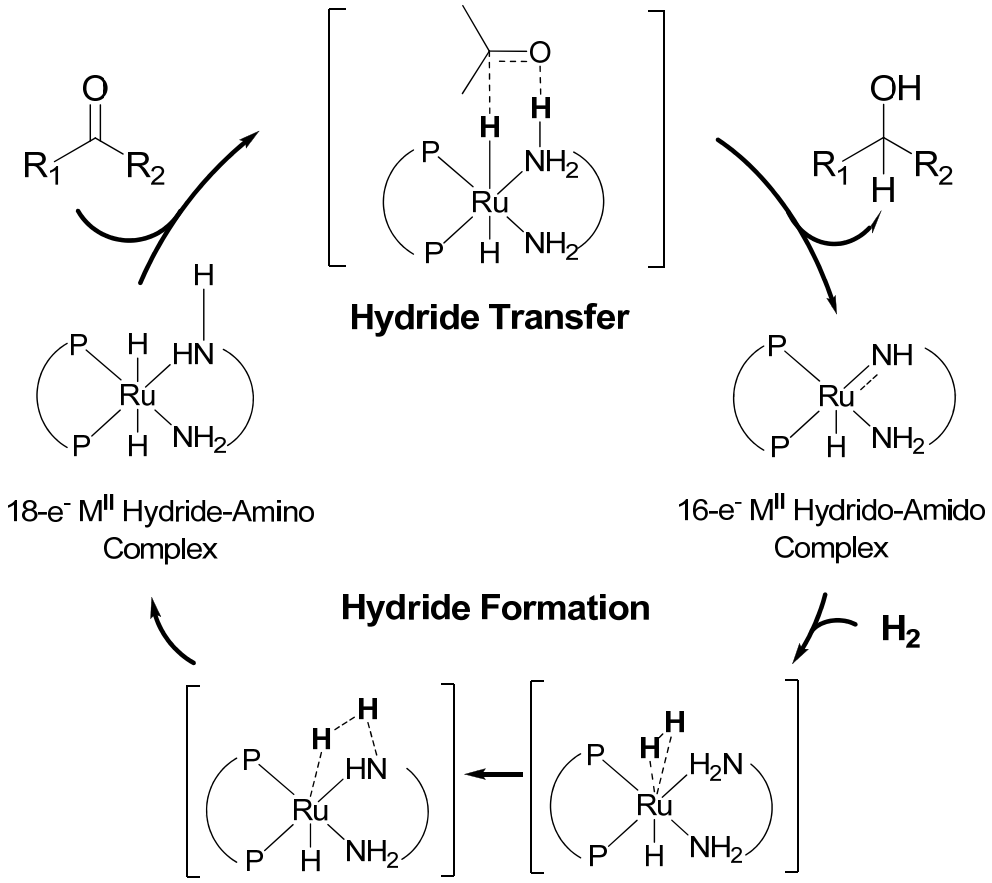

Scheme A.1: Catalytic cycle for the hydrogenation of ketones using RuH_2(diphosphine)(diamine) complexes.

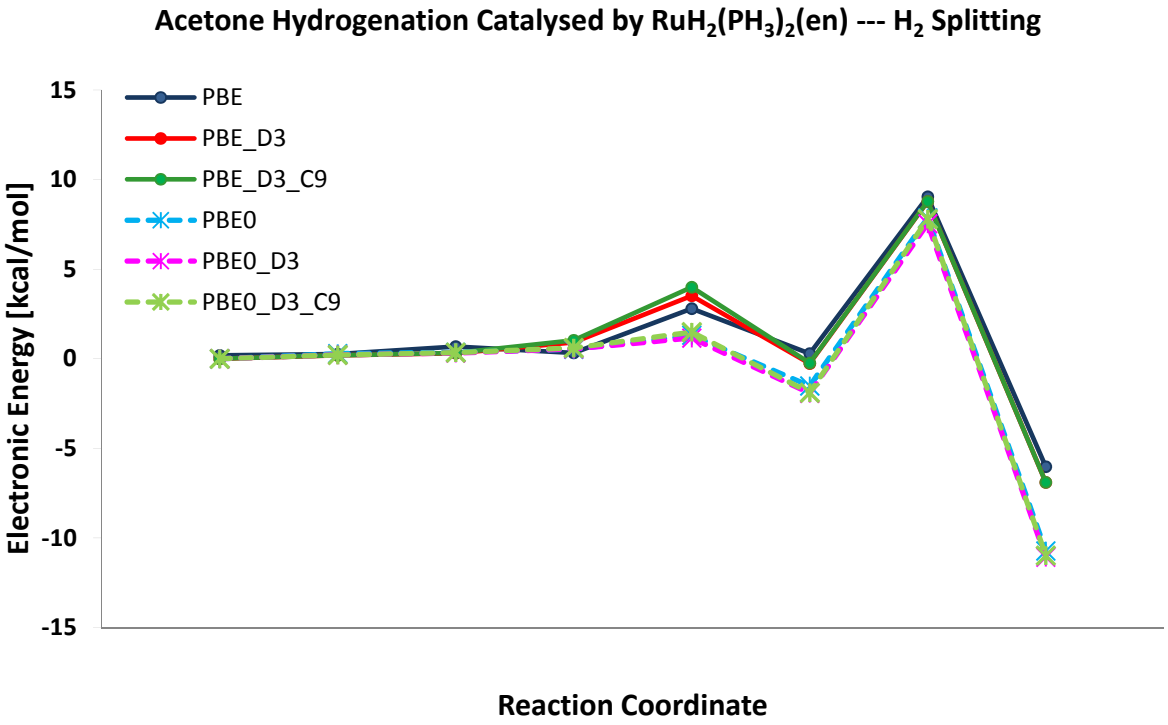

Figure A.1: Reaction coordinate diagram for the hydride formation in the hydrogenation of acetone catalysed by the $RuH_2(PH_3)_2(en)$ complex at different levels of theory.

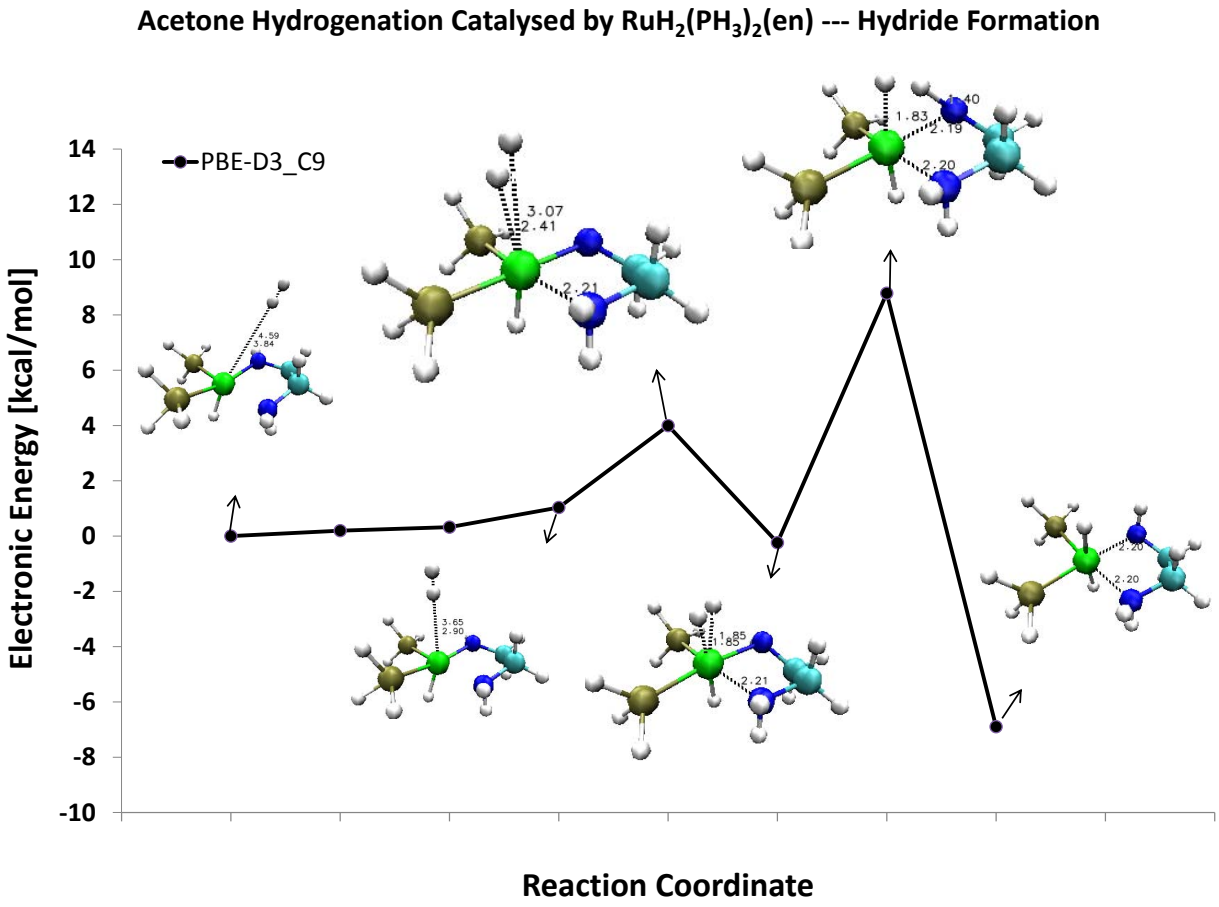

Figure A.2: Reaction coordinate diagram for the hydride formation in the hydrogenation of acetone catalysed by the $RuH_2(PH_3)_2(en)$ complex at the PBE-D level of theory.

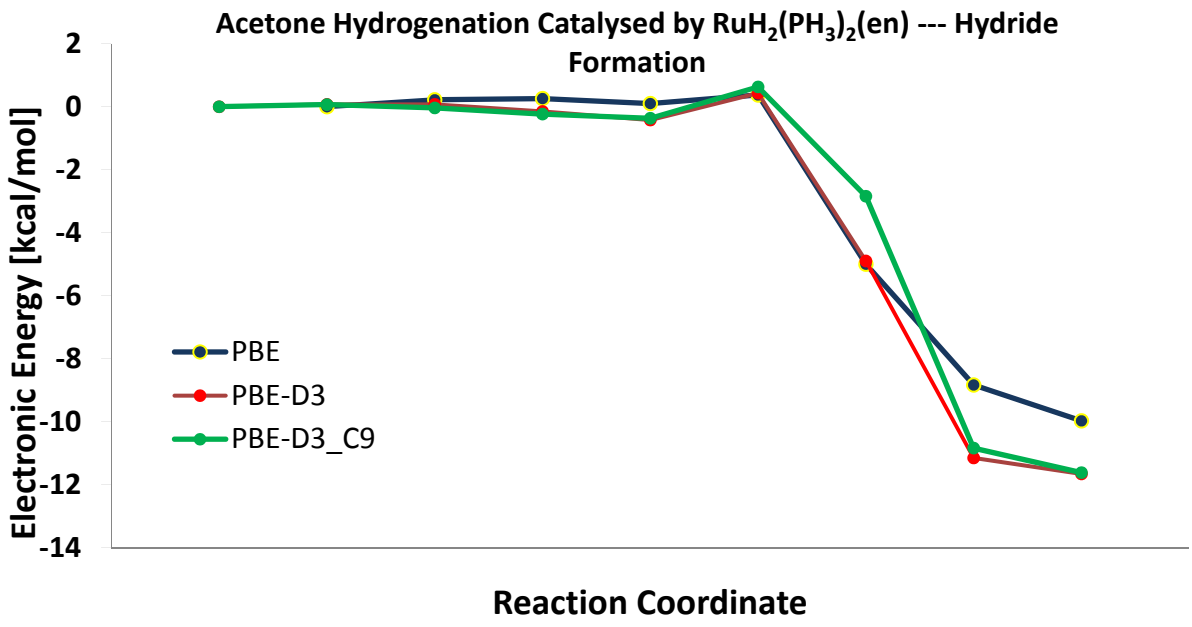

Figure A.3: Reaction coordinate diagram for the hydride transfer in the hydrogenation of acetone catalysed by the $RuH_2(PH_3)_2(en)$ complex at different levels of theory.

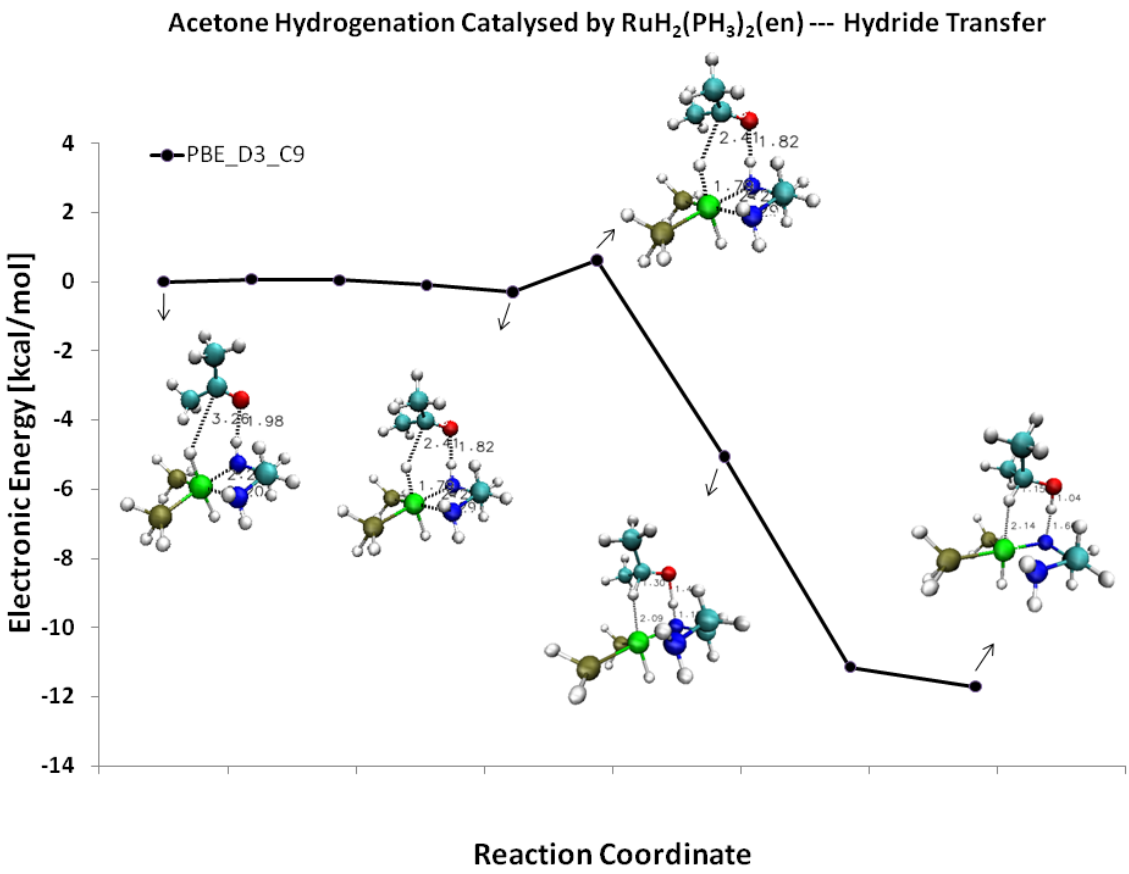

Figure A.4: Reaction coordinate diagram for the hydride transfer in the hydrogenation of acetone catalysed by the $RuH_2(PH_3)_2(en)$ complex at the PBE-D level of theory.

Table A.2: Activation energy in the hydrogenation of acetone catalysed by $RuH_2(PH_3)_2(en)$ at different levels of theory.

Reference	Chen[102]		This Thesis									
Functional	B3LYP	PBE	PBE	PBE0	B3LYP	mPW1PW91	PBE			PBE0		
|Dispersion Correction	N/A	N/A	N/A	N/A	N/A	N/A	N/A	D3	D3_C9	N/A	D3	3_C9
Basis Set	6-31G ** LAND2DZ	DNP	6-31G ** LAND2DZ			SDD	TZV2P-MOLOPT-GTH DZVP-MOLOPT-SR-GTH					
Pseudo-potential	LAND2	DSPP	LAND2			SDD	GHT					
$E_{a\ Hydrog.\ TS}$	2.85	0.53	2.20	2.77	3.40	2.68	0.37	0.43	0.67	1.57	2.92	2.22
$E_{a\ H2\text{-}Splitting}$	12.48	8.36	9.74	8.42	13.76	8.69	9.04	8.78	8.79	7.86	7.54	7.80

- $E_{a\ Hydrog.\ TS}$ is the activation in the hydrogen transfer step.
- $E_{a\ H2\text{-}Splitting}$ is the activation energy in the H_2-Splitting step.

References

1. (a) H. U. Blaser, C. Malan, B. Pugin, F. Spindler, H. Steiner and M. Studer, *Selective hydrogenation for fine chemicals: Recent trends and new developments.* Advanced Synthesis & Catalysis **2003**, *345*, 103; (b) C. Wang, A. Pettman, J. Basca and J. L. Xiao, *A versatile catalyst for reductive amination by transfer hydrogenation.* Angewandte Chemie International Edition **2010**, *49*, 7548.

2. (a) J. Halpern, J. F. Harrod and B. R. James, *Homogeneous catalysis of hydrogenation of olefinic compounds by ruthenium (II) chloride.* Journal of the American Chemical Society **1966**, *88*, 5150; (b) D. Evans, J. A. Osborn, F. H. Jardine and G. Wilkinson, *Homogeneous hydrogenation and hydroformylation using ruthenium complexes.* Nature **1965**, *208*, 1203.

3. (a) R. Noyori, *Asymmetric catalysis: science and opportunities (Nobel Lecture).* Angewandte Chemie International Edition **2002**, *41*, 2008; (b) F. Fache, E. Schulz, M. L. Tommasino and M. Lemaire, *Nitrogen-containing ligands for asymmetric homogeneous and heterogeneous catalysis.* Chemical Reviews **2000**, *100*, 2159.

4. G.-Q. Lin, Y.-M. Li and A. S.-C. Chan. *Principles and applications of asymmetric synthesis*, Wiley-Interscience **2001**.

5. A. Berkessel and H. Gröger. *Asymmetric organocatalysis:from biomimetic concepts to applications in asymmetric synthesis*, Wiley-VCH **2005**.

6. G. W. Mellin and M. Katzenstein, *The saga of thalidomide. Neuropathy to embryopathy, with case reports of congenital anomalies.* The New England Journal of Medicine **1962**, *267*, 1238.

7. S. C. Stinson, *Chiral drugs: in wake of new FDA guidelines, most drug firms are developing single enantiomers, spawning a"chirotechnology"industry.* Chemical & Engineering News **1992**, *70*, 46.

8. (a) I. Ojima. *Catalytic asymmetric synthesis*. Weinheim, Wiley-VCH **2010**; (b) E. N. Jacobsen, A. Pfaltz and H. Yamamoto. *Comprehensive asymmetric catalysis*. Berlin, Springer **1999**; (c) V. C. J. M. J. Williams. *Catalysis in asymmetric synthesis*, Wiley-Blackwell **2009**.

9. (a) J. F. Young, J. A. Osborn, F. H. Jardine and G. Wilkinson, *Hydride intermediates in homogeneous hydrogenation reactions of olefins and acetylenes using rhodium catalysts.* Chemical Communications (London) **1965**, 131; (b) W. S. Knowles and M. J. Sabacky, *Catalytic asymmetric hydrogenation employing a soluble, optically active, rhodium complex.* Chemical Communications (London) **1968**, 1445.

10. Y. Izumi, *Methods of asymmetric synthesis—enantioselective catalytic hydrogenation.* Angewandte Chemie International Edition **1971**, *10*, 871.

11. W. S. Knowles, *Application of organometallic catalysis to the commercial production of L-DOPA.* Journal of Chemical Education **1986**, *63*, 222.

12. U. Matteoli, P. Frediani, M. Bianchi, C. Botteghi and S. Gladiali, *Asymmetric homogeneous catalysis by ruthenium complexes.* Journal of Molecular Catalysis **1981**, *12*, 265.

13. J. Takehara, S. Hashiguchi, A. Fujii, S.-i. Inoue, T. Ikariya and R. Noyori, *Amino alcohol effects on the ruthenium(II)-catalysed asymmetric transfer hydrogenation of ketones in propan-2-ol.* Chemical Communications **1996**, 233.

14. (a) V. Prelog and G. Helmchen, *Basic principles of the CIP-system and proposals for a revision.* Angewandte Chemie International Edition **1982**, *21*, 567; (b) R. S. Cahn, C. Ingold and V. Prelog, *Specification of molecular chirality.* Angewandte Chemie International Edition **1966**, *5*, 385.

15. A. D. McNaught and A. Wilkinson. *IUPAC. Compendium of chemical terminology*. Oxford, Blackwell Scientific Publications **1997**.

16. F. Maseras and D. Balcells, *Computational approaches to asymmetric synthesis.* New Journal of Chemistry **2007**, *31*, 333.

17. T. Leyssens, D. Peeters and J. N. Harvey, *Origin of enantioselective hydrogenation of ketones by RuH_2(diphosphine)(diamine) catalysts: A theoretical study.* Organometallics **2008**, *27*, 1514.

18. (a) R. Noyori and T. Ohkuma, *Asymmetric catalysis by architectural and functional molecular engineering: Practical chemo- and stereoselective hydrogenation of ketones.* Angewandte Chemie International Edition **2001**, *40*, 40; (b) T. Ohkuma, H. Ooka, S. Hashiguchi, T. Ikariya and R. Noyori, *Practical enantioselective hydrogenation of aromatic ketones.* Journal of the American Chemical Society **1995**, *117*, 2675.

19. G. Wernig, M. Kharas, D. Clary, G. Gilliland and T. George, *EXEL-8232, a small molecule JAK2 inhibitor, effectively treats thrombocytosis and extramedullary hematopoiesis in a murine model of myeloproliferative disease induced by MPLW515L.* Modern Pathology **2011**, *24*, 329a.

20. T. Ohkuma, H. Ooka, S. Hashiguchi, T. Ikariya and R. Noyori, *Practical Enantioselective Hydrogenation of Aromatic Ketones.* J Am Chem Soc **1995**, *117*, 2675.

21. (a) R. Noyori and T. Ohkuma, *Rapid, productive and stereoselective hydrogenation of ketones.* Pure and Applied Chemistry **1999**, *71*, 1493; (b) *Handbook of homogeneous hydrogenation*. Weinheim, Wiley-VCH **2007**.

22. (a) T. Ohkuma, M. Koizumi, H. Doucet, T. Pham, M. Kozawa, K. Murata, E. Katayama, T. Yokozawa*, et al.*, *Asymmetric hydrogenation of alkenyl, cyclopropyl, and aryl ketones. $RuCl_2$(xylbinap)(1,2-diamine) as a precatalyst exhibiting a wide scope.* Journal of the American Chemical Society **1998**, *120*, 13529; (b) T. Ohkuma, M.

Koizumi, K. Muniz, G. Hilt, C. Kabuto and R. Noyori, *trans-RuH(η^1-BH_4)(binap)(1,2-diamine): a catalyst for asymmetric hydrogenation of simple ketones under base-free conditions.* Journal of the American Chemical Society **2002**, *124*, 6508.

23. H. Doucet, T. Ohkuma, K. Murata, T. Yokozawa, M. Kozawa, E. Katayama, A. F. England, T. Ikariya and R. Noyori, *trans-[$RuCl_2$(phosphane)$_2$(1,2-diamine)] and chiral trans-[$RuCl_2$(diphosphane)(1,2-diamine)]: Shelf-stable precatalysts for the rapid, productive, and stereoselective hydrogenation of ketones.* Angewandte Chemie International Edition **1998**, *37*, 1703.

24. A. G. Hu, H. L. Ngo and W. B. Lin, *4,4 '-disubstituted BINAPs for highly enantioselective Ru-catalyzed asymmetric hydrogenation of ketones.* Organic Letters **2004**, *6*, 2937.

25. T. Ohkuma, H. Ooka, N. Arai, K. Azuma and N. Kurono, *Asymmetric hydrogenation of aromatic ketones catalyzed by the TolBINAP/DMAPEN-ruthenium(II) complex: a significant effect of N-substituents of chiral 1,2-diamine ligands on enantioselectivity.* Journal of Organic Chemistry **2008**, *73*, 9084.

26. (a) R. H. Morris, W. W. N. O and A. J. Lough, *Mechanistic investigation of the hydrogenation of ketones catalyzed by a ruthenium(II) complex featuring an N-heterocyclic carbene with a tethered primary amine donor: evidence for an inner sphere mechanism.* Organometallics **2011**, *30*, 1236; (b) M. Z. D. Iuliis and R. H. Morris, *Kinetic hydrogen/deuterium effects in the direct hydrogenation of ketones catalyzed by a well-defined ruthenium diphosphine diamine complex.* Journal of the American Chemical Society **2009**, *131*, 11263; (c) C. P. Casey, S. E. Beetner and J. B. Johnson, *Spectroscopic determination of hydrogenation rates and intermediates during carbonyl hydrogenation catalyzed by Shvo's hydroxycyclopentadienyl diruthenium hydride agrees with kinetic modeling based on independently measured rates of elementary reactions.* Journal of the American Chemical Society **2008**, *130*, 2285; (d) C. A. Sandoval, T. Ohkuma, K. Muniz and R. Noyori, *Mechanism of asymmetric hydrogenation of ketones catalyzed by BINAP/1,2-diamine-ruthenium(II) complexes.* Journal of the American Chemical Society **2003**, *125*, 13490; (e) C. P. Casey and J. B. Johnson, *Kinetic isotope effect evidence for a concerted hydrogen transfer mechanism in transfer Hydrogenations catalyzed by [p-(Me_2CH)C_6H_4Me]Ru-(NHCHPhCHPhN$SO_2C_6H_4$-p-CH_3).* Journal of Organic Chemistry **2003**, *68*, 1998; (f) K. Abdur-Rashid, S. E. Clapham, A. Hadzovic, J. N. Harvey, A. J. Lough and R. H. Morris, *Mechanism of the hydrogenation of ketones catalyzed by trans-dihydrido(diamine)ruthenium(II) complexes.* Journal of the American Chemical Society **2002**, *124*, 15104; (g) C. P. Casey, S. W. Singer, D. R. Powell, R. K. Hayashi and M. Kavana, *Hydrogen transfer to carbonyls and imines from a hydroxycyclopentadienyl ruthenium hydride: Evidence for concerted hydride and proton transfer.* Journal of the American Chemical Society **2001**, *123*, 1090.

27. (a) C. A. Sandoval, Y. Yamaguchi, T. Ohkuma, K. Kato and R. Noyori, *Solution structures and behavior of trans-RuH(η^1-BH_4)(binap)(1,2-diamine) complexes.* Magnetic Resonance in Chemistry **2006**, *44*, 66; (b) R. H. Morris and M. Z. D. Iuliis, *Kinetic hydrogen/deuterium effects in the direct hydrogenation of ketones catalyzed by a well-defined ruthenium diphosphine diamine complex.* Journal of the American Chemical Society **2009**, *131*, 11263.

28. (a) D. Di Tommaso, S. A. French, A. Zanotti-Gerosa, F. Hancock, E. J. Palin and C. R. A. Catlow, *Computational study of the factors controlling enantioselectivity in ruthenium(II) hydrogenation catalysts.* Inorganic Chemistry **2008**, *47*, 2674; (b) S. A. French, D. Di Tommaso, A. Zanotti-Gerosa, F. Hancock and C. R. A. Catlow, *New insights into the enantioselectivity in the hydrogenation of prochiral ketones.* Chemical Communications **2007**, 2381; (c) D. Di Tommaso, S. A. French and C. R. A. Catlow, *The H_2-hydrogenation of ketones catalysed by ruthenium(II) complexes: A density functional theory study.* Journal of Molecular Structure: THEOCHEM **2007**, *812*, 39; (d) M. Yamakawa, H. Ito and R. Noyori, *The metal-ligand bifunctional catalysis: A theoretical study on the ruthenium(II)-catalyzed hydrogen transfer between alcohols and carbonyl compounds.* Journal of the American Chemical Society **2000**, *122*, 1466; (e) D. G. I. Petra, J. N. H. Reek, J. W. Handgraaf, E. J. Meijer, P. Dierkes, P. C. J. Kamer, J. Brussee, H. E. Schoemaker and P. W. N. M. van Leeuwen, *Chiral induction effects in ruthenium(II) amino alcohol catalysed asymmetric transfer hydrogenation of ketones: An experimental and theoretical approach.* Chemistry - A European Journal **2000**, *6*, 2818.

29. (a) S. Takebayashi, N. Dabral, M. Miskolzie and S. H. Bergens, *Experimental investigations of a partial Ru-O bond during the metal-ligand bifunctional addition in Noyori-type enantioselective ketone hydrogenation.* Journal of the American Chemical Society **2011**, *133*, 9666; (b) S. H. Bergens and R. J. Hamilton, *Direct observations of the metal-ligand bifunctional addition step in an enantioselective ketone hydrogenation.* Journal of the American Chemical Society **2008**, *130*, 11979; (c) R. J. Hamilton and S. H. Bergens, *An unexpected possible role of base in asymmetric catalytic hydrogenations of ketones. Synthesis and characterization of several key catalytic intermediates.* Journal of the American Chemical Society **2006**, *128*, 13700; (d) R. J. Hamilton, C. G. Leong, G. Bigam, M. Miskolzie and S. H. Bergens, *A ruthenium-dihydrogen putative intermediate in ketone hydrogenation.* Journal of the American Chemical Society **2005**, *127*, 4152; (e) K. Abdur-Rashid, M. Faatz, A. J. Lough and R. H. Morris, *Catalytic cycle for the asymmetric hydrogenation of prochiral ketones to chiral alcohols: Direct hydride and proton transfer from chiral catalysts trans-$Ru(H)_2$(diphosphine)(diamine) to ketones and direct addition of dihydrogen to the resulting hydridoamido complexes.* Journal of the American Chemical Society **2001**, *123*, 7473.

30. (a) J. S. M. Samec, J. E. Backvall, P. G. Andersson and P. Brandt, *Mechanistic aspects of transition metal-catalyzed hydrogen transfer reactions.* Chemical Society Reviews **2006**, *35*, 237; (b) S. E. Clapham, A. Hadzovic and R. H. Morris, *Mechanisms of the H_2-hydrogenation and transfer hydrogenation of polar bonds catalyzed by ruthenium hydride complexes.* Coordination Chemistry Reviews **2004**, *248*, 2201; (c) C. A. Sandoval, T. Ohkuma, K. Muniz and R. Noyori, *Mechanism of asymmetric hydrogenation of ketones catalyzed by BINAP/1,2-diamine-ruthenium(II) complexes.* Journal of the American Chemical Society **2003**, *125*, 13490; (d) K. Abdur-Rashid, S. E. Clapham, A. Hadzovic, J. N. Harvey, A. J. Lough and R. H. Morris, *Mechanism of the hydrogenation of ketones catalyzed by trans-dihydrido(diamine)ruthenium(II) complexes.* Journal of the American Chemical Society **2002**, *124*, 15104; (e) R. Noyori, M. Yamakawa and S. Hashiguchi, *Metal-ligand bifunctional catalysis: A nonclassical mechanism for asymmetric hydrogen transfer between alcohols and carbonyl compounds.* Journal of Organic Chemistry **2001**, *66*, 7931; (f) M. Yamakawa, H. Ito and R. Noyori, *The metal-ligand bifunctional catalysis: A theoretical study on the*

ruthenium(II)-catalyzed hydrogen transfer between alcohols and carbonyl compounds. Journal of the American Chemical Society **2000**, *122*, 1466.

31. K. Abdur-Rashid, A. J. Lough and R. H. Morris, *Ruthenium dihydride $RuH_2(PPh_3)_2$[(R,R)-cyclohexyldiamine] and ruthenium monohydride $RuHCl(PPh_3)_2$[(R,R)-cyclohexyldiamine]: Active catalyst and catalyst precursor for the hydrogenation of ketones and imines.* Organometallics **2000**, *19*, 2655.

32. (a) J. K. Liu, X. F. Wu, D. Di Tommaso, J. A. Iggo, C. R. A. Catlow, J. Bacsa and J. L. Xiao, *A multilateral mechanistic study into asymmetric transfer hydrogenation in water.* Chemistry-a European Journal **2008**, *14*, 7699; (b) J. W. Handgraaf and E. J. Meijer, *Realistic modeling of ruthenium-catalyzed transfer hydrogenation.* Journal of the American Chemical Society **2007**, *129*, 3099.

33. (a) J. M. Brown and R. J. Deeth, *Is enantioselectivity predictable in asymmetric catalysis?* Angewandte Chemie International Edition **2009**, *48*, 4476; (b) J.-W. Handgraaf, J. N. H. Reek and E. J. Meijer, *Iridium(I) versus ruthenium(II). A computational study of the transition metal catalyzed transfer hydrogenation of ketones.* Organometallics **2003**, *22*, 3150.

34. (a) D. A. Alonso, P. Brandt, S. J. M. Nordin and P. G. Andersson, *Ru(arene)(amino alcohol)-catalyzed transfer hydrogenation of ketones: mechanism and origin of enantioselectivity.* Journal of the American Chemical Society **1999**, *121*, 9580; (b) C. Hedberg, K. Kallstrom, P. I. Arvidsson, P. Brandt and P. G. Andersson, *Mechanistic insights into the phosphine-free RuCp*-diamine-catalyzed hydrogenation of aryl ketones: experimental and theoretical evidence for an alcohol-mediated dihydrogen activation.* Journal of the American Chemical Society **2005**, *127*, 15083.

35. T. C. Nugent and M. El-Shazly, *Chiral amine synthesis ―recent developments and trends for enamide reduction, reductive amination, and imine reduction.* Advanced Synthesis & Catalysis **2010**, *352*, 753.

36. R. P. Tripathi, S. S. Verma, J. Pandey and V. K. Tiwari, *Recent development on catalytic reductive amination and applications.* Current Organic Chemistry **2008**, *12*, 1093.

37. (a) S. Gomez, J. A. Peters and T. Maschmeyer, *The reductive amination of aldehydes and ketones and the hydrogenation of nitriles: mechanistic aspects and selectivity control.* Advanced Synthesis & Catalysis **2002**, *344*, 1037; (b) V. I. Tararov and A. Borner, *Approaching highly enantioselective reductive amination.* Synlett **2005**, 203.

38. A. F. Abdel-Magid and S. J. Mehrman, *A review on the use of sodium triacetoxyborohydride in the reductive amination of ketones and aldehydes.* Organic Process Research & Development **2006**, *10*, 971.

39. (a) D. Steinhuebel, Y. Sun, K. Matsumura, N. Sayo and T. Saito, *Direct asymmetric reductive amination.* Journal of the American Chemical Society **2009**, *131*, 11316; (b) L. Rubio-Pérez, F. J. Pérez-Flores, P. Sharma, L. Velasco and A. Cabrera,

Stable preformed chiral palladium catalysts for the one-pot asymmetric reductive amination of ketones. Organic Letters **2009**, *11*, 265; (c) C. Li, B. Villa-Marcos and J. Xiao, *Metal−Brønsted acid cooperative catalysis for asymmetric reductive amination.* Journal of the American Chemical Society **2009**, *131*, 6967; (d) M. Höhne and U. T. Bornscheuer, *Biocatalytic routes to optically active amines.* Chemcatchem **2009**, *1*, 42; (e) M. D. Bhor, M. J. Bhanushali, N. S. Nandurkar and B. M. Bhanage, *Direct reductive amination of carbonyl compounds with primary/secondary amines using recyclable water-soluble Fe^{II}/EDTA complex as catalyst.* Tetrahedron Letters **2008**, *49*, 965; (f) S. M. A. D. Wildeman, T. Sonke, H. E. Schoemaker and O. May, *Biocatalytic reductions: from lab curiosity to"first choice".* Accounts of Chemical Research **2007**, *40*, 1260; (g) D. Gnanamgari, A. Moores, E. Rajaseelan and R. H. Crabtree, *Transfer hydrogenation of imines and alkenes and direct reductive amination of aldehydes catalyzed by triazole-derived iridium(I) carbene complexes.* Organometallics **2007**, *26*, 1226; (h) R. I. Storer, D. E. Carrera, Y. Ni and D. W. C. MacMillan, *Enantioselective organocatalytic reductive amination.* Journal of the American Chemical Society **2006**, *128*, 84; (i) A. Robichaud and A. Nait Ajjou, *First example of direct reductive amination of aldehydes with primary and secondary amines catalyzed by water-soluble transition metal catalysts.* Tetrahedron Letters **2006**, *47*, 3633; (j) S. Hoffmann, M. Nicoletti and B. List, *Catalytic asymmetric reductive amination of aldehydes via dynamic kinetic resolution.* Journal of the American Chemical Society **2006**, *128*, 13074; (k) D. Imao, S. Fujihara, T. Yamamoto, T. Ohta and Y. Ito, *Effective reductive amination of carbonyl compounds with hydrogen catalyzed by iridium complex in organic solvent and in ionic liquid.* Tetrahedron **2005**, *61*, 6988; (l) T. Bunlaksananusorn and F. Rampf, *A facile one-pot synthesis of chiral β-amino esters.* Synlett **2005**, *2005*, 2682; (m) S. Ogo, K. Uehara, T. Abura and S. Fukuzumi, *pH-dependent chemoselective synthesis of α-amino acids. reductive amination of α-keto acids with ammonia catalyzed by acid-stable iridium hydride complexes in water.* Journal of the American Chemical Society **2004**, *126*, 3020; (n) G. D. Williams, R. A. Pike, C. E. Wade and M. Wills, *A one-pot process for the enantioselective synthesis of amines via reductive amination under transfer hydrogenation conditions.* Organic Letters **2003**, *5*, 4227; (o) R. Kadyrov, T. H. Riermeier, U. Dingerdissen, V. Tararov and A. Börner, *The first highly enantioselective homogeneously catalyzed asymmetric reductive amination: synthesis of α,N-benzylamino acids.* The Journal of Organic Chemistry **2003**, *68*, 4067; (p) R. Kadyrov and T. H. Riermeier, *Highly enantioselective hydrogen-transfer reductive amination: catalytic asymmetric synthesis of primary amines.* Angewandte Chemie International Edition **2003**, *42*, 5472; (q) Y. Chi, Y.-G. Zhou and X. Zhang, *Highly enantioselective reductive amination of simple aryl ketones catalyzed by Ir-f-Binaphane in the presence of titanium(IV) isopropoxide and iodine.* The Journal of Organic Chemistry **2003**, *68*, 4120; (r) M. Kitamura, D. Lee, S. Hayashi, S. Tanaka and M. Yoshimura, *Catalytic Leuckart−Wallach-type reductive amination of ketones.* The Journal of Organic Chemistry **2002**, *67*, 8685; (s) T. Gross, A. M. Seayad, M. Ahmad and M. Beller, *Synthesis of primary amines: first homogeneously catalyzed reductive amination with ammonia.* Organic Letters **2002**, *4*, 2055.

40. (a) L. Li, J. S. Wu, F. Wang, J. Liao, H. Zhang, C. X. Lian, J. Zhu and J. G. Deng, *Asymmetric transfer hydrogenation of ketones and imines with novel water-soluble chiral diamine as ligand in neat water.* Green Chemistry **2007**, *9*, 23; (b) J. Canivet and G. Suss-Fink, *Water-soluble arene ruthenium catalysts containing sulfonated diamine ligands for asymmetric transfer hydrogenation of alpha-aryl ketones and imines in aqueous solution.* Green Chemistry **2007**, *9*, 391; (c) J. S. Wu, F. Wang, Y. P. Ma, X. C.

Cui, L. F. Cun, J. G. Deng and B. L. Yu, *Asymmetric transfer hydrogenation of imines and iminiums catalyzed by a water-soluble catalyst in water.* Chemical Communications **2006**, 1766; (d) U. M. Lindstrom, *Stereoselective organic reactions in water.* Chemical Reviews **2002**, *102*, 2751.

41. D. R. Hartree, *The wave mechanics of an atom with a non-coulomb central field. Part I. theory and methods.* Proceedings of the Cambridge Philosophical Society **1928**, *24*, 89.

42. V. Fock, *Näherungsmethode zur Lösung des quantenmechanischen Mehrkörperproblems* Zeitschrift für Physik A Hadrons and Nuclei **1930**, *61*, 126.

43. A. Szabo and N. S. Ostlund. *Modern quantum chemistry: introduction to advanced electronic structure theory*. Now York, Dover Pub. Inc. **1996**.

44. C. Møller and M. S. Plesset, *Note on an approximation treatment for many-electron systems.* Physical Review **1934**, *46*, 618.

45. (a) J. Čížek, *On the correlation problem in atomic and molecular systems. calculation of wavefunction components in ursell‐type expansion using quantum‐field theoretical methods.* Journal of Chemical Physics **1966**, *45*, 4256; (b) J. Čížek, *On the use of the cluster expansion and the technique of diagrams in calculations of correlation effects in atoms and molecules.* Advances in Chemical Physics **1966**, *14*, 35.

46. (a) E. Fermi, *Eine statistische Methode zur Bestimmung einiger Eigenschaften des Atoms und ihre Anwendung auf die Theorie des periodischen Systems der Elemente.* Zeitschrift für Physik A Hadrons and Nuclei **1928**, *48*, 73; (b) L. H. Thomas, *The calculation of atomic fields.* Proceedings of the Cambridge Philosophical Society **1927**, *23*, 542.

47. P. A. M. Dirac, *On the annihilation of electrons and protons.* Mathematical Proceedings of the Cambridge Philosophical Society **1930**, *26*, 361.

48. W. Kohn and L. J. Sham, *Self-consistent equations including exchange and correlation effects.* Physical Review **1965**, *140*, 1133.

49. P. Hohenberg and W. Kohn, *Inhomogeneous electron gas.* Physical Review **1964**, *136*, B864.

50. J. P. Perdew and A. Zunger, *Self-interaction correction to density-functional approximations for many-electron systems.* Physical Review B **1981**, *23*, 5048.

51. D. M. Ceperley and B. J. Alder, *Ground-state of the electron-gas by a stochastic method.* Physical Review Letters **1980**, *45*, 566.

52. (a) J. P. Perdew and W. Yue, *Erratum: accurate and simple density functional for the electronic exchange energy: generalized gradient approximation.* Physical Review B **1989**, *40*, 3399; (b) J. P. Perdew and W. Yue, *Accurate and simple density functional for the electronic exchange energy: Generalized gradient approximation.* Physical

Review B **1986**, *33*, 8800; (c) J. P. Perdew, *Density-functional approximation for the correlation energy of the inhomogeneous electron gas.* Physical Review B **1986**, *33*, 8822; (d) J. P. Perdew, K. Burke and Y. Wang, *Generalized gradient approximation for the exchange-correlation hole of a many-electron system.* Physical Review B - Condensed Matter and Materials Physics **1996**, *54*, 16533; (e) J. P. Perdew, *Generalized gradient approximations for exchange and correlation: A look backward and forward.* Physica B: Physics of Condensed Matter **1991**, *172*, 1.

53. J. P. Perdew, K. Burke and M. Ernzerhof, *Generalized gradient approximation made simple.* Physical Review Letters **1996**, *77*, 3865.

54. (a) A. D. Becke, *Density-functional thermochemistry .V. Systematic optimization of exchange-correlation functionals.* Journal of Chemical Physics **1997**, *107*, 8554; (b) W. Kohn, A. D. Becke and R. G. Parr, *Density functional theory of electronic structure.* Journal of Physical Chemistry **1996**, *100*, 12974.

55. (a) P. J. Stephens, F. J. Devlin, C. F. Chabalowski and M. J. Frisch, *Ab-Initio calculation of vibrational absorption and circular-dichroism spectra using density-functional force-fields.* Journal of Physical Chemistry **1994**, *98*, 11623; (b) A. D. Becke, *Density functional thermochemistry. III. The role of exact exchange.* Journal of Chemical Physics **1993**, *98*, 5648; (c) C. T. Lee, W. T. Yang and R. G. Parr, *Development of the Colic-Salvetti correlation-energy formula into a functional of the electron density.* Physical Review B **1988**, *37*, 785.

56. (a) C. Adamo and V. Barone, *Toward reliable density functional methods without adjustable parameters: The PBE0 model.* Journal of Chemical Physics **1999**, *110*, 6158; (b) J. P. Perdew, M. Ernzerhof and K. Burke, *Rationale for mixing exact exchange with density functional approximations.* Journal of Chemical Physics **1996**, *105*, 9982; (c) J. P. Perdew, K. Burke and M. Ernzerhof, *Generalized gradient approximation made simple.* Physical Review Letters **1996**, *77*, 3865.

57. A. D. Becke, *Density-functional exchange-energy approximation with correct asymptotic behavior.* Physical Review A **1988**, *38*, 3098.

58. S. H. Vosko, L. Wilk and M. Nusair, *Accurate spin-dependent electron liquid correlation energies for local spin density calculations: a critical analysis.* Canadian Journal of Physics **1980**, *58*, 1200.

59. (a) S. Grimme, J. Antony, S. Ehrlich and H. Krieg, *A consistent and accurate ab initio parametrization of density functional dispersion correction (DFT-D) for the 94 elements H-Pu.* Journal of Chemical Physics **2010**, *132*; (b) S. Grimme, *Semiempirical GGA-type density functional constructed with a long-range dispersion correction.* Journal of Computational Chemistry **2006**, *27*, 1787.

60. H. Dorsett and A. White. *Overview of molecular modelling and ab initio molecular orbital methods suitable for use with energetic materials*, DSTO Aeronautical and Maritime Research Laboratory **2000**.

61. J. C. Slater, *Atomic shielding constants.* Physical Review **1930**, *36*, 57.

62. (a) E. R. Davidson and D. Feller, *Basis set selection for molecular calculations.* Chemical Reviews **1986**, *86*, 681; (b) J. B. Foresman and A. Frisch. *Exploring chemistry with electronic structure methods*, Gaussian **1996**; (c) R. C. Raffenet, *General contraction of Gaussian atomic orbitals - core, valence, polarization, and diffuse basis sets - molecular integral evaluation.* Journal of Chemical Physics **1973**, *58*, 4452.

63. (a) W. J. Hehre, R. F. Stewart and J. A. Pople, *Self-consistent molecular orbital methods. I. Use of Gaussian expansions of Slater-type atomic orbitals.* The Journal of Chemical Physics **1969**, *51*, 2657; (b) W. J. Pietro and W. J. Hehre, *Molecular-orbital theory of the properties of inorganic and organometallic compounds .3. STO-3G basis-sets for 1st-row and 2nd-row transition-metals.* Journal of Computational Chemistry **1983**, *4*, 241; (c) W. J. Hehre, R. Ditchfield, R. F. Stewart and J. A. Pople, *Self-consistent molecular orbital methods. IV. Use of gaussian expansions of slatertype orbitals. Extension to second-row molecules.* The Journal of Chemical Physics **1970**, *52*, 2763.

64. (a) A. Schafer, H. Horn and R. Ahlrichs, *Fully optimized contracted Gaussian-basis sets for atoms Li to Kr.* Journal of Chemical Physics **1992**, *97*, 2571; (b) T. H. Dunning, *Gaussian basis functions for use in molecular calculations. 1. Contraction of (9s5p) atomic basis sets for first-row atoms.* Journal of Chemical Physics **1970**, *53*, 2823; (c) T. H. Dunning, *Gaussian basis functions for use in molecular calculations. Contraction of (12s9p) atomic basis sets for the second row atoms.* Chemical Physics Letters **1970**, *7*, 423.

65. (a) K. D. Dobbs and W. J. Hehre, *Molecular-orbital theory of the properties of inorganic and organometallic compounds. 6. Extended basis-sets for 2nd-row transition-metals.* Journal of Computational Chemistry **1987**, *8*, 880; (b) K. D. Dobbs and W. J. Hehre, *Molecular-orbital theory of the properties of inorganic and organometallic compounds .5. Extended basis-sets for 1st-row transition-metals.* Journal of Computational Chemistry **1987**, *8*, 861; (c) K. D. Dobbs and W. J. Hehre, *Molecular-orbital theory of the properties of inorganic and organometallic compounds 4 - Extended basis-sets for 3rd-row and 4th-row, main-group elements.* Journal of Computational Chemistry **1986**, *7*, 359; (d) M. S. Gordon, J. S. Binkley, J. A. Pople, W. J. Pietro and W. J. Hehre, *Self-consistent molecular-orbital methods. 22. Small split-valence basis sets for second-row elements.* Journal of the American Chemical Society **1982**, *104*, 2797; (e) J. S. Binkley, J. A. Pople and W. J. Hehre, *Self-consistent molecular orbital methods. 21. Small split-valence basis sets for first-row elements.* Journal of the American Chemical Society **1980**, *102*, 939.

66. A. Schafer, C. Huber and R. Ahlrichs, *Fully optimized contracted Gaussian-basis sets of triple zeta valence quality for atoms Li to Kr.* Journal of Chemical Physics **1994**, *100*, 5829.

67. (a) T. Clark, J. Chandrasekhar, G. W. Spitznagel and P. V. Schleyer, *Efficient diffuse function-augmented basis-sets for anion calculations. 3. The 3-21+G basis set for 1st-row elements, Li-F.* Journal of Computational Chemistry **1983**, *4*, 294; (b) http://www.shodor.org/chemviz/basis/teachers/background.html.

68. D. J. Singh. *Planewaves, Pseudopotential and the LAPW method*. Massachusetts, Kluwer Aca. Pub. **1994**.

69. (a) A. Filippetti, A. Satta, D. Vanderbilt and W. Zhong, *Hardness conservation as a new transferability criterion: Application to fully nonlocal pseudopotentials.* International Journal of Quantum Chemistry **1997**, *61*, 421; (b) B. Delley, *Hardness conserving semilocal pseudopotentials.* Physical Review B - Condensed Matter and Materials Physics **2002**, *66*, 1551251.

70. (a) P. J. Hay and W. R. Wadt, *Abinitio effective core potentials for molecular calculations —potentials for the transition-metal atoms Sc to Hg.* Journal of Chemical Physics **1985**, *82*, 270; (b) P. J. Hay and W. R. Wadt, *Abinitio effective core potentials for molecular calculations —potentials for K to Au including the outermost core orbitals.* Journal of Chemical Physics **1985**, *82*, 299.

71. (a) S. Goedecker, M. Teter and J. Hutter, *Separable dual-space Gaussian pseudopotentials.* Physical Review B **1996**, *54*, 1703; (b) C. Hartwigsen, S. Goedecker and J. Hutter, *Relativistic separable dual-space Gaussian pseudopotentials from H to Rn.* Physical Review B **1998**, *58*, 3641; (c) M. Krack, *Pseudopotentials for H to Kr optimized for gradient-corrected exchange-correlation functionals.* Theoretical Chemistry Accounts **2005**, *114*, 145.

72. Arfken G B, Weber H. J. and H. F. *Mathematical methods for physicists*, Academic Press **2005**.

73. J. Daniel, *Convergence of the conjugate gradient method with computationally convenient modifications.* Numerische Mathematik **1967**, *10*, 125.

74. A. Miklavc and I. W. M. Smith, *Vibrational relaxation of C_2H_2 and C_2D_2 by vibration-rotation, translation (V-R, T) energy transfer.* Journal of the Chemical Society, Faraday Transactions 2 **1988**, *84*, 227.

75. (a) C. Peng, P. Y. Ayala, H. B. Schlegel and M. J. Frisch, *Using redundant internal coordinates to optimize equilibrium geometries and transition states.* Journal of Computational Chemistry **1996**, *17*, 49; (b) C. Peng and H. B. Schlegel, *Combining synchronous transit and quasi-Newton methods to find transition states.* Israel J. of Chem. **1993**, *33*, 449.

76. (a) H. Jónsson, G. Mills and K. W. Jacobsen, *Nudged elastic band method for finding minimum energy paths of transitions.* Classical and Quantum Dynamics in Condensed Phase Simulations **1998**, 385; (b) G. Henkelman, B. P. Uberuaga and H. Jónsson, *A climbing image nudged elastic band method for finding saddle points and minimum energy paths.* Journal of Chemical Physics **2000**, *113*, 9901; (c) G. Mills and H. Jónsson, *Quantum and thermal effects in H_2 dissociative adsorption: Evaluation of free energy barriers in multidimensional quantum systems.* Physical Review Letters **1994**, *72*, 1124; (d) S. A. Trygubenko and D. J. Wales, *A doubly nudged elastic band method for finding transition states.* Journal of Chemical Physics **2004**, *120*, 2082.

77. D. Sheppard, R. Terrell and G. Henkelman, *Optimization methods for finding minimum energy paths.* Journal of Chemical Physics **2008**, *128*.

78. A. Klamt and V. Jonas, *Treatment of the outlying charge in continuum solvation models.* Journal of Chemical Physics **1996**, *105*, 9972.

79. A. Klamt and G. Schuurmann, *COSMO: a new approach to dielectric screening in solvents with explicit expressions for the screening energy and its gradient.* J. Chem. Soc., Perkin Trans. 2 **1993**, 799.

80. J. Tomasi and M. Persico, *Molecular-interactions in solution: an overview of methods based on continuous distributions of the solvent.* Chemical Reviews **1994**, *94*, 2027.

81. A. Klamt, *Conductor-like screening model for real solvents - a new approach to the quantitative calculation of solvation phenomena.* Journal of Physical Chemistry **1995**, *99*, 2224.

82. K. Baldridge and A. Klamt, *First principles implementation of solvent effects without outlying charge error.* Journal of Chemical Physics **1997**, *106*, 6622.

83. M. Cossi, V. Barone, R. Cammi and J. Tomasi, *Ab initio study of solvated molecules: a new implementation of the polarizable continuum model.* Chemical Physics Letters **1996**, *255*, 327.

84. (a) B. Delley, *From molecules to solids with the DMol^3 approach.* Journal of Chemical Physics **2000**, *113*, 7756; (b) B. Delley, *An all-electron numerical-method for solving the local density functional for polyatomic-molecules.* Journal of Chemical Physics **1990**, *92*, 508.

85. G. W. T. M.J. Frisch, H.B. Schlegel, G.E. Scuseria, M.A. Robb, J.R. Cheeseman, J.A. Montgomery, Jr., T. Vreven, K.N. Kudin, J.C. Burant, J.M. Millam, S.S. Iyengar, J. Tomasi, V. Barone, B. Mennucci, M. Cossi, G. Scalmani, N. Rega, G.A. Petersson, H. Nakatsuji, M. Hada, M. Ehara, K. Toyota, R. Fukuda, J. Hasegawa, M. Ishida, T. Nakajima, Y. Honda, O. Kitao, H. Nakai, M. Klene, X. Li, J.E. Knox, H.P. Hratchian, J.B. Cross, C. Adamo, J. Jaramillo, R.Gomperts, R.E. Stratmann, O. Yazyev, A.J. Austin, R. Cammi, C. Pomelli, J.W. Ochterski, P.Y. Ayala, K. Morokuma, G.A. Voth, P. Salvador, J.J. Dannenberg, V.G. Zakrzewski, S. Dapprich, A.D. Daniels, M.C. Strain, O. Farkas, D.K. Malick, A.D. Rabuck, K. Raghavachari, J.B. Foresman, J.V. Ortiz, Q. Cui, A.G. Baboul, S. Clifford, J. Cioslowski, B.B. Stefanov, G. Liu, A. Liashenko, P. Piskorz,I. Komaromi, R.L. Martin, D.J. Fox, T. Keith, M.A. Al-Laham, C.Y. Peng, A. Nanayakkara, M. Challacombe, P.M.W. Gill, B. Johnson, W. Chen, M.W. Wong, C. Gonzalez, J.A. Pople, *Gaussian 03, Revision D.01.* **2004**.

86. J. VandeVondele, M. Krack, F. Mohamed, M. Parrinello, T. Chassaing and J. Hutter, *Quickstep: Fast and accurate density functional calculations using a mixed Gaussian and plane waves approach.* Computer Physics Communications **2005**, *167*, 103.

87. Y. Inada and H. Orita, *Efficiency of numerical basis sets for predicting the binding energies of hydrogen bonded complexes: Evidence of small basis set superposition*

error compared to Gaussian basis sets. Journal of Computational Chemistry **2008**, *29*, 225.

88. T. Aaltonen, J. Adelman, T. Akimoto, M. G. Albrow, B. A. Gonzalez, S. Amerio, D. Amidei, A. Anastassov*, et al.*, *Direct bound on the total decay width of the top quark in p(p)over-bar collisions at root s=1.96 TeV.* Physical Review Letters **2009**, *102*.

89. K. Raghavachari, *Perspective on "density functional thermochemistry. III. The role of exact exchange" —Becke AD (1993) J Chem Phys 98:5648-52.* Theoretical Chemistry Accounts **2000**, *103*, 361.

90. F. A. Hamprecht, A. J. Cohen, D. J. Tozer and N. C. Handy. *Development and assessment of new exchange-correlation functionals*, AIP **1998**.

91. (a) A. D. Becke, *Density-functional thermochemistry .4. A new dynamical correlation functional and implications for exact-exchange mixing.* Journal of Chemical Physics **1996**, *104*, 1040; (b) Y. Zhao, B. J. Lynch and D. G. Truhlar, *Development and assessment of a new hybrid density functional model for thermochemical kinetics.* The Journal of Physical Chemistry A **2004**, *108*, 2715.

92. S. H. Vosko, L. Wilk and M. Nusair, *Accurate spin-dependent electron liquid correlation energies for local spin density calculations: a critical analysis.* Canadian Journal of Physics **1980**, *58*, 1200.

93. C. Adamo and V. Barone, *Exchange functionals with improved long-range behavior and adiabatic connection methods without adjustable parameters: The mPW and mPW1PW models.* Journal of Chemical Physics **1998**, *108*, 664.

94. (a) T. Leininger, A. Nicklass, H. Stoll, M. Dolg and P. Schwerdtfeger, *The accuracy of the pseudopotential approximation .2. A comparison of various core sizes for indium pseudopotentials in calculations for spectroscopic constants of InH, InF, and InCl.* Journal of Chemical Physics **1996**, *105*, 1052; (b) T. Leininger, A. Nicklass, W. Kuchle, H. Stoll, M. Dolg and A. Bergner, *The accuracy of the pseudopotential approximation: Non-frozen-core effects for spectroscopic constants of alkali fluorides XF (X=K, Rb, Ca).* Chemical Physics Letters **1996**, *255*, 274; (c) D. Andrae, U. Haussermann, M. Dolg, H. Stoll and H. Preuss, *Energy-adjusted abinitio pseudopotentials for the 2nd and 3rd row transition-elements.* Theoretica Chimica Acta **1990**, *77*, 123; (d) M. Dolg, U. Wedig, H. Stoll and H. Preuss, *Energy-adjusted ab initio pseudopotentials for the first row transition elements.* The Journal of Chemical Physics **1987**, *86*, 866.

95. J. VandeVondele and J. Hutter, *Gaussian basis sets for accurate calculations on molecular systems in gas and condensed phases.* Journal of Chemical Physics **2007**, *127*, 114105.

96. G. Henkelman and H. Jonsson, *Improved tangent estimate in the nudged elastic band method for finding minimum energy paths and saddle points.* Journal of Chemical Physics **2000**, *113*, 9978.

97. B. Mennucci, J. Tomasi, R. Cammi, J. R. Cheeseman, M. J. Frisch, F. J. Devlin, S. Gabriel and P. J. Stephens, *Polarizable continuum model (PCM) calculations of solvent effects on optical rotations of chiral molecules.* The Journal of Physical Chemistry A **2002**, *106*, 6102.

98. (a) H.-Y. T. Chen, D. Di Tommaso, G. Hogarth and C. R. A. Catlow, *Correlating enantioselectivity with activation energies in the asymmetric hydrogenation of acetophenone catalysed by Noyori-type complexes* Journal. **2011**, DOI: 10.1007/s10562-011-0704-1 (in press); (b) H.-Y. T. Chen, D. Di Tommaso, G. Hogarth and C. R. A. Catlow, *The effects of ligand variation on enantioselective hydrogenation catalysed by RuH_2(diphosphine)(diamine) complexes*. Journal. **2011**, DOI: 10.1039/C1DT11244A (accepted)

99. (a) S. Enthaler, K. Junge and M. Beller, *Sustainable metal catalysis with iron: From rust to a rising star?* Angewandte Chemie International Edition **2008**, *47*, 3317; (b) C. Bolm, *A new iron age.* Nature Chemistry **2009**, *1*, 420.

100. (a) Y. Blum, D. Czarkie, Y. Rahamim and Y. Shvo, *(Cyclopentadienone) Ruthenium carbonyl complexes ―a new class of homogeneous hydrogenation catalysts.* Organometallics **1985**, *4*, 1459; (b) C. P. Casey and H. R. Guan, *An efficient and chemoselective iron catalyst for the hydrogenation of ketones.* Journal of the American Chemical Society **2007**, *129*, 5816; (c) R. H. Morris, *Asymmetric hydrogenation, transfer hydrogenation and hydrosilylation of ketones catalyzed by iron complexes.* Chemical Society Reviews **2009**, *38*, 2282.

101. (a) C. Sui-Seng, F. Freutel, A. J. Lough and R. H. Morris, *Highly efficient catalyst systems using iron complexes with a tetradentate pnnp ligand for the asymmetric hydrogenation of polar bonds.* Angewandte Chemie International Edition **2008**, *47*, 940; (b) C. Sui-Seng, F. N. Haque, A. Hadzovic, A. M. Puetz, V. Reuss, N. Meyer, A. J. Lough, M. Z. D. Iuliis and R. H. Morris, *Synthesis and characterization of iron(II) complexes with tetradentate diiminodiphosphine or diaminodiphosphine ligands as precatalysts for the hydrogenation of acetophenone.* Inorganic Chemistry **2009**, *48*, 735.

102. Y. Chen, Y. H. Tang and M. Lei, *A comparative study on the hydrogenation of ketones catalyzed by diphosphine-diamine transition metal complexes using DFT method.* Dalton Transactions **2009**, 2359.

103. K. Abdur-Rashid, M. Faatz, A. J. Lough and R. H. Morris, *Catalytic cycle for the asymmetric hydrogenation of prochiral ketones to chiral alcohols: Direct hydride and proton transfer from chiral catalysts trans-Ru(H)(2)(diphosphine)(diamine) to ketones and direct addition of dihydrogen to the resulting hydridoamido complexes.* Journal of the American Chemical Society **2001**, *123*, 7473.

104. N. Wiberg. *Holleman-Wiberg's Inorganic Chemistry*. New York, Academic Press **2011**.

105. *The CH-Pi Interaction: Evidence, Nature, and Consequences*. New York, Wiley-VCH **1998**.

106. H.-Y. T. Chen, D. Di Tommaso, G. Hogarth and C. R. A. Catlow, *trans-$Fe^{II}(H)_2$(diphosphine)(diamine) complexes as alternative catalysts for the asymmetric hydrogenation of ketones? A DFT study.* Dalton Transactions **2011**, *40*, 402.

107. (a) J. Mao and D. C. Baker, *A chiral rhodium complex for rapid asymmetric transfer hydrogenation of imines with high enantioselectivity.* Organic Letters **1999**, *1*, 841; (b) N. Uematsu, A. Fujii, S. Hashiguchi, T. Ikariya and R. Noyori, *Asymmetric transfer hydrogenation of imines.* Journal of the American Chemical Society **1996**, *118*, 4916.

108. F. L. Hirshfeld, *Bonded-atom fragments for describing molecular charge-densities.* Theoretica Chimica Acta **1977**, *44*, 129.

109. U. C. Singh and P. A. Kollman, *An approach to computing electrostatic charges for molecules.* Journal of Computational Chemistry **1984**, *5*, 129.